SEISMIC PERFORMANCE OF UNDERGROUND RESERVOIR STRUCTURES

by

Ashkaan Hushmand

B.S. Civil Engineering, University of California Irvine 2008

M.S. Civil Engineering, University of California Los Angeles 2009

A thesis submitted to the

Faculty of the Graduate School of the

University of Colorado in partial fulfillment

of the requirements for the degree of

Doctor of Philosophy

Department of Civil, Environmental, and Architectural Engineering

2016

This thesis entitled:

SEISMIC PERFORMANCE OF UNDERGROUND RESERVOIR STRUCTURES
written by Ashkaan Hushmand

has been approved for the Department of Civil, Environmental, and Architectural Engineering

_____
Dr. Shideh Dashti

_____
Dr. John S. McCartney

_____
Dr. Dobroslav Znidarcic

_____
Dr. Tad Pfeffer

_____
Dr. Scott Brandenberg

_____
Dr. Craig Davis

Date _____

The final copy of this thesis has been examined by the signatories, and we find that both the content and the form meet acceptable presentation standards of scholarly work in the above mentioned discipline.

ABSTRACT

Hushmand, Ashkaan (Ph.D., Civil, Environmental and Architectural Engineering)

Seismic Performance of Underground Reservoir Structures

Thesis directed by Professor Shideh Dashti

The majority of stiff-unyielding underground structures have performed well in recent earthquakes. The few cases of failure are mainly related to construction in poor ground conditions (e.g., soft fill, liquefiable soils, sloping ground) and inadequate or no seismic design. Currently there is disagreement among engineering professionals and design methodologies on seismic forces and deformations experienced by these structures, sometimes resulting in inaccurate design that maybe un-conservative or over-conservative. The current procedures used to evaluate seismic loading and deformations of these structures rely on over-simplified analytical methods or advance numerical tools that have not been validated against physical model tests. Previous analytical and numerical studies have identified key factors such as structural flexibility, base fixity, and wavelength as being important in the seismic response of these structures. However the commonly used simplified methods don't take into account these important factors.

Further, there is a lack of well-documented case studies and experimental research systematically evaluating the seismic response of stiff-unyielding buried structures that are restrained against excessive deformations at their base and roof. Therefore, a centrifuge experimental study of the seismic response of these structures was performed by varying the key parameters and monitoring seismic lateral earth pressures, racking displacements, bending moments, and soil-structure interaction. The results of these experiments provide a better understanding of the underlying mechanisms of soil-structure interaction near these structures and

their overall performance. The results also serve as a database for other researchers to calibrate their numerical tools.

A series of sixteen centrifuge model experiments representing 11 to 12 m-high reinforced concrete underground reservoir structures were conducted. The structure stiffness, backfill soil type and slope, embedment, container type (rigid versus flexible boundaries), fixity conditions, and ground motion characteristics were varied to evaluate their influence and relative importance on structural performance. The structures were buried in dry medium-dense sand at 60% relative density and compacted, site-specific silty sand with different backfill slopes. A suit of earthquake ground motions and sinusoidal motions with different frequencies were applied to the buried models. The application of sinusoidal motions in particular allowed for a comprehensive study of the influence of loading frequency in relation to the fundamental frequency of the site and structure.

TABLE OF CONTENTS

ACKNOWLEDGEMENT

I wish to express my sincere gratitude to my advisor, Professor Shideh Dashti, for her guidance, encouragement and helpful suggestions provided during the course of this investigation. Shideh has been an excellent advisor from the first day I arrived in Boulder. This thesis wouldn't have been possible without all the time and energy Professor Dashti invested in me throughout the entire duration of my research. A great amount of time in this research was spent implementing new centrifuge test procedures and Professor Dashti was deeply involved in every step of the way. I will never forget all the time she spent helping with the centrifuge tests and guiding me through the many challenges of this research.

I thank my co-advisor Professor John McCartney for his guidance, support and confidence in me throughout my research. His presence at CU Boulder was emotionally uplifting and motivated me to work hard. His effort in reviewing my technical papers and research is greatly appreciated.

This research was initiated and supported financially by the Los Angeles Department of Water and Power (LADWP) through HAI Inc. I would like to gratefully acknowledge Dr. Craig Davis of the LADWP for initially proposing the idea of this research and making this thesis possible. Valuable input was provided by Dr. Craig Davis during all phases of this project. I would also like to thank Dr. Craig Davis for participating in my thesis committee. I would like to thank Dr. Yangsoo Lee of the LADWP for contributing his centrifuge knowledge and overlooking the progress of this research. My special thanks also goes to Dr. Jianping Hu of the LADWP for his valuable input during the course of this research.

This project would not have been possible without the help of CU Boulder Centrifuge staff, student helpers and the staff at HAI Inc. I would like to especially thank Dr. Min Zhang for helping in all stages of the experiments and providing technical guidance in improving the tests. I learned

a great amount about instrumentation, data acquisition, data processing, and centrifuge knowledge from Dr. Min Zhang. Thanks to Dr. Majid Ghayoomi for assisting in the early phase of this research designing the FSB container and many other important things.

This thesis was partially supported by the Department of Civil, Environmental & Architectural Engineering at the University of Colorado Boulder through a Doctoral Assistantship for Completion of Dissertation.

I was fortunate enough to have the support of my good friends during this period of my life. I would like to thank Amin Hariri and Farhad Pourkamali for providing such a fun and friendly environment at CU Boulder.

Finally I would like to thank my family for supporting me all along in my journey to finish my PhD. My mom, Simin, dad, Behnam, and brother Arash have sacrificed much to make sure that I follow my dream and I owe them everything that I have ever done and will ever do. Most importantly I would like to thank my father for encouraging me to pursue my PhD.

LIST OF TABLES

LIST OF FIGURES

Chapter 1 INTRODUCTION

Underground box structures such as buried reservoirs, basements walls, box culverts, and retaining walls are an important part of our infrastructure and their design can be challenging when built in seismically active areas. The vast majority of underground box structures situated in unsaturated soils have performed very well in past earthquakes (e.g., Lew et al. 2010; Whitman 1991; Youd and Beckman 1996). Yet, there have been a few catastrophic failures (Wood 1973; Hashash et al. 2001; Hradilek 1971) that show the importance of designing these structures for seismic loading. In addition, few box structures have experienced large ground motions, which are often used in the design of modern critical buried infrastructure. The lack of appropriate design methodologies and agreement among professionals on the seismic forces and deformations experienced by these structures can lead to conservative or at times inadequate design. The current methods used to analyze the seismic response of underground box structures are based on simplified analytical or numerical tools that have not been calibrated or adequately validated against full-scale field measurements or physical model studies. Furthermore, the kinematic constraints of these structures are not fully captured by simplified seismic design procedures. Soil-structure-interaction (SSI) for these buried structures is complex and depends on foundation fixity, properties of the surrounding soil, flexibility of the structure relative to soil, and the characteristics of the earthquake motion, which are not well understood.

There is an increasing need in engineering practice to obtain a better understanding of the seismic performance of these underground structures. For example, the Los Angeles Department of Water and Power (LADWP) is replacing some of its open water reservoirs with buried, reinforced-concrete box structures to meet water quality regulations. The need for advanced physical modeling of underground reinforced concrete box structures using a geotechnical

centrifuge originated from the LADWP's Headworks Reservoir project, which will bypass the Silver Lake and Ivanhoe open reservoirs. The Headworks Reservoir consists of two reinforced concrete water storage tanks with a total capacity of 110 million gallons surrounded by earthen embankments and covered with a soil layer. These underground reservoirs are situated in a highly seismic area in southern California and thus, it is vital to understand their dynamic response. Understanding the seismic performance of these restrained underground structures will improve the structural and geotechnical seismic design of these types of projects worldwide.

Traditionally, underground structures are categorized either as *yielding* or *rigid-unyielding*, and are designed differently based on this categorization. A *yielding* wall is one that displaces sufficiently to develop an active earth pressure state. The current state of practice for assessing seismic earth pressures on *yielding* structures relies heavily on the Mononobe-Okabe (Okabe 1926; Mononobe and Matsua 1929) and Seed-Whitman (Seed and Whitman 1970) methods for cohesionless backfill. An extension of the Mononobe-Okabe method is used to calculate dynamic earth pressures with cohesive backfills using simplified charts in the NCHRP 611 manual (Anderson et al. 2008). For *rigid-unyielding* walls that don't undergo any deformation, the method of choice is often the simplified solution proposed by Wood (1973), which assumes completely rigid walls (with no flexure). Underground reservoir structures fall in between the two extreme cases of *yielding* and *rigid-unyielding*, due to their kinematic constraints. The lateral and rocking movement of these structures is limited by the soil backfill on both sides of the structure. The wall movement is limited by rotational constraints at the top and bottom by the connections to the roof and base, respectively. Lastly, the walls themselves are much stiffer than typical flexible underground structures such as tunnels. Therefore, in this study, these buried reservoir structures are classified as *stiff-unyielding* structures. The primary factors in the seismic design of

underground box structures include: 1) seismic lateral earth pressures; 2) magnitude and location of lateral thrust; 3) bending strain and moment distribution; and 4) racking deformations. Although recent physical model studies have evaluated the seismic performance of *yielding* retaining walls (e.g., Al Atik 2008 and Mikola 2012) and flexible tunnels with large soil cover (e.g., Cilingir and Madabhushi 2011; Tsinidis et al. 2013), the seismic response of *stiff-unyielding* underground structures has not been sufficiently evaluated experimentally in order to validate the numerical tools used in design.

Centrifuge experiments were conducted as part of this study at the University of Colorado Boulder to evaluate the seismic performance of relatively stiff underground structures buried in granular soils. The structure stiffness, backfill soil type and slope, embedment, container type (rigid versus flexible boundaries), fixity conditions, and ground motion characteristics were varied to evaluate their influence and relative importance on structural performance. Three different model box structures were designed to represent simplified prototype reinforced concrete buried reservoirs of varying stiffness characterizing those evaluated by the LADWP. The proposed reservoirs have 11 to 12 m-high walls that will be buried and restrained against rotational movement at the top and bottom by the roof and floor, restricting deformation. Experiments were performed at 60g of centrifugal acceleration using the 5.5 m-radius, 400 g-ton centrifuge at the University of Colorado Boulder (Ko 1988). Earthquake motions were applied to the model specimen in flight using the servo-controlled electro-hydraulic shake table, which is mounted on the basket of the centrifuge.

A series of five earthquake motions and eight harmonic motions were applied to the base of the models in the different experiments. The experiments were instrumented with accelerometers, LVDTS, strain gages, and pressure transducers to measure various design parameters such as

lateral earth pressures, racking displacements, bending moments, and soil-structure-interaction. The centrifuge experiments served two primary goals: 1) to provide insight into soil-structure-interaction near buried reservoir structures and the influence of various testing parameters on their seismic performance; 2) to provide data for comparison with simplified procedures as well as advanced numerical tools.

The specific research objectives of this study are as follows:

i. Evaluate the mechanisms of soil-structure-interaction and its effects on seismic-induced lateral earth pressures and displacements of buried reservoir structures via physical modeling.

ii. Evaluate the influence of soil properties, geometry of the backfill soil, structure stiffness, ground motion properties, base fixity, and boundary effects on the overall seismic performance of the class of stiff-unyielding buried structures.

iii. Compare the experimental dynamic earth pressures with analytical methods for evaluating dynamic earth pressures such as Mononobe-Okabe (Okabe 1926; Mononobe and Matsua 1929), Seed-Whitman (Seed and Whitman 1970), and Wood (1973).

iv. Provide experimental data for engineers and researchers at the LADWP, CU-Boulder, and other academic and government agencies to compare numerical simulation results against experimental recordings and document the capabilities and limitations of the numerical tools in capturing the key experimental observations.

This dissertation is organized as follows: Chapter 2 first provides an extensive literature review of previous analytical, numerical, and experimental research on the seismic response of underground structures. Chapter 3 describes the centrifuge model design methodology, soil properties, instrumentation and calibration, model preparation method, ground motions, and challenges. Chapter 4 presents the key results from the centrifuge experiments. Chapter 4 is itself

a collection of three journal articles, two of which have been accepted and one is under review. Chapter 5 summarizes the key conclusions and recommendations based on the centrifuge experimental results. Lastly, Chapter 6 summarizes some of the primary limitations in this research and recommendations for future research.

Chapter 2 LITERATURE REVIEW

Seismic performance of underground box structures has been studied in the past through case history observations, analytical methods, numerical methods, and through physical modeling. First, the seismic response of underground box structures are discussed as observed in previous case histories. Then, the previous analytical, numerical, and physical model studies performed on these structures are presented. The existing analytical methods for estimating seismic lateral earth pressures are categorized as pseudo-static and elastic methods. More emphasis is placed on elastic methods, since the buried structures of interest are relatively stiff and non-yielding. The numerical methods can take into account earthquake time histories, soil nonlinearity, wall flexibility, flexibility of the base, and complex geometries. A few of the most relevant numerical studies are discussed to help understand the nature of dynamic earth pressures. Lastly, a number of physical model studies at 1g or increased gravity are summarized on gravity walls, flexible retaining walls, braced walls, and tunnels to provide insights into the response of these structures and the existing gaps in the available experimental data.

2.1 Performance of Underground Box Structures as Observed in Previous Case Histories

Damage to underground box structures can be categorized as being caused by either ground shaking or ground failure by phenomena including liquefaction, fault displacement, or slope instability (Hashash 2001). The focus of this research is on ground shaking in dry soils and the resulting soil-structure interaction effects that induce dynamic lateral earth pressures, strains, and racking displacements on the buried structure. The underground box structures of interest in this study are buried reservoirs, box culverts, bridge abutments, basements, retaining walls, and shallow tunnels with minimal cover.

Underground box structures have historically performed well during earthquakes. However, a few cases of failure serve as reminders of the need to consider seismic loading in their design. Youd and Beckman (1996) studied the performance of thirty reinforced box highway culverts during six earthquakes. The primary causes of damage were identified as liquefaction induced embankment penetration or spreading, slope instability, and fault rupture. The culverts generally perform well during earthquakes except in areas affected by foundation failure or large lateral inertial forces. There were only two cases of slight damage due to excessive dynamic earth pressures. One of the structures suffered a few cracks that were repaired easily, while the other structure had the walls tilt in requiring major repair. The case studies showed that box culverts with a deeper fill on top experienced more damage due to inertial forces from the overlying fill.

Severe damage was sustained by the Daikai Subway Station during the 1995 Nanbu earthquake in Kobe, Japan. The station box structure was not designed for earthquake loading. Many of the center columns of the box structure failed, causing the roof to collapse and walls to crack. There are several hypotheses on what caused the failure of the subway station. One idea according to Ida et al. (1996) is that the subway station experienced a large horizontal force because of relative displacement between the base and ceiling levels due to subsoil movement. Another hypothesis is that the damage occurred due to the addition of inertial forces from the overburden (Hashash et al. 2001).

Hradilek (1972) evaluated the damage to channel box culverts after the 1971 San Fernando earthquake. Most of the damage to these structures was attributed to permanent ground displacement or fault slippage, which caused large, permanent passive earth pressures. However, the underground structures were not designed for seismic loading at the time, and their damage could be partly caused by excessive seismic earth pressures. Wood (1973) describes the failure of

the walls of a reinforced concrete underground reservoir at the Balboa water treatment plant during the 1971 San Fernando earthquake. The reservoir walls were 6.1 m high and restrained at the top and bottom, and the structure was buried in a soft fill deposit. With no evidence of soil liquefaction at the site, this failure may have occurred due to a combination of permanent ground movement and excessive seismic lateral earth pressures.

Seed and Whitman (1970) reported of damage to many bridge abutments during earthquakes due to earthquake-induced lateral earth pressures causing distortion or even sometimes collapse of the bridge superstructure. The Isla-Teja Bridge in Valdivia was distorted due to the inward movement of the abutment during the Chilean earthquake in 1960. A flexible bridge buckled due to the inward movement of the abutments during the 1964 Alaska earthquake. The performance of building basements during previous earthquakes has generally been satisfactory, as reported by Lew et al. (2010). Retaining wall structures have generally performed well also (Whitman 1991), with the exception of cases with ground failure such as liquefaction or slope instability.

2.2 Analytical Methods

Mononobe-Okabe (1926-1929)

The Mononobe-Okabe (M-O) method is a pseudo-static approach based on the analytical work of Okabe (1926) and the experimental work of Mononobe and Matsuo (1929). This method is intended for yielding retaining walls with dry cohesionless backfill soil. The M-O method is based on Coulomb's limit equilibrium earth pressure theory, except that it includes horizontal and vertical inertial forces due to seismic loading. Figure 2-1 shows a basic retaining wall system with the different loads acting on the failure wedge assumed in this method.

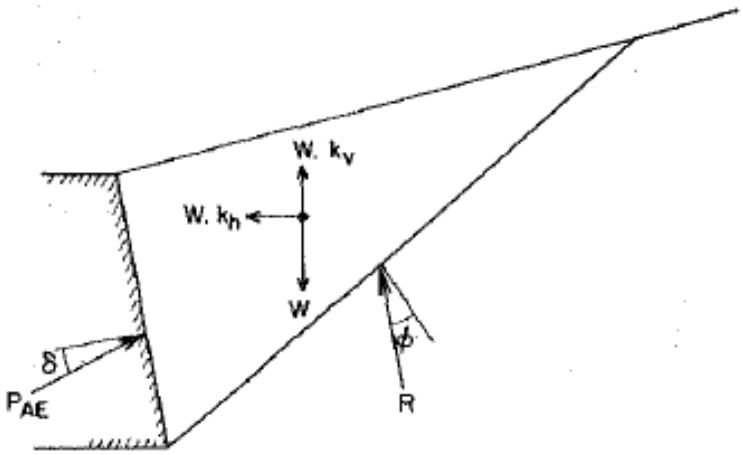

Figure 2-1. Retaining wall system and the applied forces on an active wedge (Seed and Whitman 1970).

The M-O method provides the total thrust on the wall and assumes the point of application of the total thrust is at H/3 above the base of the wall. The method was based on the assumptions that:

1. The wall yields sufficiently to produce minimum active pressures;
2. When the minimum active pressure is attained, a soil wedge behind the wall is at the point of incipient failure, and the maximum shear strength is mobilized along the potential sliding surface;
3. The soil behind the wall behaves as a rigid body so that the accelerations are uniform throughout the mass

The total active earth pressure caused by earthquake loading, P_{AE}, is expressed in Equation 2.1:

$$P_{AE} = \frac{1}{2}\gamma H^2(1 - k_v)K_{AE} \qquad 2.1$$

where K_{AE} is the total dynamic earth pressure coefficient due to earthquake loading, given as follows:

$$K_{AE} = \frac{cos^2(\phi-\theta-\beta)}{cos\theta cos^2\beta \cos(\delta+\beta+\theta)\left[1+\sqrt{\frac{\sin(\phi+\delta)\sin(\phi-\theta-i)}{\cos(\delta+\beta+\theta)\cos(i-\beta)}}\right]^2} \qquad 2.2$$

where the value of θ is defined as:

$$\theta = tan^{-1}\frac{k_h}{1-k_v} \quad 2.3$$

and γ is the unit weight of soil, H is the height of the wall, ϕ is the angle of friction of soil, δ is the soil-wall interface friction angle, i is the slope of ground surface behind wall, β is the slope of back of wall to vertical, k_h is the horizontal ground acceleration divided by g, and k_v is the vertical ground acceleration divided by g.

Seed and Whitman (1970)

Seed and Whitman performed a parametric study of the M-O method studying the influence of wall-interface friction, resultant horizontal force, backfill friction angle, and backfill slope angle on the total dynamic earth pressure coefficient (K_{AE}). They showed that the interface friction angle does not have much influence on K_{AE} for the case of a horizontal backfill and no vertical inertia component. They also showed that soil friction angle has a large influence on K_{AE} (horizontal component). For example, the horizontal pressure increased by 50% when the friction angle decreased from 40 to 30 degrees. The authors showed through parametric studies that the influence of k_v on K_{AE} is minimal and can be neglected.

Seed and Whitman (1970) then simplified the M-O method by separating K_{AE} into an active static lateral earth pressure coefficient, K_A, and a dynamic earth pressure coefficient increment, ΔK_{AE}. The Seed-Whitman (S-W) method assumes the resultant dynamic increment of thrust acts on the wall at a height of 0.6H above the base. The point of application of the dynamic increment of thrust was based on model scale shake table tests performed by previous researchers. In geotechnical practice, an inverted triangular pressure distribution for the seismic earth pressure is used by many practitioners.

Wood (1973)

This study was motivated by the lack of a suitable earthquake design criteria for relatively rigid structures on firm foundations in situations where the foundation, structure, and the retained soil remain elastic. Wood's method (Wood 1973) was developed for rigid, restrained walls having a fixed base with a linear elastic soil backfill, as shown in Figure 2-2. Equivalent static solutions were derived for the dynamic problem of interest by applying a 1g body force to the elastic soil. Wood (1973) provided simple plot solutions as shown in Figure 2-3 for the static 1g horizontal body forces to calculate normal stress, force, and moment. The solutions depend on L (horizontal length of backfill), H (height of backfill), ν (Poisson's ratio) of soil which is assumed to be elastic, and soil unit weight. For walls with a very long backfills, the dynamic thrust from Wood's method is applied at 0.63H above the base of the wall (Ebeling and Morrison 1992). The earthquake force component calculated using Wood's method is more than two times greater than the M-O method. Variables not taken into account by the simplified Wood's method are: soft deformable foundations, increase in soil shear modulus with depth, soil nonlinearity, wave propagation, and motion amplification (or de-amplification at large strains).

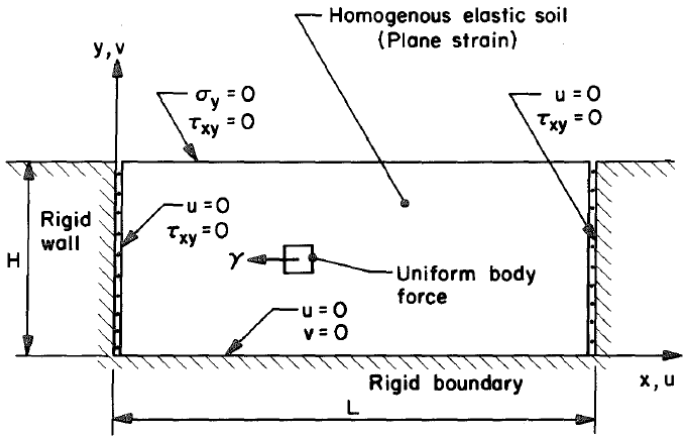

Figure 2-2. Model of elastic backfill behind a rigid wall (Wood 1973).

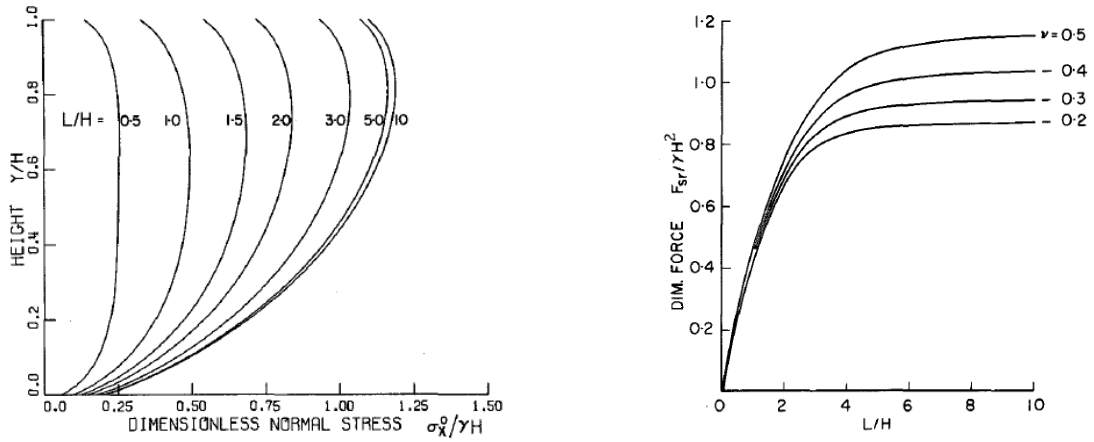

(a) (b)

Figure 2-3. (a) Pressure distribution (Poisson's ratio = 0.3); and (b) dynamic thrust on the wall based on Wood's simplified procedure for 1g static horizontal body force (Wood 1973).

Scott (1973)

Scott (1973) studied the dynamic response of a rigid retaining wall where the soil was treated as a 1-D elastic shear beam attached to the wall by mass-less Winkler springs representing the soil-wall interaction. The soil-wall system examined in this work was a semi-infinite uniform layer of viscoelastic material free at its upper surface, bonded to a non-deformable rigid base, and retained along one of its vertical boundaries by a rigid wall. These analyses showed that the first mode was principally responsible for the pressure distribution on the wall during the design earthquake. The spring stiffness does not take into account ground motion parameters. The maximum pressure distribution on the wall was a cosine function with the maximum occurring at the ground surface which decreased to zero at the base. The point of application of the thrust was at 0.64H above the base, which was similar to the recommendation of Seed and Whitman (1970). The influence of a constant soil shear modulus, increasing shear modulus with depth, and wall flexibility (by allowing the base to rotate) was evaluated.

Veletsos and Younan (1994a,b, 1997)

Veletsos and Younan (1994a,b, 1997) developed analytical solutions for dynamic pressures induced on a vertical rigid wall retaining a semi-infinite, uniform viscoelastic soil layer that is free at its upper surface and is bonded to a non-deformable, rigid base. The analytical solutions were later extended to account for flexural wall rigidity, base rotation flexibility, and an increase in soil shear modulus with depth. Veletsos and Younan (1994b) improved upon Scott's solution by including radiational damping by modeling the restraining action of the medium by a series of elastically supported, semi-infinite horizontal bars with distributed mass rather than by springs of constant stiffness that simulate the action of finite-length, massless, and unconstrained bars. They showed how increasing relative flexibility of rotational base constraint and retained medium (d_θ) at the wall base decreases dynamic earth pressures and the associated shear forces and bending moments acting on the wall, as shown in Figure 2-4b. Increasing the relative flexibility of the wall and the restrained medium (d_w) reduced the pressure especially near the top of the wall as shown in Figure 2-4a. An increase in shear modulus with depth causes the dynamic soil pressure to be zero at the top of the wall as shown in Figure 2-5. A few shortcomings of this method include: 1) an assumption of complete bonding between the soil and a rigid base; 2) an assumption of complete bonding between the wall and the soil; 3) no consideration for horizontal translation of the wall; and 4) the complexity of the solution and lack of simple computational steps for design applications.

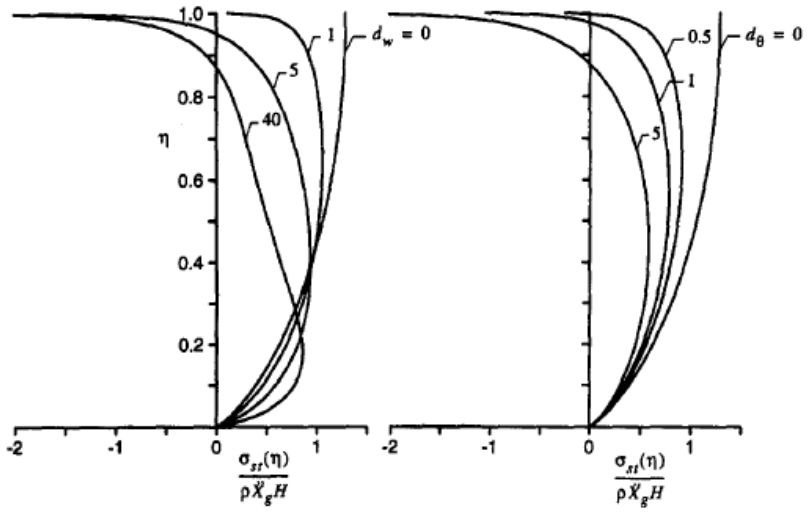

(a) (b)

Figure 2-4. Distribution of lateral earth pressures for the case of: (a) base rotationally constrained and varying wall flexibility; and (b) rigid wall and varying rotational base flexibility (Veletsos and Younan 1997).

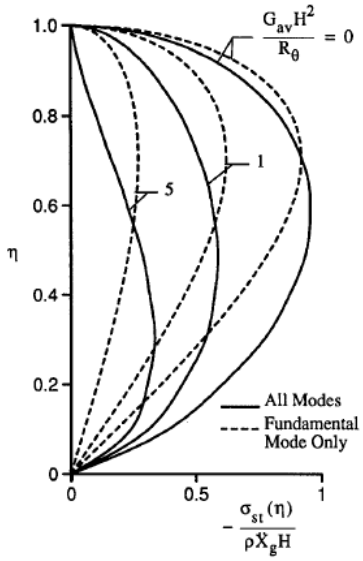

Figure 2-5. The effect of increasing soil shear modulus with depth on the lateral earth pressure profile (Veletsos and Younan 1994B).

Richards et al. (1999)

Richards et al. (1999) proposed a simplified analytical method to determine the distribution of dynamic earth pressures on rigid retaining walls with a granular soil backfill, while taking into

account soil's nonlinear (elastic perfectly plastic material with Mohr-Coulomb yield criterion) and plastic behavior and wall's horizontal translation, but not wave propagation. This method considered a semi-infinite layer of cohesionless soil that is free at its upper surface, is bonded to a rigid base, and is retained on its vertical boundary by a rigid wall. The approach is similar to Scott (1973) and Veletsos and Younan (1994), where stress on the wall is calculated by multiplying a spring stiffness representing the soil by the relative displacement of free-field and wall. Results from the method compared well with finite-element analyses and 1g small scale shake table tests. The authors concluded that the earth pressure distribution with depth under plastic soil conditions is similar to earth pressure distributions under elastic soil conditions, which depend on the distribution of soil shear modulus with depth.

Li (1999)

Li (1999) expanded upon Veletsos and Younan's (1994) solution by representing the base foundation as elastic with damping as opposed to a fixed base assumed by previous researchers as shown in Figure 2-6. The rotational stiffness used by Veletsos and Younan (1994) to allow the wall more flexibility at the base is a difficult parameter to determine and is not used in this model. Li (1999) proposed an alternative approach to express the foundation flexibility by using foundation damping, shear wave velocity, and base geometry of the wall. The shear wave velocity of the foundation was found to have a significant impact on the magnitude of dynamic pressures developed on the walls. Li showed that increasing the foundation shear wave velocity infinitely (i.e. fixed based conditions) produces the greatest base shear, while reducing the shear wave velocity of the foundation makes the system more flexible, creating more damping and thus decreasing the thrust.

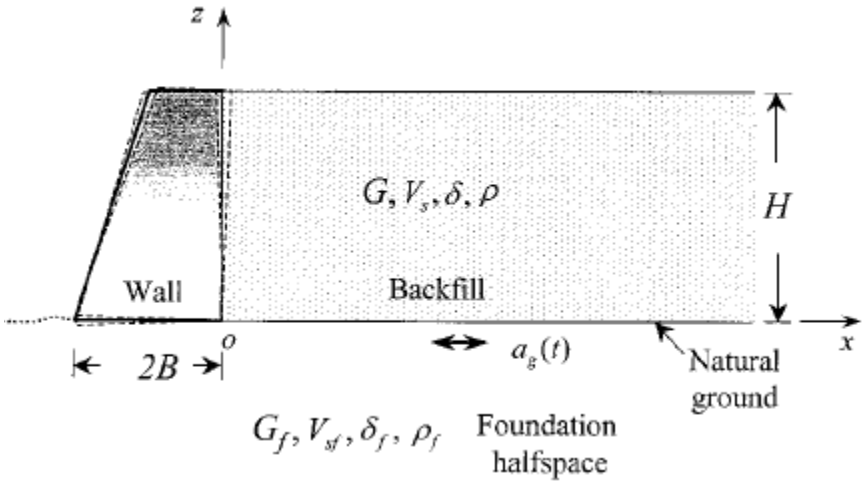

Figure 2-6. Schematic of system analyzed by Li (2001).

Davis (2003)

Davis (2003) introduced a simplified analytical method to calculate dynamic earth pressures from propagating waves on the walls of a perfectly rigid-unyielding (no lateral movement) underground structure embedded within an infinite elastic half space. It improves upon the methods of Wood

(1973), Scott (1973), Veletsos and Younan (1994a, 1994b), and Richards et al. (1999) by taking into account a non-rigid base and allowing embedment of the box structure. The soil takes into account increase in shear modulus with depth but not nonlinearity. Figure 2-7 compares dynamic increment of pressure for case of no overburden and with overburden. The addition of the overburden increases the pressure slightly and most importantly shifts the centroid up. The maximum wall pressures results from waves having highest acceleration with shortest wavelength (highest frequency). For simple design calculations, Davis (2003) recommends obtaining the maximum stress with depth by using an input frequency of 6.67 Hz and PGA. This model compared reasonably well to the results from the methods of Wood (1973) and Veletsos and Younan (1994b) when modifying the equation to account for rigid base conditions, as shown in Figure 2-8.

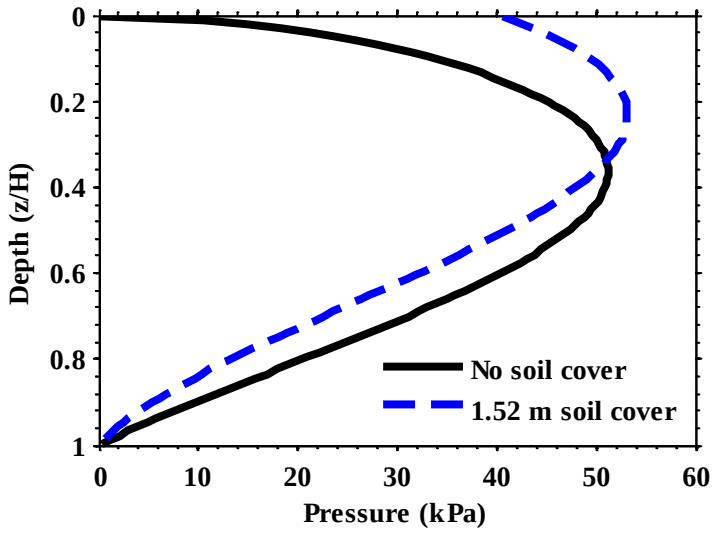

Figure 2-7. The effect of soil cover using structure height=10.44 m, γ=15.1 kN/m^3, β=174 m/s, ν=0.35, f=6.67 Hz, a_h=0.5g, K_E=0.

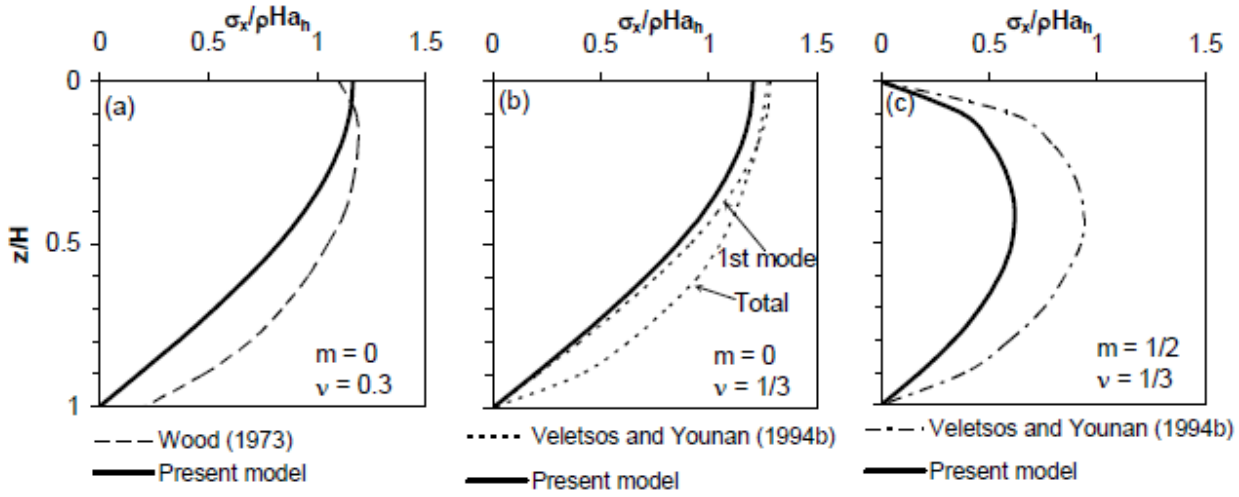

Figure 2-8. Comparison of Davis (2003) model with previous solutions of Wood (1973) and Veletsos and Younan (1994b).

Kloukinas et al. (2012)

Kloukinas et al. (2012) derived elastodynamic solutions to calculate the dynamic thrust that are simpler than the mathematically complex method of Veletsos and Younan (1994), with the intention that they could be used more easily in practice. The system considered a visco-elastic soil medium with rigid walls and rigid base. The solution was also extended to rotationally constrained walls. The thrust is applied at a height of 0.64H above the base of the wall. The solution compared well with Wood (1973) and Veletsos and Younan (1994).

Brandenberg et al. (2015)

Brandenberg et al. (2015) introduced an analytical method to calculate the kinematic induced dynamic increment of pressure on rigid walls that varies strongly with ratio of wavelength to wall height. The interaction between the free field soil and wall (k_y and k_z) as well as the base compliance of the foundation (translation=K_y and rotation=K_{xx}) are represented by Winkler springs as shown in Figure 2-9. The pressure on the wall is calculated by multiplying the relative displacement between the free field and wall by the soil-wall reaction stiffness (k_y). The soil non-linearity is taken into account indirectly by computing a strain compatible shear modulus using a

conventional 1-D site response program such as SHAKE. Figure 2-10 shows the influence of wave length as well as base compliance on the dynamic increment of thrust (P_E). P_E is largest for the rigid base case and decreases when base compliance stiffness are reduced. The most important interval of Figure 2-10 is for $\lambda/H \geq 2.3$ because that is when the energy of the ground motion is close to the natural frequency of a soil column. The method is used to explain the high seismic pressure relative to M-O predictions from numerical analyses of Ostadan (2005) and the low seismic pressures relative to M-O predictions observed from centrifuge tests of Al Atik and Sitar (2009, 2010). Ostadan (2005) considers a fixed based condition and input motions close to the natural frequency of the backfill which translates to high pressures (λ/H =4) compared to M-O method as shown in Figure 2-11a. Al Atik and Sitar (2009,2010) studied a deep soil layer, and reduced shear modulus due to soil non-linearity which translates to smaller pressures relative to M-O when considering ground motions close to the natural frequency of the soil column (λ/H =12) as shown in Figure 2-11b. The shape of the dynamic increment of pressure from this method is much different than from the centrifuge tests because it doesn't consider an increase in shear modulus with depth for the soil wall reaction stiffness, k_y.

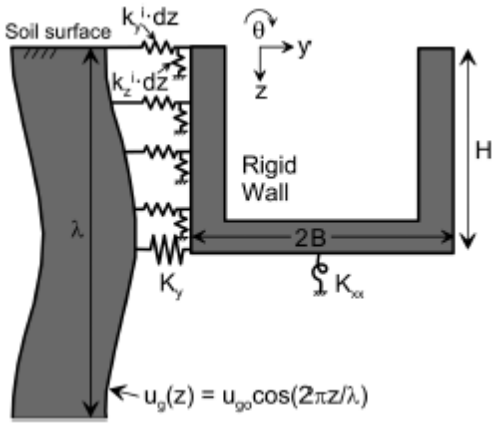

Figure 2-9. Schematic of embedded rigid strip foundation excited by vertically propagating shear wave (Brandenberg et al., 2015).

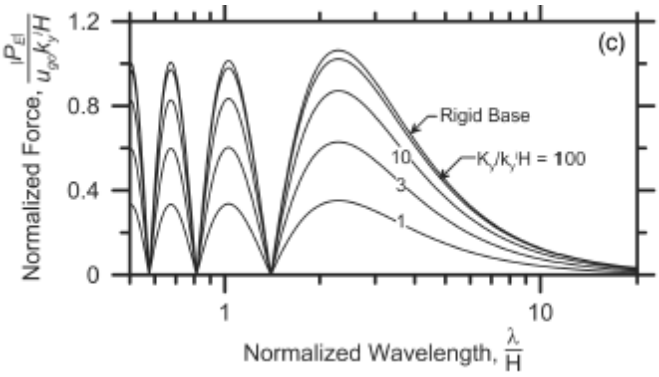

Figure 2-10. Normalized dynamic increment of thrust, (P_E) vs. normalized wavelength (λ) for various contributions of translational wall stiffness (K_y) and soil-wall reaction stiffness in y direction (k_y).

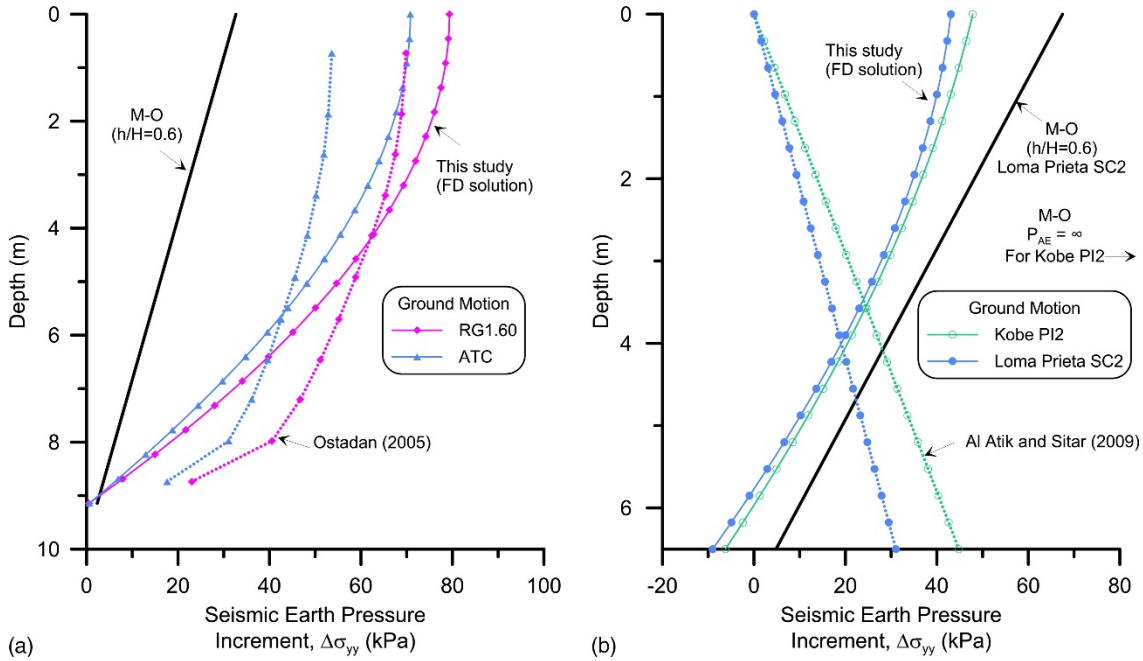

Figure 2-11. Dynamic increment of pressure calculated by Brandenberg et al. (2015) compared to: (a) Ostadan (2005); and (b) Al Atik and Sitar (2009, 2010).

2.3 Insight from Numerical Simulations

2.3.1 Lateral Earth Pressures

Al Homoud and Whitman (1999)

A nonlinear numerical analysis using an advanced viscous cap constitutive model for soil was performed by Al Homoud and Whitman (1999) to study the response of a bridge abutment. The abutment studied was very similar to a yielding gravity retaining wall (since it could rotate about

its base and translate laterally). The predictions of the finite element model showed satisfactory agreement to results from three dynamic centrifuge tests conducted by Andersen et al. (1987) on tilting gravity walls. The main emphasis of the study was on the outward tilt/rotation of the gravity wall during and after dynamic excitation. The Seed and Whitman (1970) method over-predicted the maximum dynamic horizontal earth force compared with the numerical analyses. However, the location of the maximum dynamic horizontal force behind the wall was approximately 0.58*H* above the wall base, which was close to the 0.60*H* value suggested by Seed–Whitman. The soil constitutive model employed didn't take into consideration hysteretic volumetric strains that develop in sand during dynamic loading. Volumetric compaction should cause an increase in horizontal stresses mainly near the bottom of the wall and thus, a downward shift in the location of the resultant horizontal force.

Gazetas et al. (2004)

Gazetas et al. (2004) used finite element analyses to evaluate the magnitude and distribution of dynamic earth pressures on L-shaped reinforced concrete walls, piled walls with horizontal anchors, and reinforced soil walls. The effects of soil nonlinearity (elasto-plastic Mohr-Coulomb criteria), foundation flexibility (retaining wall situated on deep soil), and loading frequency were studied. Both soil nonlinearity and foundation flexibility reduced the magnitude of pressure and changed the pressure profile shape significantly, as showed in Figure 2-12. Dynamic pressures were generally smaller than those predicted by the M-O method when high frequency motions (Ricker 4) were applied.

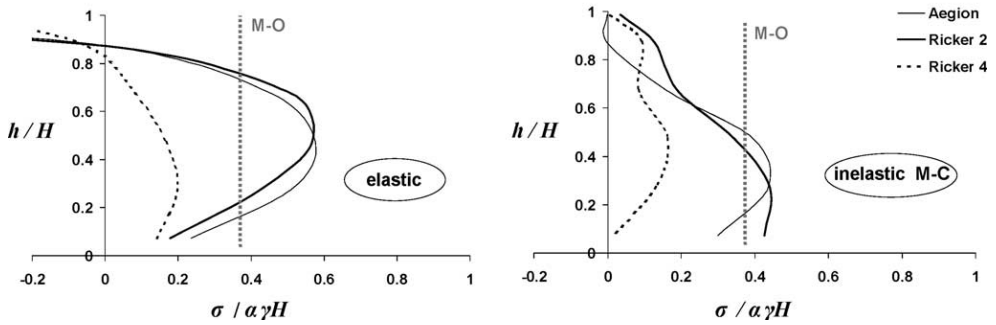

Figure 2-12. The effect of soil nonlinearity and frequency on dynamic earth pressures (Gazetas 2004).

Psarropoulos et al. (2005)

Finite element analyses were conducted by Psarropoulos et al. (2005) to verify the analytical solutions of Veletsos and Younan (1997) for stiff and flexible walls (rotation about base and flexural rigidity). 2-D plain strain conditions using visco-elastic materials were used. Complete bonding was modeled to compare directly with Veletsos and Younan. After showing the finite element model produced similar results to the method proposed by Veletsos and Younan, the analysis was extended to include inhomogeneous backfill soils (increase in shear modulus with depth) and translational flexibility. The effect of increase in shear modulus with depth, softening of soil due to large shearing deformations, and nonlinear wall-soil interface behavior including separation and slippage were evaluated. Unlike the Veletsos and Younan method, Psarropoulos et al. (2005) showed the capabilities of the finite element to include more realistic representation of wall behavior by including soil inhomogeneity and flexural rigidity together. Figure 2-13 below shows the effect of non-homogeneous soil on dynamic earth pressures when flexural rigidity is varied. It was also found that the introduction of a soil layer beneath the retaining wall resulted in a more flexible system, thus reducing dynamic earth pressures.

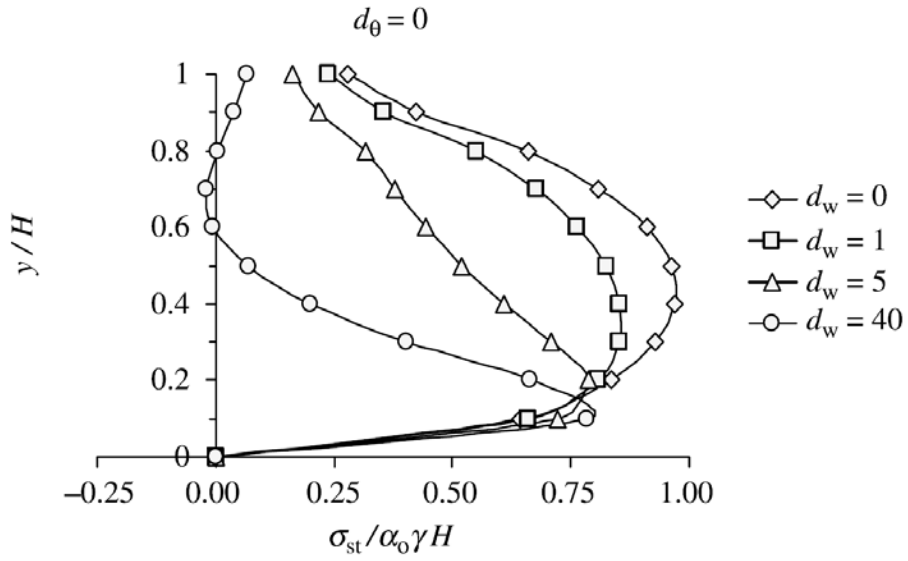

Figure 2-13. Effect of non-homogeneous soil when varying flexural rigidity.

Ostadan (2005)

Ostadan (2005) introduced a method based on elastic wave propagation using SASSI2000 finite element code to calculate dynamic increment of pressure on fixed base rigid basement walls retaining an infinite, uniform elastic soil layer. It was found that the natural frequency of the soil column adjacent to the wall is the controlling frequency that determines the maximum soil pressure. Based on this finding Ostadan (2005) developed the simplified method on the concept of single degree-of-freedom. The method consists of obtaining the response spectra at the base of the wall using a one-dimensional soil column analysis (SHAKE), spectral acceleration at the natural frequency of the soil column and applying a few equations to obtain the pressure profile. The dynamic soil properties and soil-nonlinearity are indirectly incorporated in the method through 1-D site response analysis used to obtain the base response spectra. The simplified method was verified with SASSI for a wide variety of ground motions. The maximum earth pressure occurs at the top of the wall because highest amplification occurs at the ground surface. The simplified

method was also compared to methods of Wood (1973) and Mononobe-Okabe, (Okabe 1926; Mononobe and Matsua 1929) as shown in Figure 2-14.

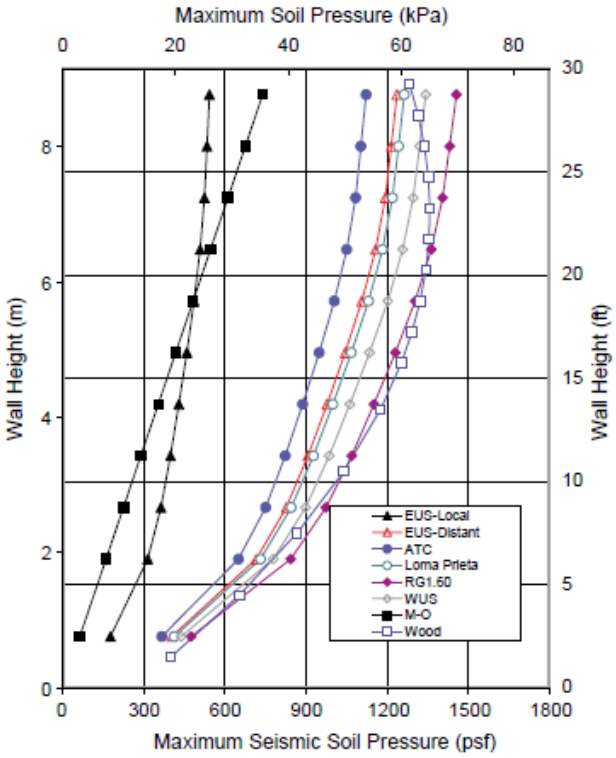

Figure 2-14. Comparison of Ostadan (2005) model for various earthquakes with Wood (1973) and Mononobe-Okabe (1926, 1929) solutions.

Taiebat et al. (2011)

A nonlinear numerical analysis was done by Taiebat et al. (2011) using the Mohr-Coulomb constitutive model to assess the seismic performance of existing basements in Vancouver and check the applicability of the Mononobe Okabe method. The analysis was motivated by new regulations that required a higher PGA to be used for the design of basement walls using the M-O method. Three different basement structures with varying flexibilities were studied. The basements were modeled with floors, which affect the pressure distribution greatly. Results of the dynamic analysis showed that the flexible basement had most of the pressure concentrated at the floor levels, while not apparent in the stiffer basements as shown in Figure 2-15. The point of application of

the thrust was calculated to be about 0.5H above the base of the wall for all three basements. The moments and drifts developed during the earthquake show that the suggested PGA in the code may result in conservative estimates of earth pressures when using the M-O method.

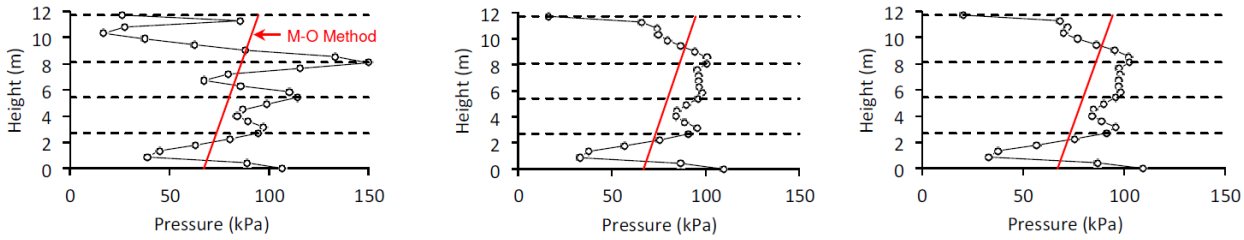

(a) (b) (c)

Figure 2-15. Dynamic earth pressures at the time of maximum thrust for basement: (a) W1 (b) W2 and (c) W3.

Psarropoulos et al. (2011)

Psarropoulos et al. (2011) studied the effect of soil-nonlinearity on the seismic response of rigid retaining walls using 2-D finite element analysis. The system considered was a rigid fixed-based wall retaining a single homogeneous soil layer with strain dependent material. Various PGA levels were used in this study aiming at the development of different degrees of material nonlinearity. The equivalent-linear approach was used to initially take into account soil nonlinearity in a simplified manner. The effect of the increase in PGA on the amplification of surface accelerations with respect to base was studied. At very low PGAs, the amplification factor increased substantially, as distance from the wall increased. At higher PGAs, soil nonlinearity increased, hence making the system more flexible. Therefore there was no apparent amplification on the soil surface with increasing distance from the wall. The same trends are observed with dynamic earth pressures. The increase in PGA caused greater soil nonlinearity, which led to lower dynamic earth pressures.

2.3.2 Racking Displacements

Wang (1993)

Wang (1993) noted that the three principal types of deformations experienced by tunnels during seismic shaking are axial, curvature, and racking deformations. Axial and curvature deformations are more applicable for long and flexible tunnels. Seismic racking is defined as the transverse sideways motion experienced by rectangular box structures due to shear distortions of the ground, as shown in Figure 2-16. Racking deformations are computed on the structure, so that the resulting bending moments and internal forces can be found. The common approaches for obtaining seismic racking displacements on box structures are: 1) the free-field racking deformation method; 2) the soil-structure-interaction finite element method; and 3) the simplified frame analyses method. The free-field approach doesn't take into account the stiffness of the structure. It assumes the amount of racking imposed on the structure is equal to the free-field shear distortions of the surrounding medium. This method is applicable mainly when the structure is flexible compared to its surround medium. This method is overly conservative for tunnel structures significantly stiffer than the ground.

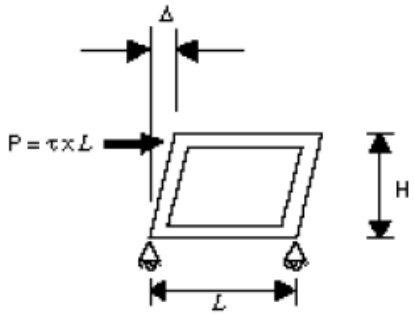

Figure 2-16. Racking distortion of a rectangular frame (Wang 1993).

Wang (1993) performed finite element analyses on 25 different cases of buried box structures to develop simple design charts (Figure 2-17), which can be used to calculate racking. The soil was modeled as linear elastic, and a no slip condition was assumed along the soil-structure

interface. The parameters considered were embedment depth, soil-structure relative stiffness (Flexibility Ratio), structure geometry, and ground motion characteristics. The relative stiffness between the soil medium and structure, as represented by the Flexibility Ratio, F, was shown to have the greatest effect on racking. Flexibility ratio is defined as:

$$F = \frac{G_m L}{K_s H} \qquad 2.4$$

where G_m is average, strain-compatible, shear modulus of the surrounding ground, L is the width of the structure, K_s is the racking stiffness of the structure, and H is the height of the structure. Wang (2003) also showed through parametric numerical analyses that a decrease in embedment depth causes a decrease in racking displacements.

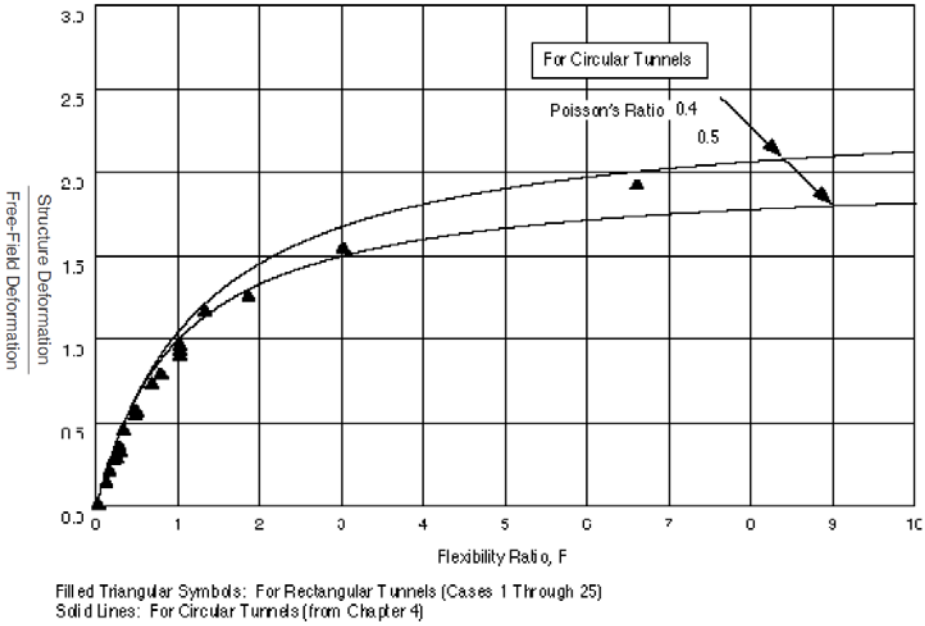

Figure 2-17. Design chart for normalized racking derived from synthesis of finite element analysis results (Wang 1993).

Anderson et al. (2008)

Anderson et al. (2008) summarized the simplified procedure for obtaining the racking of box structures originally introduced by Wang (1993). The original design charts by Wang (1993) were intended for transportation tunnels. Anderson et al. (2008) did a parametric study on box culverts using finite difference analyses to see if the design charts by Wang (1993) can be used for these types of small box structures. The parametric analysis revealed that burial depth does not have a significant influence on the racking deformation for rectangular rigid culverts. The following simplified equation was used to represent the design curve introduced by Wang (1993)

$$R=2F(1+F) \qquad 2.5$$

where R is the racking ratio and F is the flexibility ratio. The results of the finite difference analyses on the box structures matched reasonably well with the simplified equation.

Hashash et al. (2010)

Hashash et al. (2010) describes procedures to analyze the seismic racking response of box structures using pseudo-static and dynamic soil-structure interaction numerical analyses. In the pseudo-static method, a 1-D site response analysis was performed to obtain the free-field lateral strain along the height of the structure and the average strain-compatible elastic shear modulus. The pseudo-static analysis is done by placing the box frame in a soil stratum and imposing lateral displacements along the edges of the model such that free-field racking along the boundaries is equal to the free-field racking computed from a 1-D site response analysis. This method is efficient but not valid for shallow box structures and does not take into account soil profiles with significant stiffness variations. In the dynamic soil-structure interaction method, the soil surrounding the box frame is modeled as several layers of equivalent-linear elastic material assigned with strain-compatible shear modulus and damping obtained from 1-D site response analyses. A displacement

time history is assigned to the bottom of soil column allowing the motion to propagate through the soil and simulate soil-box interaction. A series of numerical analyses (pseudo-static and dynamic soil-structure interaction) were conducted on two different box structures buried in stiff and soft soil using 14 different ground motions. The linear elastic soil properties were obtained using both equivalent-linear and non-linear site response analyses.

The results of the numerical analyses are summarized in Figure 2-18 along with the relationship for R vs. F proposed by NCHRP 611 (Anderson et al., 2008). The results of the numerical analyses are fairly consistent with the NCHRP 611 recommendations, but there is some noticeable scatter especially for moderately stiff to stiff soils. The racking ratio calculated from numerical dynamic soil structure is more accurate than racking ratio obtained from the NCHRP 611 guidelines. The R vs. F curve by NCHRP 611 is an average of many finite element analysis and may not be applicable to a unique problem. For the case of a moderately stiff soil, the NCHRP 611 guideline under-predicted racking ratios by a large factor in a number of cases, which is concerning. The variability in the comparisons indicates the importance of a better understanding of the influence of the properties of the ground motion, soil, and structure on racking displacements.

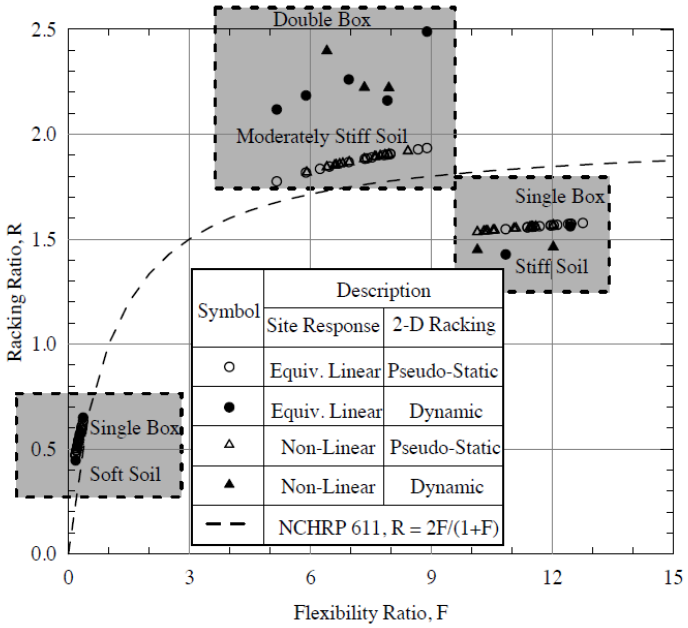

Figure 2-18. Results of pseudo-static and dynamic soil-structure interaction for underground box structures (Hashash et al. 2010).

2.4 Experimental Observations

Sherif et al. (1982)

Shake table tests were performed at 1g on a 1m tall (3 ft-5 in) rigid wall that could translate laterally retaining dry Ottawa silica sand. Thrust and point of application of thrust for cases of at rest, active, dynamic yielding, and dynamic unyielding were studied and compared to Coulomb, M-O, and Wood (1973) methods. A sinusoidal motion with amplitude of 0.5g and frequency of 3.5 Hz was used. Results indicated that K_o increased with soil densification after each motion, because stresses became locked in the soil. The dynamic increment of thrust for a stationary wall (no translation) increased with the horizontal acceleration coefficient. The elastic methods of Wood (1973) and Matsuo-Ohara (1960), however, overestimated the experimental dynamic stresses greatly. This overestimation was associated with the soil's nonlinear, elasto-plastic behavior in reality. The incremental dynamic-neutral earth thrust acted at approximately 0.52H above the base of the wall.

Ortiz and Scott (1983)

A series of dynamic centrifuge tests were performed on retaining walls of different stiffness measuring 4.88 m (16 ft) high in prototype. Medium-dense, fine sand with a range of backfill slopes were used. Earthquake motions were applied to the base of the containers in flight. The response of the model was analyzed through stain gages, earth pressure cells (Entran Model No. EPF-200-50), and accelerometers. The authors found substantial errors associated with the numerical differentiation of strain gage recordings (for the indirect measurement of earth pressures). The primary conclusions were:

1. The static and dynamic earth pressure distributions were erratic and nonlinear with depth.
2. The experimental resultant dynamic forces were in reasonable agreement with those calculated using the Mononobe-Okabe method.
3. The centroid of the dynamic earth pressures was found at approximately H/3 above the base.
4. A substantial amount of residual pressures and bending moments developed on the walls after each ground motion.
5. The static and dynamic design parameters (bending moment, lateral earth pressures) appeared to be independent of wall stiffness.

Stadler (1996)

A series of dynamic centrifuge tests were conducted on retaining walls with a fixed base retaining dry Nevada Sand. The effects of varying wall stiffness, height, and backfill density were assessed. The response of the model was analyzed with stain gages, earth pressure cells (Entran Model EPL-200-100S), and accelerometers. Overall, the measured pressures showed a substantial amount of scatter and thus their results were restricted to identifying behavioral trends. The shapes of the

total pressure profiles ranged from trapezoidal to triangular and the shape of the dynamic increment of pressure ranged from rectangular to triangular. The more reliable bending moment results showed that in almost all cases, the M-O method over-predicted the actual earth pressures especially on flexible walls. Residual pressures were higher than the initial static values (approximately 30 to 50 percent of the maximum dynamic pressures)

Dewoolkar et al. (2001)

A series of dynamic centrifuge tests were conducted on retaining walls with a fixed base retaining saturated Nevada Sand. Walls with varying dimensions were used to assess the effects of bending stiffness on soil-structure-interaction. The effect of ground motion properties was also assessed. The response of the model was analyzed using strain gages, earth pressure cells (Entran Model No. EPL-200-100S), accelerometers, and pore water pressure transducers. For simplicity, sinusoidal motions with a prototype frequency of 1 Hz were applied to the container in flight. To assess the quality of the pressure cell recordings, the authors double integrated the total pressures to obtain strain and compared it directly to the recorded strain data. The time histories of the recorded and calculated strain compared reasonably well. The pressure distributions with depth had much less scatter as compared to dry tests. The total pressures increased with depth in a triangular fashion, while the dynamic increment of pressure varied from triangular to inverted triangular. The line of action of the total thrust varied between 0.2H and 0.4H above the base during shaking. The wall stiffness had insignificant effects on the line of action. But the magnitude of oscillations increased with wall flexibility. The maximum dynamic thrust increased in a linear fashion with increase in base acceleration.

Nakamura (2006)

A series of dynamic centrifuge tests were conducted by Nakamura (2006) on concrete gravity retaining walls measuring 9 m high (prototype) resting on and retaining dry Toyoura sand. The intent of these tests was to understand the applicability of the M-O method to gravity retaining walls. The response of the model was assessed using accelerometers and load cells to measure lateral earth pressures. A series of sinusoidal motions and broadband earthquake motions were applied to the model. The earth pressures were not triangular and changed with time, unlike what was assumed by the M-O method. It was found that when inertia was highest in the active direction, the earth pressures were at their minimum. The total earth pressure magnitudes developed from the sine wave motions were greater than those developed from the earthquake motions.

Al Atik and Sitar (2010)

Two dynamic centrifuge tests were conducted by Al Atik and Sitar (2010) on ~6 m high, U-shaped retaining walls (flexible and stiff) resting on and retaining dry Nevada sand. The goal was to realize the discrepancy between current theoretical methods of obtaining pressure distribution and magnitude and the performance of actual retaining walls during seismic events. The response of the model was assessed with accelerometers, strain gages, tactile pressure sensors (Flexiforce), and force sensing bolts. It was found that the maximum dynamic increment of pressure increased with depth in a triangular fashion unlike what Seed and Whitman (1973) proposed. Similar to findings of Nakamura (2006), it was concluded that the dynamic increment of pressure and wall inertia do not occur at the same time. The M-O (using full PGA) method overestimated the dynamic bending moments and dynamic earth pressures. The back-calculated dynamic increment of earth pressure vs. PGA of surface motions showed that seismic earth pressures could generally

be ignored for free-field surface PGAs of less than approximately 0.4g. It must be noted, however, that the tactile sensors used in this study did not record at an adequate sampling rate for dynamic centrifuge modeling, and the amplitude of pressure was obtained indirectly in most cases, using strain gage measurements.

Sitar and Mikola (2012)

Two dynamic centrifuge tests were conducted by Sitar and Mikola (2012) on ~6 m high, L-shaped cantilever walls, U-shaped cantilever walls, and U-shaped cantilever walls (basement walls) with bracings resting on and retaining dry Nevada sand. These tests were similar to those performed by Al Atik (2008), except that they included struts for the U shaped cantilever walls to represent a stiffer basement structure restrained at the top. The response of the model was assessed with accelerometers, strain gages, tactile pressure sensors (Tactilus), and force sensing struts. One of the major problems of these tests was that that the sampling rate of the pressure sensors was too low for dynamic centrifuge testing, and thus dynamic pressures were mostly interpreted through strain gage recordings (similar to the tests performed previously by Al Atik 2008). Despite these shortcomings it was shown that the dynamic increment of pressure for all three structures increased in a triangular fashion, similar to the trends shown by Al Atik and Sitar (2010). The braced wall structure experienced dynamic pressure magnitudes similar to the U-shaped cantilever retaining wall. The flexural rigidity of the braced wall was, therefore, not large enough to experience any significant difference in dynamic pressure magnitude and distribution as compared with the U-shaped wall. Consequently, it was found that the Wood (1973) method greatly over-predicted the dynamic pressures measured on the walls of the braced structure. The Seed and Whitman (1973) method was shown to provide a reasonable upper bound for the seismic earth pressure increments for open and braced U-shaped cantilever walls.

Candia and Sitar (2013)

Dynamic centrifuge tests were conducted on structures retaining low plasticity compacted clay. They used the same structures and similar instrumentation to the tests conducted by Sitar and Mikola (2012). The dynamic increment of pressure increased with depth in a triangular fashion with centroid located around 0.35H to 0.4 H above the base. The cohesion in the backfill soil was shown to have relatively minor effect on the dynamic increment of pressure.

Tsinidis et al. (2015)

Dynamic centrifuge tests were conducted on flexible tunnels embedded in dry sand and compared with numerical simulations. The tunnels experienced rocking, racking, and inward wall bending deformations. Accelerations, displacements, lateral earth pressures, and strains were measured. The centrifuge results were used to calibrate a finite element numerical model in Abaq. The calibrated numerical model was used to evaluate racking ratios calculated by the simplified method of NCHRP611. The racking ratios for rigid structures (F=0.29) were overestimated by the numerical analysis compared to the NCHRP611.

Wilson and Elgamal (2015)

Wilson and Elgamal (2015) performed 1g shake table tests on short, rigid, retaining walls (1.7m high) with a dense c-φ backfill material. They showed a similar distribution of lateral earth pressure as observed in prior analytical and numerical studies (e.g., Veletsos and Younan 1994; Psarropoulos et al. 2005; Davis 2003) where the dynamic increment of earth pressure increases toward the center and then decreases near the bottom for stiff retaining structures. Relatively low dynamic lateral earth pressures were recorded at smaller acceleration levels (less than 0.7g), because of the high shear strength of the backfill soil, preventing a limit equilibrium type failure.

Due to the deformation patterns in their retaining wall and the higher strength of the backfill soil, the lateral earth pressure time histories along the height of the wall were observed to be out of phase, which reduced the total applied force. At stronger accelerations, however, the lateral earth pressure distributions became more in phase, significantly amplifying the applied seismic force. Previous numerical analysis by Wilson (2009) showed that wall rotation and translation has a much more significant influence on earth pressures than backfill shear strength.

2.5 Summary

The main parameters considered by the analytical methods related to the seismic design of underground structures are: the foundation soil properties, base translation and rotation constraints, wall flexural rigidity, soil cover, increase in G_{max} with depth, soil nonlinearity, damping, Poisson's ratio, and the amplitude and frequency of the motion. Table 2-1 summarizes the parameters considered in different analytical models.

The limitations and assumptions of some of the analytical methods may result in unrealistic dynamic earth pressures. The analytical methods most relevant to this research in terms of parameters and kinematic constraints need to be validated against the centrifuge experimental results.

Numerical approximation methods allow for considering more realistic boundary conditions and soil properties that are often not possible analytically. Seismic earth pressures acting on deformable but stiff, unyielding underground box structures with realistic soil properties have not been adequately studied numerically nor experimentally. The current numerical methods need to be validated against physical model studies before they can be used in design.

There have been many centrifuge tests performed on retaining structures and tunnel box structures that have provided valuable information. However, the focus of these studies was

different from this study, which is focused on relatively stiff unyielding box structures. The retaining structure centrifuge tests performed by previous researchers (e.g., Al Atik and Sitar 2008; Mikola and Sitar 2012) studied mostly yielding (no constraint against rotation at top of the wall) and flexible walls. The box structures tested previously (e.g., Cilingir and Madabhushi 2011; Tsinidis et al. 2013) considered much thinner linings and larger soil covers where the inertia of the surrounding ground is large relative to the inertia of the buried structure.

Table 2-1. Summary of parameters used in previous analytical procedures.

Method	**Soft foundation**	**Base translation**	**Wall flexural rigidity**	**Base rotation**	**Soil cover**	**Variation of G_{max} with depth**	**Soil nonlinearity**	**Frequency**	**Damping**
M-O (Okabe 1926; Mononobe and Matsua 1929),	no	no	no	no	no	no	no	no	no
Wood (1973)	no	no	no	yes	no	no	no	yes	yes
Scott (1973)	no	no	no	yes	no	yes	no	yes	yes
Veletsos and Younan (1994a,b, 1997)	no	no	yes	yes	no	yes	no	yes	yes
Richards et al. (1999)	no	yes	no	yes	no	yes	yes*	no	no
Li (1999)	yes	no	no	yes	no	no	no	yes	yes
Davis (2003)	yes	no	no	no	yes	yes	no	yes	yes
Kloukinas et al. (2012)	no	no	no	yes	no	no	no	yes	yes
Brandenberg et al. (2015)	yes	yes	no	yes	no	no	yes**	yes	yes
Ostadan (2005)	no	no	no	no	no	no	yes**	yes	yes

* Mohr Coulomb ** Indirectly using site response analysis

Chapter 3 EXPERIMENTAL METHOD

3.1 Background on Centrifuge Testing

The study of seismic soil-structure-interaction near underground box structures is strongly influenced by the nonlinear, pressure-dependent properties of the surrounding soil. Reduced scale 1g model tests are not ideal because of the difficulty of replicating realistic stress conditions in soil. Full scale testing is ideal but in most circumstances not practical because of high costs and time. The best approach to study the behavior of soil-structure systems such as box structures is to conduct static and dynamic tests on a properly scaled model in a centrifuge. The goal of centrifuge testing is to enable small scale models to feel the same stresses as a full scale prototype.

3.1.1 Scaling laws

The centrifuge produces confining stresses in a reduced scale model that are equal to prototype by increasing the centrifugal acceleration ($\omega^2 r$). The fundamental scaling relationships used to derive the other laws are shown in equations 3.1, 3.2, and 3.3. The asterisk (*) signifies the ratio of quantity in model to the quantity in prototype. N is the scaling factor. Using these relationships, it is shown in equation 3.4 that stress in model scale under a correct acceleration is equal to stress in prototype. Equation 3.5 shows the derivation of the scaling laws for dynamic time, which is essential in dynamic centrifuge modeling.

$$L^* = \frac{L_{model}}{L_{prototype}} = \frac{1}{N} \quad \text{, L=length} \tag{3.1}$$

$$\rho^* = \frac{\rho_{model}}{\rho_{prototype}} = 1 \quad \text{, ρ=density} \tag{3.2}$$

$$a^* = g^* = \frac{a_{model}}{a_{prototype}} = N, \quad \text{a=acceleration} \tag{3.3}$$

$$\sigma^* = \frac{F^*}{(L^*)^2} = \frac{m^* a^*}{(L^*)^2} = \frac{\rho^* (L^*)^3 a^*}{(L^*)^2} = 1 * \frac{1}{N} * N = 1 \quad 3.4$$

$$L^* = 0.5 a^* (t^*)^2 = a^* (t^*)^2 \rightarrow \frac{1}{N} = N (t^*)^2 \rightarrow t^* = \frac{1}{N} \quad 3.5$$

Table 3-1. Centrifuge scaling laws.

Quantity	**Scale Factor (model/prototype)**
Length	1/N
Mass, Volume	$1/N^3$
Acceleration, Gravity	N
Force	$1/N^2$
Stress, Moduli, Strength	1
Time (dynamic)	1/N
Velocity (dynamic)	1
Frequency	N

3.1.2 Centrifuge Facility

The 400-g ton centrifuge at the University of Colorado Boulder (Figure 3-1) was used to conduct the tests. This centrifuge has an asymmetric rotor arm, with a swinging platform at one end to carry the payload and counterweight on the opposite side. The radius of the centrifuge is 5.49 m from the center of rotation to the platform. It has the capacity to carry payloads as large as 1.22 m by 1.22 m by 0.91 m with a mass of 2000 kg. A maximum weight of 2 tons can be tested at 200 g. A 684 kW Direct Current (DC) drive system powers the centrifuge through a right-angle gearbox with a 6.4 to 1 gear reduction. A few other important features of the centrifuge include a cooling system along the interior walls and an inflight balancing system to ensure rotor balancing continuously. A full description of the centrifuge facility was provided by Ko (1988).

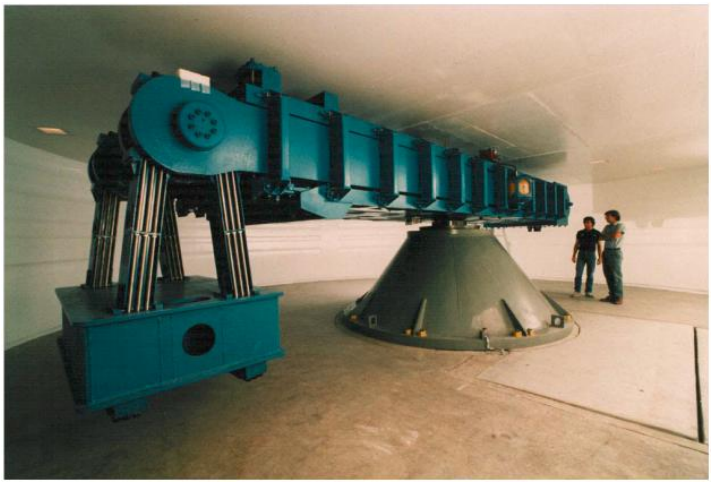

Figure 3-1. The 400-g ton centrifuge at the University of Colorado Boulder.

3.1.3 Shake Table

The electrohydraulic servo-controlled shake table system is mounted to the top of the platform of the centrifuge swing basket. The components of the shake table system consist of an MTS hydraulic power supply, linear actuator, LVDT, servo-valve combination, linear bearings, and bearing mounts. A schematic and picture of the shake table are shown below in Figure 3-2. The maximum controllable frequency is about 360 Hz in model scale and the maximum stroke is +/- 1.27 cm. A full description of the centrifuge shake table was provided by Ketcham et al. (1988).

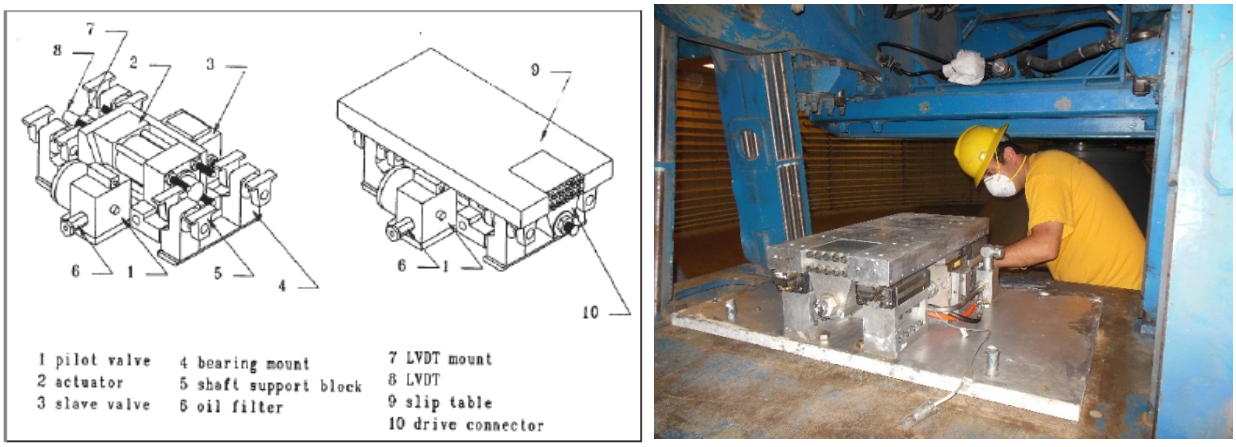

(a) (b)

Figure 3-2. (a) Schematic (Ketchum 1989) and (b) picture of installation of shake table.

3.1.4 Data Acquisition System

The centrifuge at the University of Colorado Boulder is equipped with a full complement of state-of-the-art data acquisition (DAQ) and experiment control systems. A high-speed, high channel count, modular data acquisition system by National Instruments (NI) mounted on the centrifuge arm acquires data from transducers, including accelerometers, pressure transducers (pressure cells), LVDTs, and strain gages. All acquired data is communicated to display terminals in the control room, or elsewhere, via a high-speed wireless network. A full array of equipment including video, digital still, and machine vision systems allow visual monitoring of the test specimen and provide additional data acquisition capabilities.

Figure 3-3 shows the configuration of this data acquisition system and connection with transducers for this study. The red arrows in Figure 3-3 show the direction of data transferring from transducers to where the control program is running and data is saving. All the transducers from the centrifuge model are plugged into the patch panels (terminals) on the testing basket (swinging platform) side, directly above the centrifuge model, before the test. The panels for strain gages and pressure transducers are connected to SCXI Chassis, which is connected with one PXI module for data acquisition. SCXI (Signal Conditioning eXtensions for Instrumentation) and PXI (PCI eXtensions for Instrumentation) are signal conditioning equipment manufactured by National Instruments. The panel for accelerometers is connected directly to one PXI module for data processing. Tekscan tactile pressure sensors are connected to its own recorder mounted on top of the centrifuge arm and then the recorder was plugged into the USB port on the PXI controller. The PXI controller works as a computer and it is usually remotely controlled during the spinning of the centrifuge from the control room. The data from all the transducers were collected and saved in the controller. Any command such as triggering the shake table is also sent from the controller.

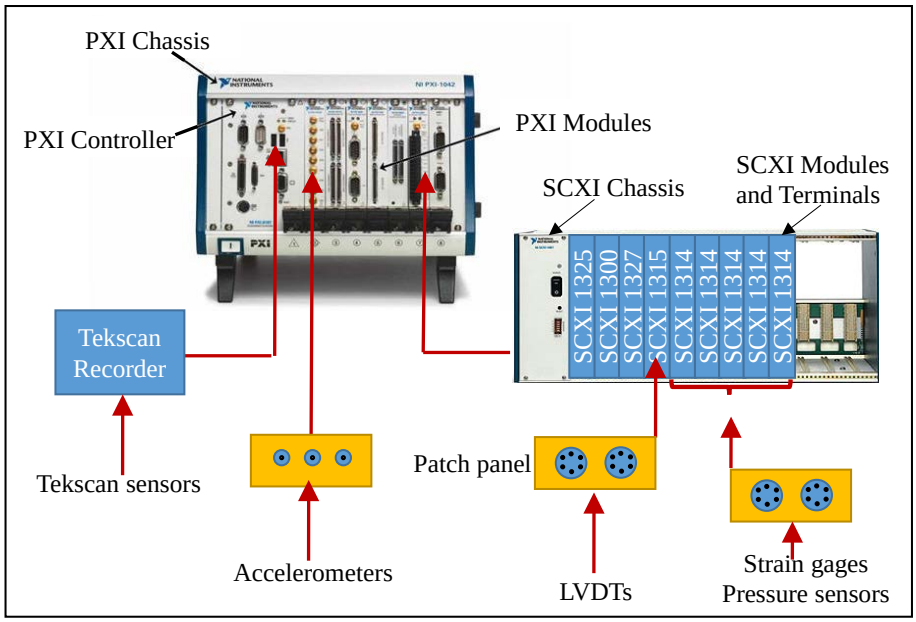

Figure 3-3. Data Acquisition System (DAQ) in the 400 g-ton centrifuge at University of Colorado Boulder.

3.1.5 Flexible Shear Beam Container

The intent of an ideal centrifuge container is to allow for simulating the response of a prototype soil layer with infinite lateral extents. In reality, the soil is confined in a finite container with boundary effects and deformation restrictions. One of the greatest challenges in dynamic centrifuge testing is minimizing the boundary effects created by the artificial boundaries of a model container. A few important qualities of an ideal model container are:

1. The container should allow for development of complementary shear stresses during shaking;
2. The container should maintain a constant horizontal cross-section during shaking;
3. The container end and side walls should be stiff enough to maintain a K_o condition;
4. Container walls should have small mass to minimize dynamic lateral forces at the boundary.

The centrifuge tests conducted in this study were performed using a transparent flexible-shear-beam (FSB) type container developed by Ghayoomi et al. (2012, 2013) to reduce boundary effects and allow transparency at the same time. The container was constructed of four acrylic frames separated by sheets of Neoprene rubber shown in Figure 3-4. The nominal inside dimensions are 698.5 mm x 304.8 mm x 336.6 mm (L x W x H). Shear rods were installed at both ends of the container to create shear stresses to counteract the rocking moment induced by the inertia of the soil mass. The container was designed to represent the lateral stiffness of a soil deposit in its softened state, with a low fundamental frequency, in order not to add to the stiffness of the soil specimen. Wave reflections are reduced when the first mode natural frequency of the container is much lower than the first mode natural frequency of the soil layer. Extensive dynamic centrifuge and numerical analyses were conducted by Ghayoomi et al. (2012, 2013) showing boundary effects are minimal and K_o conditions are maintained for the soil type and centrifugal acceleration levels of interest in this study.

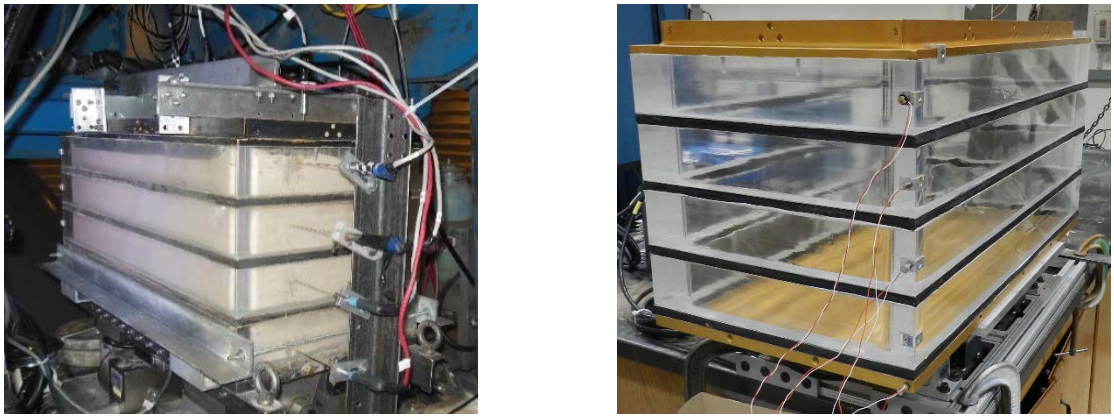

(a) (b)

Figure 3-4. Flexible-shear-beam container: (a) container mounted to the shake table during a free-field test; (b) empty container.

3.2 Centrifuge Model Design Methodology

All tests were performed at a centrifugal acceleration of 60 g based on limitations of the shake table (maximum achievable acceleration based on payload capacity) and desired prototype

dimensions. A simplified equivalent prototype (SEP) structure of the reservoir was developed with flexural stiffness and dynamic properties as close as possible to the original full-scale reservoir structure (Baseline model). Two other model structures, one with a 5 times smaller lateral stiffness (Flexible model) and the other with about 15 times higher lateral stiffness (Stiff model) compared to the Baseline model were constructed. The tests were all performed in the FSB container except one test (Test 7) which was performed in a rigid stainless steel container. The nominal inside dimensions of the rigid container are 1219 mm x 304.8 mm x 428.8 mm (L x W x H) and its wall thickness is about 13 mm. Two types of soil were used in the tests: 1) Nevada sand, and 2) site-specific soil, which is the native silty sand soil at the Headworks reservoir site, used to support the reservoir and also as backfill behind the reservoir walls. Recorded earthquake ground motions and sinewave motions in the frequency range of 0.33 to 6.67 Hz (prototype scale) were applied as input motions at the base of the test container. Detailed descriptions of the model configurations, model structures design and construction procedures, soil properties, instrumentation and calibration, model preparation methods, and ground motions applied during the tests are provided in Sections 3.2.1 through 3.6.

3.2.1 Testing Configuration

The centrifuge testing program, including the repeat tests are summarized in Table 3-2. The table describes the structure type, soil type, container type, input ground motion sequence and general description of the test. Figure 3-5 shows a schematic drawing of the different types of tests performed in this study. The instrumentation layout for all tests are shown in Figure 3-6 through Figure 3-29. All dimensions are presented in model scale. The prototype height of the box structures were approximately 34.3 ft and spanned the width of the container in all tests.

Tests 1A, 1A-R, 1A-R2, 3A, 3A-R, 4A, 4A-R, and 4A-R2 investigated the seismic response of the buried box structures focusing mainly on the effect of varying the flexural rigidity of the structure, while keeping the soil type, base fixity, and container type the same. Tests 1B, 3B, and 4B investigated the effect of adding a 1.52 m-thick soil cover (prototype scale) on top of the box structures. Test 2 studied the effect of a fixed base condition on the baseline underground structure (same structure as Test 1A and Test 1B). Test 7 was similar to Test 1A except that the rigid container was used instead of the FSB container. Tests 5 and 6 were similar to Test 1B, except that a site-specific compacted silty-sand was used. Tests 1A (1A-R2), 3A (3A-R), 4A (4A-R2), 1B, 2, 5, and 6 are referred to as T-BL, T-Stiff, T-Flexible, T-NS-Cover, T-Fixed, T-SS, and T-SS-Slope, respectively, in the results Section Chapter 4.

Table 3-2. Summary of the centrifuge test program.

Test No.	Test Name	Structure Type	Soil Type	Container	Input Ground Motion Sequence	General Description of Test	Test Layout Figures
1	Test 1A	Baseline	Nevada sand Dr = 60%	FSB	1) Northridge-L 2) Northridge-M 3) Northridge-H 4) Izmit 5 to 12) Sine 0.33 Hz to 6.67 Hz 13) Loma	Response of the buried baseline structure that is in between flexible and stiff	**Elevation View:** Figure 3-6 **Plan View**: Figure 3-7 **Tactile Pressure Sensor and Strain Gage Layout:** Figure 3-8
2	Test 1A-R	Baseline	Nevada sand Dr = 60%	FSB		Repeating Test 1A	**Elevation View:** Figure 3-9 **Plan View**: Figure 3-10 **Tactile Pressure Sensor and Strain Gage Layout**: Figure 3-8
3	Test 1A-R2	Baseline	Nevada sand Dr = 60%	FSB	1) Northridge-L 2) Northridge-M 3) Northridge-H 4) Izmit 5 to 12) Sine 0.33 Hz to 6.67 Hz 13) Loma 14) Northridge-L2 15) Izmit-2	Repeating Test 1A	**Elevation View:** Figure 3-16 **Plan View:** Figure 3-17 **Pressure Sensor Layout:** Figure 3-18 **and** Figure 3-19 **Strain Gage Layout:** Figure 3-20
4	Test 1B	Baseline	Nevada sand Dr = 60%	FSB	1) Northridge-L 2) Northridge-M 3) Northridge-H 4) Izmit 5 to 12) Sine 0.33 Hz to 6.67 Hz 13) Loma	Response of the baseline structure when a 5 ft soil cover is added	**Elevation View:** Figure 3-12 **Plan View**: Figure 3-7 **Tactile Pressure Sensor and Strain Gage Layout**: Figure 3-8
5	Test 2	Baseline	Nevada sand Dr = 60%	FSB		Response of the baseline structure fixed to bottom of container	**Elevation View:** Figure 3-13 **Plan View**: Figure 3-14 **Tactile Pressure Sensor Layout**: Figure 3-15 **Strain Gage Layout**: Figure 3-20
6	Test 3A	Stiff	Nevada sand Dr = 60%	FSB		Response of the buried stiff structure	Same as Test 1A

Table 3-2. Summary of the centrifuge test program (continued).

Test No.	Test Name	Structure Type	Soil Type	Container	Input Ground Motion Sequence	General Description of Test	Test Layout Figures
7	Test 3A-R	Stiff	Nevada sand Dr = 60%	FSB	1) Northridge-L 2) Northridge-M 3) Northridge-H 4) Izmit 5 to 11) Sinewave motions, Sine 0.33 Hz through Sine 6 Hz 12) Northridge-L2 13) Izmit-2 14) Loma	Repeating Test 3A	**Elevation View**: Figure 3-16 **Plan View**: Figure 3-21 **Pressure Sensor Layout**: **:** Figure 3-18 **and** Figure 3-19 **Strain Gage Layout:** Figure 3-22
8	Test 3B	Stiff	Nevada sand Dr = 60%	FSB	1) Northridge-L 2) Northridge-M 3) Northridge-H 4) Izmit 5 to 12) Sine 0.33 Hz to 6.67 Hz 13) Loma	General response of the stiff structure when a 5 ft soil cover is added	Same as Test 1B
9	Test 4A	Flexible	Nevada sand Dr = 60%	FSB		Response of the buried flexible structure	Same as Test 1A
10	Test 4A-R	Flexible	Nevada sand Dr = 60%	FSB		Repeating Test 4A	**Elevation View**: Figure 3-9 **Plan View**: Figure 3-10 **Tactile Pressure Sensor and Strain Gage Layout**: Figure 3-11
11	Test 4A-R2	Flexible	Nevada sand Dr = 60%	FSB	1) Northridge-L 2) Northridge-M 3) Northridge-H 4) Izmit 5 to 11) Sinewave motions, Sine 0.33 Hz through Sine 6 Hz 12) Northridge-L2 13) Izmit-2 14) Loma 15) Sine 6.67 Hz	Repeating Test 4A	**Elevation View**: Figure 3-16 **Plan View**: Figure 3-23 **Pressure Sensor Layout**: Figure 3-18 and Figure 3-19 **Strain Gage Layout:** Figure 3-24

Table 3-2. Summary of the centrifuge test program (continued).

Test No.	Test Name	Structure Type	Soil Type	Container	Input Ground Motion Sequence	General Description of Test	Test Layout Figures
12	Test 4B	Flexible	Nevada sand Dr = 60%	FSB	1) Northridge-L 2) Northridge-M 3) Northridge-H 4) Izmit 5 to 12) Sine 0.33 Hz to 6.67 Hz 13) Loma	General response of the flexible structure when a 5 ft soil cover is added	Same as Test 1B
13	Test 5	Baseline	Compacted silty sand (site-specific soil)	FSB		Response of buried baseline structure when using compacted site-specific silty sand soil	Same as Test 1B
14	Test 6	Baseline	Compacted silty sand (site-specific soil)	FSB	1) Loma 2) Izmit 3 to 10) Sine 0.33 Hz to 6.67 Hz 11) Northridge-L 12) Northridge-M 13) Northridge-H	Response of buried baseline structure when using sloped compacted site-specific silty sand soil	**Elevation View:** Figure 3-25 **Plan View:** Figure 3-26 **Tactile Pressure Sensor Layout**: Figure 3-15 **Strain Gage Layout**: Figure 3-20
15	Test 7	Baseline	Nevada sand Dr = 60%	Rigid	1) Northridge-L 2) Northridge-M 3) Northridge-H 4) Izmit 5 to 12) Sine 0.33 Hz to 6.67 Hz 13) Loma	Response of the buried baseline structure when a rigid container is used	**Elevation View:** Figure 3-27 **Plan View**: Figure 3-28 **Tactile Pressure Sensor and Strain Gage Layout**: Figure 3-8
16	Free Field	None	Nevada sand Dr = 60%	FSB		General free field conditions	Figure 3-29

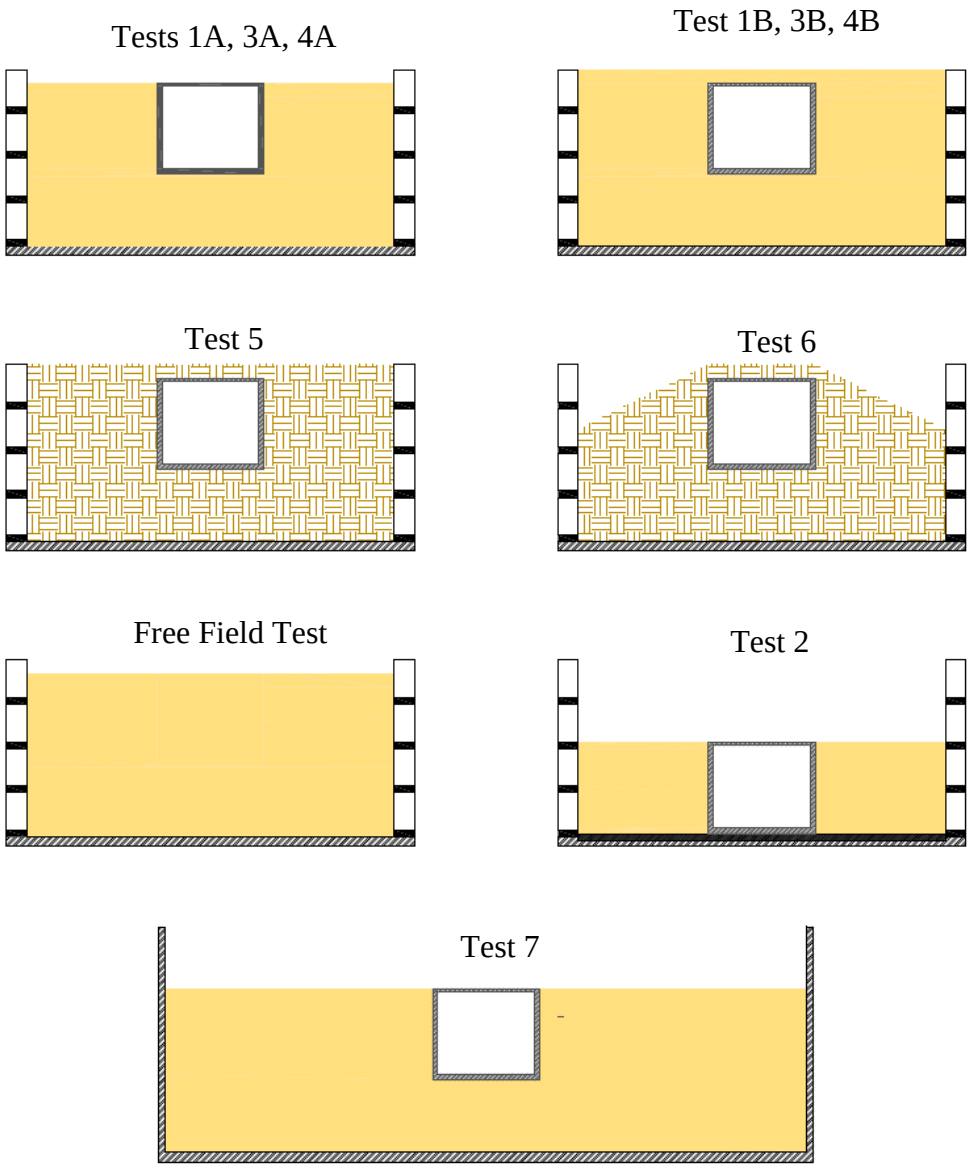

Figure 3-5. Schematic of centrifuge experiments to evaluate the seismic response of underground reservoir structures.

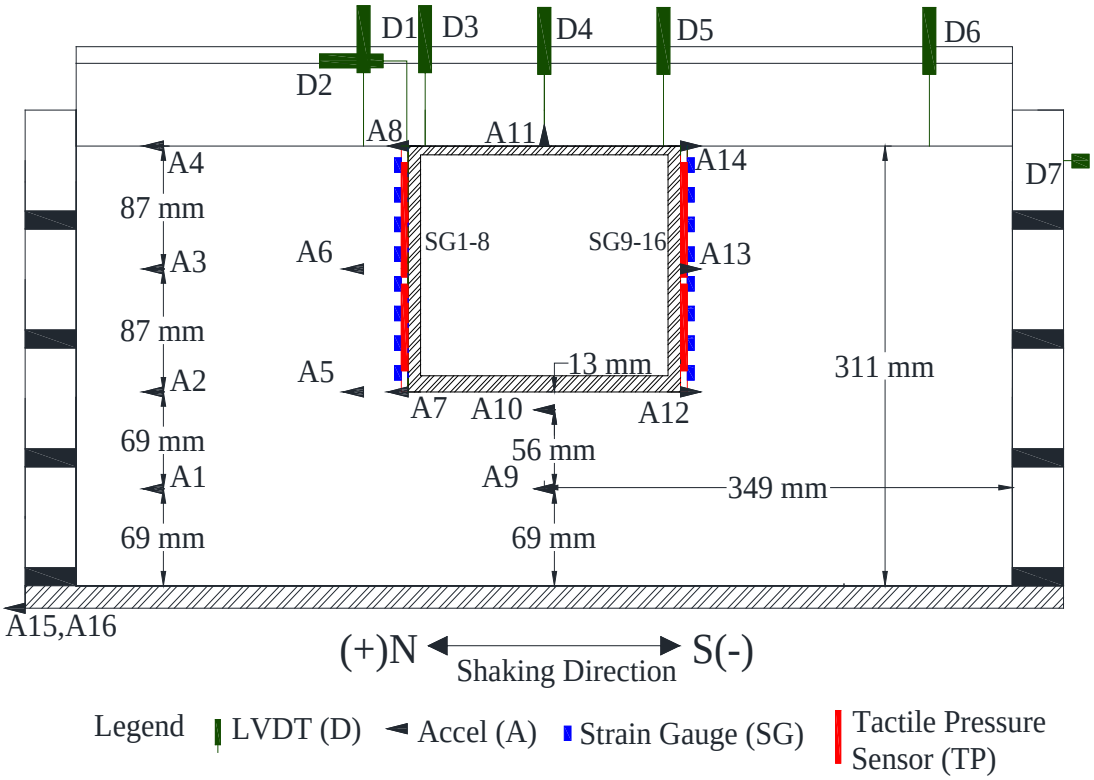

Figure 3-6. Elevation view of Tests 1A, 3A, and 4A.

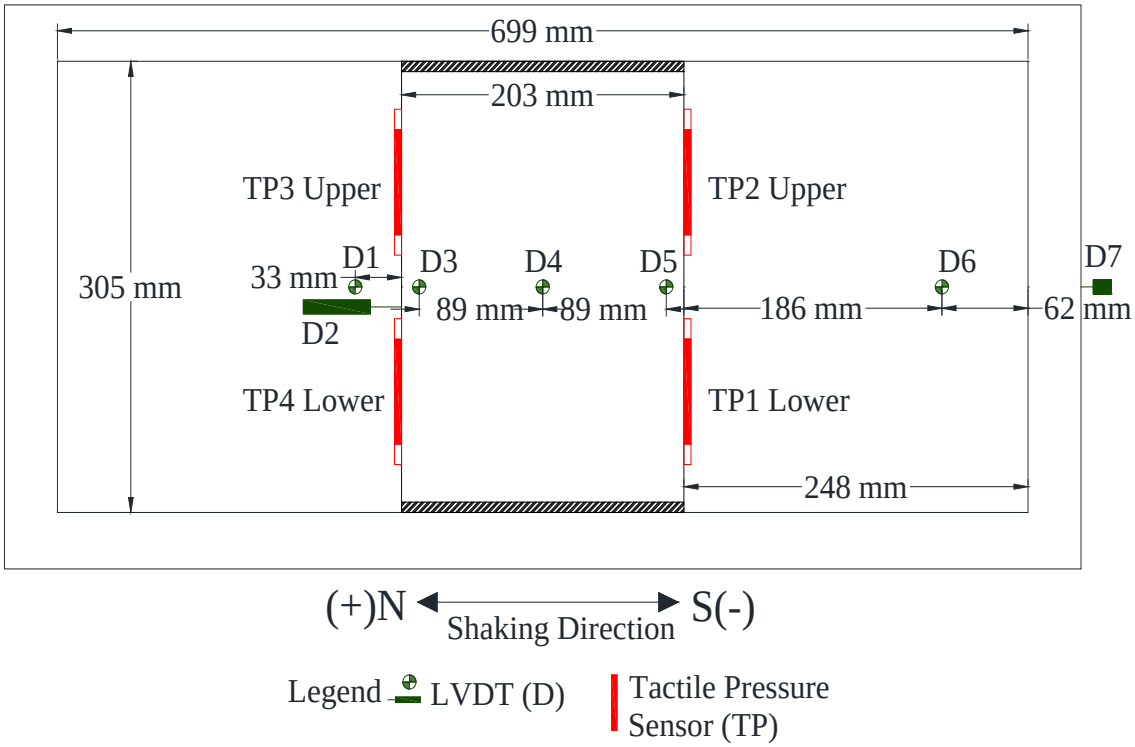

Figure 3-7. Plan view of Tests 1A, 1B, 3A, 3B, 4A, 4B, and 5.

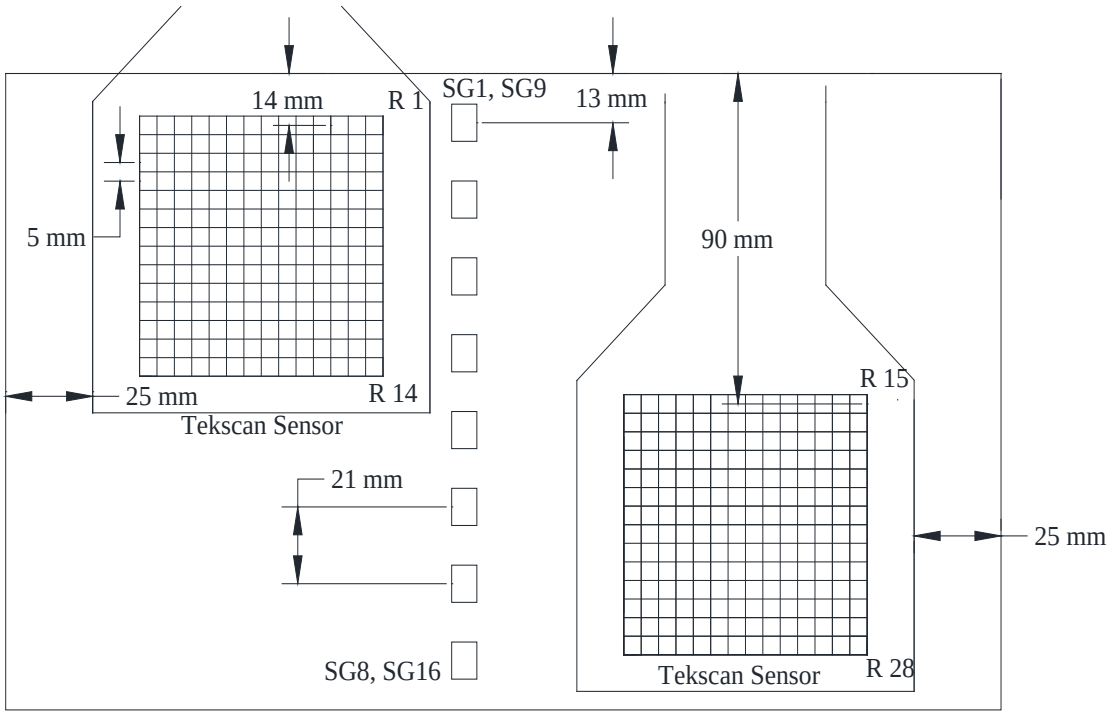

Figure 3-8. Tactile pressure sensor and strain gage layout in Tests 1A, 1B, 3A, 3B, 4A, 4B, 5, 7, and 1A-R.

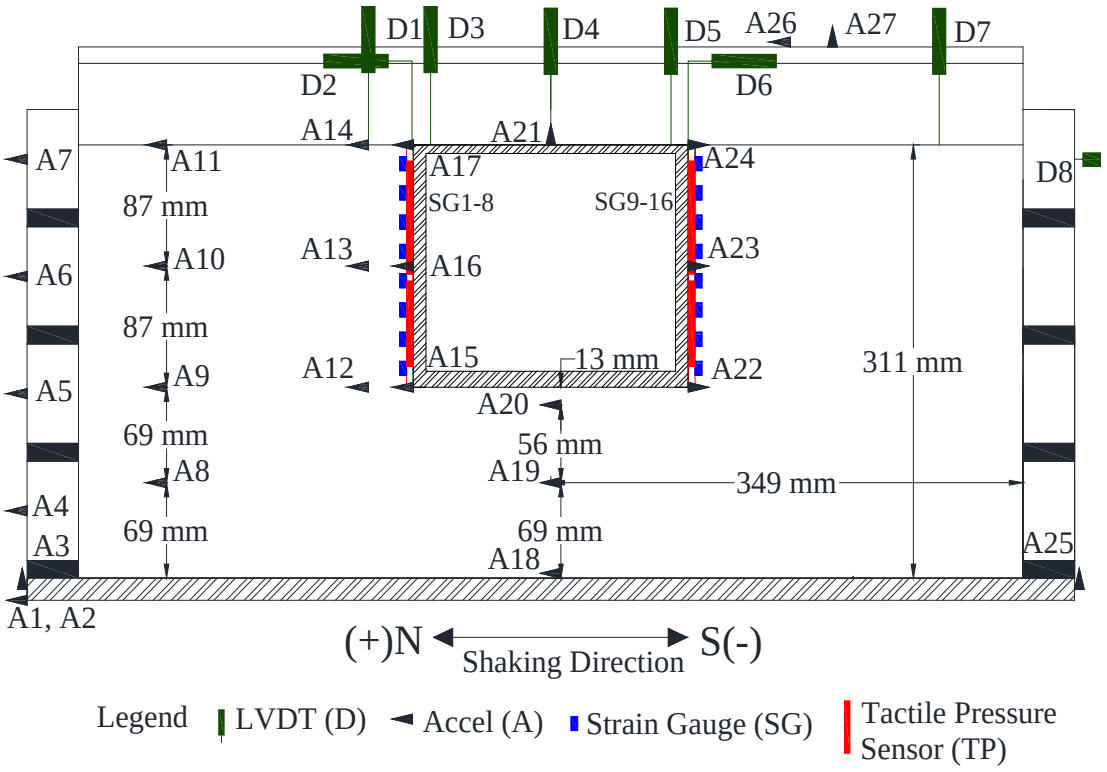

Figure 3-9. Elevation view of Tests 1A-R and 4A-R.

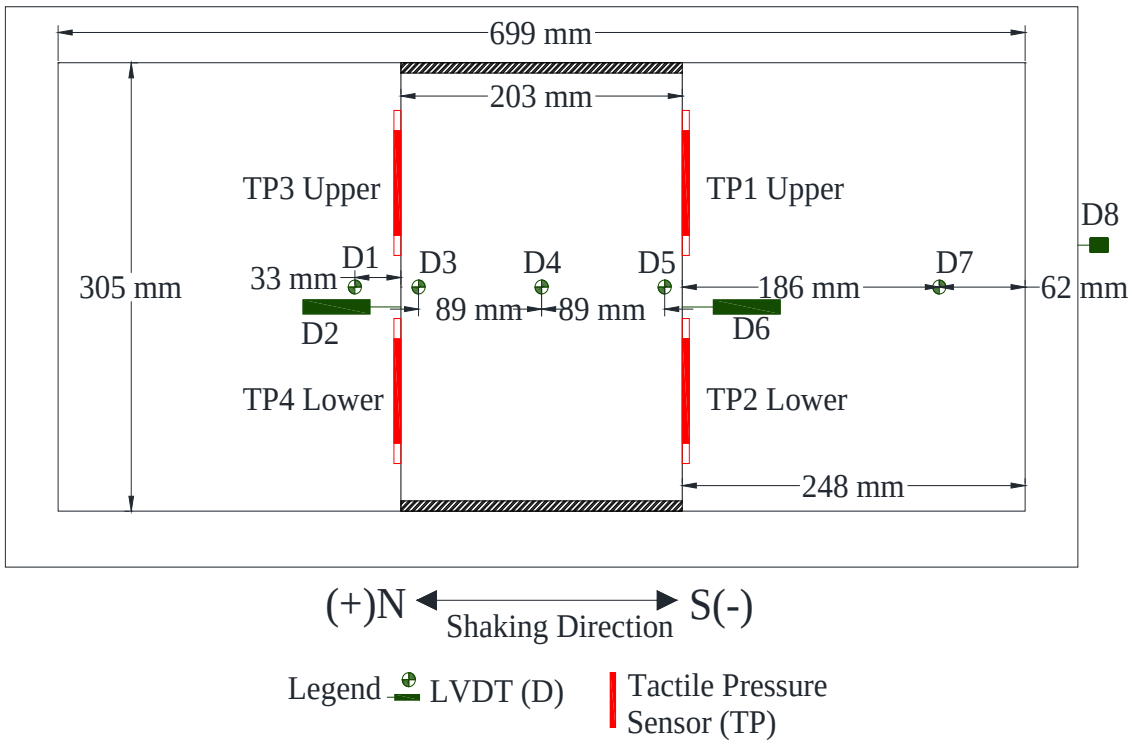

Figure 3-10. Plan view of Tests 1A-R and 4A-R.

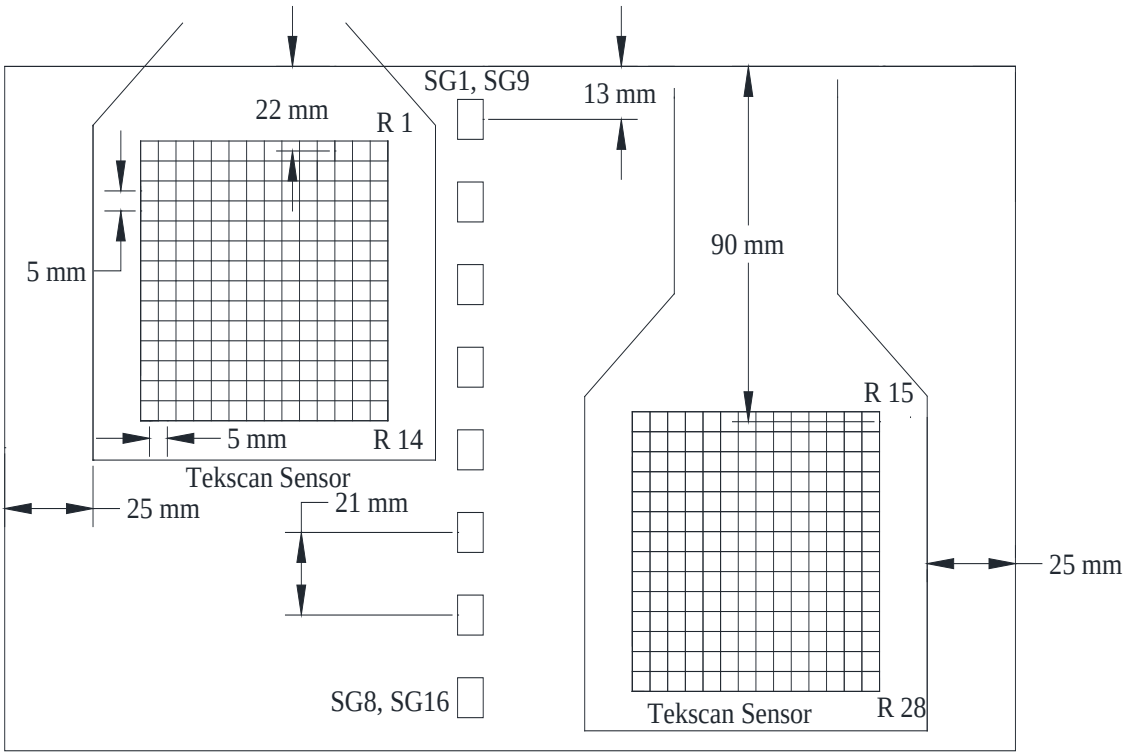

Figure 3-11. Tactile pressure sensor and strain gage layout in Test 4A-R.

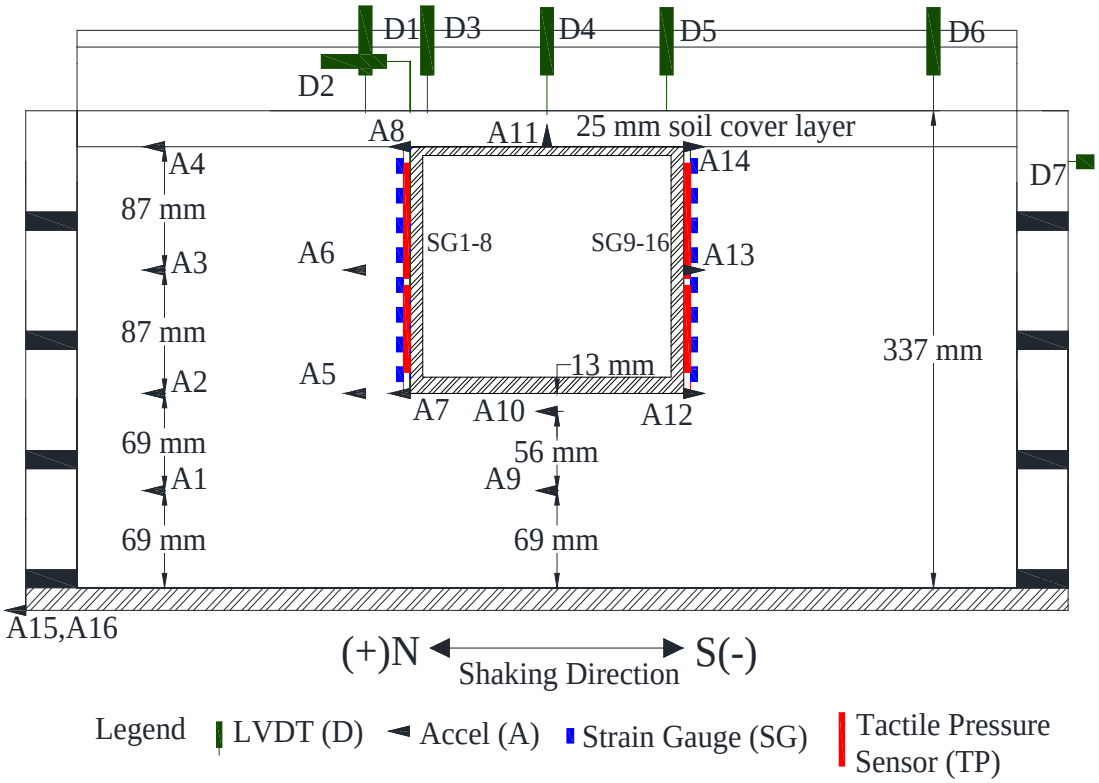

Figure 3-12. Elevation view of Tests 1B, 3B, 4B, and 5.

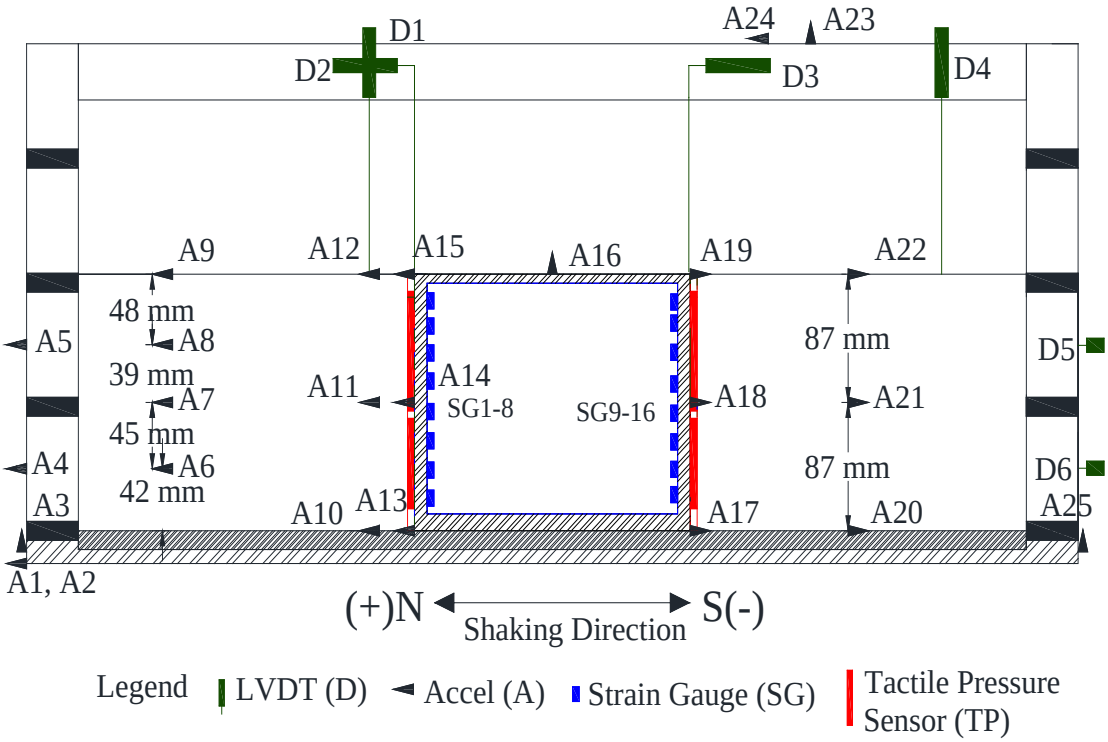

Figure 3-13. Elevation view of Test 2.

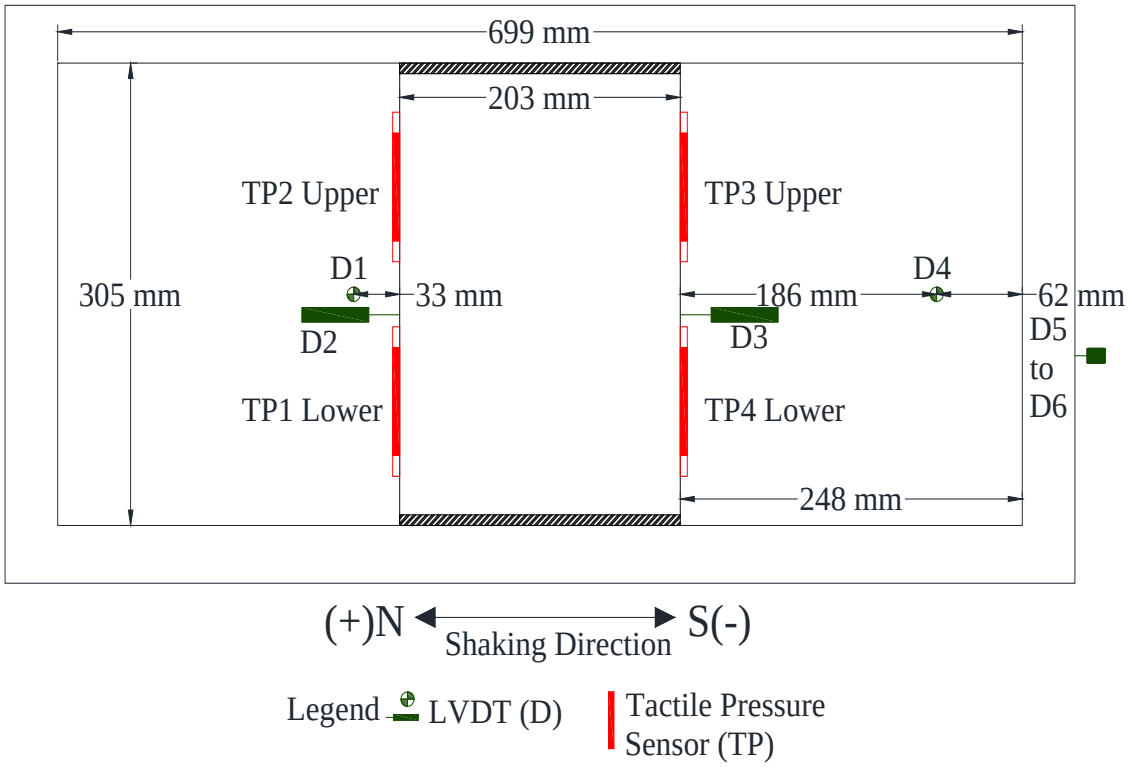

Figure 3-14. Plan view of Test 2.

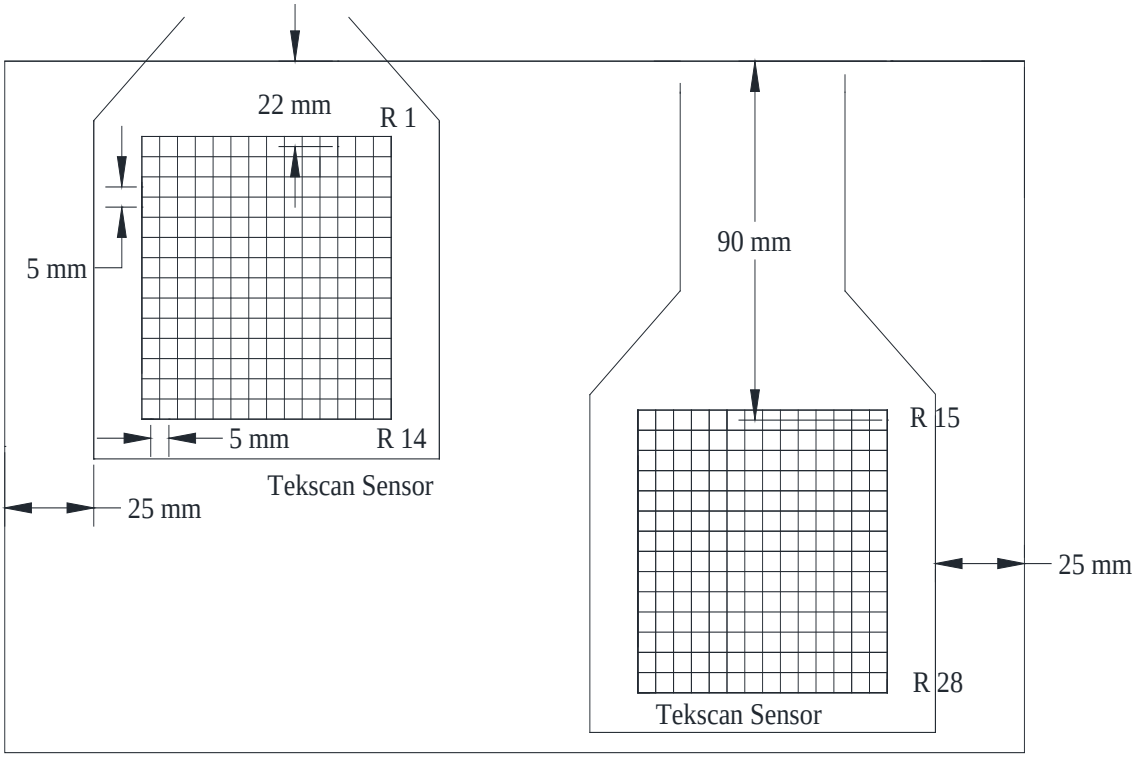

Figure 3-15. Tactile pressure sensor layout in Test 2 and Test 6.

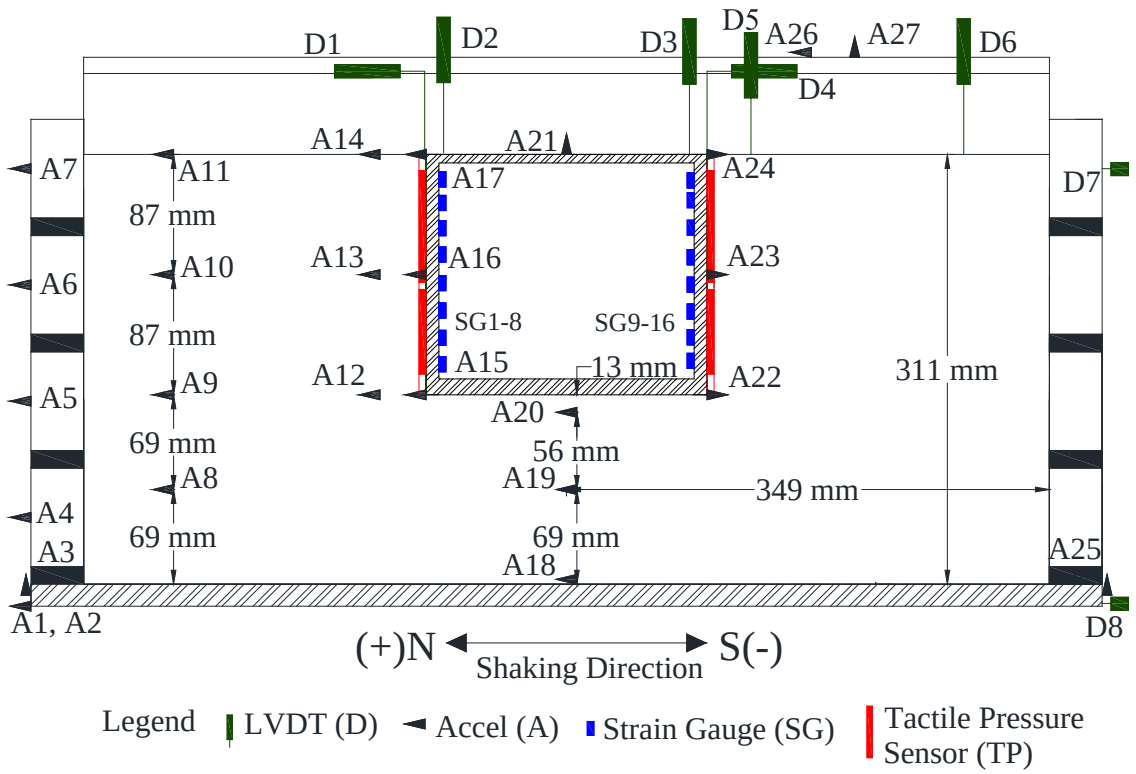

Figure 3-16. Elevation view of Tests 1A-R2, 4A-R2, and 3A-R.

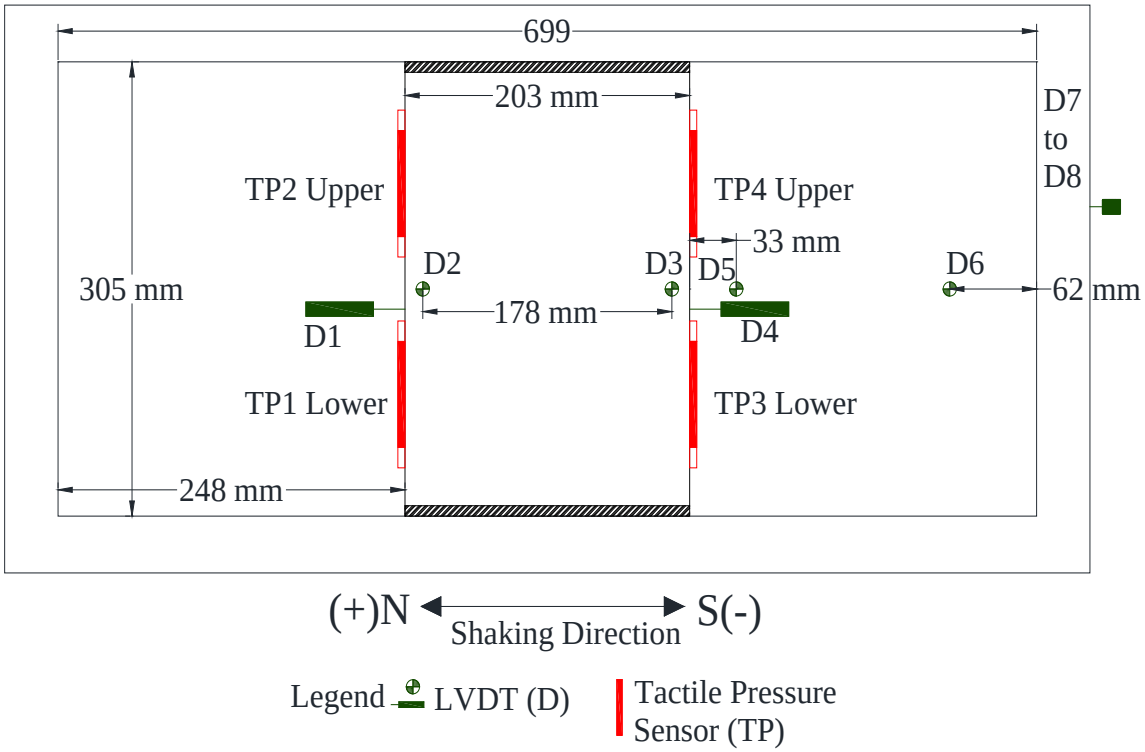

Figure 3-17. Plan view of Test 1A-R2.

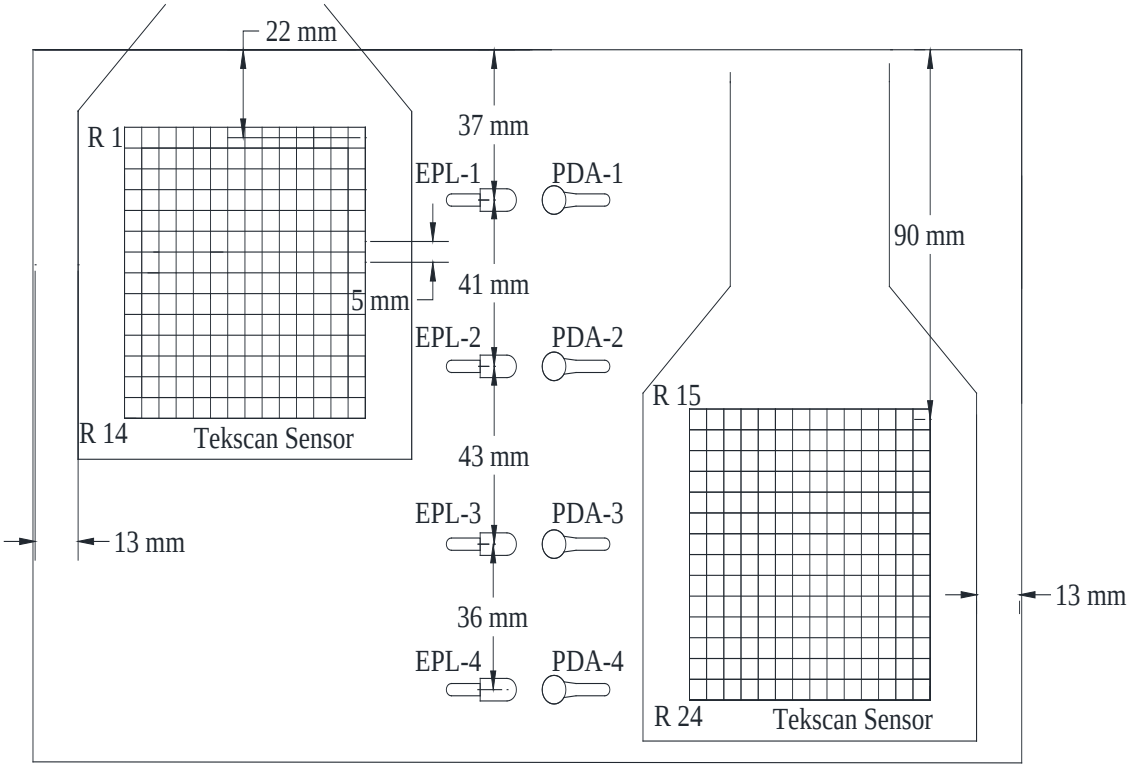

Figure 3-18. Tactile pressure sensor and pressure cell layout in Tests 1A-R2, 3A-R, and 4A-R2 (North Wall).

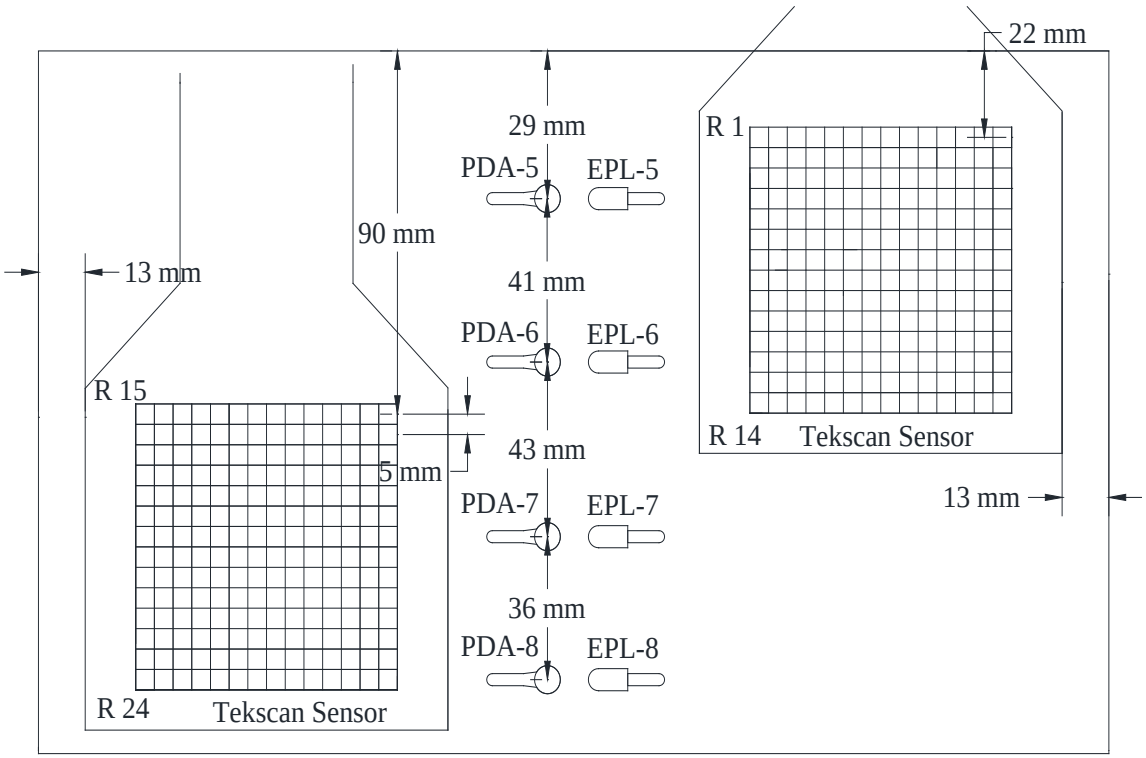

Figure 3-19. Tactile pressure sensor and pressure cell layout in Tests 1A-R2, 3A-R, and 4A-R2 (South Wall).

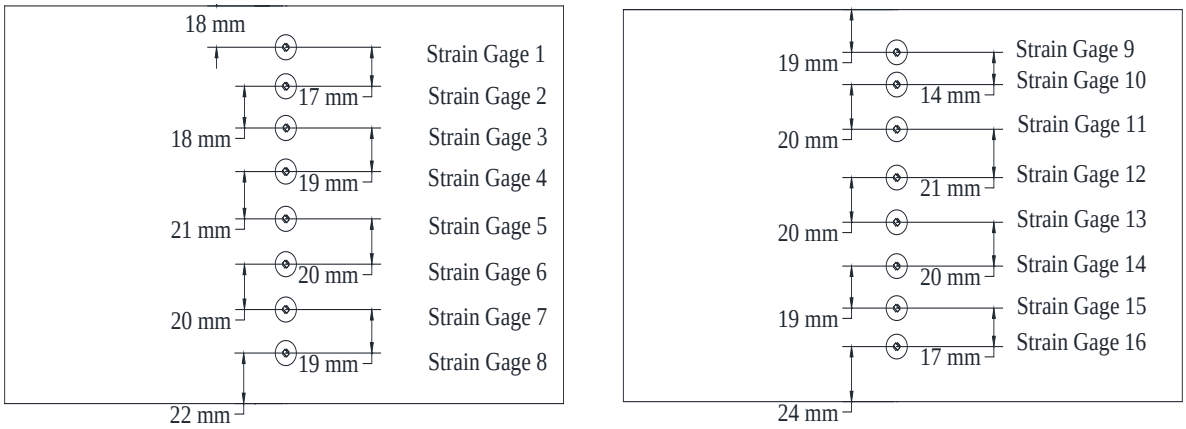

Figure 3-20. Strain gage layout in Tests 1A-R2, 2, and 6 (inner side of wall).

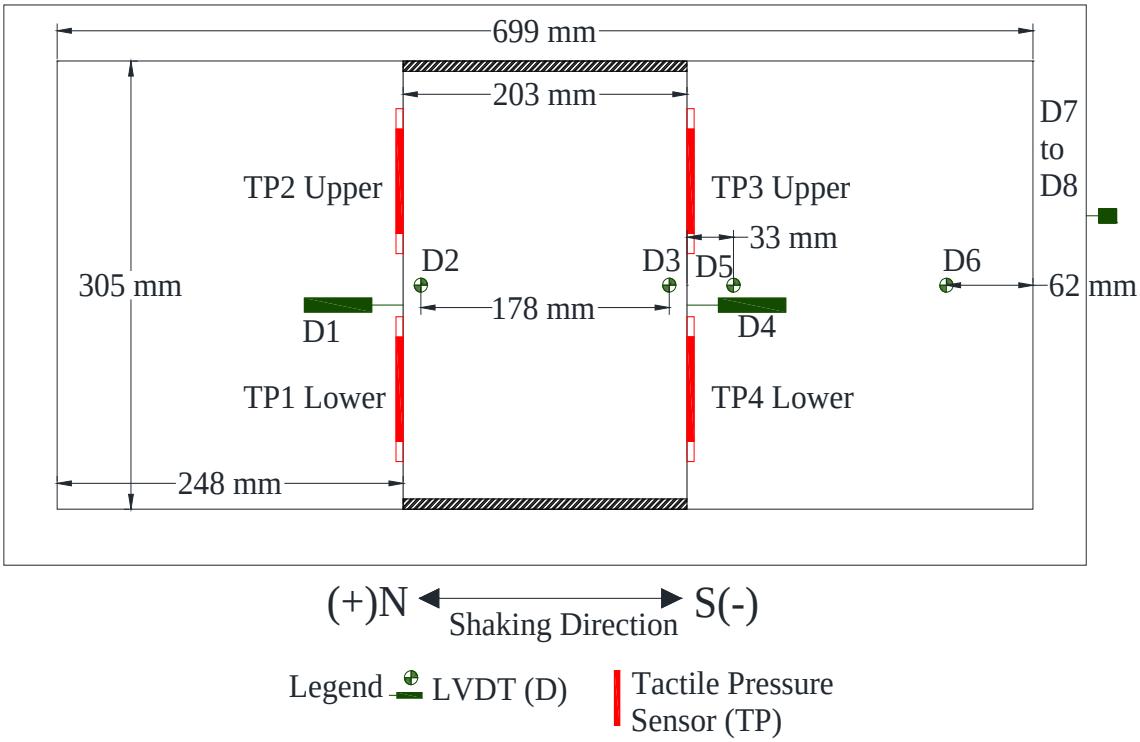

Figure 3-21. Plan view of Test 3A-R (different numbering of tactile pressure sensor).

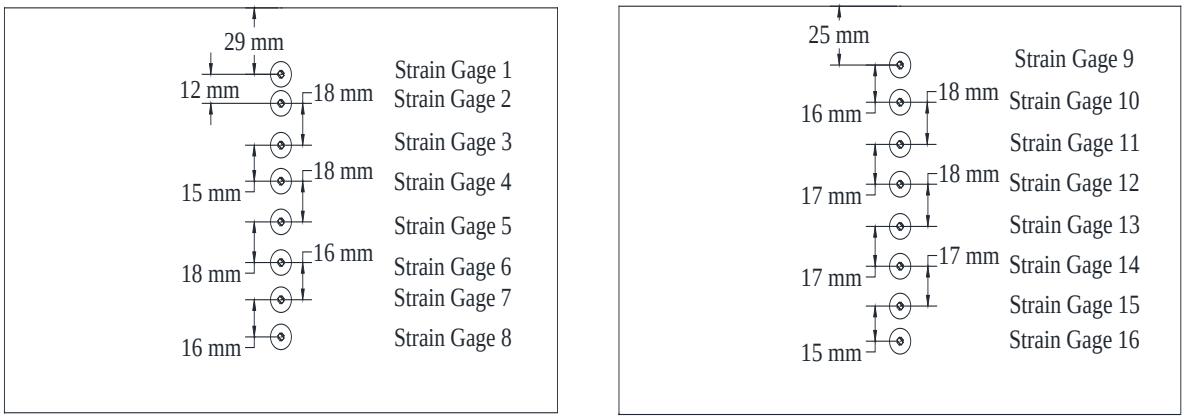

Figure 3-22. Strain gage layout in Test 3A-R (inner side of wall).

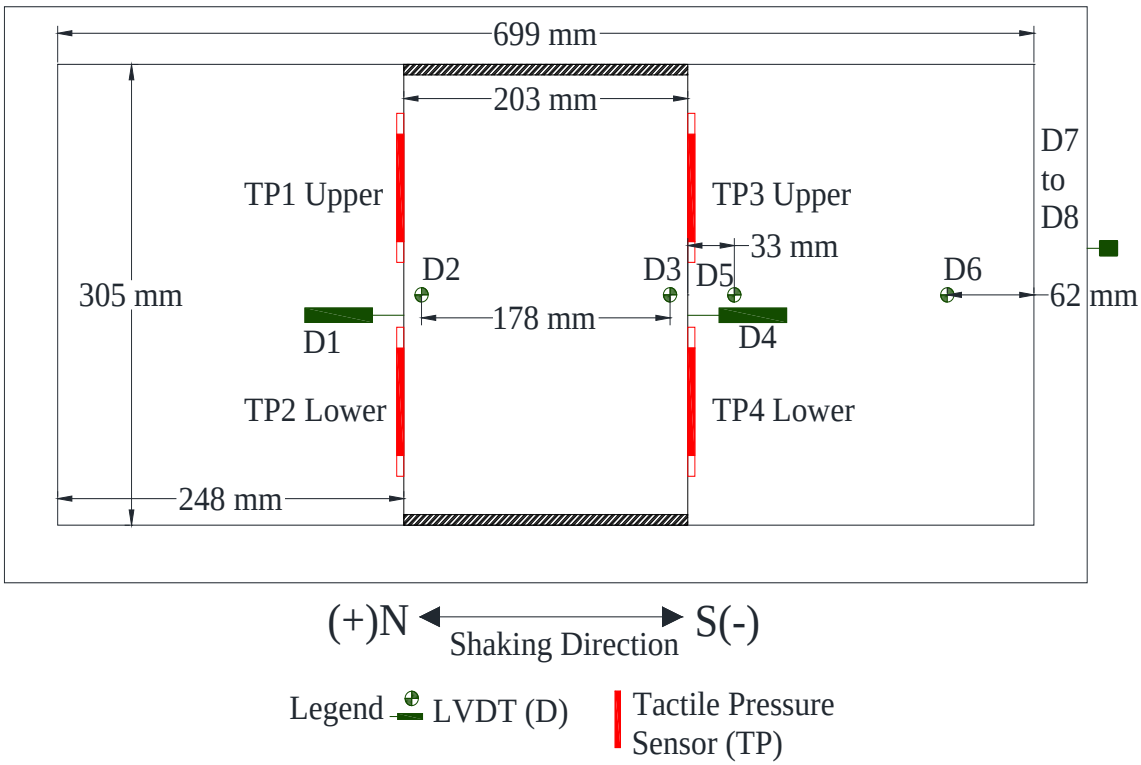

Figure 3-23. Plan view of Test 4A-R2.

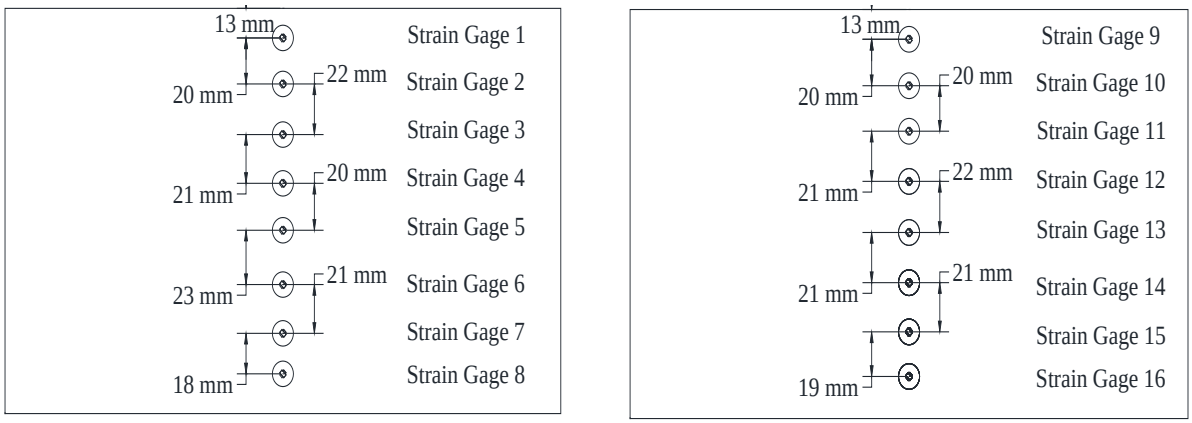

Figure 3-24. Strain gage layout in Test 4A-R2 (inner side of wall).

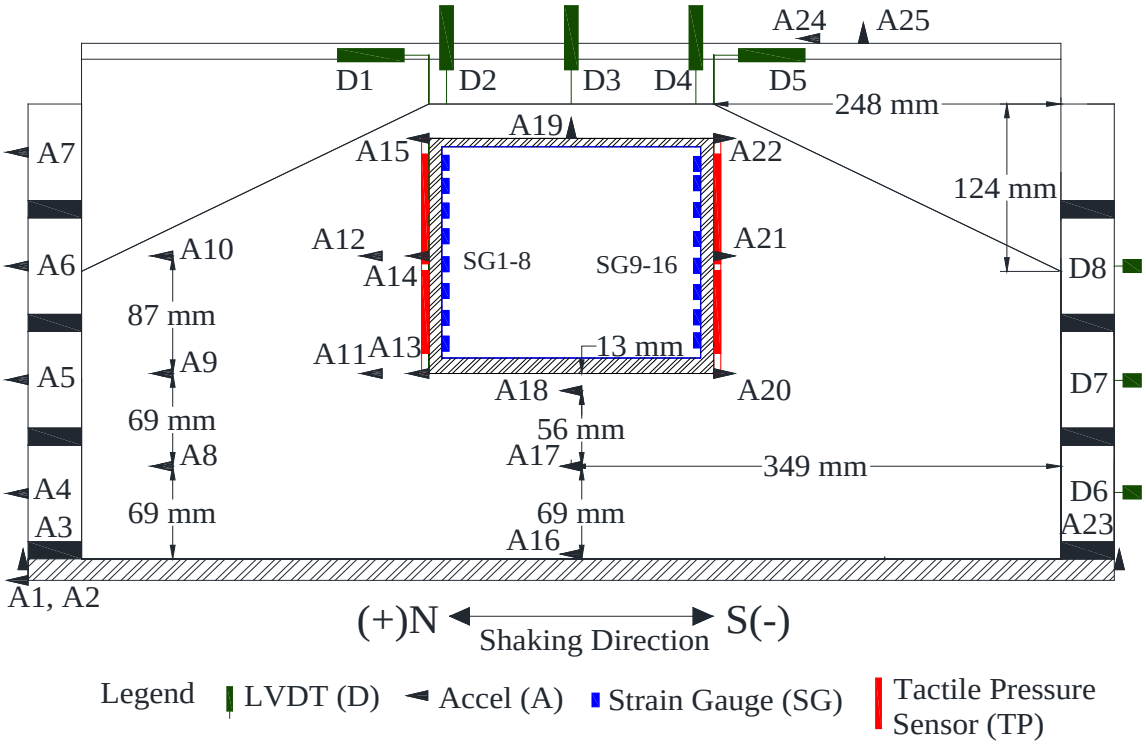

Figure 3-25. Elevation view of Test 6.

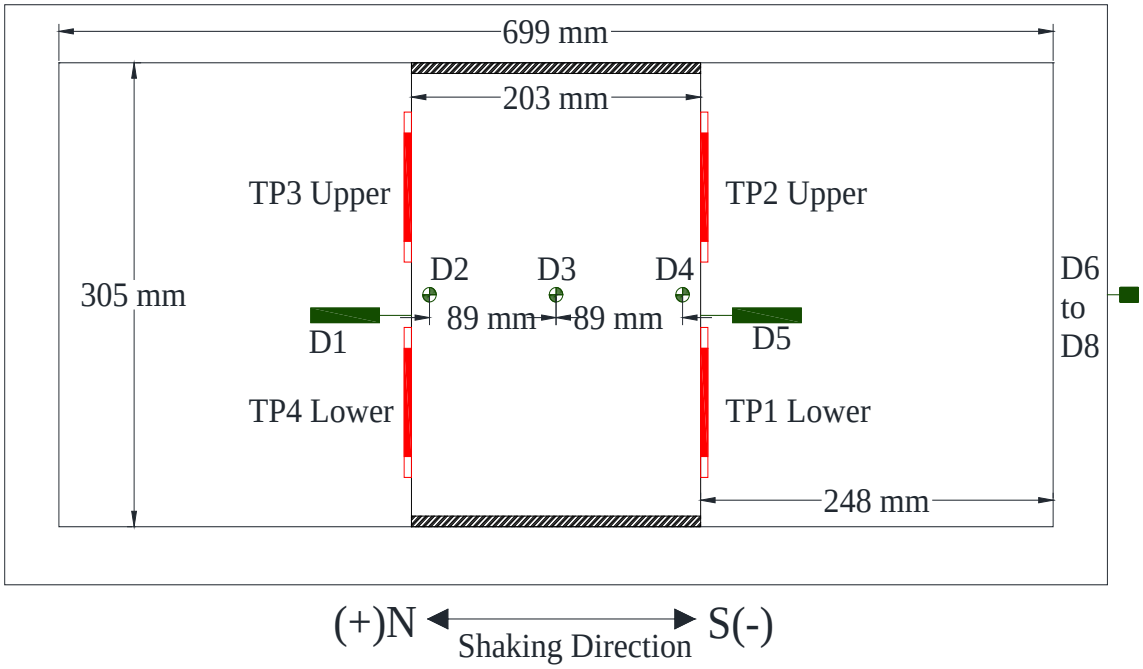

Figure 3-26. Plan view of Test 6.

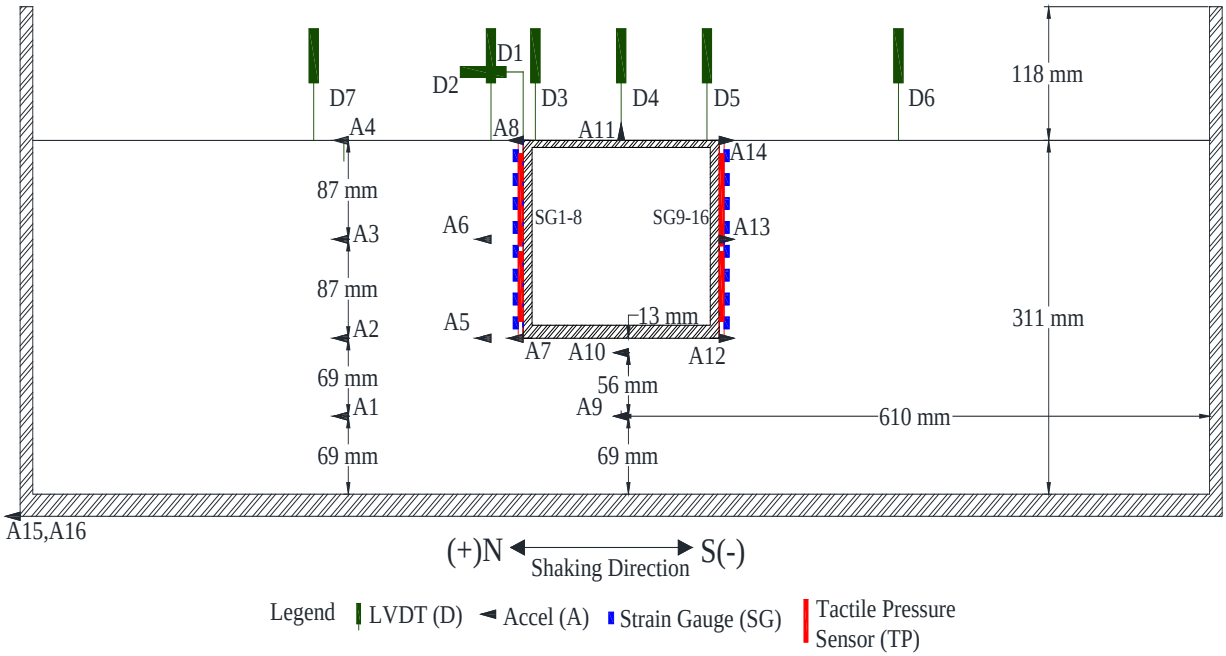

Figure 3-27. Elevation view of Test 7.

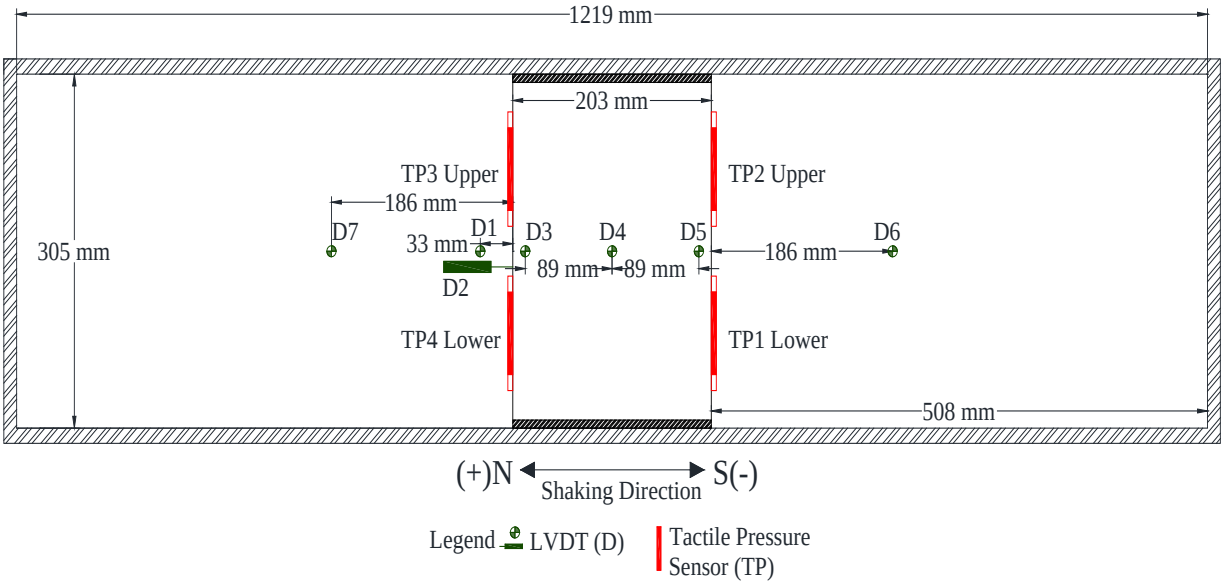

Figure 3-28. Plan view of Test 7.

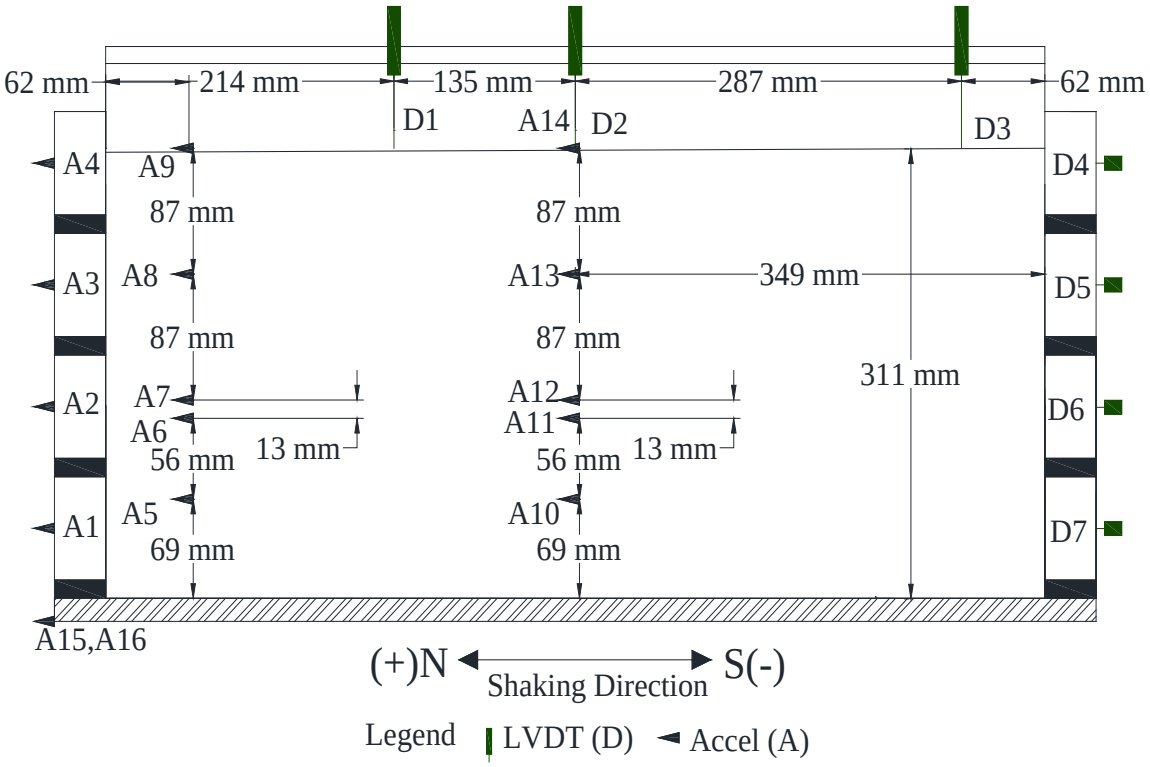

Figure 3-29. Elevation view of Free Field test.

3.2.2 Model Underground Structures

The actual prototype reservoirs are complex structures with many columns and interior walls that support the weight of the roof slabs as well as other structural details, the 3D response of which cannot be simulated properly in a scaled centrifuge model. Accordingly, simplified, equivalent prototype 2-D box structures were identified to match the lateral stiffness, and natural frequency of the actual prototype reservoir structures. The dimensions of these equivalent prototype box structures were then converted to model scale dimensions at 60g, to design and fabricate three model structures referred to as Baseline (BL), Flexible, and Stiff. Figure 3-30 and Figure 3-31 show the dimensions and pictures of the model structures. These model structures were designed with uniform 1018 Carbon Steel (density = 7870 kg/m^3; Young's Modulus = 200 GPa, Poisson's ratio=0.29). Their stiffness was varied by changing the geometry of the models, as summarized in Table 3-3. The model structures were fabricated by welding steel plates to ensure a strong moment connection at the corners. The fundamental frequencies of the structures were estimated by performing 3-D finite element simulations of structures in Abaqus. These values were then confirmed experimentally using vibration tests at 1g, in which the structures were bolted to a heavy plate atop the shaking table. The results are summarized in Table 3-3. The numerical and experimental values of fundamental frequency were consistent for all structures, confirming the validity of the model structures for simulating the prototype structures.

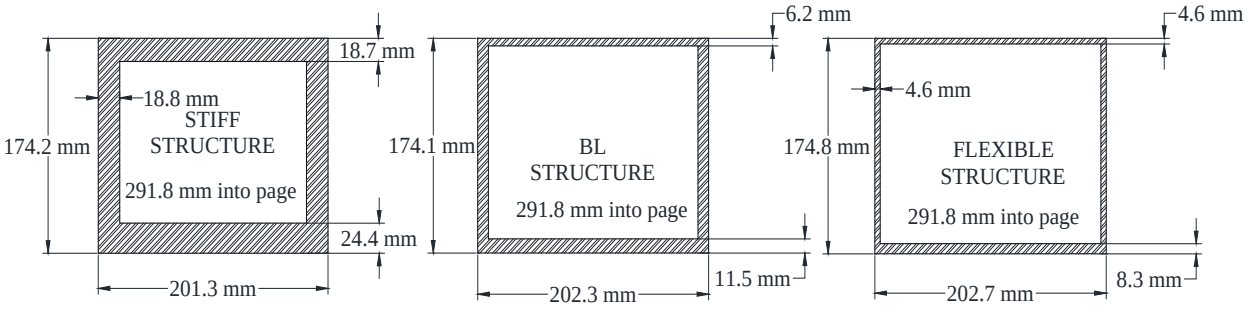

Figure 3-30. Dimensions of the three model underground reservoir structures.

Stiff Baseline (BL) Flexible

Figure 3-31. Photograph of the stiff, baseline, and flexible model structures.

Table 3-3. Properties of the underground structures used in centrifuge (model scale).

Structure	Lateral Stiffness, K_L (kN/m/m)	Fundamental Frequency (Hz)	
		Numerical	Experimental
Baseline	0.15	238	232
Flexible	0.03	120	116
Stiff	2.19	592	548

3.3 Soil Properties

3.3.1 Nevada Sand

A new batch of Nevada sand No. 120 was delivered to CU Boulder and mixed thoroughly before index tests were performed. Table 3-4 summarizes the properties of the Nevada sand and Figure 3-32 shows the grain size distribution. Figure 3-33 shows photographs taken while obtaining the minimum density (ASTM D4254) and maximum density (ASTM D4253) of Nevada sand.

Table 3-4. Mechanical properties of Nevada sand.

Source	G_s	ρ_d, min (kg/m^3)	ρ_d, max (kg/m^3)	e_{min}	e_{max}
Cooper Labs (2014)	2.66	1403.65	1696.43	0.565	0.892
Hushmand and Karimi (2014)	2.65	1437.62	1703.73	0.555	0.843

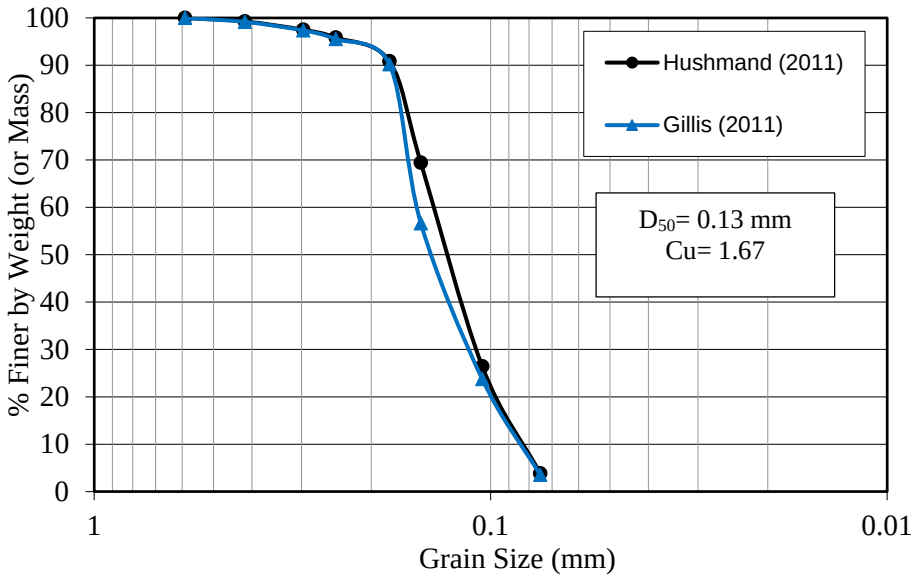

Figure 3-32. Grain size distribution of Nevada sand.

(a) (b)

Figure 3-33. (a) Minimum density (ASTM D4254) and Maximum density (ASTM D4253) tests performed on Nevada sand.

3.3.2 Site Specific Soil

Gradation (particle size analysis of soils, ASTM D422), modified proctor compaction tests (ASTM D1557), and direct shear tests (ASTM D3080) were performed on the site specific backfill soil

from the reservoir construction sites in Los Angeles. The orginal backfill material was classified as a brown, silty sand with gravel as show in Figure 3-34. The soil used in the centrifuge test was passed through the no. 40 sieve to reduce the particle size when taking into account centrifuge scaling laws. The grain size distribution curve for the silty sand used in the centrifuge test is shown in Figure 3-35.

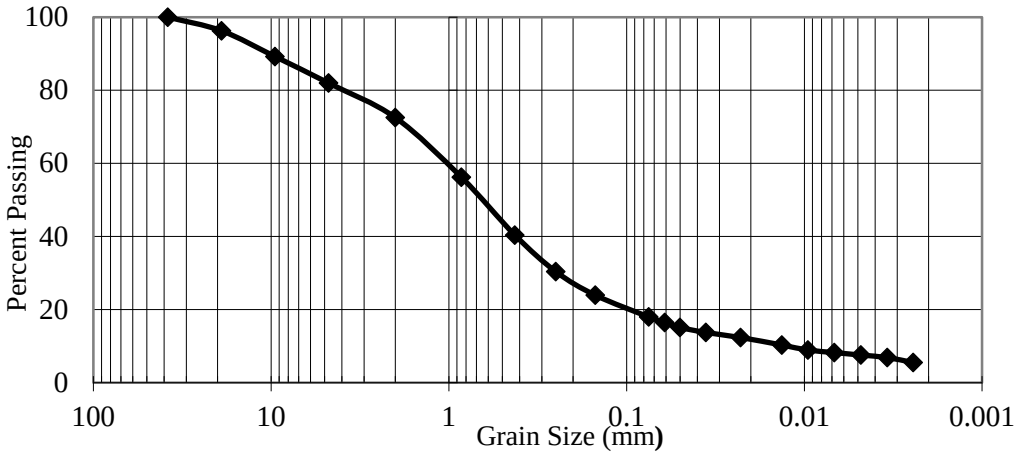

Figure 3-34. Grain size distribution of site-specific soil.

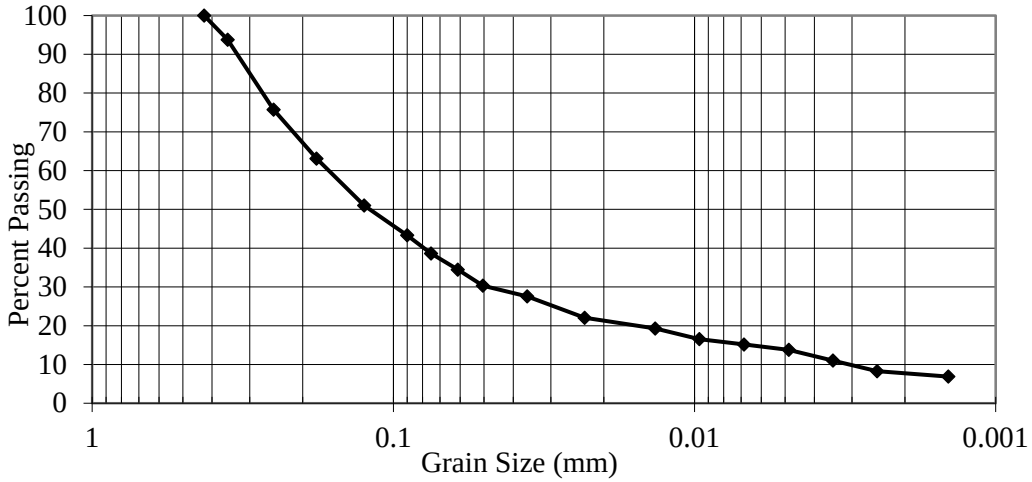

Figure 3-35. Grain size distribution of site-specific soil after passing through no. 40 sieve.

The results of the modified Proctor compaction test (ASTM D1557) performed on the site-specific silty sand to determine the maximum dry unit weight and optimum moisture content are

shown in Figure 3-36 and Table 3-5. The silty sand was compacted to 95% relative compaction at a total unit weight of 20.3 kN/m^{3}in Tests 5 and 6.

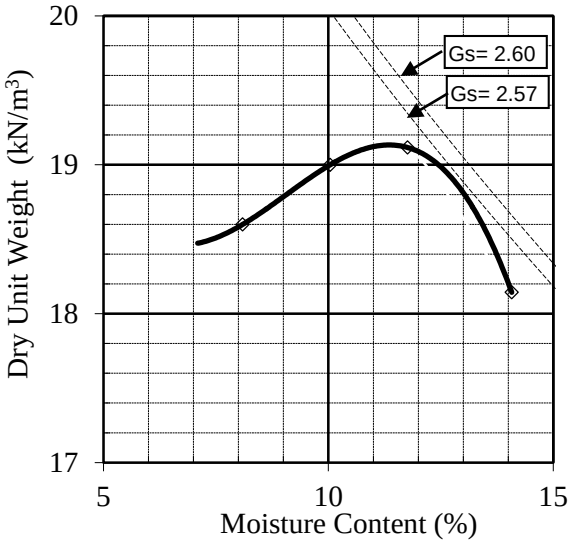

Figure 3-36. Modified proctor compaction test results on site-specific silty sand.

Table 3-5. Mechanical properties of compacted silty sand.

USCS	silty sand (SM)
Sand content	61.4 %
Fine Content	38.6 %
Water content	11.5 %
Maximum Dry Unit Weight	19.1 kN/m^3
Total Unit Weight	21.3 kN/m^3
Site Specific Relative Compaction	95 %
Desired Unit Weight	20.3 kN/m^3

Direct shear tests were conducted on samples remolded similarly to centrifuge test conditions at a total unit weight of 20.3 kN/m^3 and 11.5 % water content. One set (5 different nomral stresses) of direct shear tests were conducted at a saturation level as shown in Figure 3-37 similar to centrifuge test conditions and another set of tests were perfomed for specimens inundated in water as shown in Figure 3-39. The peak strength, ultimate strength friction angle and cohesion intercept for the in-situ test and inundate tests are shown in Figure 3-38 and Figure 3-40.

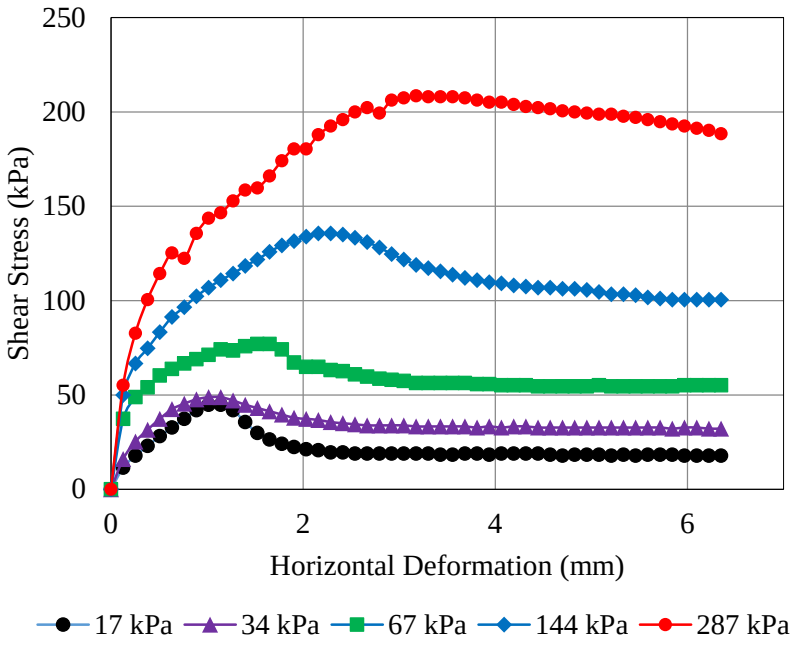

Figure 3-37. Shear stress-deformation curves from direct shear laboratory tests conducted on in-situ prepared compacted silty sand.

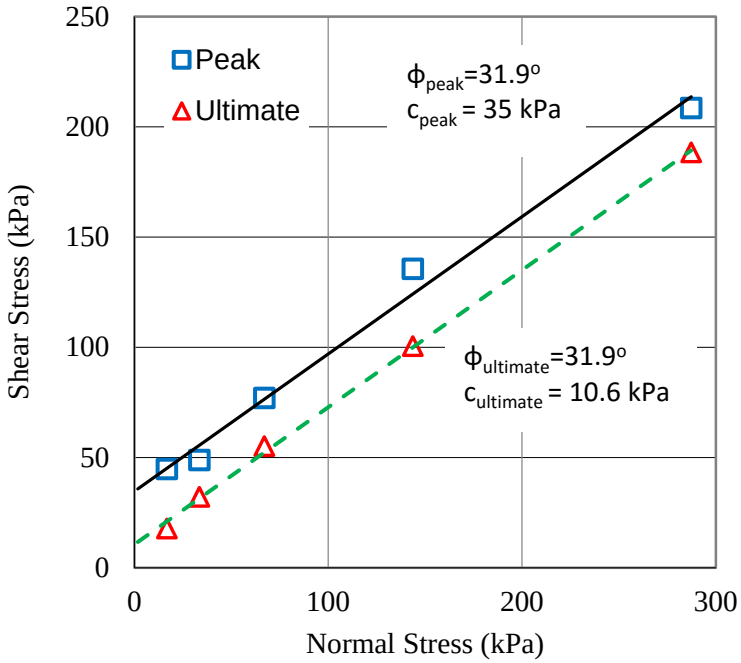

Figure 3-38. Peak and ultimate shear strength parameters from direct shear tests (in-situ tests).

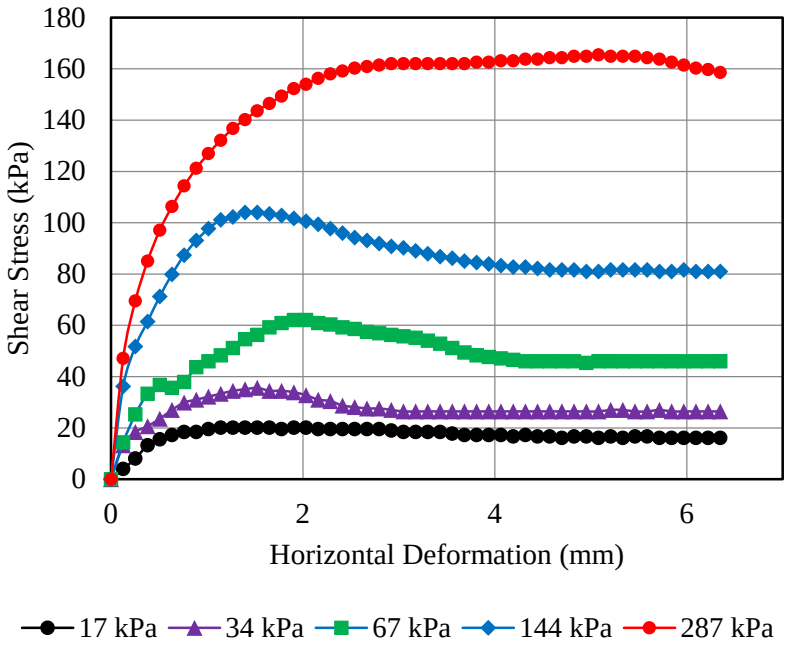

Figure 3-39. Shear stress-deformation curves from direct shear laboratory tests conducted on inundated compacted silty sand.

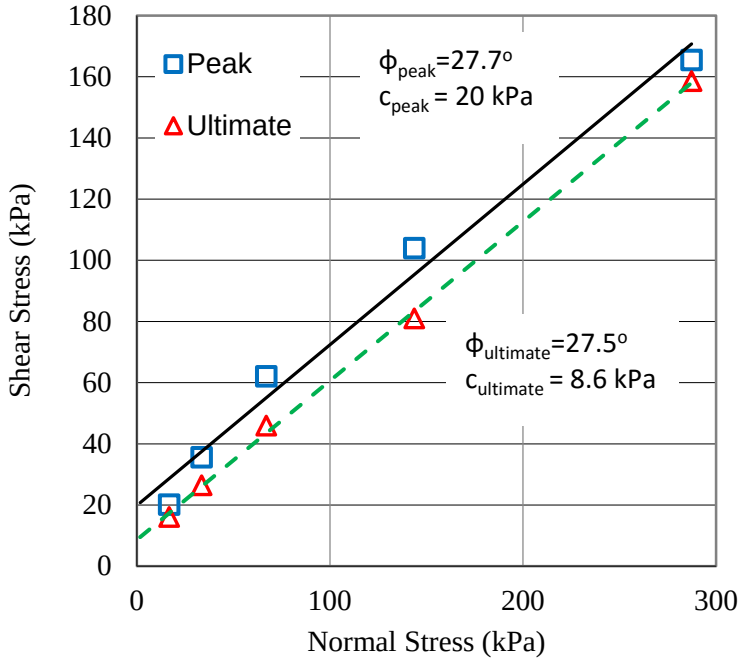

Figure 3-40. Peak and ultimate shear strength parameters from direct shear tests (inundated tests).

3.4 Instrumentation and Calibration

3.4.1 Overview

In each centrifuge test, data was acquired using accelerometers, LVDTs, strain gages, tactile pressure transducers, and pressure cells. The accelerometers, LVDTs, strain gages, and pressure cells were recorded on a separate data acquisition system at a model scale frequency of 3000 Hz (50 Hz prototype scale). The tactile pressure transducers measured data on a separate data acquisition system at a model-scale frequency of 4000 Hz (66.67 Hz prototype scale). Accelerometers were placed horizontally at the container base, shake table, on the container frames, at different elevations within the soil in the far-field and adjacent to the structure, on the structure, and on the instrumentation rack to monitor movement. Vertical accelerometers were also placed at the container base, roof of the structure, and instrumentation rack to monitor vertical movement. LVDTs were used to measure the settlement of soil and structure, the lateral displacement of structure, lateral displacement of FSB container frames, and lateral movement of container base. Eight strain gages (total of sixteen) were installed on each wall of the structure to measure bending strains and hence, bending moments. Four tactile pressure sensors were used to measure total pressure on both sides of the structures. Eight PDA pressure cells and eight EPL pressure cells were used to measure total pressures on both sides of the structures. Tactile pressure sensors calibration information are directly saved and used by the data acquisition and processing software provided by the transducer manufacturer (I-Scan software) for processing of the pressure data as explained in detail in Section 3.4.5.

3.4.2 Accelerometers

Models 352C67, 353B17, and 357B67 miniature accelerometers (Figure 1) manufactured by PCB Piezotronics, Inc. were used in these tests. Accelerometer models 353B17 and 357B67 have a

±500g level range and accelerometer model 352C67 has a ±50g range. Range is the +/- maximum amplitude that the accelerometer can measure before distorting or clipping the output signal. The calibration data provided by the manufacturer were used for all accelerometers, as is typically done for accelerometers.

The manufacturer usually recommends to calibrate the accelerometers once a year. Calibration was performed by fixing the accelerometers to the centrifuge shake table along with a new reference accelerometer as shown in Figure 3-41b. The calibration was done similar to actual test conditions by mounting the sand filled FSB to the shake table, spinning to 60g's and applying a series of harmonic motions with different amplitudes. Figure 3-42 is a typical plot of the calibration results showing the reference accelerometer on the x-axis and the accelerometer being tested on the y-axis. The results of the test showed negligible difference between the manufacturer calibration and experimental calibration.

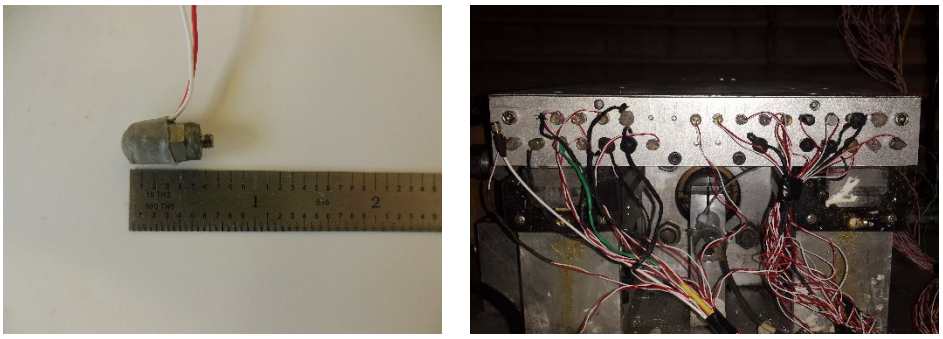

(a) (b)

Figure 3-41. (a) PCB Piezotronics accelerometer and (b) calibration of accelerometers.

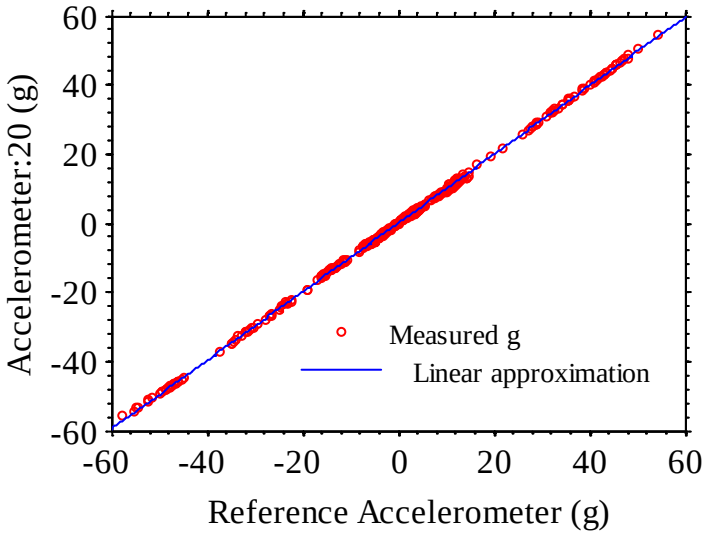

Figure 3-42. Amplitude of reference accelerometer vs. amplitude of accelerometer 21 in one sinewave motion.

3.4.3 LVDTs

Model MHR-500 LVDTs, (Figure 3-43a) manufactured by Measurement Specialties were used in these tests. The LVDTs have a nominal stroke range of ±12.7 mm. The LVDTs were calibrated by fixing them to a bracket allowing them to displace vertically as shown in Figure 3-43b. A set of precise gage blocks were used to displace the core as the output voltage was recorded for each increment using the centrifuge data acquisition system. The LVDT is a linear transducer and therefore requires a slope and an intercept for proper calibration. The calculated slope was used to convert the voltage output from the tests to displacement units. Figure 3-44 is an example plot of a LVDT calibration showing the DAQ output on the x-axis and measured displacement from blocks on the y-axis.

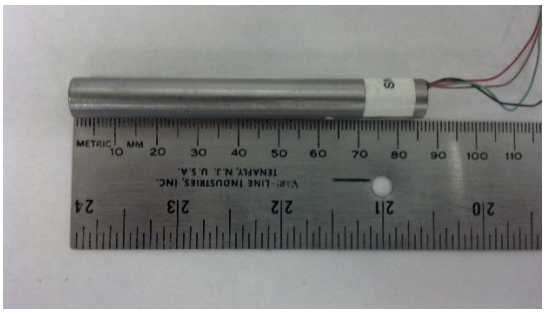

(a)

(b)

Figure 3-43. (a) Photograph of an LVDT manufactured by Measurement Specialties (b) LVDT calibration set-up.

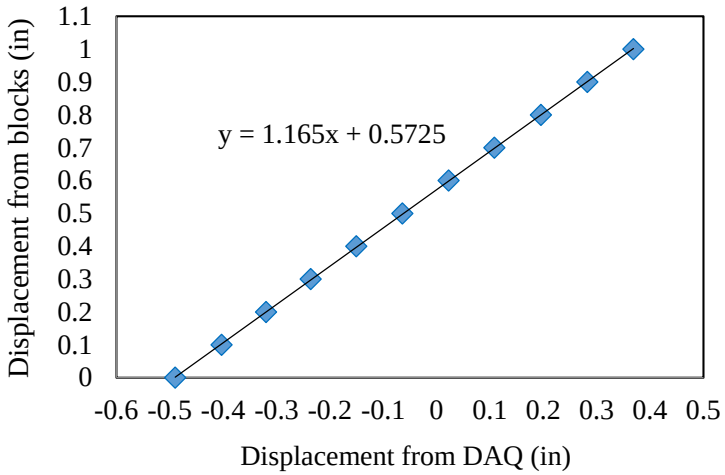

Figure 3-44. Example LVDT calibration.

3.4.4 Strain Gages

Two different brands of strain gages were used in these experiments (due to a lack of supply). The earlier tests used model C2A-06-125LT-350 strain gages as shown in Figure 3-45a manufactured by Vishay Precision Group. These strain gages were installed on the outside of both walls of the structures (see Figure 3-46). Later tests (Tests 2, 6, 1A-R2, 4A-R2 and 3A-R) used model FCA-3-11 strain gages manufactured by Tokyo Sokki Kenkyujo (see Figure 3-45b). These strain gages were installed on the inside wall of the structure to create more space for other sensors (see Figure 3-47).

Although it is ideal to use a full bridge configuration to measure pure bending, this was not possible due to space constraints on the reservoir model structure. Both types of gages were wired in a half bridge configuration to measure both bending and axial strain. The manufacturer gage factor, gage resistance, Poisson's ratio and excitation voltage were used as input in the DAQ to calculate output strain. Gage factor (also known as sensitivity to strain) is defined as the ratio of fractional change in electrical resistance to mechanical strain ε. The manufacturer provided information used for the two kinds of strain gages which are listed in Table 3-6.

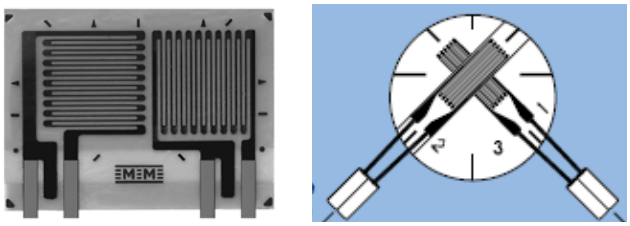

(a) (b)

Figure 3-45. (a) Vishay Precision Group strain gages, (b) Tokyo Sokki Kenkyujo strain gages.

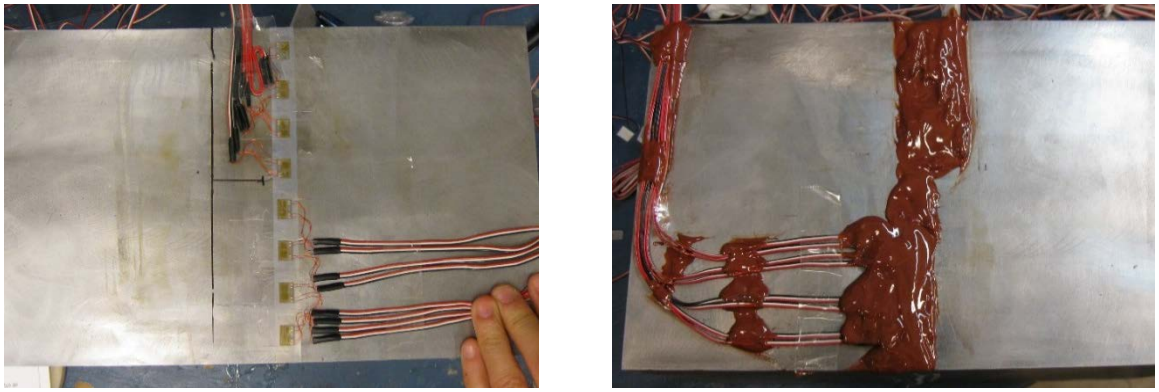

(a) (b)

Figure 3-46 (a) Placement of Vishay strain gages on outside wall of structures, and (b) application of epoxy to protect strain gages.

(a) (b)

Figure 3-47. (a) Structure with no strain gages on the outside wall (b) installed Tokyo Sokki Kenkyujo strain gages on the inside wall of structure.

Table 3-6. Strain gage properties.

Model	C2A-06-125LT-350	FCA-3-11
Gage factor	2.11±0.5%	2.12±1%.
Gage resistance (Ω)	350	120
Excitation (V)	2~10	2~6

Performance of the strain gages was checked statically and dynamically prior to centrifuge testing as shown in Figure 3-48. A uniform vacuum pressure was applied to the inside of the structure to check if the strain gages on both walls of the structure were registering an expected pattern of deformation. Figure 3-48b shows the measured strain profiles along the walls of the flexible structure. The deformation pattern shown is expected for the structure under vacuum pressure inside.

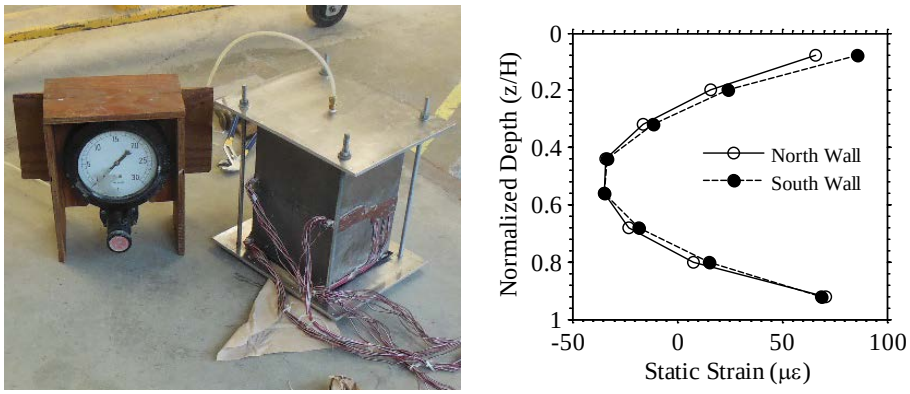

(a) (b)

Figure 3-48. Vacuum testing of strain gages prior to centrifuge testing: (a) applying uniform vacuum pressure; (b) measured strain profile under vacuum pressure of 45.7 kPa for flexible structure.

3.4.5 Tactile Pressure Sensors

Tactile sensors consist of two flexible polyester sheets with semi-conductive ink printed on them in stripe patterns, as shown in Figure 3-49. A grid pattern of sensing elements is formed when the two polyester sheets are placed on top of each other. When a force is applied to these sensing elements, the electrical resistance in the ink changes in inverse proportion to the applied normal force. Tactile sensor model 9500 manufactured by Tekscan Inc. was used to measure total pressures on the walls of the structures. Each tactile sensor model 9500 has 14 rows by 14 columns of sensels (measuring points) adding to 196 sensels, each 5.1 by 5.1 mm. Theses sensors recorded data using a separate data acquisition system compared to the accelerometers, strain gages, and LVDTS. Each of the 196 sensels recorded pressure at a rate of 4,000 samples per sec (sps) during dynamic loading and 1 sps during spin up and spin down.

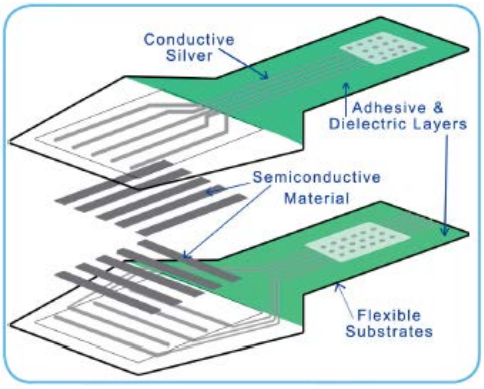

(a)

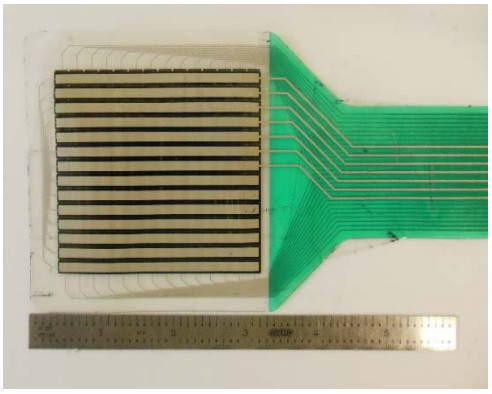

(b)

Figure 3-49. (a) Schematic of tactile sensor construction (b) Tekscan model 9500.

The sensors were first conditioned, equilibrated, and then calibrated both statically and dynamically, prior to use in the centrifuge. Conditioning was done by loading the sensor to high pressures several times using the PB100E pneumatic pressure device to minimize drift and hysteresis. Equilibration is a method of normalizing the sensor so that the output of every sensing element is the same when a uniform pressure is applied. The equilibrator device applies uniform air pressure to the sensors. The software then determines a unique scale factor for each sensing element to compensate for the slight variation of their outputs.

Static calibration was first done using the centrifuge by fixing the sensors to the bottom of the FSB container and placing a layer of Nevada sand at Dr=60% as shown in Figure 3-50. The raw output of the sensors was recorded as the container was spun in several steps from 1g to 60g, and the corresponding theoretical vertical pressures were calculated. Static calibration was also done using the pneumatic pressure device and a 320 grit sand paper as shown in Figure 3-50b. The 320 grit sand paper has a similar gradation to Nevada Sand. The sand paper was placed face down on the sensor to simulate similar test conditions as the pneumatic device applied pressure. The sensors were calibrated using three points in the equilibrator device (three measurement points for pressure and sensor recordings). The equilibration and static calibration results were used to convert the

raw pressure data to units of pounds per square inch (psi) inside the software I-Scan (Tekscan Inc.) as shown in Figure 3-51b.

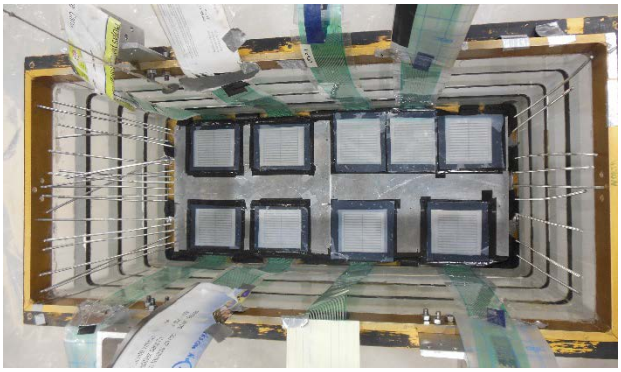

Figure 3-50. Calibration of tactile sensors using the centrifuge.

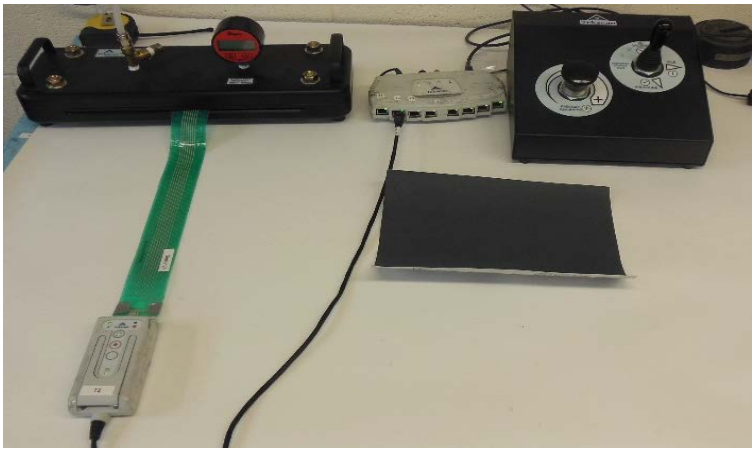

(a)

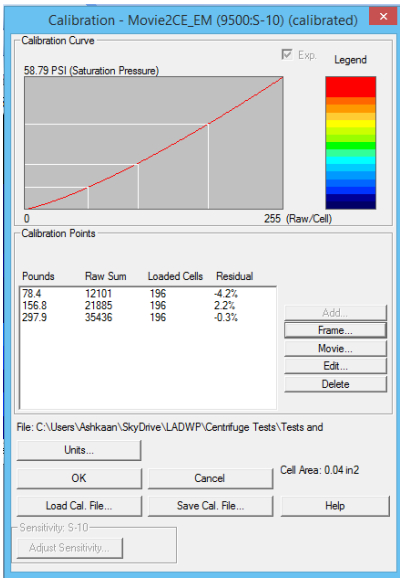

(b)

Figure 3-51. (a) Model PB100E pneumatic pressure device used for conditioning, equilibration, and static calibration; (b) static calibration result in I-Scan (Tekscan Inc.).

Tactile sensors were known to underestimate the full amplitude content of a dynamic signal in the high frequency environment of the centrifuge (Olson et al. 2011). This is partially caused by under-sampling of the signal with older sensor models. It is recommended to sample at least 10 times as fast as the highest frequency in the signal to ensure that it is accurately reconstructed in

the time domain (Derrick 2004). Centrifuge shake tables typically cannot produce controlled motions at frequencies greater than approximately 300 Hz (model scale). Hence, a minimum sampling rate of 3,000 sps is required in dynamic centrifuge experiments, which was satisfied in these tests.

The inability to measure the full amplitude of the dynamic pressure signal is also partially caused by the tactile sensor's frequency-dependent response, which needs to be characterized and accounted for (Dashti et al. 2012). By characterizing how the sensor records load over a range of frequencies, a transfer function was developed and applied to sensor recordings to compensate for the loss of pressure amplitude. This frequency-dependent, amplitude correction procedure is referred to as the sensor's dynamic calibration (detailed by Gillis et al. 2015).

The tactile sensors were first thoroughly de-aired by creating small holes to allow air to vent followed by sealing, according to the procedure recommended by Tessari et al. (2014). After they were conditioned and equilibrated, these sensors were statically calibrated using a pneumatic loading device and a fine sandpaper, as recommended by Tessari et al. (2014). Then, they were dynamically calibrated using the procedure described by Gillis et al. (2015).

3.4.6 Earth Pressure Cells

The two types of pressure cells used in some of the repeated experiments to compare with tactile sensors were Entran EPL-D12-50P and the Tokyo Sokki Kenkyujo PDA-500KPA earth pressure cells, as shown in Figure 3-52. The Entran sensors have a range of 0 to 345 kPa and the PDA sensors has a range of 0 to 500 kPa. These sensors consist of semiconductor strain gages bonded to a circular, stainless steel sensing membrane. The Entran sensors have a diameter of 5 mm and thickness of 1mm. The PDA sensors have a diameter of 6.5 mm and thickness of 1 mm. Figure 3-53 shows the installed earth pressure cells and tactile sensors on a model structure.

The pressure transducers were calibrated using air pressure. The response of the pressure transducers in terms of voltage changes were recorded and a calibration constant in terms of psi/volt or kPa/volt was determined for each sensor. The experimentally calculated calibration factors using air pressure were very similar to those provided by the manufacturer.

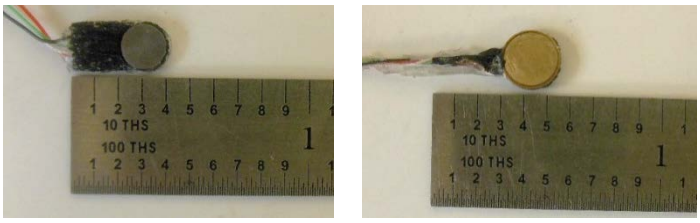

(a) (b)

Figure 3-52. (a) The EPL-D12-50 pressure sensor manufactured by Measurement Specialties, and (b) the PDA-500KPA pressure sensor manufactured by Tokyo Sokki Kenkyujo

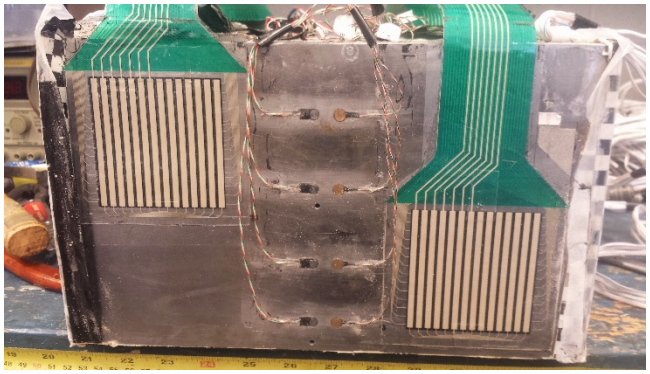

Figure 3-53. Placement of EPL and PDA sensors on the walls of the structure along with tactile sensors.

3.5 Model Preparation Method

Construction of the model specimens using Nevada sand consisted of several steps as shown in Figure 3-54. Model preparation began by pluviating sand from a pre-determined calibrated height to achieve a relative density of 60%. The sand was then leveled and accelerometers were placed at pre-selected locations until the elevation of the structure base was reached. Teflon sheets were placed between the sidewalls of the container and the ends of the structure to allow relative sliding and minimize friction, in order to simulate plane strain conditions. The structure was placed in the

middle of the long side of the FSB container parallel to its width followed by sand pluviation on the two sides of the structure until reaching its top elevation. The relative density of the sand adjacent to the structure was not very uniform because the sand would reflect off the structure during pluviation. However, it is believed that after a couple of shakes the relative density of the soil became more uniform throughout the model. Tests 1B, 3B, and 4B were created by pluviating a 1 inch layer of sand over the specimen already used in Tests 1A, 3A, and 4A, respectively.

The construction of Tests 5 and 6 was affected by a number of factors including the natural water content in the soil, compaction technique, and previous experience. The models construction consisted of several stages as described below and shown in Figure 3-55.

- **Soil preparation and sieving**: For each test, site-specific silty sand soil was retrieved from the Headworks reservoir site in Los Angeles, California. The soil was passed through sieve No. 40 to remove large particles. Approximately 136 kilograms of the sieved site-specific soil was used for each test.
- **Soil mixing:** The soil was mixed together to ensure uniformity of gradation and initial moisture content. The target moisture content was 11.5% and the natural moisture content was about 5%. The water was slowly sprayed on the soil and mixed thoroughly to ensure uniform moisture content.
- **Soil compaction:** A certain amount of soil was poured by weight and spread evenly. The soil was compressed lightly using a wooden board to make the surface even. The layer of soil was compacted using a 4.5 kg guided falling hammer.

- **Placement of instruments and structure:** The soil was scarified and the accelerometers were placed at pre-determined locations. The accelerometers were covered with a layer of firm soil to prevent damage due to compaction.

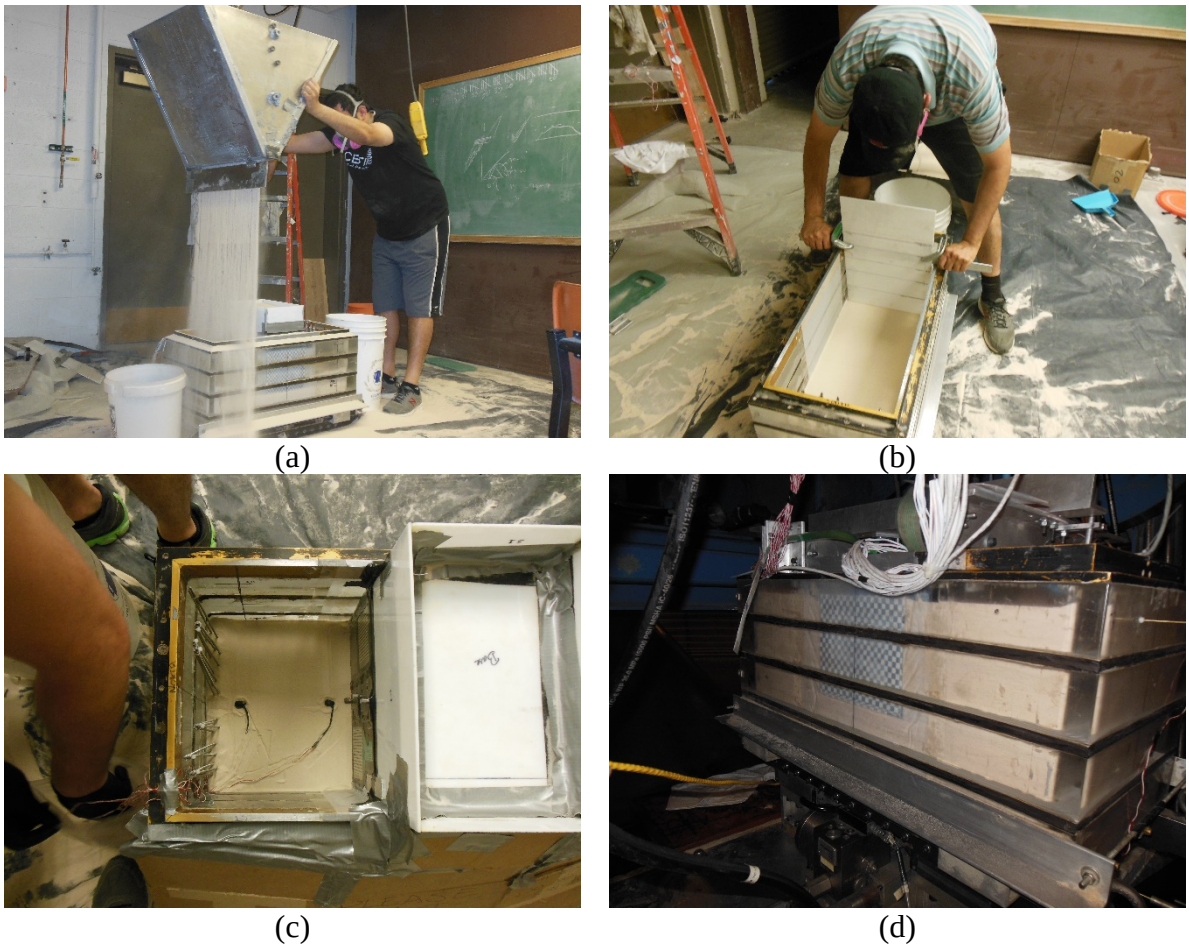

(a) (b)

(c) (d)

Figure 3-54. Construction of typical soil-structure centrifuge specimen: (a) sand pluviation,(b) levelling of sand layer, (c) installation of accelerometers, and(d) finished model specimen on the arm.

(a)

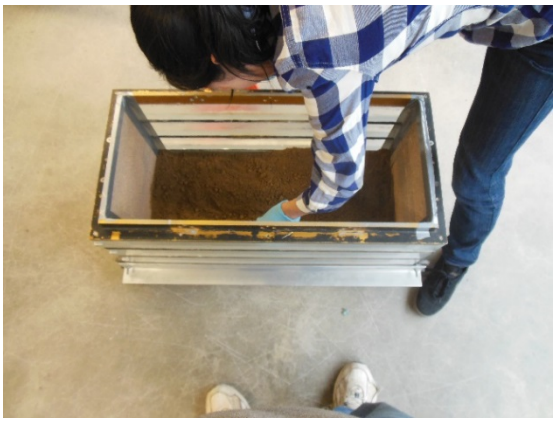

(b)

(c)

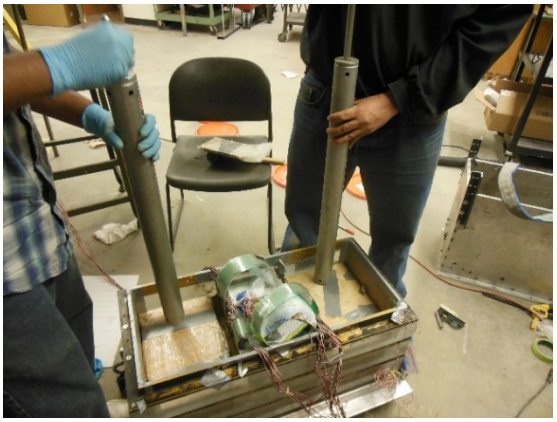

(d)

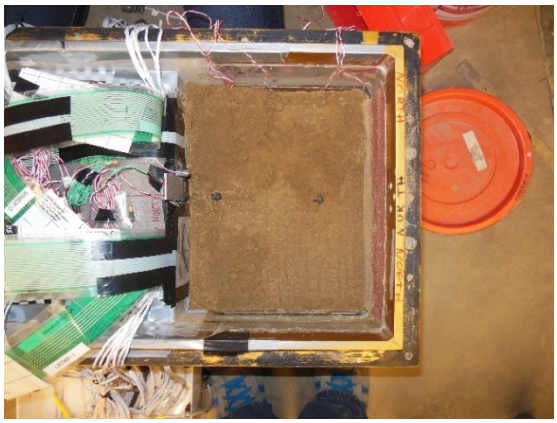

(e)

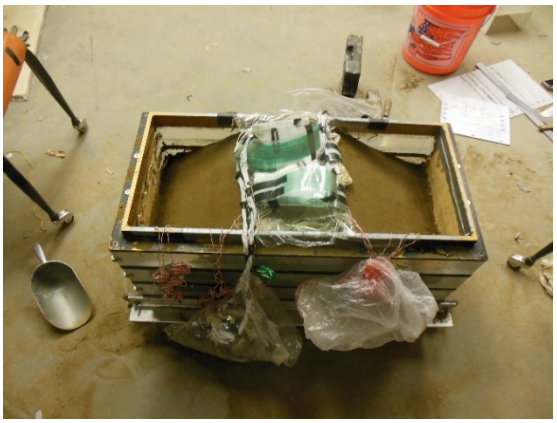

(f)

Figure 3-55. Construction of model with silty sand soil: (a) soil mixing, (b) placement of soil, (c) levelling of soil, (d) compaction of soil, (e) placement of accelerometers, and (f) finished specimen.

3.6 Ground Motions

Five earthquake base motions were selected by LADWP for the specific site of interest, here referred to as desired motions. These motions included three scaled versions of the horizontal acceleration recording at the Sylmar Converter Station during the 1994 Northridge Earthquake (NSC52) at three different intensities, one at the LGPC Station during the 1989 Loma Prieta Earthquake (LGP000), and one at the Istanbul Station during the 1999 Izmit Earthquake in Turkey (IST180), all obtained from the PEER database. Of these motions, the Loma Prieta Motion was selected and modified to match the target, site-specific, deterministic acceleration response spectrum at the project site (Harounian et al. 2014). The other motions were selected to evaluate the influence of different ground motion characteristics (i.e., in terms of intensity, frequency content, and duration) on the performance of the buried structures and their interaction with the surrounding soil.

The desired horizontal base motions were converted from prototype to model scale units and filtered to remove certain frequencies. These include the first mode natural frequency of the centrifuge arm, 5 Hz in model scale (0.08 Hz in prototype scale when tested at 60g) and frequencies higher than approximately 900-1200 Hz in model scale (15-20 Hz in prototype scale), which are typically outside the range of interest for earthquake engineering applications and are too high for the shake table system. These acceleration time histories were then double integrated to obtain displacement command signals. An iterative procedure similar to that described by Ketcham et al. (1991) was then implemented to obtain a command signal that produced a shaking table motion close to that desired both in terms of spectral accelerations and Arias Intensity time histories.
One accelerometer was placed on the shake table and another was placed on the base of the FSB container to measure the achieved motion. Both accelerometers measured very similar motions in

terms of amplitude and frequency during all tests. The seismic parameters of the achieved base motions for all tests are summarized in Table 3-7 through Table 3-22. For each ground motion the parameters listed are the Peak Ground Acceleration (PGA), Arias Intensity (I_a), Significant Duration of the acceleration record ($D_{5\text{-}95}$), Mean Period (T_m), and Predominant Period (T_p). The Arias Intensity I_a, is a measure of the total energy released and is defined as:

$$I_a = \frac{2\pi}{g}\int a^2(t)dt \qquad 3.6$$

The Significant Duration $D_{5\text{-}95}$ (Trifunac and Brady 1975), is defined as the time required for 90% of total energy to be released, i.e. the interval between 5% and 95% of the Arias Intensity. Mean Period, T_m (Rathje et al. 1998), is a frequency content characterization parameter estimated as:

$$T_m = \sum c_i^2 f_i^{-1} / \sum c_i^2 \qquad 3.7$$

where c_i is the Fourier amplitude of the acceleration series, fi is the discrete frequencies between 0.25-20 Hz. Predominant Period, T_p, is the period at which the maximum spectral acceleration occurs in an acceleration response spectrum at 5% damping. Figures 3-51 through 3-53 show the acceleration response spectra (5% damped) of the filtered (fifth order Butterworth low-pass filter with prototype scale corner frequency of 18 Hz for noise reduction, as well as a fifth order Butterworth high-pass filter with a prototype scale corner frequency of 0.1 Hz) recorded base ground motions during all tests. The *achieved* base motions were slightly different during various experiments because the weight and natural frequency of the model specimens varied, affecting the shake table performance. Therefore, the base motions are presented during each test when discussing results. A total of eight sinusoidal motions, each with a target amplitude of approximately 0.3 g in the prototype scale, was applied to the base of the specimen for a duration

of 15 cycles in the following order in terms of frequency: 0.33 Hz, 1 Hz, 2 Hz, 3 Hz, 4 Hz, 5 Hz, 6 Hz, and 6.67 Hz.

Table 3-7 Achieved base motion parameters in sequence from accelerometer A15 (units in prototype scale) in Test 1A.

Sequence Number	Ground Motion Name	PGA (g)	Arias Intensity I_a (m/s)	Significant[4] Duration $D_{5\text{-}95}$ (s) / Number of Cycles	Mean Period T_m (s)	Predominant[5] Period T_p (s) / Frequency (Hz)
1	Northridge[1]-L (trial 1)	0.34	1.5	15.54 s	0.70	0.37
2	Northridge-L (trial 2)	0.36	1.56	15.4 s	0.71	0.35
3	Northridge-M	0.81	5.45	19.54	0.66	0.28
4	Northridge-H	1.2	11.56	25.11 s	0.63	0.28
5	Izmit[2] 0.3	0.33	2.1	39.52 s	0.56	0.24
6	Sine 0.33 Hz	0.33	---	15	---	0.33
7	Sine 1 Hz	0.34	---	15	---	1
8	Sine 2 Hz	0.4	---	15	---	2
9	Sine 3 Hz	0.39	---	15	---	3
10	Sine 4 Hz	0.31	---	15	---	4
11	Sine 5 Hz	0.5	---	15	---	5
12	Sine 6 Hz	0.32	---	15	---	6
13	Sine 6.67 Hz	0.35	---	15	---	6.67
14	Loma[3] 0.9	1.0	12.39	13.29 s	0.50	0.27

Notes:
1. Northridge: 1994 M 6.7 Northridge Earthquake, Sylmar Converter Station, NSC52 Record
2. Izmit: 1999 M 7.5 Izmit, Turkey (Koceali) Earthquake, Istanbul Station, IST180 Record
3. Loma: 1989 M 6.9 Loma Prieta Earthquake, LGPC Station, LGP000 Record
4. This column is "Significant Duration $D_{5\text{-}95}$ (s)" for earthquake motions, and "Number of Cycles" for sinewave motions.
5. This column is "Predominant Period T_p (s)" for earthquake motions, and "Frequency (Hz)" for sinewave motions.

Table 3-8 Achieved base motion parameters in sequence from accelerometer A1 (units in prototype scale) in Test 1A-R.

Sequence Number	Ground Motion Name	PGA (g)	Arias Intensity I_a (m/s)	Significant Duration $D_{5\text{-}95}$ (s) / Number of Cycles	Mean Period T_m (s)	Predominant Period T_p (s) / Frequency (Hz)
1	Northridge-L (trial 1)	0.08	0.24	19	1.67	0.89
2	Northridge-L (trial 2)	0.14	0.33	18.4	1.25	1.1
3	Northridge-L (trial 3)	0.17	0.47	17.7	1.16	1.1
4	Northridge-L (trial 4)	0.25	0.99	18	0.98	1.1
5	Northridge-M	0.74	5.36	20	0.68	0.3
6	Northridge-H	1.21	10.7	25.7	0.65	0.27
7	Izmit 0.3	0.33	1.97	39.48	0.6	0.25
8	Sine 0.33 Hz	0.34	---	15	---	0.33
9	Sine 1 Hz	0.35	---	15	---	1
10	Sine 2 Hz	0.38	---	15	---	2
11	Sine 3 Hz	0.42	---	15	---	3
12	Sine 4 Hz	0.34	---	15	---	4
13	Sine 5 Hz	0.48	---	15	---	5
14	Sine 6 Hz	0.31	---	15	---	6
15	Sine 6.67 Hz	0.38	---	15	---	6.67
16	Loma 0.9	0.99	12.28	13.13	0.5	0.28

Notes:

(*) The Northridge 0.3 ground motion was applied four times until the proper base PGA amplitude was achieved. The first trials were needed to warm up the shake table in an extremely cold weather during that week.

Table 3-9 Achieved base motion parameters in sequence from accelerometer A1 (units in prototype scale) in Test 1A-R2.

Sequence Number	Ground Motion Name	PGA (g)	Arias Intensity I_a (m/s)	Significant[4] Duration $D_{5\text{-}95}$ (s) / Number of Cycles	Mean Period T_m (s)	Predominant[5] Period T_p (s) / Frequency (Hz)
1	Northridge-L	0.26	1.30	21.62	1.06	1.1
2	Northridge-M	0.73	5.84	26.65	0.67	0.30
3	Northridge-H	1.26	12.87	26.71	0.60	0.28
4	Izmit	0.30	2.64	37.60	0.57	0.23
5	Sine 0.33 Hz	0.27	---	15	---	0.33
6	Sine 1 Hz	0.31	---	15	---	1
7	Sine 2 Hz	0.40	---	15	---	2
8	Sine 3 Hz	0.44	---	15	---	3
9	Sine 4 Hz	0.41	---	15	---	4
10	Sine 5 Hz	0.92	---	15	---	5
11	Sine 6 Hz	0.50	---	15	---	6
12	Sine 6.67 Hz	0.50	---	15	---	6.67
13	Loma	1.05	15.04	12.75	0.43	0.19
14	Northridge-L2	0.31	1.78	18.4	0.76	0.25
15	Izmit-2	0.32	2.81	39.12	0.54	0.25

Table 3-10 Achieved base motion parameters in sequence from accelerometer A16 (units in prototype scale) in Test 1B.

Sequence Number	Ground Motion Name	PGA (g)	Arias Intensity I_a (m/s)	Significant[4] Duration $D_{5\text{-}95}$ (s) / Number of Cycles	Mean Period T_m (s)	Predominant[5] Period T_p (s) / Frequency (Hz)
1	Northridge-L	0.32	1.48	16.0	0.73	0.33
2	Northridge-M	0.71	4.7	21.1	0.70	0.29
3	Northridge-H	1.1	10.1	26.2	0.66	0.28
4	Izmit	0.32	2.10	40.3	0.57	0.24
5	Sine 0.33 Hz	0.31	---	15	---	0.33
6	Sine 1 Hz	0.34	---	15	---	1
7	Sine 2 Hz	0.38	---	15	---	2
8	Sine 3 Hz	0.41	---	15	---	3
9	Sine 4 Hz	0.29	---	15	---	4
10	Sine 5 Hz	0.45	---	15	---	5
11	Sine 6 Hz	0.31	---	15	---	6
12	Sine 6.67 Hz	0.43	---	15	---	6.67
13	Loma	1.0	11.1	13.3	0.51	0.45

Table 3-11 Achieved base motion parameters in sequence from accelerometer A1 (units in prototype scale) in Test 2.

Sequence Number	Ground Motion Name	PGA (g)	Arias Intensity I_a (m/s)	Significant[4] Duration $D_{5\text{-}95}$ (s) / Number of Cycles	Mean Period T_m (s)	Predominant[5] Period T_p (s) / Frequency (Hz)
1	Northridge-L	0.37	1.99	17.96	0.71	0.73
2	Northridge-M	0.96	8.88	19.88	0.61	0.23
3	Northridge-H	1.39	18.27	25.99	0.56	0.23
4	Izmit	0.33	3.39	39.42	0.52	0.45
5	Sine 0.33 Hz	0.34	---	15	---	0.33
6	Sine 1 Hz	0.44	---	15	---	1
7	Sine 2 Hz	0.54	---	15	---	2
8	Sine 3 Hz	0.33	---	15	---	3
9	Sine 4 Hz	0.24	---	15	---	4
10	Sine 5 Hz	0.35	---	15	---	5
11	Sine 6 Hz	0.35	---	15	---	6
12	Sine 6.67 Hz	0.38	---	15	---	6.67
13	Loma	1.23	22.07	14.13	0.44	0.28

Table 3-12 Achieved base motion parameters in sequence from accelerometer A16 (units in prototype scale) in Test 3A.

Sequence Number	Ground Motion Name	PGA (g)	Arias Intensity I_a (m/s)	Significant[4] Duration $D_{5\text{-}95}$ (s) / Number of Cycles	Mean Period T_m (s)	Predominant[5] Period T_p (s) / Frequency (Hz)
1	Northridge-L	0.30	1.33	16.24	0.78	0.36
2	Northridge-M	0.70	4.88	21.68	0.69	0.31
3	Northridge-H	1.14	10.26	26.0	0.66	0.28
4	Izmit	0.33	1.92	40.38	0.59	0.25
5	Sine 0.33 Hz	0.33	---	15	---	0.33
6	Sine 1 Hz	0.33	---	15	---	1
7	Sine 2 Hz	0.38	---	15	---	2
8	Sine 3 Hz	0.41	---	15	---	3
9	Sine 4 Hz	0.34	---	15	---	4
10	Sine 5 Hz	0.48	---	15	---	5
11	Sine 6 Hz	0.35	---	15	---	6
12	Sine 6.67 Hz	0.47	---	15	---	6.67
13	Loma	0.97	10.65	13.58	0.50	0.27

Table 3-13 Achieved base motion parameters in sequence from accelerometer A1 (units in prototype scale) in Test 3A-R.

Sequence Number	Ground Motion Name	PGA (g)	Arias Intensity I_a (m/s)	Significant[4] Duration $D_{5\text{-}95}$ (s) / Number of Cycles	Mean Period T_m (s)	Predominant[5] Period T_p (s) / Frequency (Hz)
1	Northridge-L	0.3	1.42	21.14	0.83	0.36
2	Northridge-M	0.78	5.5	27.6	0.68	0.34
3	Northridge-H	1.15	11.86	27.23	0.61	0.28
4	Izmit-1	0.32	2.75	38.8	0.58	0.25
5	Sine 0.33 Hz	0.29	---	15	---	0.33
6	Sine 1 Hz	0.32	---	15	---	1
7	Sine 2 Hz	0.34	---	15	---	2
8	Sine 3 Hz	0.42	---	15	---	3
9	Sine 4 Hz	0.39	---	15	---	4
10	Sine 5 Hz	0.51	---	15	---	5
11	Sine 6 Hz	0.46	---	15	---	6
12	Northridge-L-2	0.30	1.73	18.5	0.78	0.25
13	Izmit-2	0.33	2.78	38	0.57	0.25
14	Loma	1.14	14.27	12.77	0.42	0.19

Table 3-14 Achieved base motion parameters in sequence from accelerometer A16 (units in prototype scale) in Test 3B.

Sequence Number	Ground Motion Name	PGA (g)	Arias Intensity I_a (m/s)	Significant[4] Duration $D_{5\text{-}95}$ (s) / Number of Cycles	Mean Period T_m (s)	Predominant[5] Period T_p (s) / Frequency (Hz)
1	Northridge-L	0.29	1.37	17.76	0.82	0.36
2	Northridge-M	0.66	4.49	24.40	0.74	0.30
3	Northridge-H	1.0	9.0	27.0	0.69	0.27
4	Izmit	0.34	1.80	40.50	---	0.25
5	Sine 0.33 Hz	0.32	---	15	---	0.33
6	Sine 1 Hz	0.32	---	15	---	1
7	Sine 2 Hz	0.34	---	15	---	2
8	Sine 3 Hz	0.36	---	15	---	3
9	Sine 4 Hz	0.34	---	15	---	4
10	Sine 5 Hz	0.47	---	15	---	5
11	Sine 6 Hz	0.34	---	15	---	6
12	Sine 6.67 Hz	0.44	---	15	---	6.67
13	Loma	0.97	9.61	13.30	0.51	0.27

Table 3-15 Achieved base motion parameters in sequence from accelerometer A16 (units in prototype scale) in Test 4A.

Sequence Number	Ground Motion Name	PGA (g)	Arias Intensity I_a (m/s)	Significant[4] Duration $D_{5\text{-}95}$ (s) / Number of Cycles	Mean Period T_m (s)	Predominant[5] Period T_p (s) / Frequency (Hz)
1	Northridge-L	0.24	1.25	16.72	0.80	0.37
2	Northridge-M	0.75	5.71	19.14	0.66	0.40
3	Northridge-H	1.20	12.0	24.48	0.63	0.27
4	Izmit	0.30	2.17	38.46	0.56	0.35
5	Sine 0.33 Hz	0.3	---	15	---	0.33
6	Sine 1 Hz	0.35	---	15	---	1
7	Sine 2 Hz	0.43	---	15	---	2
8	Sine 3 Hz	0.41	---	15	---	3
9	Sine 4 Hz	0.27	---	15	---	4
10	Sine 5 Hz	0.47	---	15	---	5
11	Sine 6 Hz	0.32	---	15	---	6
12	Sine 6.67 Hz	0.43	---	15	---	6.67
13	Loma	1.0	13.38	13.10	0.50	0.45

Table 3-16 Achieved base motion parameters in sequence from accelerometer A1 (units in prototype scale) in Test 4A-R.

Sequence Number	Ground Motion Name	PGA (g)	Arias Intensity I_a (m/s)	Significant[4] Duration $D_{5\text{-}95}$ (s) / Number of Cycles	Mean Period T_m (s)	Predominant[5] Period T_p (s) / Frequency (Hz)
1	Northridge-L	0.37	1.78	18.34	0.73	0.37
2	Northridge-M	0.82	5.88	23.58	0.67	0.34
3	Northridge-H	1.32	11.81	27.01	0.64	0.28
4	Izmit	0.35	2.56	39.62	0.58	0.22
5	Izmit_2*	0.36	2.53	39.30	0.57	0.22
6	Sine 0.33 Hz	0.31	---	15	---	0.33
7	Sine 1 Hz	0.30	---	15	---	1
8	Sine 1 Hz_2**	0.36	---	15	---	1
9	Sine 2 Hz	0.44	---	15	---	2
10	Sine 3 Hz	0.41	---	15	---	3
11	Sine 3 Hz_2**	0.36	---	15	---	3
12	Sine 2 Hz_2**	0.39	---	15	---	2
13	Sine 4 Hz	0.26	---	15	---	4
14	Sine 4 Hz_2**	0.29	---	15	---	4
15	Sine 5 Hz	0.26	---	15	---	5
16	Sine 6 Hz	0.39	---	15	---	6
17	Sine 6.67 Hz	0.49	---	15	---	6.67
18	Loma	1.11	14.80	12.73	0.47	0.19

*Izmit motion was repeated because the Tekscan software malfunctioned.

**Sine 1 Hz, Sine 2 Hz, Sine 3 Hz, and Sine 4 Hz were repeated because the base motion amplitude was not satisfactory.

Table 3-17 Achieved base motion parameters in sequence from accelerometer A1 (units in prototype scale) in Test 4A-R2.

Sequence Number	Ground Motion Name	PGA (g)	Arias Intensity I_a (m/s)	Significant[4] Duration $D_{5\text{-}95}$ (s) / Number of Cycles	Mean Period T_m (s)	Predominant[5] Period T_p (s) / Frequency (Hz)
1	Northridge-L	0.32	1.44	21.62	0.82	0.33
2	Northridge-M	0.74	6.16	23.86	0.66	0.32
3	Northridge-H	1.15	12.95	26.65	0.61	0.28
4	Izmit-1	0.28	2.58	38.0	0.59	0.22
5	Sine 0.33 Hz	0.29	---	15	---	0.33
6	Sine 1 Hz	0.32	---	15	---	1
7	Sine 2 Hz	0.42		15		2
8	Sine 3 Hz	0.43	---	15	---	3
9	Sine 4 Hz	0.33	---	15	---	4
10	Sine 5 Hz	0.48	---	15	---	5
11	Sine 6 Hz	0.55	---	15	---	6
12	Northridge-L-2	0.32	1.73	17.8	0.77	1.1
13	Izmit-2	0.29	2.6	37.78	0.57	0.22
14	Loma	0.96	15.83	12.39	0.44	0.19
15	Sine 6.67 Hz	0.37	---	15	---	6.67

Table 3-18 Achieved base motion parameters in sequence from accelerometer A16 (units in prototype scale) in Test 4B.

Sequence Number	Ground Motion Name	PGA (g)	Arias Intensity I_a (m/s)	Significant[4] Duration $D_{5\text{-}95}$ (s) / Number of Cycles	Mean Period T_m (s)	Predominant[5] Period T_p (s) / Frequency (Hz)
1	Northridge-L	0.28	1.53	16.24	0.76	0.37
2	Northridge-M	0.71	5.15	21.5	0.69	0.39
3	Northridge-H	1.1	10.8	25.95	0.65	0.27
4	Izmit	0.3	2.49	40.2	0.54	0.35
5	Sine 0.33 Hz	0.33	---	15	---	0.33
6	Sine 1 Hz	0.33	---	15	---	1
7	Sine 2 Hz	0.43		15		2
8	Sine 3 Hz	0.47	---	15	---	3
9	Sine 4 Hz	0.25	---	15	---	4
10	Sine 5 Hz	0.42	---	15	---	5
11	Sine 6 Hz	0.33	---	15	---	6
12	Sine 6.67 Hz	0.42	---	15	---	6.67
15	Loma	0.89	12.2	13.27	0.52	0.44

Table 3-19 Achieved base motion parameters in sequence from accelerometer A16 (units in prototype scale) in Test 5.

Sequence Number	Ground Motion Name	PGA (g)	Arias Intensity I_a (m/s)	Significant[4] Duration $D_{5\text{-}95}$ (s) / Number of Cycles	Mean Period T_m (s)	Predominant[5] Period T_p (s) / Frequency (Hz)
1	Northridge-L	0.31	1.60	15.72	0.77	0.34
2	Northridge-M	0.62	4.27	24.16	0.73	0.37
3	Northridge-H	1.06	8.17	27.81	0.70	0.28
4	Izmit	0.28	2.10	37.72	0.59	0.35
5	Sine 0.33 Hz	0.33	---	15	---	0.33
6	Sine 1 Hz	0.31	---	15	---	1
7	Sine 2 Hz	0.33		15		2
8	Sine 3 Hz	0.56	---	15	---	3
9	Sine 4 Hz	0.24	---	15	---	4
10	Sine 5 Hz	0.41	---	15	---	5
11	Sine 6 Hz	0.25	---	15	---	6
12	Sine 6.67 Hz	0.43	---	15	---	6.67
15	Loma	0.94	10.24	13.11	0.51	0.45

Table 3-20 Achieved base motion parameters in sequence from accelerometer A1 (units in prototype scale) in Test 6.

Sequence Number	Ground Motion Name	PGA (g)	Arias Intensity I_a (m/s)	Significant[4] Duration $D_{5\text{-}95}$ (s) / Number of Cycles	Mean Period T_m (s)	Predominant[5] Period T_p (s) / Frequency (Hz)
1	Loma	1.35	14.79	11.11	0.43	0.19
2	Izmit	0.32	2.44	37.84	0.62	0.24
3	Sine 0.33 Hz	0.33	---	15	---	0.33
4	Sine 1 Hz	0.33	---	15	---	1
5	Sine 2 Hz	0.34	---	15	---	2
6	Sine 3 Hz	0.53	---	15	---	3
7	Sine 4 Hz	0.37	---	15	---	4
8	Sine 5 Hz	0.69	---	15	---	5
9	Sine 6 Hz	0.52	---	15	---	6
10	Sine 6.67 Hz	0.52	---	15	---	6.67
11	Northridge-L	0.30	1.57	17.78	0.77	0.30
12	Northridge-M	0.74	4.94	22.06	0.67	0.34
15	Northridge-H	1.26	10.59	25.67	0.59	0.28

Table 3-21 Achieved base motion parameters in sequence from accelerometer A16 (units in prototype scale) in Test 7.

Sequence Number	Ground Motion Name	PGA (g)	Arias Intensity I_a (m/s)	Significant[4] Duration $D_{5\text{-}95}$ (s) / Number of Cycles	Mean Period T_m (s)	Predominant[5] Period T_p (s) / Frequency (Hz)
1	Northridge-L	0.27	1.53	19.0	0.90	1.1
2	Northridge-M1	0.43	3.84	27.09	0.89	0.92
3	Northridge-M2	0.41	3.83	27.07	0.89	0.92
4	Northridge-H	0.59	6.13	30.0	0.91	0.92
5	Izmit	0.22	1.95	38.64	0.72	0.34
6	Sine 0.33 Hz	0.32	---	15	---	0.33
7	Sine 1 Hz	0.34	---	15	---	1
8	Sine 2 Hz	0.22		15		2
9	Sine 3 Hz	0.31	---	15	---	3
10	Sine 4 Hz	0.10	---	15	---	4
11	Sine 5 Hz	0.18	---	15	---	5
12	Sine 6 Hz	0.14	---	15	---	6
13	Sine 6.67 Hz	0.16	---	15	---	6.67
14	Loma	0.42	5.04	17.38	0.70	0.46

Table 3-22 Achieved base motion parameters in sequence from accelerometer A16 (units in prototype scale) in Free Field Test.

Sequence Number	Ground Motion Name	PGA (g)	Arias Intensity I_a (m/s)	Significant[4] Duration $D_{5\text{-}95}$ (s) / Number of Cycles	Mean Period T_m (s)	Predominant[5] Period T_p (s) / Frequency (Hz)
1	Northridge-L	0.30	1.45	15.64	0.79	0.37
2	Northridge-M	0.75	5.26	20.84	0.70	0.39
3	Northridge-H	1.19	10.57	26.11	0.68	0.28
4	Izmit	0.34	1.95	40.60	0.61	0.25
5	Sine 0.33 Hz	0.35	---	15	---	0.33
6	Sine 1 Hz	0.37	---	15	---	1
7	Sine 2 Hz	0.39		15		2
8	Sine 3 Hz	0.35	---	15	---	3
9	Sine 4 Hz	0.33	---	15	---	4
10	Sine 5 Hz	0.55	---	15	---	5
11	Sine 6 Hz	0.35	---	15	---	6
12	Sine 6.67 Hz	0.36	---	15	---	6.67
15	Loma	0.98	11.84	13.21	0.51	0.45

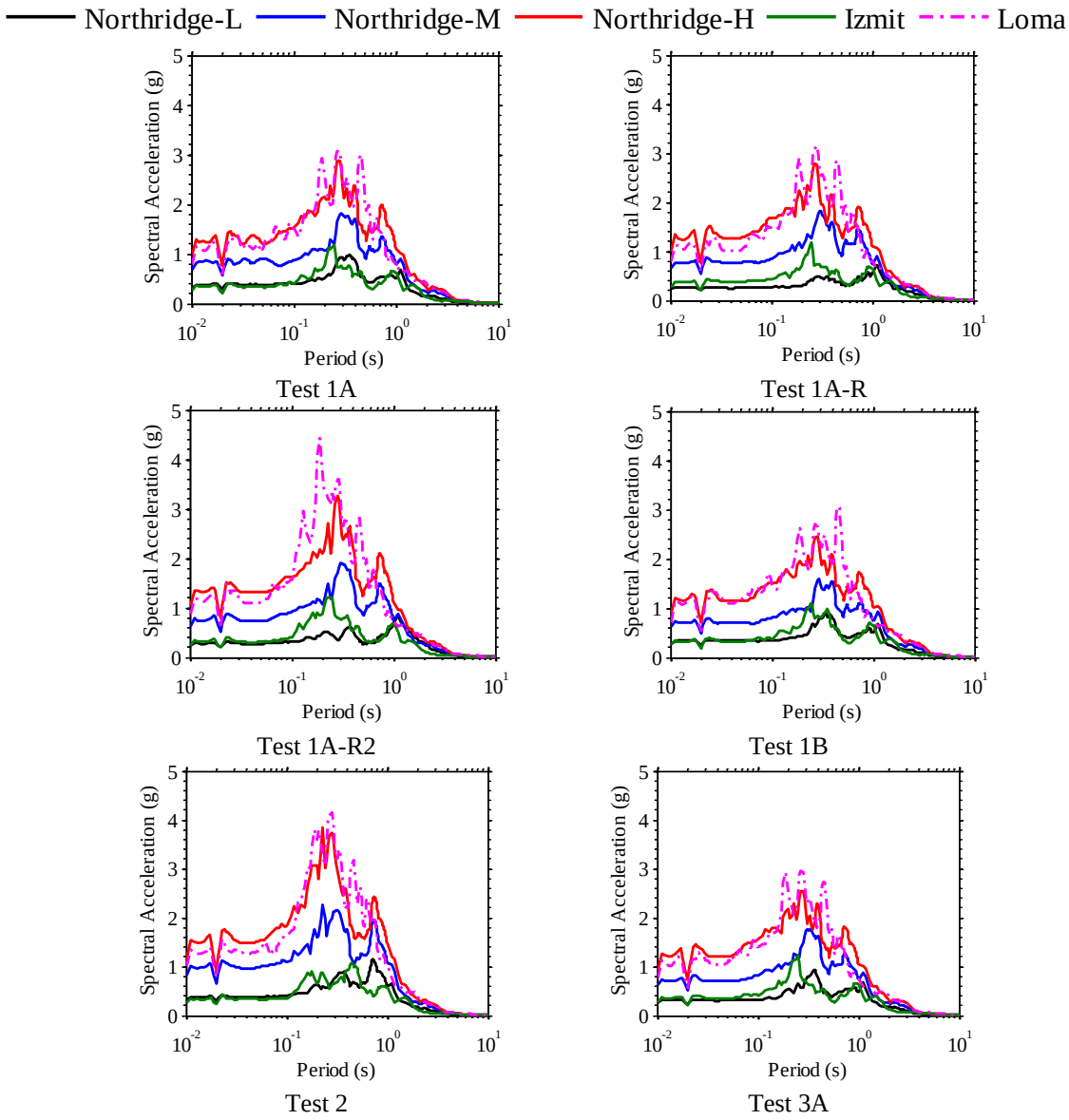

Figure 3-56. Acceleration response spectra (5%-damped) of the recorded base motions in Tests 1A, 1A-R, 1A-R2, 1B, 2, and 3A.

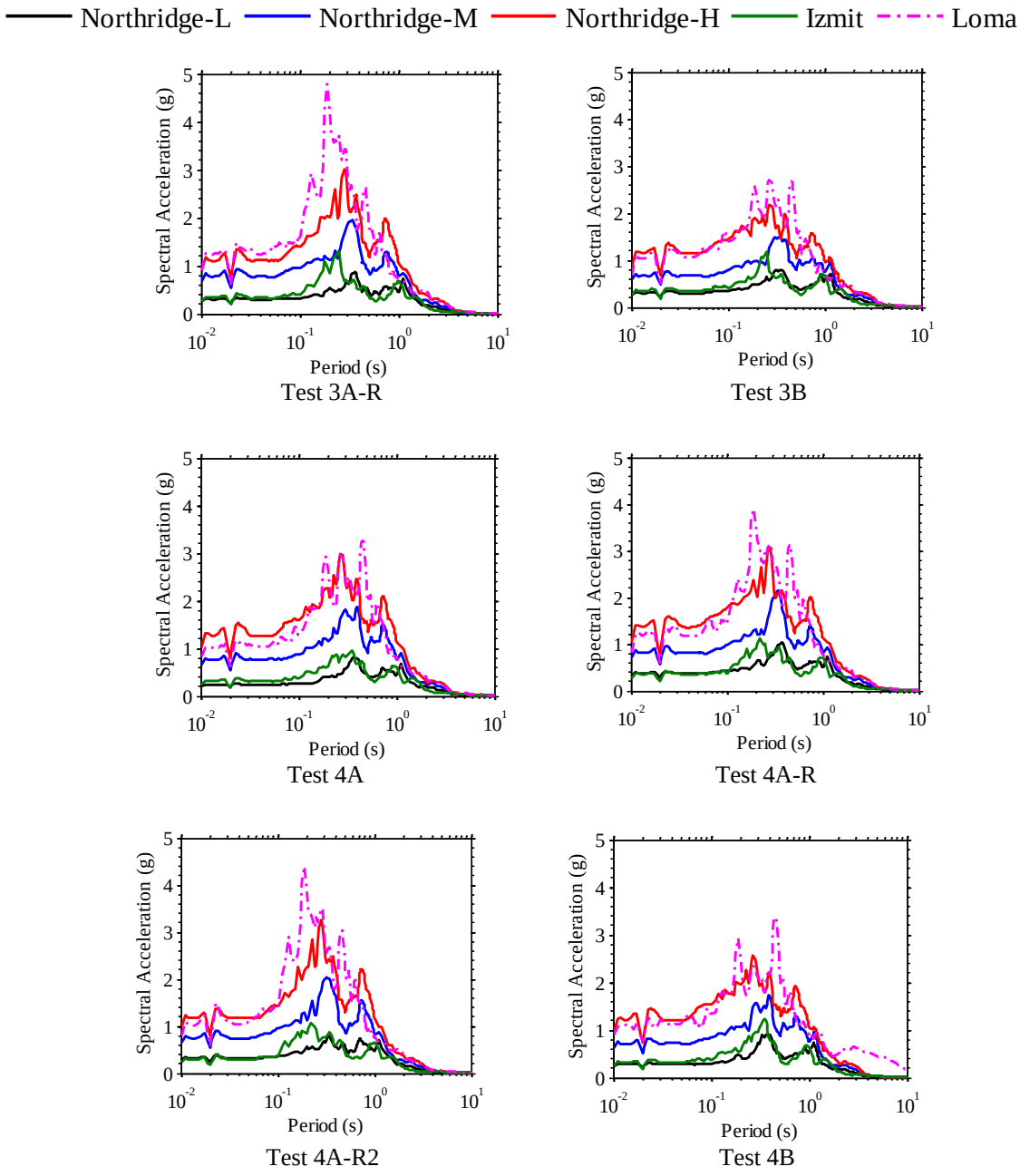

Figure 3-57. Acceleration response spectra (5%-damped) of the recorded base motions in Tests 3A-R, 3B, 4A, 4A-R, 4A-R2, and 4B.

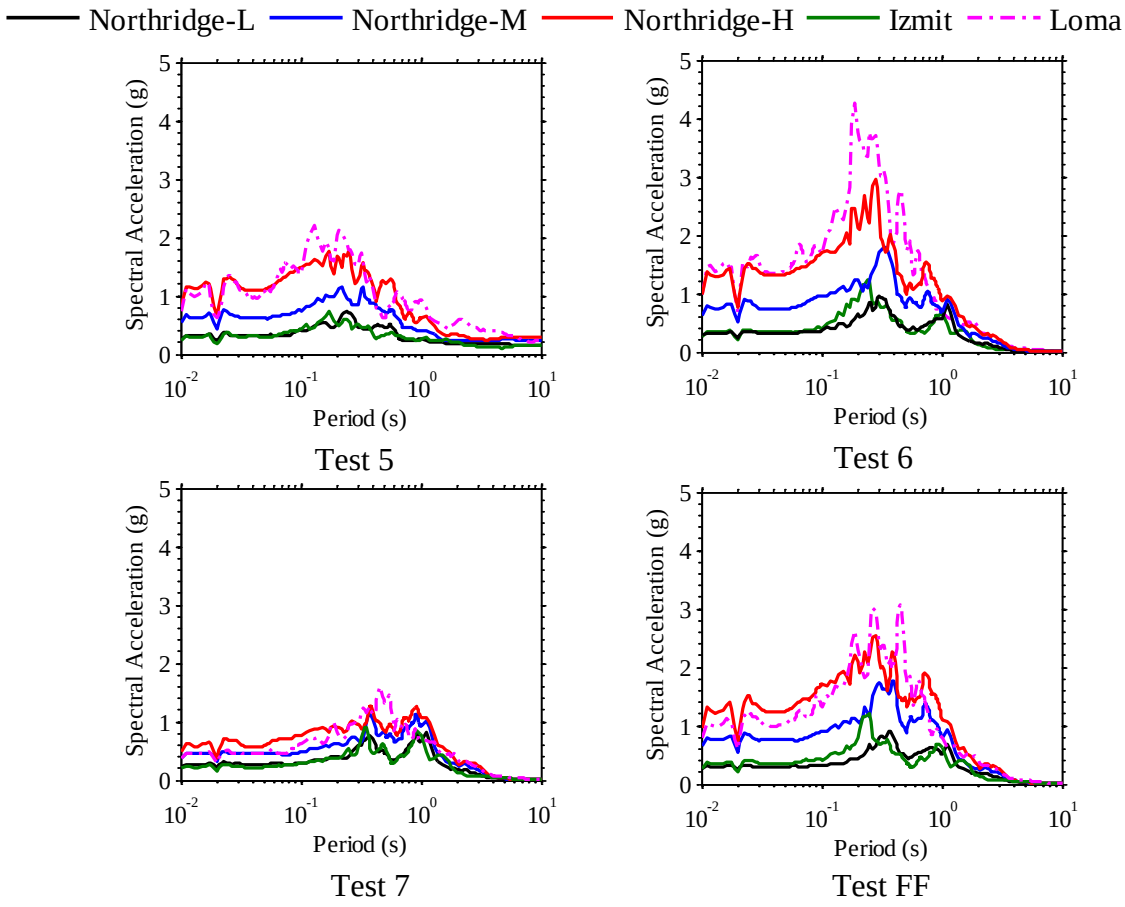

Figure 3-58. Acceleration response spectra (5%-damped) of the recorded base motions in Tests 5, 6, 7, and FF.

3.7 Challenges and Improvements

As expected in dynamic centrifuge model tests with a large number of transducers (up to 71 transducers including four tactile pressure transducers, each with 196 pressure sensels), there were challenges involved with satisfactory performance of transducers and data acquisition system such as damage to transducer wiring, unwanted movement of transducers, electrical noise interference and other electronic related problems. The following difficulties and limitations in performance of the transducers and the centrifuge hydraulic shake table were encountered during the tests:

- The tactile pressure sensors were not synced with the other sensors (strain gages, LVDTS, accelerometers, pressure cells) since they used separate data acquisition system.
- The tactile pressure sensors performed inconsistently because of the presence of air bubbles between the sensels and the protection cover sheet which was in direct contact with the soil. Attempts were made in later tests to minimize the air bubbles by creating vents in the sensors and pushing out the air using a roller.
- There was an unreliable connection from the north wall strain gages to the data acquisition panel. The connection became very unstable during centrifuge spin up causing large drift in the static strain data. This problem occurred during Tests 1A, 1B, 3A, 3B, 4A, 4B, 5, and 7. The problem was mitigated by replacing the RJ45 plugs soldered to the strain gages with military cables and also installing a new data acquisition panel.
- A few of accelerometers and LVDTs did not work properly during some of the tests.
- The hydraulic shake table could not produce the desired shaking intensity on a very cold day for the few initial shakings.

Chapter 4 EXPERIMENTAL RESULTS

4.1 Analysis of Centrifuge Data

After each test a preliminary review of the acceleration, LVDT, strain, and pressure data was performed. The review consisted of plotting and evaluating acceleration time histories, frequency amplitude spectra, response spectra, Arias Intensity, displacements, strain time histories, static strain profiles, dynamic strain profiles, pressure time histories, static pressure profiles, and maximum total pressure profiles. The preliminary study, however, did not include an in-depth analysis and evaluation of the trends in results. But it did help evaluate sensor performance, after which a few of the experiments were repeated with improvements made either to the data acquisition system or the sensor's placement on the structure. Detailed analysis of all the centrifuge tests have been completed. The results obtained from these experiments are summarized in this section, focusing on the following responses:

1. Kinematic soil-structure interaction between the buried structure and far-field soil. This is studied by observing the amplification or de-amplification of accelerations and displacements between the soil and structure during various ground motions.
2. The lateral deformation of the structure is studied by calculating racking versus flexibility ratios, as is often done in practice. The racking ratio quantifies the lateral distortion of the structure compared to the far-field soil. The flexibility ratio measures the relative stiffness between the soil and structure during shaking.

3. Lateral earth pressures:
    a. Measured static earth pressures are compared to common theoretical methods under at-rest and active conditions;
    b. The resultant force (thrust) time histories are calculated by integrating the pressure profile along the wall at each time step of the ground motion;
    c. The total pressure profile is plotted at the time of maximum thrust;
    d. The dynamic increment of pressure is calculated at the time of maximum thrust and compared to the common theoretical methods proposed by Wood (Wood 1973) , Mononobe-Okabe (Okabe 1926; Mononobe and Matsua 1929), and Seed and Whitman (1970);
    e. The equivalent dynamic coefficient of lateral earth pressure (ΔK_E) is calculated at the time of maximum thrust and compared to theoretical methods;
    f. The centroid of the dynamic increment of pressure at the time of maximum thrust.
4. Static and dynamic increment of strain and moment are obtained from strain gages along the two walls, and trends compared with deformations (obtained from accelerometers) and earth pressures.

Three journal papers (the first has been published, the second has been accepted and the last is under review) are presented next, which summarize the insight obtained from a selection of tests. The results from Tests 1A, 3A, and 4A were presented in a journal article titled, “Seismic Performance of Underground Reservoir Structures: Insight from Centrifuge Modeling” (Section 4.2), which has been published in the ASCE Journal of Geotechnical and Geo-Environmental Engineering. The results from Test 1A, 1B, 5, and 6 were presented in a journal article titled, “Seismic Performance of Underground Reservoir Structures: Insight from Centrifuge Modeling

on the Influence of Backfill Soil Type and Geometry" (Section 4.3), which has been accepted by the ASCE Journal of Geotechnical and Geo-Environmental Engineering. The results from Test 1A, 1A-R2, 2, 3A, 3A-R, 4A, and 4A-R2 were presented in a journal article titled, "A Centrifuge Study of the Influence of Site Response, Relative Stiffness, and Kinematic Constraints on the Seismic Performance of Buried Reservoir Structures" (Section 4.4), which is currently under second review by the Journal of Soil Dynamics and Earthquake Engineering. Because of space limitations in journal articles that do not apply to this dissertation, a number of figures and more in-depth discussions were added to the journal articles presented in the following sections.

4.2 Journal Paper 1: ASCE Journal of Geotechnical and Geoenvironmental Engineering (Status: Published)

Seismic Performance of Underground Reservoir Structures: Insight from Centrifuge Modeling on the Influence of Structure Stiffness

A. Hushmand[1], S. Dashti[2], C. Davis[3], B. Hushmand[4], M. Zhang[5], M. Ghayoomi[6], J.S. McCartney[7], Y. Lee[8], J. Hu[9]

ABSTRACT: The available simplified analytical methods for the seismic design of underground structures either assume *yielding* or *rigid-unyielding* conditions. Underground reservoir structures do not fall into either of these categories. In this paper, we present the results of three centrifuge experiments that investigate the seismic response of *stiff-unyielding* buried structures in medium dense, dry sand and the influence of structure stiffness and earthquake motion properties on their performance. The structure to far-field spectral ratios were observed to amplify with increased structural flexibility and decreased soil confining pressure at the predominant frequency of the base motion. Lateral earth pressures and racking displacements for a range of structural stiffnesses were compared with procedures commonly used in design. Pre-earthquake measured lateral earth pressures compared well with expected at-rest pressures. However, none of the commonly used procedures adequately captured the structural loading and deformations across the range of stiffness and ground motions for which these reservoirs must be designed. Further, it is unclear if the current methods of analysis provide conservative or unconservative results for engineering

[1] Graduate Student Researcher, University of Colorado Boulder, Civil, Env. and Arch. Engineering, Boulder, CO.
[2] Assistant Professor, Univ. of Col. Boulder, Civil, Env. and Arch. Eng., Boulder, CO, shideh.dashti@colorado.edu.
[3] Trunk Line Design Manager, Los Angeles Department of Water and Power, Los Angeles, CA.
[4] President and Principal Engineer, Hushmand Associates, Inc., Irvine, CA.
[5] Centrifuge Engineer, Civil Eng., Univ. of Colorado Boulder, Boulder, CO.
[6] Assistant Professor, University of New Hampshire, Durham, NH.
[7] Associate Professor, University of California at San Diego, San Diego, CA.
[8] Civil Engineering Associate, Los Angeles Department of Water and Power, Los Angeles, CA.
[9] Civil Engineering Associate, Los Angeles Department of Water and Power, Los Angeles, CA

design purposes. This identifies a critical need for improved methodologies to analyze and design underground reservoir structures.

INTRODUCTION

The current methods used to analyze the seismic response of underground box structures are based on simplified analytical or numerical tools that have not been adequately validated against full scale field measurements or physical model studies. Furthermore, the kinematic constraints of these structures are not fully captured by simplified seismic design procedures. Soil-structure-interaction (SSI) for these buried structures is complex and depends on foundation fixity, properties of the surrounding soil, flexibility of the structure relative to soil, and the characteristics of the earthquake motion. There is an increasing need in engineering practice to obtain a better understanding of the seismic performance of these underground structures. For example, the Los Angeles Department of Water and Power (LADWP) is replacing some of its open water reservoirs with buried, reinforced-concrete reservoirs to meet water quality regulations. Understanding the seismic performance of these restrained underground structures will improve the structural and geotechnical seismic design of these type of projects.

Traditionally, underground structures are categorized either as *yielding* or *rigid-unyielding*, and are designed differently based on the categorization. A *yielding* wall is one that displaces sufficiently to develop an active earth pressure state. The current state of practice for assessing seismic earth pressures on *yielding* structures relies heavily on the Mononobe-Okabe (Okabe 1926; Mononobe and Matsua 1929) and Seed-Whitman (Seed and Whitman 1970) methods. For *rigid-unyielding* walls that don't undergo any deformation, the method of choice is often the simplified solution proposed by Wood (1973), which assumes a completely rigid wall (with no flexure). Underground reservoir structures fall in between the two extreme cases of *yielding* and *rigid-*

unyielding, because they are not completely rigid, as they exhibit some deformation. But their deformation is less than that of a vertical element in the ground because of the restraint provided by the floor and roof of the structure. Therefore, in this paper, these buried reservoir structures are classified as *stiff-unyielding* structures.

The primary factors in the seismic design of underground box structures include: 1) seismic lateral earth pressures; 2) magnitude and location of lateral thrust; 3) bending strain and moment distribution; and 4) racking deformations. Although recent physical model studies have evaluated the seismic performance of *yielding* retaining walls (e.g., Al Atik 2010 and Mikola 2012), the seismic response of *stiff-unyielding* underground structures has not been sufficiently evaluated experimentally in order to validate the numerical tools used in design.

A series of fourteen centrifuge experiments were conducted at the University of Colorado Boulder to evaluate the seismic performance of relatively stiff underground structures buried in granular soils. The structure stiffness, backfill soil type and slope, embedment, container type (rigid versus flexible boundaries), fixity conditions, and ground motion characteristics were varied to evaluate their influence and relative importance on structural performance. Three different model box structures were designed to represent simplified prototype reinforced concrete buried reservoirs of varying stiffness characterizing those evaluated by the LADWP. The proposed reservoirs have 11 to 12 m high walls that will be buried and restrained against rotational movement at the top and bottom by the roof and floor, restricting deformation. Additionally, the reservoir's foundation can rock or slide laterally as it rests on soil. This paper focuses on a comparison of the behavior of the three structures having different stiffness values in tests with the same backfill soil, container, and base fixity. These experiments enabled a comprehensive and fundamental evaluation of the influence of structure stiffness and ground motion characteristics on

seismic SSI for reservoir structures buried in medium-dense dry sand as well as lateral earth pressures, racking deformations, and bending strains and moments of these structures.

BACKGROUND

Underground box structures have historically performed well during earthquakes. However, a few cases of failure serve as reminders of the need to consider seismic loading in their design. Severe damage was sustained by the Daikai Subway Station during the 1995 Hyogo Ken Nanbu earthquake in Kobe, Japan. Many of the center columns of the box structure failed causing the roof to collapse and walls to crack. The station box structure was not designed for earthquake loading (Lew et al. 2010). Hradilek (1972) evaluated the damage to channel box culverts after the 1971 San Fernando earthquake. Most of the damage to these structures was attributed to permanent ground displacement or fault slippage, which caused large, permanent passive earth pressures. However, the underground structures were not designed for seismic loading at the time, and their damage could be partly caused by excessive seismic earth pressures. As an example, the walls of a reinforced concrete underground reservoir at the Balboa water treatment plant failed during the San Fernando earthquake (Wood 1973). The reservoir walls were 6.1 m high and restrained at the top and bottom, and the structure was buried in a soft fill deposit. With no evidence of soil liquefaction at the site, this failure may have occurred due to a combination of permanent ground movement and excessive seismic lateral earth pressures. The performance of building basements during previous earthquakes has generally been satisfactory, as reported by Lew et al. (2010).

Most analytical methods for evaluating dynamic earth pressures were inspired by the pioneering work of Mononobe-Okabe (Okabe 1926; Mononobe and Matsua 1929). The Mononobe-Okabe (M-O) method is based on Coulomb's limit equilibrium earth pressure theory, with the addition of horizontal and vertical inertial forces due to seismic loading. They assumed

total (static and dynamic) lateral earth pressures increase with depth in a triangular fashion, and the resultant force is applied at H/3 above the base, where H is the total height of the wall. A major assumption in this method is that the wall yields (or displaces) sufficiently to produce the minimum active pressure condition. Seed and Whitman (1970) later simplified the M-O method by separating the total lateral earth pressure coefficient, K_{ae}, into an active static lateral earth pressure coefficient, K_a, and a dynamic earth pressure coefficient increment, ΔK_{ae}. The Seed-Whitman (S-W) method assumes the resultant dynamic increment of thrust acts on the wall at a height of 0.6H above the base. In geotechnical practice, an inverted triangular pressure distribution for the seismic earth pressure is used by many practitioners.

Wood's method (Wood 1973) was developed for infinitely rigid, restrained walls having a fixed base with a linear elastic soil backfill. For walls with very long backfills, the dynamic thrust from Wood's method is applied at 0.63H above the base of the wall (Ebeling and Morrison 1992). Equivalent static solutions were derived for the dynamic problems of interest. Variables not taken into account by the simplified Wood's method are: a soft, deformable foundation soil, an increase in soil modulus with depth, soil nonlinearity, and wave propagation with motion amplification (or de-amplification at large strains).

Veletsos and Younan (1994) numerically investigated rigid, yielding, and unyielding retaining walls with a linear viscoelastic soil backfill. They showed that increasing rotational flexibility at the wall base decreases dynamic earth pressures and the associated shear forces and bending moments acting on the wall. A few shortcomings of this method include: 1) assumption of complete bonding between the soil and a rigid base; 2) assumption of complete bonding between the wall and the soil; 3) no consideration for horizontal translation of the wall; and 4) the complexity of the solution and lack of simple computational steps for design applications. Richards

et al. (1999) proposed a simplified analytical method to determine the distribution of dynamic earth pressures on rigid, yielding, and unyielding retaining walls with a granular soil backfill, while taking into account soil's nonlinear and plastic behavior and wall's horizontal translation, but not wave propagation. Davis (2003) subsequently introduced a simplified analytical method to calculate dynamic earth pressures from propagating waves on the walls of a rigid-unyielding underground structure with a non-rigid base, taking into account the increase in small-strain shear modulus of the soil with depth but not soil nonlinearity.

Psarropoulos et al. (2005) performed finite element analyses on rigid and flexible walls to build upon the work of Veletsos and Younan (1994) by taking into consideration the influence of flexural wall rigidity, inhomogeneous backfill soil, and translational flexibility on the amplitude and distribution of earth pressures acting on the wall. Subsequently, Ostadan (2005) proposed a simplified method to calculate dynamic earth pressures acting on a rigid-unyielding basement wall with a rigid foundation, taking into account wave propagation and soil nonlinearity, but not the increase in shear modulus with depth. The resulting pressure envelopes proposed by Ostadan (2005) were similar to those of Wood (1973). Seismic earth pressures acting on deformable but stiff, unyielding underground box structures with realistic soil properties have not been adequately studied numerically. Further, many of the previous analytical and numerical methods were not sufficiently calibrated and validated against case histories or realistic physical model studies.

The majority of previous physical model studies have focused on the seismic response of *yielding* retaining walls under realistic pressures using the centrifuge (Ortiz 1982; Bolton and Steedman 1982; Steedman and Zeng 1991; Andersen 1991; Stadler 1996; Dewoolkar 1996; Nakamura 2006; Al Atik 2010; and Mikola 2012). Mikola (2012) studied the seismic response of a restrained basement wall in addition to a retaining wall. Both sets of experiments indicated that

dynamic earth pressures increase with depth in a triangular manner and their magnitudes were generally less than those obtained from the M-O and S-W methods. This conclusion contradicted the method proposed by Ostadan (2005) for basement structures that were closer to Wood's method. Recent dynamic centrifuge tests have been performed on rectangular cross section tunnels in cohesionless soils by Cilinger and Madhabhushi (2011) and Tsinidis et al. (2015). However, these tunnels have much thinner linings and are buried much deeper than the structures evaluated in this study and are expected to have different behavior than *stiff-unyielding* structures near the surface. Some of the more complex conditions found in practice are often evaluated using numerical modeling techniques (e.g., Roth et al. 2010; Zhai et al. 2013), which have not been validated to conform to the seismic performance of *stiff-unyielding* structures.

In summary, the state of practice for the seismic design of underground box structures relies heavily on simplified analytical methods that either assume *yielding* or *rigid-unyielding* conditions. Analytical, numerical, and physical model studies have been limited on the class of *stiff-unyielding* underground box structures. Centrifuge modeling can help fundamentally evaluate soil-structure-interaction, deformations, and lateral earth pressures for this class of buried structures and the relative importance of different testing parameters on their seismic performance.

CENTRIFUGRE TESTING PROGRAM

Three centrifuge tests were performed with similar instrumentation and soil conditions but different model underground structures. The lateral stiffness and natural period was varied among the three model structures, which were buried in medium-dense, dry sand. The three experiments are referred to as T-Flexible, T-BL (baseline), and T-Stiff, based on the relative stiffness of the structures. Experiments were performed at 60g of centrifugal acceleration using the 400 g-ton

centrifuge at the University of Colorado Boulder (Ko 1988). Earthquake motions were applied to the model specimen in flight using the servo-controlled electro-hydraulic shake table, which is mounted on the basket of the centrifuge. A series of five earthquake motions were applied to the base of the models in the same sequence in the three experiments.

Model Structure Design and Properties

The actual prototype reservoirs are complex structures with many columns and interior walls that support the weight of the roof slabs, walls resisting lateral shear forces, and other structural details, the 3D response of which is difficult to simulate properly in a scaled centrifuge model. Accordingly, simplified, equivalent prototype 2-D box structures were identified to match the mass, lateral stiffness, and natural frequency of the actual prototype reservoir structures. The dimensions of these equivalent prototype box structures were then converted to model scale dimensions at 60g, to design and fabricate three model structures referred to as Baseline (BL), Flexible, and Stiff (corresponding to experiments T-BL, T-Flexible, and T-Stiff, respectively). These model structures were designed with uniform 1018 Carbon Steel (density = 7870 kg/m^3; Young's Modulus = 200 GPa; Poisson's ratio = 0.29). The structural stiffness was varied by changing the thickness of the models and keeping all other dimensions (outer height, width, length) the same, as summarized in Table 4-1. The model structures were fabricated by welding steel plates to ensure a strong moment connection at the corners. The fundamental frequencies of the structures were estimated by performing 3-D finite element simulations of structures in Abaqus. These values were then confirmed experimentally using vibration tests on a shaking table at 1g, in which the structures were bolted to the shaking table using temporarily-welded steel tabs. The results are summarized in Table 4-1. The numerical and experimental values of fundamental

frequency were consistent for all structures, confirming the validity of the model structures for simulating the prototype structures.

Table 4-1. Dimensions and properties of model structures used in centrifuge (prototype scale).

Structure	Height & Width (m) (Outer Edge to Outer Edge)	Thickness			Lateral Stiffness, K_L (kN/m/m)	Fundamental Frequency (Hz)	
		Base (m)	Roof (m)	Walls (m)		Numerical	Experimental
Baseline (BL)	10.5 & 12.1	0.69	0.37	0.56	31,500	4.0	3.9
Flexible		0.50	0.28	0.28	6,115	2.0	1.9
Stiff		1.46	1.12	1.13	472,518	9.9	9.1

Note: Model structures were 17.46 m long (approximately equal to the inside width of the centrifuge container).

Preparation of Model Specimens

The instrumentation layout and testing configuration shown in Figure 4-1 was the same in all three tests. These tests were conducted using a transparent flexible shear beam (FSB) type container developed by Ghayoomi et al. (2012, 2013). Dry Nevada sand No. 120 (G_s=2.65; e_{min}=0.56; e_{max}=0.84; D_{50}=0.13 mm; C_u=1.67) was pluviated into the FSB container to achieve a uniform soil layer with a relative density of $D_r \approx 60\%$. This corresponds to a dry unit weight of 15.6 kN/m^3. The fundamental frequency of the far-field soil column at small strains ranged from approximately 2.1 to 2.4 Hz, while its effective fundamental frequency during different motions obtained from the transfer function of acceleration recordings at the surface to base ranged from approximately 1.0 to 1.7 Hz.

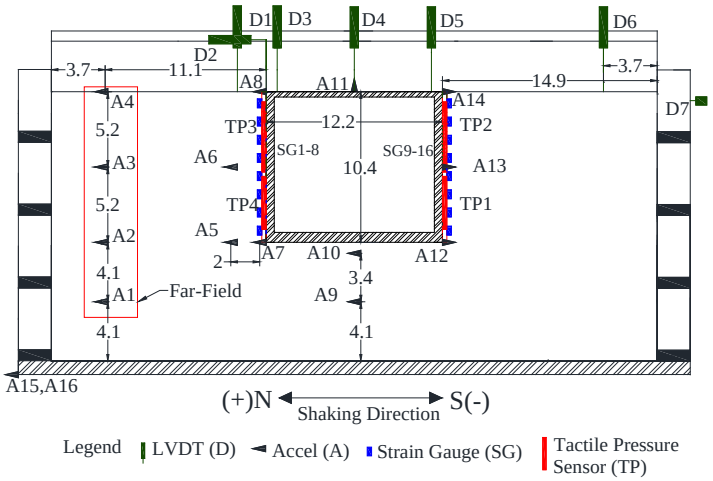

Figure 4-1. Instrumentation layout in experiments T-BL, T-Flexible, and T-Stiff (dimensions in prototype scale meters).

Model preparation began by placing accelerometers at the pre-selected locations during pluviation of the sand layer until the elevation of the structure base was reached (Figure 4-1). Teflon sheets were placed between the sidewalls of the container and on the ends of the structure to allow relative sliding and minimize friction, in order to simulate plane strain conditions. The structure was placed in the middle (along the length) of the FSB container followed by sand pluviation on the two sides of the structure until reaching its top elevation. A photograph taken of the completed model from the side of container is shown in Figure 4-2.

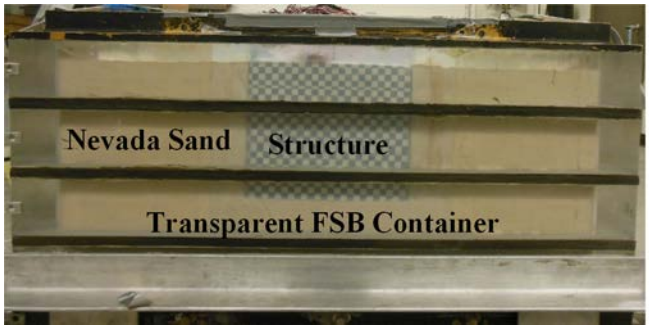

Figure 4-2. Elevation view of model specimen in experiment T-BL.

Instrumentation

As shown in Figure 4-1 data was acquired from accelerometers (A1-A16), LVDTs (D1-D7), tactile pressure sensors (TP1-4), and strain gauges (SG1-16). Accelerometers were placed horizontally at the container base, on the structure, and within the soil at different elevations to monitor movement. The accelerometer array A1-4 representing far-field conditions (approximating free-field) was placed 11.1 m from the structure wall toward the flexible container boundary (3.7 m from container boundary).

LVDTs were used to measure the settlement of soil and structure as well as the lateral displacement of structure and the FSB container top frame. Eight strain gauges were installed on each wall of the structure to measure bending strains and hence, bending moments. Tactile pressure sensors are flexible, thin sheets containing a matrix of sensors, which may be used to measure total earth pressures. Four high speed, tactile pressure sensors (model 9500) manufactured by Tekscan Inc. were used to measure total pressures on both sides of the structure. Each tactile sensor has a total of 196 sensels in 14×14 grid with a spacing of 5.1 mm in model scale. Each of the 196 sensels recorded pressure simultaneously at a rate of 4,000 samples per sec (sps) during dynamic loading. All other instruments on the National Instruments data acquisition system recorded data at 3,000 sps during shaking.

Tactile sensors were known to underestimate the full amplitude content of a dynamic signal in the high frequency environment of the centrifuge (Olson et al. 2011). This is partially caused because older sensor models under-sampled the dynamic signals. It is recommended to sample at least 10 times as fast as the highest frequency in the signal to ensure that it is accurately reconstructed in the time domain (Derrick 2004). Centrifuge shake tables typically cannot produce controlled motions at frequencies greater than approximately 300 Hz (model scale). Hence, a

minimum sampling rate of about 3,000 sps is required in dynamic centrifuge experiments, which was satisfied in these tests.

The inability to measure the full amplitude of the dynamic pressure signal is also partially caused by the tactile sensor's frequency-dependent response, which needs to be characterized and accounted for (Dashti et al. 2012). By characterizing how the sensor records load over a range of frequencies, a transfer function was developed and applied to sensor recordings to compensate for the loss of pressure amplitude. This frequency-dependent, amplitude correction procedure is referred to as the sensor's dynamic calibration (detailed by Gillis et al. 2015).

The tactile sensors were first thoroughly de-aired by creating small holes to allow air to vent followed by sealing, according to the procedure recommended by Tessari et al. (2014). After they were conditioned and equilibrated, these sensors were statically calibrated using a pneumatic loading device and a fine sandpaper, as recommended by Tessari et al. (2014). Then, they were dynamically calibrated using the procedure described by Gillis et al. (2015).

Ground Motions

A suite of base motions were first selected by LADWP for the specific site of interest, here referred to as *desired* motions. These motions included scaled versions of the horizontal acceleration recordings at the Sylmar Converter Station during the 1994 Northridge Earthquake (NSC52), the LGPC Station during the 1989 Loma Prieta Earthquake (LGP000), and the Istanbul Station during the 1999 Izmit Earthquake in Turkey (IST180), all obtained from the PEER database. Of these motions, the Loma Prieta Motion was selected and modified to match the target, site-specific, deterministic acceleration response spectrum at the project site (Harounian et al. 2014). The other motions were selected to evaluate the influence of different ground motion characteristics (i.e., in

terms of intensity, frequency content, and duration) on the performance of the buried structures and their interaction with the surrounding soil.

The *desired* horizontal base motions were converted from prototype to model scale units and filtered to remove unwanted frequencies and to limit displacements to the stroke of the shaking table. These acceleration time histories were then double integrated to obtain displacement command signals. An iterative procedure similar to that described by Ketcham et al. (1991) was then implemented to obtain a command signal that produced a shaking table motion close to that *desired* both in terms of spectral accelerations and Arias Intensity time histories. The accelerations recorded on the shaking table and base of the container are referred to as *achieved* motions. The properties of the *achieved* base motions are summarized in Table 4-2 as recorded sequentially during a representative experiment, T-BL. Figure 4-3 shows the acceleration response spectra (5% damped) and Arias Intensity time histories of the base motions in T-BL. The *achieved* base motions varied slightly during different experiments because the weight and natural frequency of the model specimens were not the same, affecting the shake table performance. Therefore, the base motions are presented during each test when discussing results.

Table 4-2. Base motion properties as recorded in T-BL (all units in prototype scale).

Ground Motion Name	PGA (g)	Arias Intensity I_a (m/s)	Significant Duration $D_{5\text{-}95}$ (s)	Mean Frequency f_m (Hz)	Predominant Frequency f_p (Hz)
Northridge-L	0.36	1.6	15.4	1.41	2.86
Northridge-M	0.81	5.4	19.5	1.52	3.57
Northridge-H	1.20	11.6	25.1	1.59	3.57
Izmit	0.33	2.1	39.5	1.79	4.17
Loma	1.00	12.4	13.3	2.00	3.70

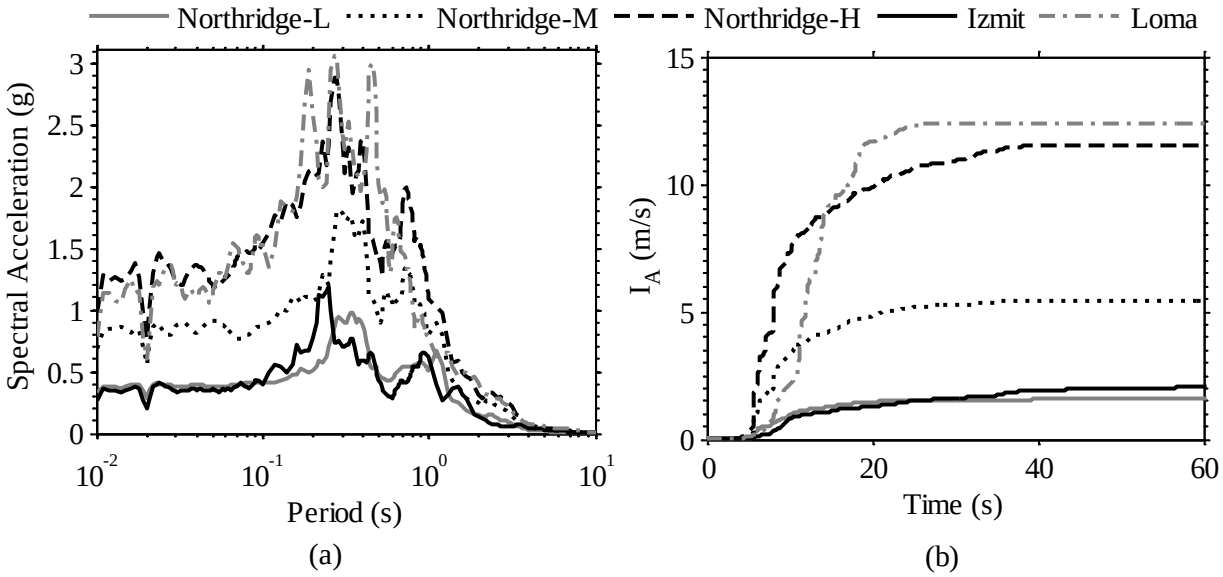

Figure 4-3. (a) Acceleration response spectra (5% damped) and (b) Arias Intensity time histories of the achieved base motions in T-BL.

EXPERIMENTAL RESULTS

Acceleration Response

The presence of the model structure was expected to alter the accelerations at different elevations compared to far-field primarily due to kinematic interaction. The accelerations measured on the structure walls were compared to those measured in the far-field at the corresponding elevation. Figure 4-4 shows the spectral ratios of accelerations at the bottom, middle, and top of each model structure to those in the far-field in each test during three representative ground motions (Northridge L, M, and H). These ratios indicate whether accelerations were amplified or de-amplified due to the presence of the structure. The structure to far-field spectral ratios increased from the bottom of the structure to the top in all cases. The highest amplification of spectral ratios was observed at the top of the structure near the predominant frequency of the base motion (near 3 Hz).

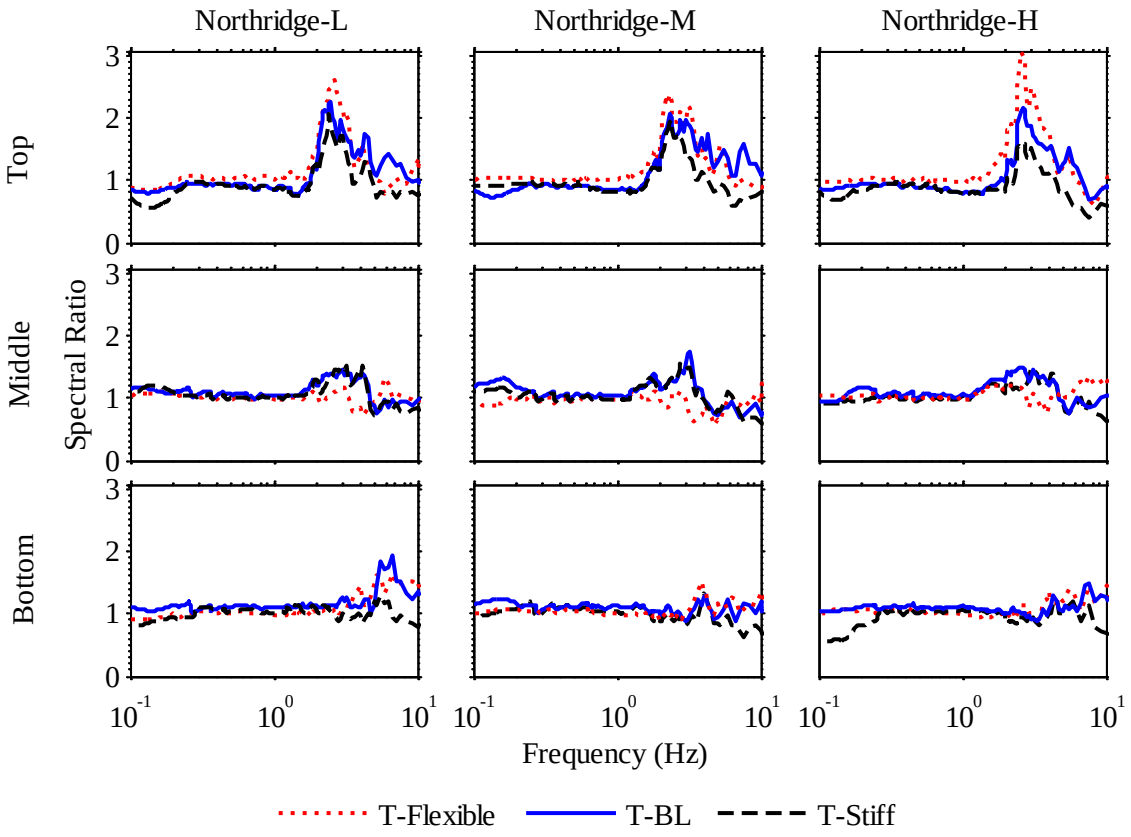

Figure 4-4. Spectral ratio (5% damped) of structure to far-field accelerations in three tests (T-BL, Flexible, Stiff) during the Northridge-L, Northridge-M, and Northridge-H motions.

As confining pressure increased, the movement of the buried structure was more controlled by the surrounding soil in terms of phase and amplitude. As shown in Figure 4-5 for a representative case (Northridge-H), the vibration of the structures were consistently in phase with the soil during all motions. This observation is consistent with the conclusions from numerical simulations presented by Murono and Nishimura (2000) when the structure fundamental frequency was greater than the effective fundamental frequency of the backfill soil, as is the case for all structures evaluated in this study.

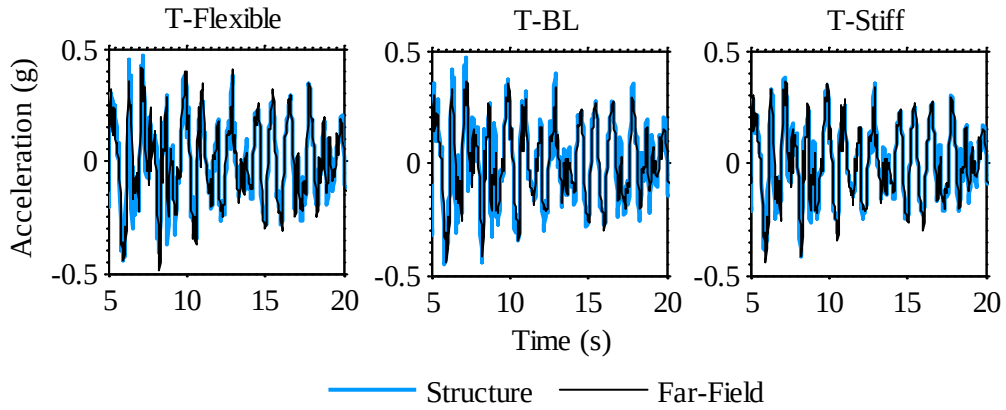

Figure 4-5. Acceleration time histories in the middle of the structure and at the corresponding depth within the far-field soil in T-Flexible, T-BL, and T-Stiff during the Northridge-H motion.

Structure to far-field spectral ratios of near 1.0 were observed at elevations corresponding to the bottom and middle of the structure in all cases, meaning that the structure had a negligible impact on accelerations at these elevations (higher confining pressure) when compared to far-field. However, the top acceleration was amplified compared to the far-field, and its amplification was affected by the stiffness of the model structure. As the flexibility of the structure increased (i.e., going from T-Stiff to T-BL, and to T-Flexible), the degree of amplification increased. This is caused by a greater independent movement of the more flexible structure with respect to the surrounding soil at shallower depths (i.e., lower confinement).

Lateral Displacements

Racking displacement (Δ) is a critical seismic design parameter for buried box structures when shear waves propagate in a direction perpendicular to their longitudinal axis, distorting their cross-sectional shape (Anderson et al. 2008). Racking is described as the lateral displacement of the roof of the structure relative to its base. The peak racking displacement is often used to evaluate peak bending moments in a simple frame analysis of the 2D box structure.

In practice, the transverse racking of a box structure is often estimated using the NCHRP 611 guideline, which is based on the simplified method proposed by Wang (1993). In this simplified

procedure, the structure racking is estimated indirectly from the deformations of the far-field soil and the stiffness of the structure relative to soil. The NCHRP 611 guideline is, however, based on the results of dynamic finite element analyses performed by Wang (1993) on buried box structures. The centrifuge experiments presented in this paper enabled us to experimentally evaluate the applicability of this guideline to the specific class of underground structures of interest.

The racking deformation time histories of the structure and far-field soil are shown in Figure 4-6 for one experiment and ground motion (T-Flexible, Northridge-L). The lateral displacement time histories were obtained by applying a band-pass, 5th order, a-causal, Butterworth filter with corner frequencies of 0.2 and 15 Hz, double integrating, and baseline correcting the accelerometer recordings on the structure (A12 and A14) and in the far-field at the elevations corresponding to the top and bottom of the structure (A2 and A4). Since no permanent deformation was measured on the buried structures with strain gauges, obtaining displacements indirectly from accelerometers was judged appropriate. The peak values of racking displacement on the structure ($\max|\Delta_{structure}|$) and far-field ($\max|\Delta_{FF}|$) were subsequently used to obtain the racking ratio ($R= \max|\Delta_{structure}|/\max|\Delta_{FF}|$) in each test and motion.

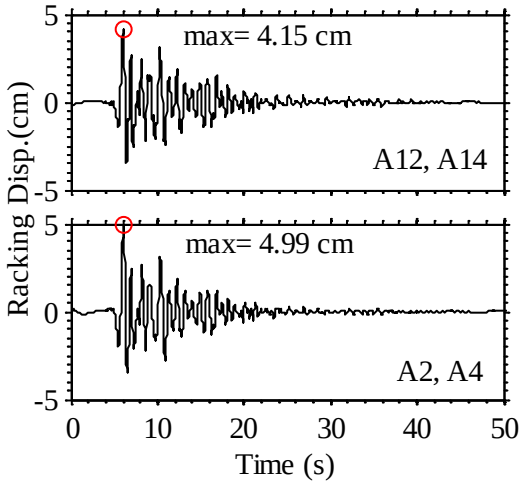

Figure 4-6. Structure and far-field racking displacement time histories in T-Flexible during the Northridge-L motion.

To calculate the flexibility of the structure relative to the far-field soil in accordance with the NCHRP 611 guidelines, the flexibility ratio, $F = (G_m.B)/(K_s.H)$, needed to be calculated, where G_m is the mean strain-compatible shear modulus of soil in the far-field, B is the structure width, K_s is the racking stiffness of the structure, and H is its height (Anderson et al. 2008). The far-field shear strain was calculated by dividing the corresponding racking displacement time history by the height of the structure (H), as shown in Figure 4-7. The normalized shear modulus (G_m/G_{max}) of the far-field soil at mid-depth of the structure (Darendeli 2001) was then evaluated at 65% of maximum far-field shear strain (Schnabel 1972) during each motion, an example of which is demonstrated in Figure 4-8. By using 65% of the peak shear strain, the goal was to roughly estimate the effective shear modulus of the far-field soil as opposed to its modulus at a single time corresponding to peak shear strain. The small-strain shear modulus of soil (G_{max}) was obtained at the mid-depth of the buried structure by using an empirical equation proposed by Bardet (1993) specifically for Nevada sand. Subsequently, the strain-compatible soil shear modulus (G_m) was calculated from G_m/G_{max} at the equivalent shear strain corresponding to each motion. Lastly, the K_s of each box structure was obtained from a standard frame analysis following the NCHRP 611 guideline.

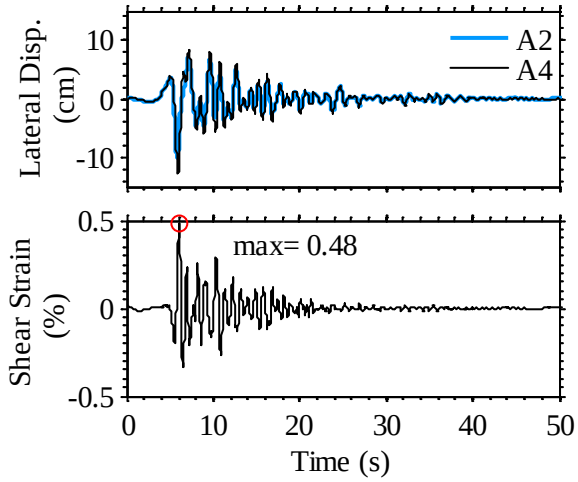

Figure 4-7. Lateral displacement and shear strain time histories in the far-field in T-Flexible during the Northridge-L motion.

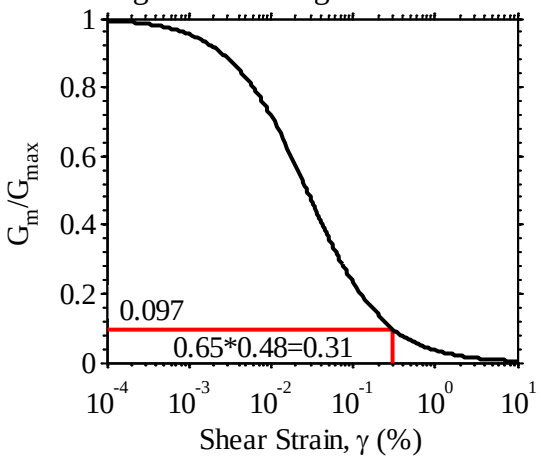

Figure 4-8. The modulus reduction (Darendeli 2001) curve used to calculate G_m of soil in the far-field in T-Flexible during the Northridge-L motion.

The experimentally obtained values of racking versus flexibility ratio (R versus F) in T-Flexible, T-BL, and T-Stiff during all motions are compared with the numerically obtained NCHRP 611 guideline in Figure 4-9. The flexibility ratio (F) was shown to significantly influence the structure's transverse racking deformation both experimentally and numerically. The F values were near zero on the Stiff structure, implying a very stiff structure and negligible expected deformations according to NCHRP 611. The F values were less than 1.0 for the BL structure, implying a stiffer structure compared to the surrounding soil, hence less deformation. The Flexible structure with F values ranging from 0.5 to 2 during different motions implied a structure more

flexible than the far-field soil, with the largest expected racking deformations. In general, the trends observed on the Flexible structure were consistent with the NCHRP 611 guideline, but NCHRP 611 overestimated the racking deformations slightly. Importantly, however, the NCHRP 611 procedure appeared to underestimate racking deformations on the stiffer structures (particularly the Stiff structure).

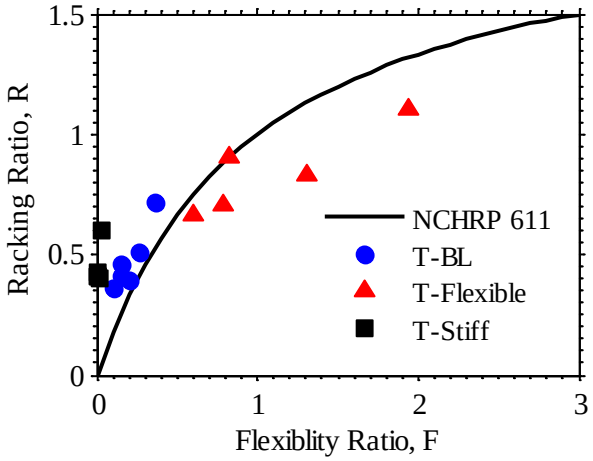

Figure 4-9. Experimental racking vs. flexibility ratios of three structures during different ground motions as compared to the NCHRP 611 guideline.

Lateral Earth Pressures

Tactile pressure sensors mounted on the south wall malfunctioned in T-BL and T-Stiff during some motions. Therefore, for consistency, only the pressure recordings obtained from tactile sensors mounted on the north wall of the three model structures are presented in this section. The sensors were conditioned and equilibrated prior to each test and they were calibrated both statically and dynamically, as discussed previously. To reduce scatter, the data obtained from nine sensels were averaged to represent a larger pressure area, as shown in Figure 4-10, after removing the nonworking sensels. After averaging the nine cells, the matrix of pressure time histories recorded was reduced from 28 rows × 14 columns (for two sensors) to 24 rows × 12 columns. Afterwards, the pressure time histories were averaged over the corresponding row to obtain one time history at a given depth (i.e., pressure matrix reducing to 24 rows × 1 column). This method was successful

in reducing the scatter in pressure recordings, particularly when in contact with granular materials with local inhomogeneities (Gillis et al. 2015).

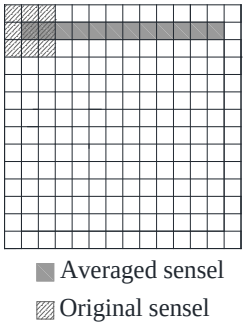

Figure 4-10. Schematic of tactile pressure sensor cell averaging.

The dynamic increment of thrust was estimated by numerically integrating the dynamic pressure profile on the wall at each instance of time. The resulting dynamic thrust time histories estimated on three structures (BL, Flexible, and Stiff) during the Northridge-L motion are presented in Figure 4-11. The presented thrust time histories were subject to a band-pass, 5^{th} order, a-causal, Butterworth filter with corner frequencies of 0.1 and 15 Hz, to remove low and high frequency noise that was sometimes present in the record and could affect the estimated peak dynamic thrust. As a result, the permanent change in thrust cannot be shown in this figure. From these time histories, however, the time corresponding to maximum dynamic thrust could be determined on each structure during each ground motion. Figure 4-12 shows the Fourier amplitude spectra of dynamic thrust on the three structures during the Northridge-L motion compared with that of acceleration at the mid-depth of structure walls (A13). This figure shows that the frequency content of dynamic thrust is similar to that of the acceleration recorded on the buried structure.

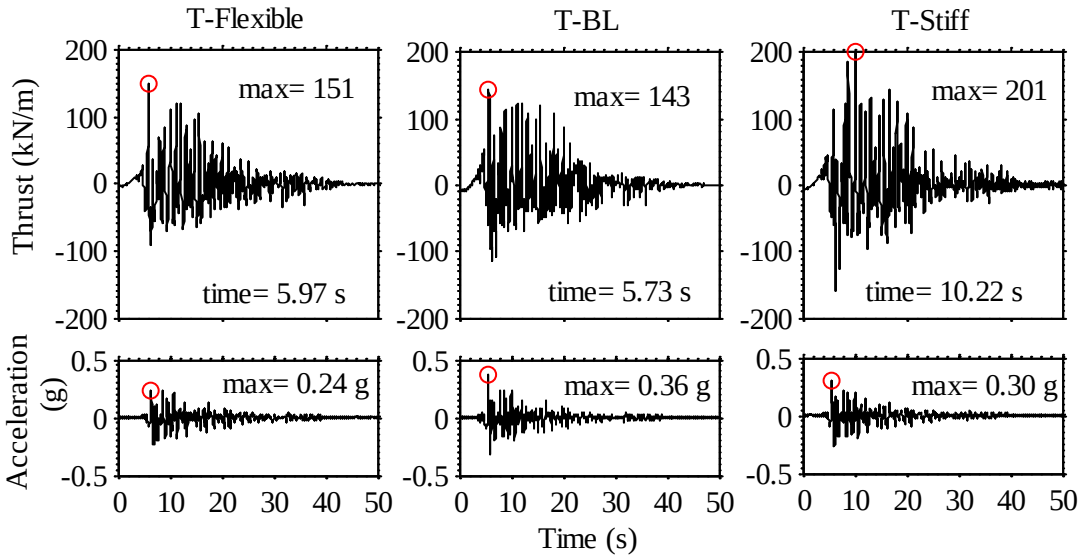

Figure 4-11. Dynamic thrust time histories on the structures in T-Flexible, T-BL, and T-Stiff compared to the container base motion during the Northridge-L motion.

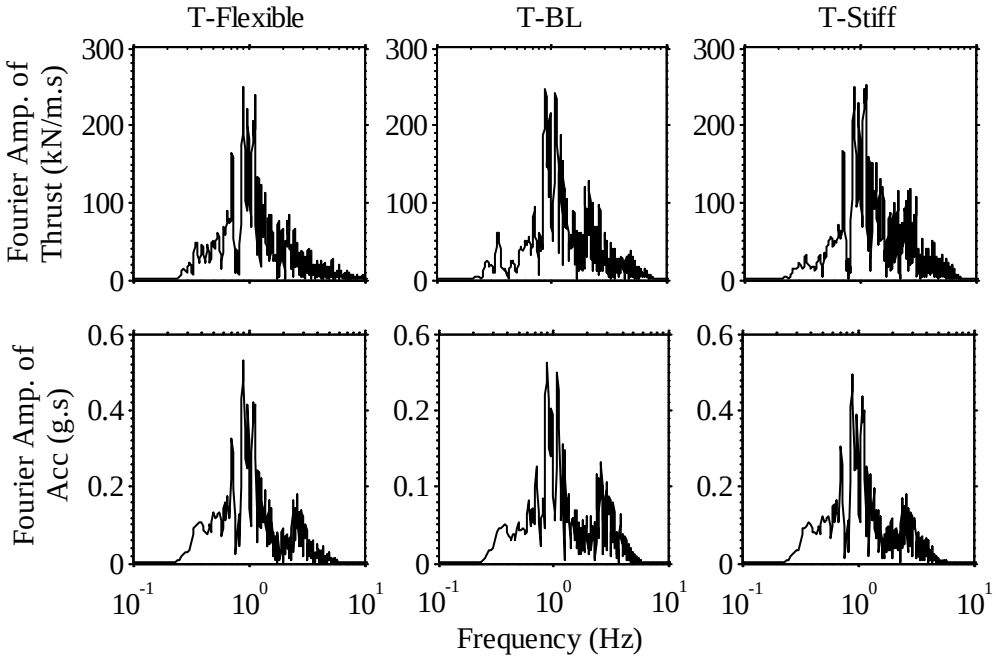

Figure 4-12. Fourier amplitude spectra of dynamic thrust and mid-depth acceleration (A13) recorded on the structure in T-Flexible, T-BL, and T-Stiff during the Northridge-L motion.

The static, pre-shake and post-shake lateral earth pressure and total (static and dynamic) pressure profiles at the time corresponding to maximum dynamic thrust on each structure are shown in Figure 4-13 during the Northridge-L event. These plots also include the theoretically

expected range of static, at-rest (K_o conditions) and active (K_a) lateral earth pressures for comparison. A friction angle of 35° was assumed for Nevada sand at a relative density of 60% in these experiments (Popescu 1993). All three structures showed a reasonable trend in static earth pressure recordings. In most cases, static lateral earth pressures acting on the structure slightly increased after each shake, due to soil densification. The dynamic earth pressures at the time of maximum thrust were not negligible on any of the structures, even during the Northridge-L event with a base PGA of about 0.35g.

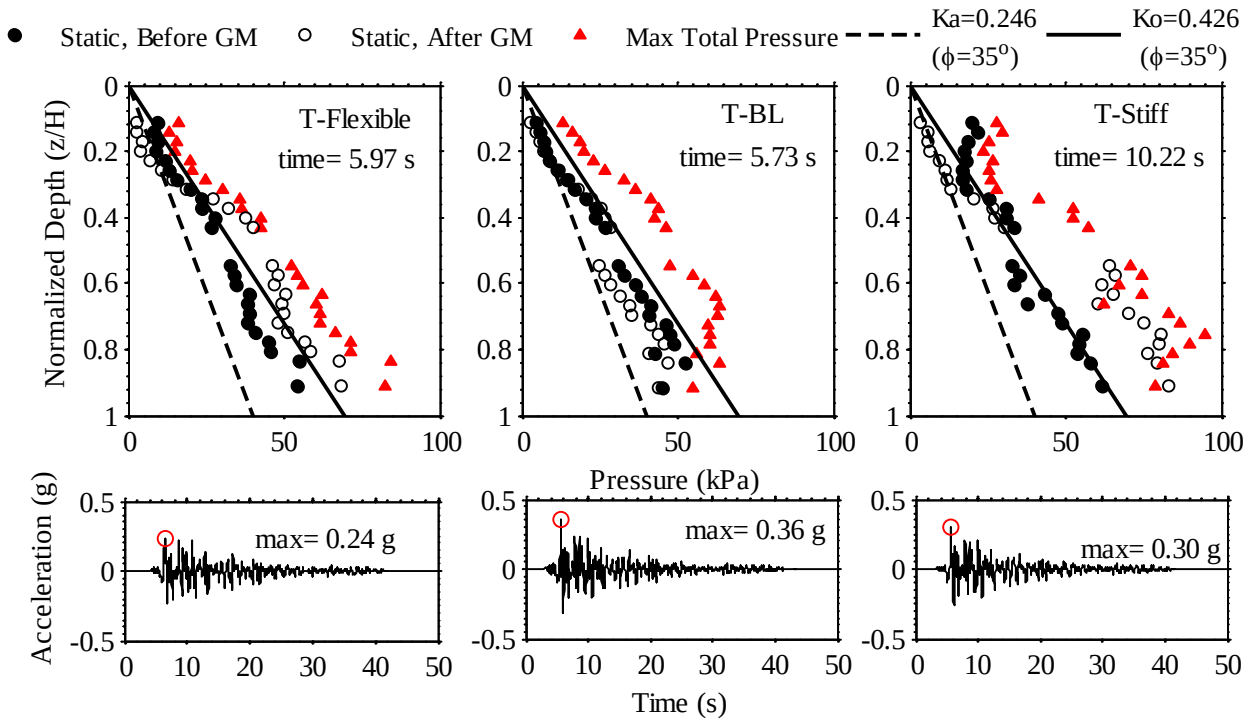

Figure 4-13. Static and total (static and dynamic) pressure profiles measured by tactile pressure sensors at the time of maximum thrust in T-Flexible, T-BL, and T-Stiff during the Northridge-L motion.

The dynamic increment of lateral earth pressures ($\Delta\sigma_E$) at the time of maximum thrust is shown in Figure 4-14 along with the predictions from the Mononobe-Okabe (M-O), Seed and Whitman (S-W), and Wood methods during three representative motions: Northridge-L, Northridge-M, and Northridge-H. The $\Delta\sigma_E$ values were estimated as the difference between total and pre-shake, static earth pressure recordings. The analytical methods were employed using 100% of the PGA

recorded at the far-field soil surface (A4), for the purpose of this comparison. The M-O method provides indeterminate values of pressure at PGA values greater than 0.7g for a soil friction angle of 35°. Therefore, the M-O solution is not presented in Figure 4-14 during the Northridge-H motion. Wood's simplified procedure was once computed based on an L/H ratio of 1.5 corresponding to the centrifuge tests and once based on a larger L/H of 10 as an upper bound for comparison, where L is the lateral extent of the backfill soil and H the wall height. Wood's procedure does not take into account the increase of soil shear modulus with depth and therefore predicted large $\Delta\sigma_E$ values near the top of the wall.

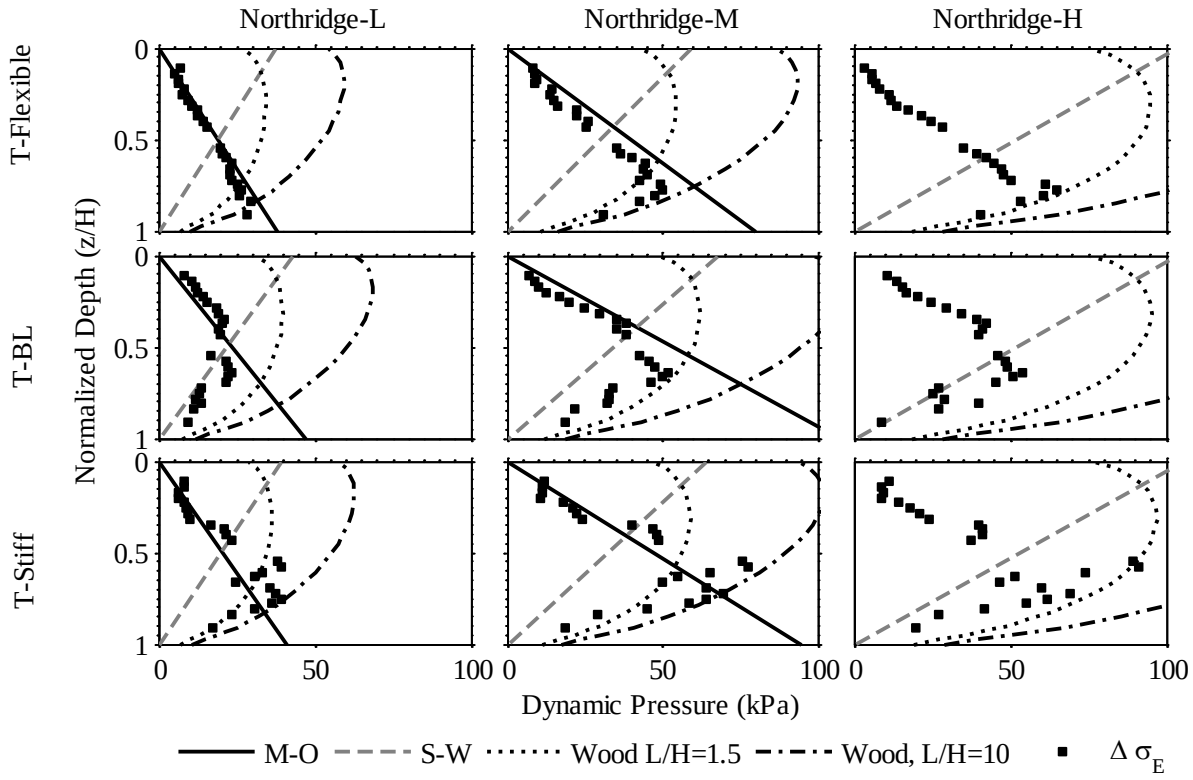

Figure 4-14. Dynamic pressure ($\Delta\sigma_E$) profiles at the time of maximum thrust measured by tactile pressure sensors on three structures (BL, Flexible, Stiff) compared to the M-O, S-W, and Wood methods.

The flexural rigidity of the buried structure significantly influenced the distribution or shape of the dynamic increment of pressure in a consistent manner. The $\Delta\sigma_E$ profile increased linearly with depth on the Flexible structure during all motions, while it followed a more rounded shape on the more rigid structures with its peak occurring closer to the center of the wall. Similar trends in the dynamic increment of earth pressure were observed in finite element analyses performed by Psarropoulos et al. (2005): as the flexural rigidity of the wall was increased from flexible to completely rigid, the shape of $\Delta\sigma_E$ profiles changed from triangular to a higher order polynomial. As shown in Figure 4-14, the $\Delta\sigma_E$ values measured on the Flexible structure roughly followed the M-O solution both in terms of shape and amplitude. This may have been due to the more flexible nature of this structure and its larger deformations (as confirmed by accelerometers and strain gauges). The more stiff structures (i.e., BL and Stiff) experienced $\Delta\sigma_E$ increments that fell between those predicted by M-O, S-W, and Wood's procedures. At shallower depths and lower confining pressures, the $\Delta\sigma_E$ increments were closer to M-O, while they fell between S-W and Wood's procedures near the bottom of the BL and Stiff structures.

The dynamic coefficient of lateral earth pressure (ΔK_E) was calculated for an equivalent triangular dynamic earth pressure profile by dividing the actual dynamic thrust by $\gamma H^2/2$, where γ is the unit weight of backfill soil and H the wall height. The equivalent ΔK_E values obtained experimentally at the time of maximum thrust on all three structures as a function of the PGA of far-field surface motion (A4) are shown in Figure 4-15. This figure also includes the results obtained from previous centrifuge experiments performed by Mikola (2012) on a model basement structure (more flexible than those considered in this study) as well as the predictions from the M-O, S-W, and Wood methods for comparison. The ΔK_E values obtained in all experiments generally increased with increasing PGA. The experiments performed by Mikola (2012) indicated that the

S-W method could serve as an upper-bound method for dynamic lateral earth pressures. This conclusion was not valid in all cases for the specific class of underground structures of interest in this study (*stiff-unyielding*): the dynamic earth pressures acting on the BL and Flexible structures were in line with those of Mikola (2012), being either close to or smaller than the S-W method; but dynamic earth pressures acting on the Stiff structure often exceeded the S-W method and approached Wood's procedure. It must be noted, however, that the reliability of pressure sensors is a topic of ongoing research, and therefore it is important to evaluate bending strains in parallel with numerical simulations before drawing definite conclusions on pressure trends.

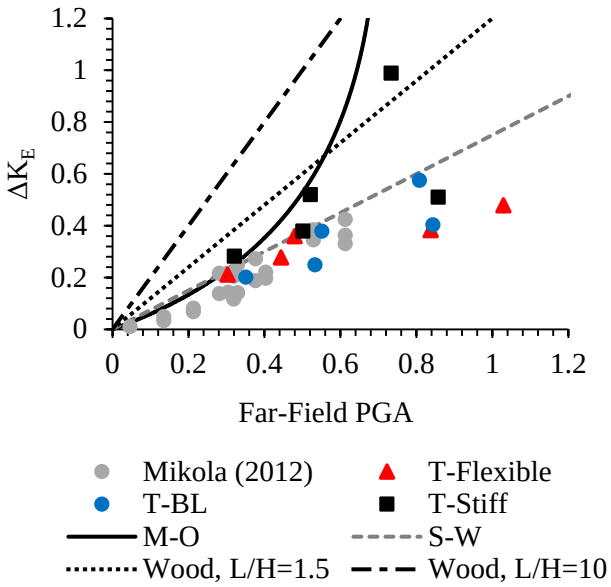

Figure 4-15. Dynamic coefficient of lateral earth pressure (ΔK_E) at the time of maximum thrust as a function of far-field surface PGA in T-BL, T-Flexible, and T-Stiff compared with analytical procedures and previous centrifuge experiments performed by Mikola (2012) on a basement.

Figure 4-16 shows the centroid of the dynamic increment of pressure ($\Delta\sigma_E$) measured at the time of maximum thrust on all three structures against the PGA of the far-field surface motion (A4). The centroid was calculated by fitting the dynamic increment of pressure at the time of maximum thrust with a polynomial that was extrapolated to the entire height of the wall. The plot

also includes the centroids derived from the M-O, S-W, and Wood methods for comparison. The depth of dynamic pressure centroid did not appear to be significantly affected by shaking intensity (e.g., PGA), but was influenced by the structure's stiffness. The depth of dynamic pressure centroids on the Flexible structure followed closely the M-O method (as expected based on the trends in Figure 4-14). The dynamic pressure centroid depths on the BL and Stiff structures generally fell between those predicted by the M-O, S-W, and Wood methods.

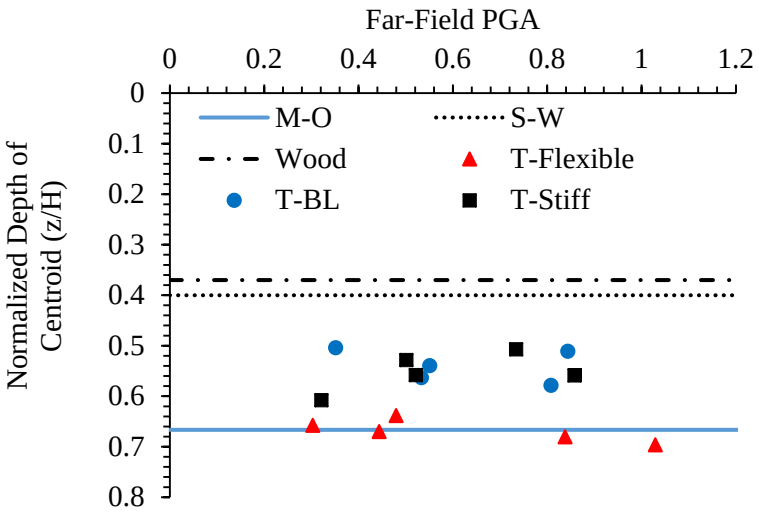

Figure 4-16. Centroid of dynamic increment of pressure at the time of maximum thrust as a function of far-field surface PGA in T-BL, T-Flexible, and T-Stiff compared with analytical procedures.

Bending Strains and Moments

Bending strains were measured on both walls before, during, and after each ground motion. Only strains from the south wall are presented because some of the sensors on the north wall malfunctioned. The deformation patterns, however, were expected and confirmed to be symmetric. Dynamic bending strain ($\Delta\varepsilon_E$) profiles are presented at the time of maximum strain or moment during each motion in Figure 4-17. Because the tactile sensors had a different data acquisition system, to avoid uncertainties associated with time synchronization of different sensors, the

dynamic strain profiles are shown at the time one of the strain gauges recorded maximum strain on that wall, as opposed to the time of maximum thrust used in the previous section.

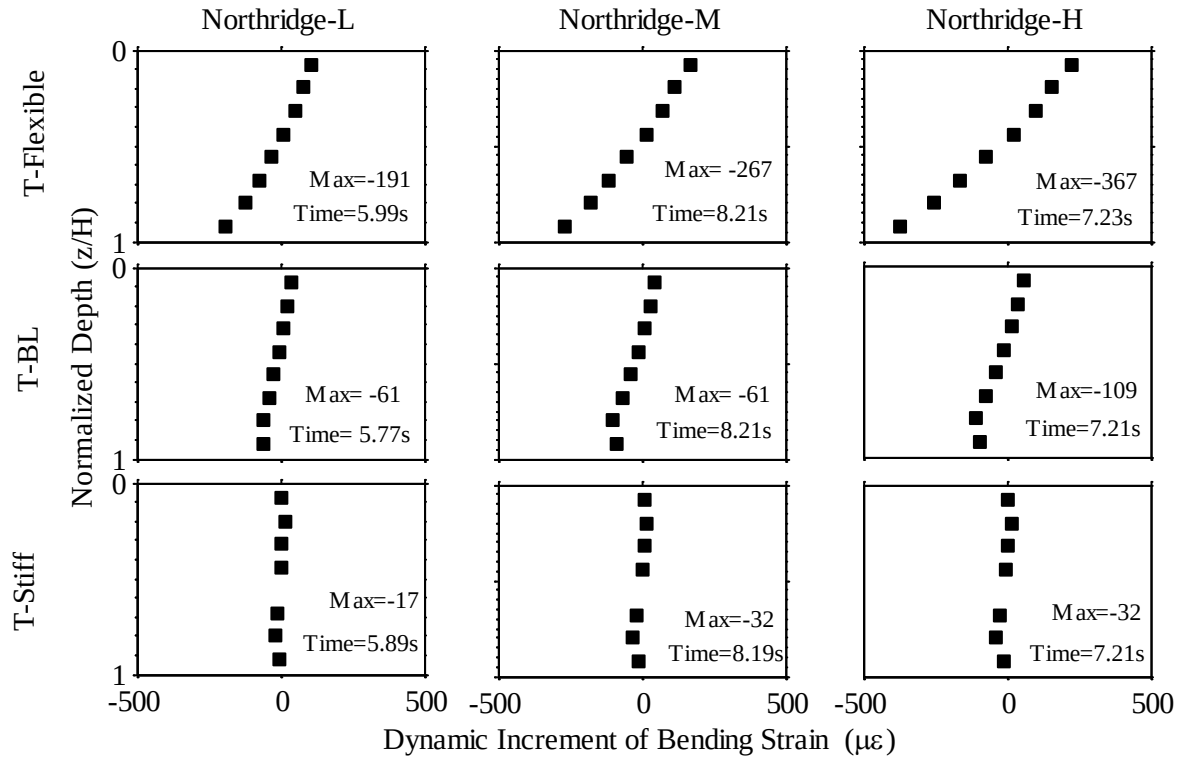

Figure 4-17. The dynamic increment of bending strains ($\Delta\varepsilon_E$) on the walls of three structures (BL, Flexible, Stiff) at the time of maximum moment during the Northridge-L, Northridge-M, and Northridge-H motions.

The measured $\Delta\varepsilon_E$ values generally increased as shaking intensity increased. The distribution and amplitude of $\Delta\varepsilon_E$ profiles varied greatly among the three structures. The amplitude of $\Delta\varepsilon_E$ was proportional to the structure's flexibility, as expected. The distribution of $\Delta\varepsilon_E$ was approximately linear on the Flexible structure, and transitioned to a higher order polynomial on stiffer structures (BL and Stiff structures). The dynamic increment of bending moments (ΔM_E) at the same time were subsequently calculated from the corresponding strain values, as shown in Figure 4-18. Eventhough the $\Delta\varepsilon_E$ profiles were significantly smaller on stiffer structures, in most cases ΔM_E slightly increased as the structure's flexural stiffness increased, because bending moments take into account the wall's moment of inertia. The distribution of ΔM_E changed from approximately

linear to a higher order polynomial as the structure stiffness increased, a trend consistent with the $\Delta\sigma_E$ distributions.

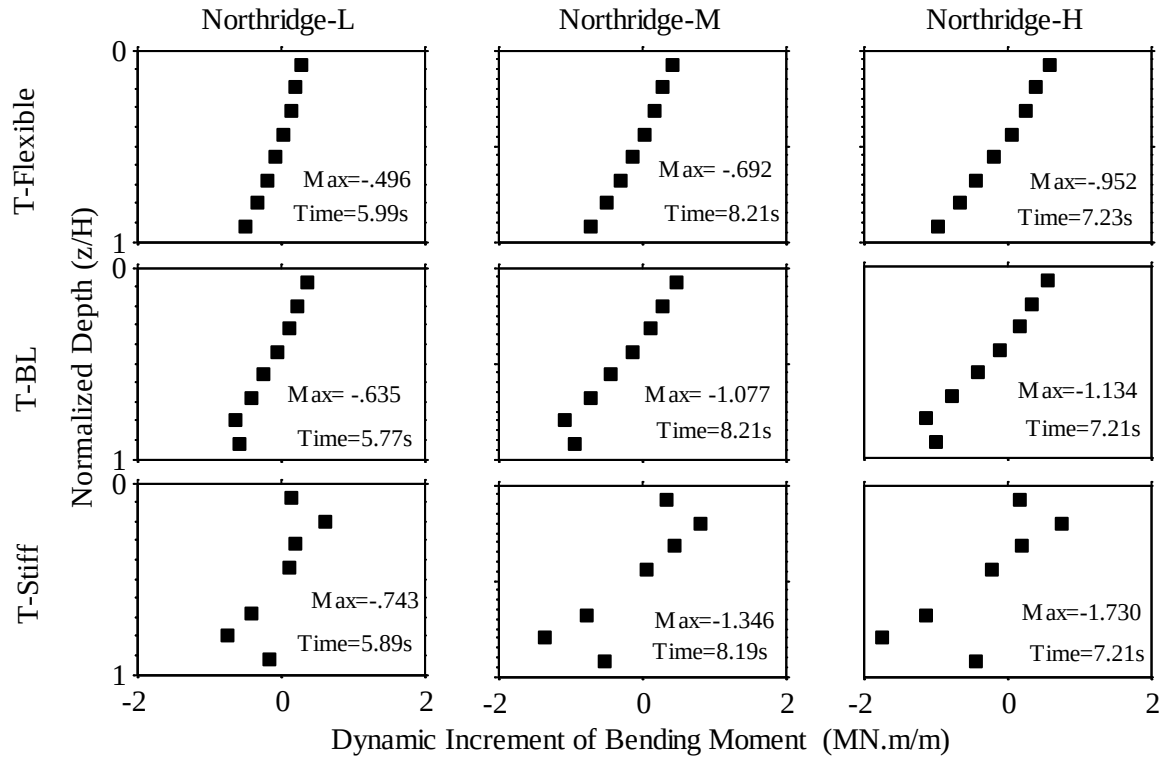

Figure 4-18. The dynamic increment of bending moments (ΔM_E) on the walls of three structures (BL, Flexible, Stiff) at the time of maximum moment during the Northridge-L, Northridge-M, and Northridge-H motions.

CONCLUDING REMARKS

Traditionally, underground structures are categorized either as *yielding* or *rigid-unyielding*, and designed using simplified analytical methods that were developed for one of these two extreme conditions. Underground reservoir structures of interest in this study fall in neither of these categories, because they are not fully rigid, but their wall deformation is limited as they are stiff and restrained at their base and roof (in this paper classified as *stiff-unyielding* structures). The kinematic constraints of these structures are not fully captured by simplified seismic procedures, and advanced numerical tools have not been calibrated or validated adequately against physical model studies. SSI effects near these structures depend on foundation fixity, properties of the

surrounding soil, flexibility of the structure relative to soil, and the characteristics of the earthquake motion. In this paper, we present the results of three centrifuge experiments that investigate the seismic response of *stiff-unyielding* buried reservoir structures in medium dense, dry sand and the influence of structure stiffness and characteristics of the earthquake motion on accelerations, racking deformations, lateral earth pressures, and bending strains and moments. The primary conclusions of this paper are as follows:

1. The acceleration response of the box structure with respect to the far-field was influenced by the confining pressure in soil and the flexural rigidity of the structure. The structure to far-field spectral ratios increased from the bottom of the structure to the top during all motions. As the confining pressure increased, the movement of the buried structure was more controlled by the inertia of the surrounding soil. The highest amplification of spectral ratios was observed at the top of the more flexible structure near the predominant frequency of the base motion.
2. Peak racking deformations measured on the box structures increased as the structural flexibility increased compared to the far-field soil. The NCHRP 611 guideline was observed to be more appropriate for flexible structures, but importantly, it underestimated racking displacements for stiffer underground box structures during all motions.
3. The flexural rigidity of the box structure was shown to affect the distribution of dynamic earth pressures ($\Delta\sigma_E$) measured during different motions. The most flexible structure experienced a triangular distribution of $\Delta\sigma_E$, similar to those predicted by the M-O method, while the stiffer structures displayed a higher order polynomial distribution.
4. The experimentally obtained equivalent dynamic coefficients of lateral earth pressure (ΔK_E) at the time of maximum thrust increased with increasing ground motion intensity (e.g., PGA) in most cases. The ΔK_E values on the more flexible structures (BL and Flexible) were in line with

previous experiments conducted on relatively flexible basement walls and were either close to or smaller than those predicted by the S-W method. The ΔK_E values on the Stiff structure, however, often exceeded the predictions of the S-W method and approached those of Wood's.

5. The centroid of the dynamic earth pressures ($\Delta\sigma_E$) at the time of maximum thrust did not appear to be affected by the intensity of shaking (e.g., PGA), but was influenced by the flexural stiffness of the structure. The estimated centroid locations on the Flexible structure were close to the M-O predictions, and the centroid locations on the BL and Stiff structures generally fell between those predicted by M-O, S-W, and Wood's methods.
6. Dynamic bending moments (ΔM_E) at the time of maximum thrust slightly increased with increasing structural flexural stiffness. Further, the distribution of ΔM_E changed from approximately linear to a higher order polynomial as the structure stiffness increased, a trend similar to the $\Delta\sigma_E$ profiles.

Comparing the experimental results with methods commonly used to evaluate the performance of underground and retaining structures identifies the following key points:

- None of the existing methods adequately capture the structural loading and deformations across the entire range of stiffness and ground motions in which critical underground facilitates must be designed.
- The analysis procedures are not consistently conservative or unconservative with respect to seismic design.
- There is insufficient guidance in practice on how to select different methods for different classes of underground structures, especially for s*tiff-unyielding* structures. As a result, there is a need for improved methodologies and guidance for design of underground structures.

The presented experimental results are intended to provide important insights into the influence of structure stiffness and ground motion properties on seismic forces as well as the seismic performance of an entire class of *stiff-unyielding* buried structures with translational and rotational restraints at the top and bottom. Additionally, parallel nonlinear numerical simulations are necessary before the results can be used to provide general and definite recommendations for practice.

4.3 Journal Paper 2: ASCE Journal of Geotechnical and Geoenvironmental Engineering (Status: Accepted and In Press)

Seismic Performance of Underground Reservoir Structures: Insight from Centrifuge Modeling on the Influence of Backfill Soil Type and Geometry

A. Hushmand[10], S. Dashti[11], C. Davis[12], B. Hushmand[13], J.S. McCartney[14], J. Hu[15], Y. Lee[16]

ABSTRACT: The seismic response of underground reservoir structures is a complex soil-structure interaction problem that depends on the properties of the earthquake motion, surrounding soil, and structure. More experimental and field data of the response of these structures under different boundary conditions is needed to validate analytical and numerical tools. This paper presents the results of four centrifuge experiments that investigate the seismic performance of reservoir structures, restrained from rotational movement at their roof and floor, buried in dry, medium-dense sand and compacted, partially saturated, silty sand. This study focuses on the influence of backfill soil properties, cover, and slope on accelerations, strains, lateral distortions, and lateral earth pressures experienced by the buried structure. The structure to far-field acceleration spectral ratios were observed to approach unity with added soil confinement, density, and stiffness. Both dynamic thrust and accelerations on the structure showed a peak near the effective fundamental frequency of the backfill soil. The addition of a shallow soil cover and stiffness slightly increased seismic earth pressures and moved their centroid upward, hence slightly amplifying seismic moments near the base. The added stiffness, density, and apparent cohesion of the compacted site-specific soil did not influence the magnitude of dynamic earth pressures

[10] Graduate Student Researcher, University of Colorado Boulder, Civil, Env. and Arch. Engineering, Boulder, CO.
[11] Assistant Professor, Univ. of Col. Boulder, Civil, Env. and Arch. Eng., Boulder, CO, shideh.dashti@colorado.edu.
[12] Trunk Line Design Manager, Los Angeles Department of Water and Power, Los Angeles, CA.
[13] President and Principal Engineer, Hushmand Associates, Inc., Irvine, CA.
[14] Associate Professor, Univ. of California at San Diego, Department of Structural Engineering, San Diego, CA.
[15] Civil Engineering Associate, Los Angeles Department of Water and Power, Los Angeles, CA
[16] Civil Engineering Associate, Los Angeles Department of Water and Power, Los Angeles, CA.

significantly but often moved their centroid upward. A sloping backfill reduced the earth pressures and bending moments near the top of the wall, because of the reduced soil mass. The trends in the experimental results indicate that new analytical procedures and design guidelines are needed to account for the backfill soil conditions and ground motions for which these underground structures must be designed.

INTRODUCTION

An experimental study was conducted on the seismic response of shallow buried reservoir structures. This study was inspired by the design of prototype reinforced concrete buried reservoirs (e.g. Headworks reservoir under construction) in Los Angeles, California to replace open water reservoirs for the purpose of improving water quality and safety. These reservoir structures have 11 to 12 m-high walls that will be buried after construction. Further, they are restrained against rotational movement at the top and bottom by a roof and floor, restricting their deformation. These structures have limited movement near the top of their walls unlike cantilever retaining walls. However, they are also not completely rigid and deform according to their flexural stiffness. Hence, they are classified as stiff-unyielding structures (Hushmand et al. 2014, 2016). The reservoirs will be covered with a shallow layer of compacted silty sand with a 2:1 sloped embankment on either side. The structure's foundation can rock or slide laterally, as it rests on a prepared soil subgrade. Soil-structure interaction (SSI) for these buried structures is complex and depends on the properties of the earthquake motion, properties and geometry of the surrounding soil, foundation fixity, and the flexibility of structure relative to soil. There is an increasing need in engineering practice to obtain a better understanding of the seismic performance of these stiff-unyielding underground structures for a range of surrounding soil and loading conditions.

The available simplified methods used to estimate seismic lateral earth pressures on the walls of underground structures are limited in several ways, preventing their reliable application to the design of reservoir structures. For example, the kinematic constraints of the structures at their roof and base against rotation are quite different from the assumption of yielding or active conditions by Mononobe-Okabe, M-O (Okabe 1926; Mononobe and Matsuo 1929) or Seed-Whitman, S-W (Seed and Whitman 1970). Further, the walls of these structures are not completely rigid and deform depending on their stiffness, which is different from the rigid assumption behind the simplified Wood (1973) procedure. Also, none of the available simplified analytical methods consider the complexities introduced by soil cover, backfill slope, and apparent cohesion of the backfill soil.

A few important parameters used in the seismic design of buried reservoir structures include: dynamic lateral earth pressures, bending moments, and the lateral distortions induced by earthquake loading. A time history analysis of the soil-structure system is typically warranted to obtain these parameters for design. However, numerical simulations of these structures (e.g., Harounian et al. 2014, Zhai et al. 2014, Roth et al. 2010) need to be validated against well-documented case histories or physical model studies, which are currently lacking for stiff-unyielding buried reservoir structures.

A series of centrifuge experiments were conducted at the University of Colorado Boulder to evaluate the seismic performance of these shallow buried reservoir structures. The structure stiffness, backfill soil type and slope, cover height, container type (rigid versus flexible boundaries), fixity conditions, and ground motion characteristics were varied to evaluate their influence and relative importance on structural performance. The focus of this paper is on the influence of backfill soil type, soil cover, and backfill slope on the seismic performance of these

stiff-unyielding buried structures. A dry, cohesionless soil layer (Nevada sand) with and without cover as well as a compacted silty sand backfill (site-specific soil from Headworks reservoir construction site) that was either leveled or sloped, were used to evaluate the influence of structure embedment as well as backfill soil type and geometry. The model specimens were instrumented with accelerometers, linearly-variable differential transformers (LVDTs), strain gauges, and tactile pressure transducers. The data from these instruments were used to calculate seismic lateral earth pressures, magnitude and location of dynamic lateral thrust, bending strain and moment distributions, and lateral deformations along the structure walls.

BACKGROUND

The influence of shallow soil cover on the seismic response of underground box structures has not been evaluated experimentally in the past. Youd and Beckman (1996) studied the performance of reinforced highway box culverts during past earthquakes and showed that box culverts with a deeper fill cover experienced more damage due to increased inertial forces. Wang (1993) showed through a series of linear-elastic, finite element analyses that a shallow soil cover similar to that considered in this study does not increase the racking of the structure significantly. Cilingir and Madabhushi (2011) experimentally and numerically studied the effect of embedment on the seismic response of relatively deeply buried (~2.5 and 6.5 m from soil surface to the top of structure), flexible box structures (flexibility ratios ranging from 14 to 330). They showed that larger seismic earth pressures are experienced on deeper tunnels. The influence of a shallow cover on seismic lateral earth pressures and bending moments has not been evaluated for stiffer box structures of interest (e.g., flexibility ratios ranging from about 0.1 to 2), which are important in design of critical buried reservoirs.

The effect of apparent cohesion induced by suction in the unsaturated backfill (Lu and Likos 2006) on seismic lateral earth pressures has previously been studied analytically, numerically, and experimentally. For example, analytical limit state procedures have evaluated the effects of cohesion on dynamic earth pressures acting on yielding retaining walls (e.g., Okabe 1926; Chen and Liu 1990; Das 1996; Anderson et al. 2008). These studies showed that increasing cohesion leads to a significant decrease in dynamic earth pressures, assuming peak strength in the backfill soil and no change in the structure's stiffness, rotation, or translation.

Wilson (2009) performed numerical analyses of rigid retaining walls with compacted silty sand backfill and showed that rotation and wall translation have more influence on dynamic earth thrust than cohesion. Allowing for rotation and translation of the wall significantly reduced seismic earth pressures, whereas adding cohesion reduced earth pressures only slightly. Numerical analyses by Candia (2013) on braced basement walls and flexible cantilever walls retaining compacted low plasticity clay also showed that cohesion has a minor effect on dynamic earth pressures.

Wilson and Elgamal (2015) performed 1g shake table tests on short, rigid, retaining walls (1.7m high) with a dense c-ϕ backfill material. They showed a similar distribution of lateral earth pressure as observed in prior analytical and numerical studies (e.g., Veletsos and Younan 1994; Psarropoulos et al. 2005; Davis 2003) where the dynamic increment of earth pressure increases toward the center and then decreases near the bottom for stiff retaining structures. Relatively low dynamic lateral earth pressures were recorded at smaller acceleration levels (less than 0.7g), because of the high shear strength of the backfill soil including cohesion, preventing a limit equilibrium type failure. Due to the deformation patterns in their retaining wall and the higher strength of the backfill soil, the lateral earth pressure time histories along the height of the wall were observed to be out of phase, which reduced the total applied force. At stronger accelerations,

however, the lateral earth pressure distributions became more in phase, significantly amplifying the applied seismic force.

A realistic wave propagation, mean effective stress, and wall height cannot be properly simulated in 1g shake table tests. Therefore, Candia (2013) and Mikola (2012) performed centrifuge experiments to evaluate the seismic response of braced basement walls and flexible cantilever walls retaining clean sand and low plasticity clay with a relative compaction of 90% with respect to the standard Proctor compaction effort. They observed that the dynamic increment of pressure was affected by ground shaking intensity and wall displacement, but it was relatively independent of cohesion for free-field acceleration levels up to 0.6g. They also observed that the dynamic lateral earth pressures acting on the basement walls increased linearly with depth. The basement struts did not prevent excessive bending of the walls in this case, which resulted in a more linear distribution of seismic earth pressures, as expected for more flexible retaining structures (e.g., Hushmand et al. 2016). Further, these experiments obtained earth pressures indirectly from strain gauges, which may increase the uncertainty.

In summary, a limited number of analytical, numerical, and experimental studies have been conducted on the influence of soil cover and cohesion on the seismic response of retaining and underground box structures. Previous studies have not evaluated the influence of backfill slope on the structure's seismic performance. The numerical simulations of the effect of soil cover presented in the literature focused primarily on the racking response and have not been validated sufficiently against physical model studies. Analytical, numerical, and experimental studies of the influence of cohesion of the surrounding soil on seismic lateral earth pressures involved different types of structures with different kinematic constraints, and accordingly led to results that did not always agree in terms of the magnitude and distribution of lateral earth pressures. Lastly, and

importantly, the data available is limited for the seismic response of stiff-unyielding buried box structures, which are of interest in the design of underground reservoir structures. Hence, the amplitude and distribution of seismic earth pressures on these underground structures in different types of soils are not well understood. Centrifuge modeling with adequate instrumentation can help evaluate SSI, deformations, and lateral earth pressures for this class of buried reservoir structures and the relative importance of different testing parameters on their seismic performance. Developing a fundamental understanding of these topics is a necessary step for the validation of advanced numerical tools before they can be used in design or parametric studies.

CENTRIFUGE EXPERIMENTS

A series of four centrifuge tests were conducted with the same structure, but different backfill soil properties and geometries, as shown schematically in Figure 4-19. In this paper, the four experiments are referred to as T-NS (Nevada sand used as the backfill soil without a cover), T-NS-Cover (Nevada sand with a cover), T-SS (site-specific, compacted silty sand as the backfill soil with a cover), and T-SS-Slope (site-specific compacted silty sand with a cover and a 2:1 slope). The model specimens were prepared in a flexible shear beam (FSB) container to reduce boundary effects (Ghayoomi et al. 2012, 2013). The instrumentation layout of different tests is presented in Figure 4-20. Experiments were performed at 60g of centrifugal acceleration using the large, 400 g-ton centrifuge at the University of Colorado Boulder (Ko 1988). Earthquake motions were applied to the model specimens in flight using the servo-controlled, electro-hydraulic shake table (Ketcham et al. 1991) mounted on the basket at the end of the centrifuge arm. A series of five earthquake motions were applied to the base of the models in the same sequence in the four experiments, followed by sinusoidal motions. All dimensions presented in this paper are in prototype scale, unless stated otherwise.

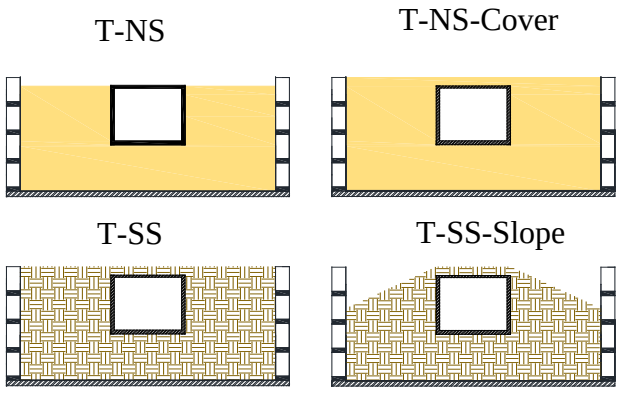

Figure 4-19. Schematics of the centrifuge experiments to evaluate the influence of the properties and geometry of backfill soil.

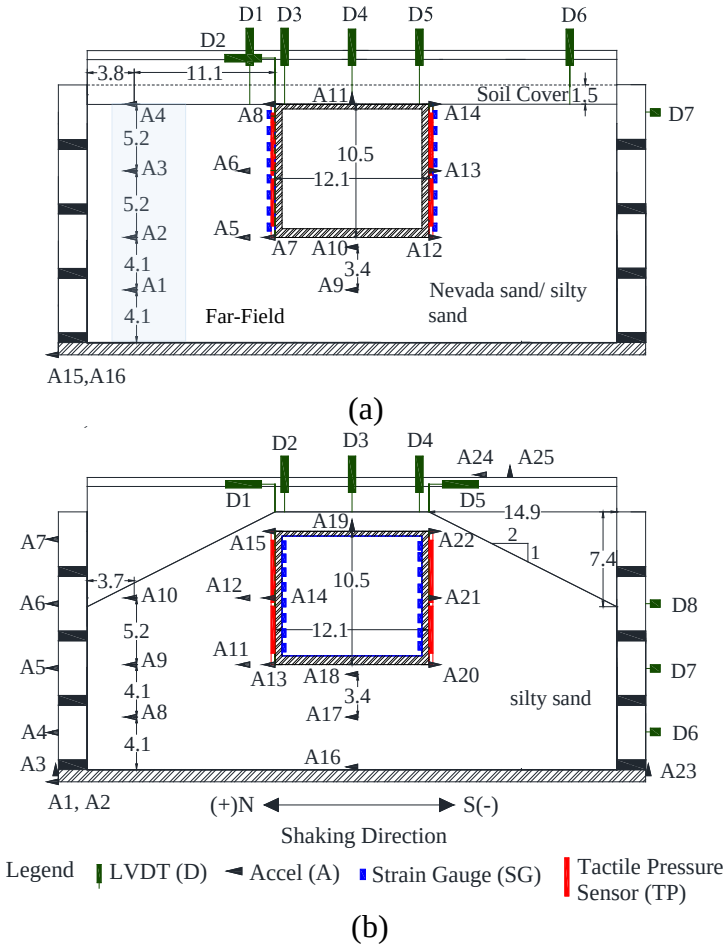

Figure 4-20. Setup and instrumentation layout of centrifuge experiments: (a) T-NS, T-NS-Cover, and T-SS; and (b) T-SS-Slope (dimensions are in prototype scale meters).

Soil Properties and Preparation

Experiments T-NS and T-NS-Cover were prepared with medium-dense, dry Nevada sand (G_s=2.65; e_{min}=0.56; e_{max}=0.84; D_{50}=0.13 mm; C_u=1.67) as backfill. In these tests, Nevada sand was pluviated from a predetermined height to achieve a relative density (D_r) of approximately 60% in T-NS. In T-NS-Cover, a 1.5 m (prototype scale) cover was added by pluviating a layer of Nevada sand over the specimen already used in T-NS after removing it from the centrifuge platform. Even though some densification of the Nevada sand layer in T-NS was expected after application of different motions, the densification inferred from LVDT measurements in T-NS

indicate that it was roughly uniform across the container. Accordingly, it was deemed that the effects of soil cover could still be evaluated on the response of the underground structure in T-NS-Cover compared to T-NS, while keeping in mind the changes in the properties of the backfill soil due to densification and seismic history. Further, T-NS-Cover had similar backfill geometry and cover as T-SS, which enabled evaluating the influence of soil properties alone on the response of the buried structure.

Compacted, site-specific, silty sand obtained from the reservoir site in Los Angeles, California was used in T-SS and T-SS-Slope. The site-specific soil that was used in the centrifuge experiments was first passed through sieve No. 40 to remove large particles. The properties of the site-specific soil are summarized in Table 4-3, based on the gradation test (ASTM D422), modified Proctor compaction test (ASTM D1557), and direct shear test under consolidated drained conditions (ASTM D3080) performed by the authors.

Table 4-3. Mechanical properties of site-specific, compacted, silty sand used in T-SS and T-SS-Slope (Note: compaction corresponding to the modified Proctor compaction effort).

USCS	**Silty Sand (SM)**
Sand content	61.4 %
Fines content	38.6 %
Optimum water content	11.5 %
Maximum dry unit weight	19.1 kN/m3
Total unit weight	21.3 kN/m3
Site-specific relative compaction	95 %
Desired total unit weight	20.3 kN/m3
Friction angle (peak)	32^{o}
Cohesion (peak)	35 kPa

The preparation of T-SS and T-SS-Slope took place in several steps: First, the soil was homogenized and the initial gravimetric content was measured to determine the amount of water to add to reach the optimum gravimetric water content of 11.5 %. The soil was then moisture

conditioned for 24 hours. The moisture-conditioned soil was placed in several layers using specific lift heights and weights. It was subsequently compacted using a 44 N guided hammer to a certain volume to achieve the desired total unit weight of 20.3 kN/m^3. Accelerometers were added to the model between soil layers at the locations shown in Figure 4-20. The profiles in T-SS and T-NS-Cover were similar, only with different soil types. The model specimen in T-SS-Slope was prepared first in the same manner as T-SS, after which a flat spatula was used to cut the backfill soil to a 2:1 downward slope on either side of the structure.

Structure Properties

The actual reservoirs are complex structures with many details that are difficult to scale and test in centrifuge. Hence, a simplified version of the reservoir was designed by maintaining a similar natural frequency and lateral stiffness as the designed prototype reservoir structure (Hushmand et al. 2014, 2016). The model structure was constructed of four pieces of welded 1018 Carbon Steel (density = 7870 kg/m^3; Young's modulus = 2×10^8 kPa). Table 4-4 presents the dimensions, racking stiffness, and natural frequency of the structure used in the centrifuge experiments. Teflon sheets were used on the container sides and ends of the structure to reduce friction at the structure-container interface. The test soil was glued on all sides of the structure to provide a more realistic interface friction between the structure and the soil in each test.

Table 4-4. Dimensions and properties of model underground structure (prototype scale).

Height & Width (m) Outer to Outer	Thickness			Lateral Stiffness, K_s (kN/m/m)	Fundamental Frequency (Hz)	
	Base (mm)	Roof (mm)	Walls (mm)		Numerical	Experimental
10.5 & 12.1	688	371	558	31.5	4.0	3.9

Instrumentation

Data was acquired using accelerometers, LVDTs, strain gauges, and tactile pressure sensors, as shown in Figure 4-20. Accelerometers were placed horizontally at the container base, on the container frames, at different elevations within the soil in the far-field, adjacent to the buried structure, on the structure, and on the instrumentation rack to monitor movement. Vertical accelerometers were similarly placed at the container base, roof of the structure, and instrumentation rack. LVDTs were used to measure the settlement of soil and structure, the lateral displacement of the structure, lateral displacement of FSB container frames, and lateral movement of container base. Eight strain gauges were installed on each wall of the structure (total of sixteen) to measure bending strains and hence, bending moments. Four tactile pressure sensors were used to measure total pressure directly on both sides of the structures. Tactile sensors were equilibrated, conditioned, statically and dynamically calibrated prior to use in centrifuge, following the procedure recommended by Dashti et al. (2012), Gillis et al. (2015), and El Ganainy et al. (2014).

Ground Motions

A series of earthquake motions were selected with a range of amplitudes, frequency contents, and durations and applied during T-NS, T-NS-Cover, T-SS, and T-SS-Slope. These motions included scaled versions of the horizontal acceleration recordings at the Sylmar Converter Station during the 1994 Northridge Earthquake (NSC52), the LGPC Station during the 1989 Loma Prieta Earthquake (LGP000), and the Istanbul Station during the 1999 Izmit Earthquake in Turkey (IST180), all obtained from the PEER database. Sinusoidal motions were also applied in these tests after the earthquake motion sequence, which are not presented in this paper. The achieved base motions in the centrifuge are referred to as Northridge-L (low intensity), Northridge-M

(medium intensity), Northridge-H (high intensity), Izmit and Loma. The properties of the achieved base motions in T-NS are presented in Table 4-5.

Table 4-5. Base earthquake motion properties as recorded during T-NS by accelerometer A15 (all units in prototype scale).

Motion Name	PGA (g)	Arias Intensity I_a (m/s)	Significant Duration $D_{5\text{-}95}$ (s)	Mean Frequency f_m (Hz)	Predominant Frequency f_p (Hz)
Northridge-L	0.36	1.6	15.4	1.4	2.9
Northridge-M	0.81	5.4	19.5	1.5	3.6
Northridge-H	1.2	11.6	25.1	1.6	3.6
Izmit	0.33	2.1	39.5	1.8	4.2
Loma	1.0	12.4	13.3	2.0	3.7

A small degree of variation in the base motions among different tests was expected due to the change in weight and natural frequency of the model specimen as well as inconsistencies of the shake table. The spectral acceleration (5% damped) of the achieved base motions in T-NS, T-NS-Cover, T-SS, and T-SS-Slope are compared in Figure 4-21, showing a reasonable comparison particularly for weaker motions. More variation was observed during stronger motions (e.g., Northridge-H and Loma) at higher frequencies that are more difficult for the shake table to control and reproduce.

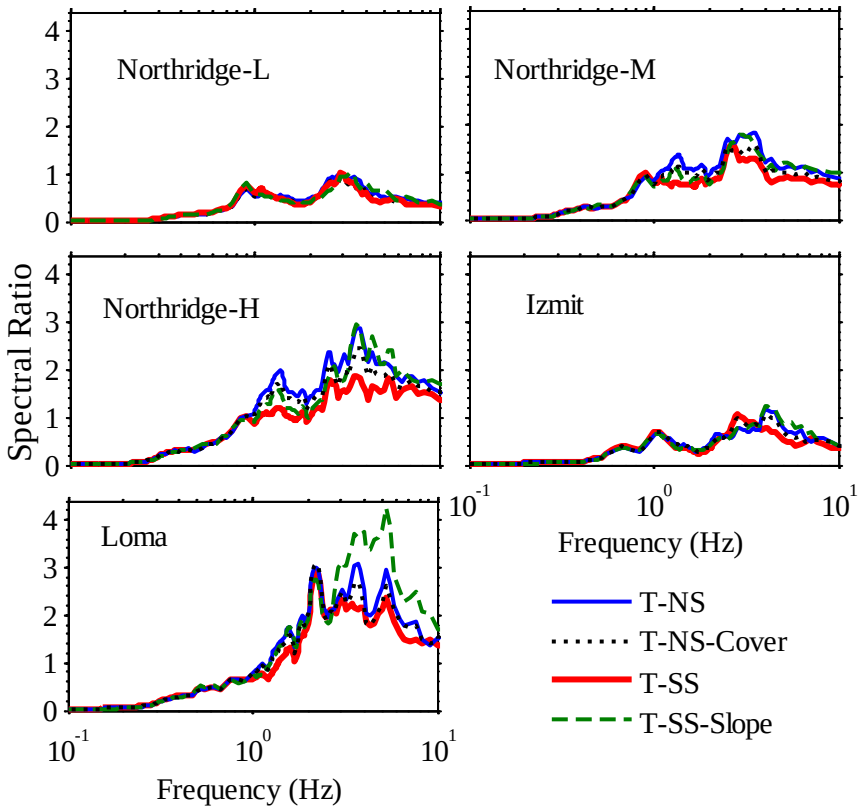

Figure 4-21. Comparison of the recorded base motion spectral accelerations (5% damped) in T-NS, T-NS-Cover, T-SS, and T-SS-Slope.

EXPERIMENTAL RESULTS

Acceleration Response

The influence of backfill soil type and geometry was evaluated on soil-structure interaction effects (both inertial and kinematic) near the underground structure through spectral ratios of structure to far-field accelerations in the four experiments. Figure 4-22 shows the spectral ratios of accelerations at the bottom, middle, and top of the structure to those in the far-field in each test during three representative ground motions (Northridge L, M, and H). These ratios provide insight into whether accelerations were amplified or de-amplified on the structure compared to the far-field recordings that approximate 1-D free-field site response. Due to a lack of 1-D far-field conditions in T-SS-Slope, the spectral ratios are not presented for this experiment.

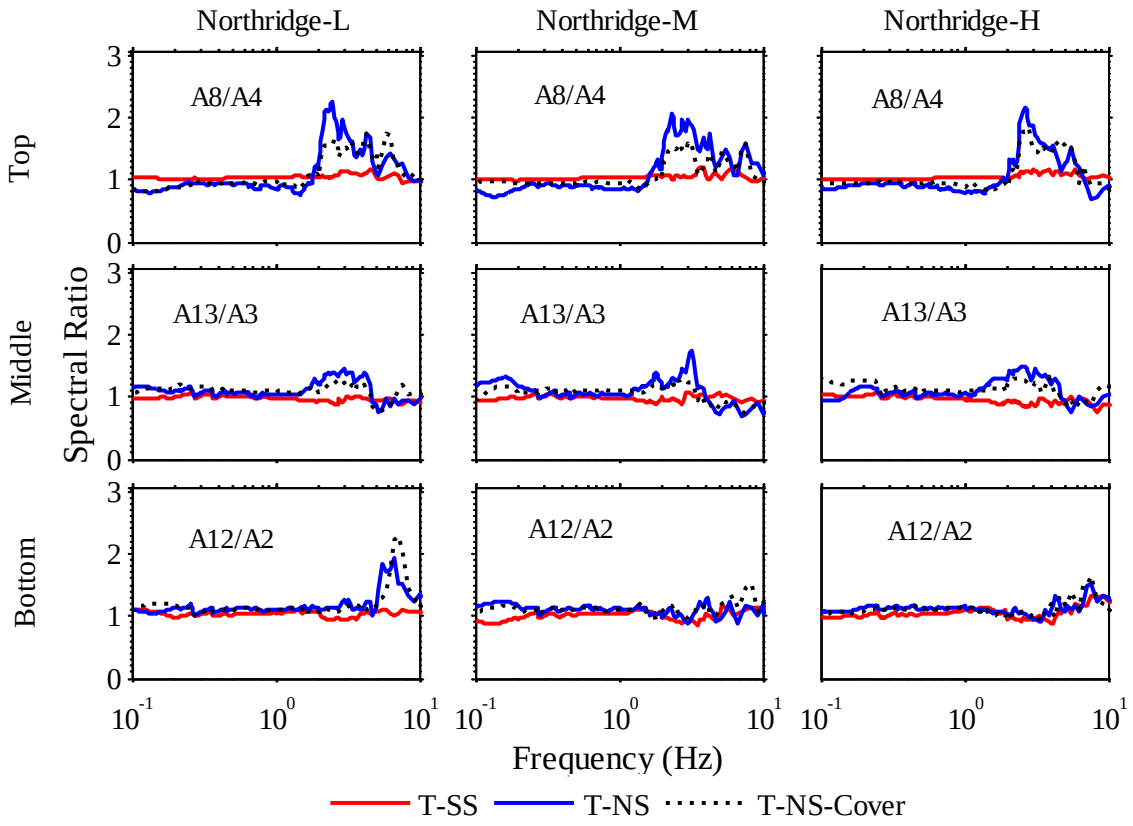

Figure 4-22. Spectral ratio (5% damped) of structure to far-field accelerations in three tests (T-NS, T-NS-Cover, T-SS) during the Northridge-L, Northridge-M, and Northridge-H motions.

The structure to far-field spectral ratios increased at shallower depths in T-NS and T-NS-Cover. As the confining pressure increased, the movement of the buried structure was controlled more by the surrounding soil. The highest amplification of spectral ratios was observed at the top of the structure near the predominant frequency of the motion ($f_p \approx 3$ Hz). The added cover and stiffness of the backfill soil slightly reduced the degree of amplification in structural accelerations during T-NS-Cover compared to T-NS.

The properties of the backfill soil significantly influenced the accelerations on the structure. For example, when Nevada sand was replaced with the site-specific, compacted silty sand in T-SS, no noticeable change was observed in accelerations recorded on the structure compared to the far-field at any depth (e.g., spectral ratios of near 1.0). It appeared that the structure closely followed the movement of the compacted silty sand at all depths during this test. In all experiments,

however, the impact of structural inertia on accelerations appeared to be minor, as no particular amplification was observed near the structure's fundamental frequency of 4 Hz.

Racking Displacements

Racking is defined as the lateral displacement of the roof of the box structure relative to its base. The racking displacement is often used in design to evaluate peak bending moments in a simple frame analysis of the 2D box structure. In practice, the peak transverse racking of a box structure is often estimated with respect to that in the free-field using the NCHRP 611 guideline (Anderson et al. 2008). The NCHRP 611 guideline is, however, based on the results of dynamic finite element analyses performed by Wang (1993) on buried box structures. The centrifuge results presented in this paper enable an experimental evaluation of the applicability of this guideline to stiff-unyielding, underground reservoir structures with varying backfill soil and geometry.

Lateral displacement time histories were obtained by double integrating and baseline correcting the accelerometer recordings. Racking (Δ) was then calculated as the difference in lateral displacements at the top and bottom of the structure ($\Delta_{structure}$) and in the far-field at the same elevations (Δ_{FF}). The peak values of racking displacement on the structure ($\max|\Delta_{structure}|$) and far-field soil ($\max|\Delta_{FF}|$) were subsequently used to obtain the racking ratio ($R= \max|\Delta_{structure}|/\max|\Delta_{FF}|$) during each test and motion. Since there was no location in T-SS-Slope approximating 1-D free-field conditions, the far-field response in T-SS was used instead to obtain the racking ratios in T-SS-Slope. Even though the achieved base motions were slightly different in the two experiments, particularly during stronger motions, this comparison was still insightful.

To calculate the flexibility of the structure relative to the far-field in accordance with the NCHRP 611 guidelines, the flexibility ratio, $F = (G_m.B)/(K_s.H)$, needed to be calculated, where G_m is defined as the mean strain-compatible shear modulus of soil in the free-field, B is the

structure width, K_s is the racking stiffness of the structure, and H is its height (Anderson et al. 2008). Table 4-4 summarizes the properties of the structure used in centrifuge testing. The G_m of soil was experimentally obtained by calculating the effective fundamental frequency (f_{so}') of the far-field soil from the transfer function of accelerations at the surface with respect to base during a given motion (e.g., Figure 4-23). The strain-compatible, average shear wave velocity of the far-field soil, $\overline{Vs}$', was computed as $\overline{Vs}' = 4H \times f_{so}'$, and the strain-compatible G_m of soil as $G_m = \rho \overline{Vs}'^2$, where H is the height of the far-field soil column and ρ is the soil's mass density in a given test. As expected, the f_{so}' of the far-field soil in T-SS was observed in Figure 4-23 to decrease with stronger shaking due to softening.

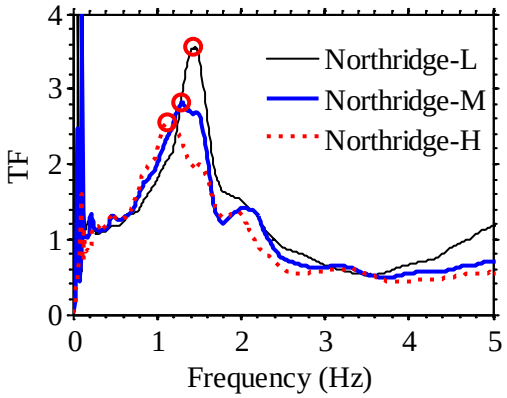

Figure 4-23. Transfer function of surface to base accelerations in the far-field in T-SS during the Northridge-L, Northridge-M, and Northridge-H motions to determine the strain-compatible fundamental frequency and shear modulus of the soil column away from the structure.

The experimentally obtained values of racking versus flexibility ratio (R versus F) in all four tests during all motions are compared with the numerically obtained values from the NCHRP 611 guideline shown in Figure 4-24. In general, the results compared well, although the experimental values of R were often slightly greater than those from the NCHRP guideline. Both R and F values increased slightly in T-NS-Cover compared to T-NS. This trend was likely due to the increase in soil stiffness (and hence, flexibility ratio or F) in T-NS-Cover compared to T-NS after the

application of many motions and soil densification. The impact of soil cover is more evident when racking is plotted vs. far-field surface PGA, as shown in Figure 4-25. As expected, the racking of the buried structure increased with increasing motion intensity. The racking of the structure during T-NS-Cover was overall larger than T-NS for the range of applied ground motions. The figure also shows that racking increases with far field PGA regardless of the soil type or the geometry of the backfill soil.

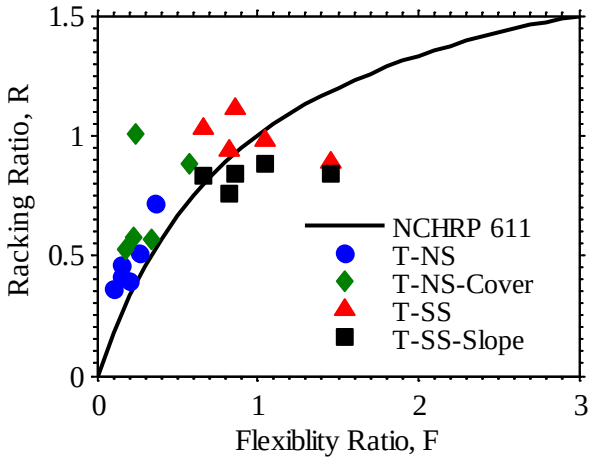

Figure 4-24. Experimental racking vs. flexibility ratios of the underground reservoir structure during different ground motions and tests as compared to the NCHRP 611 guideline.

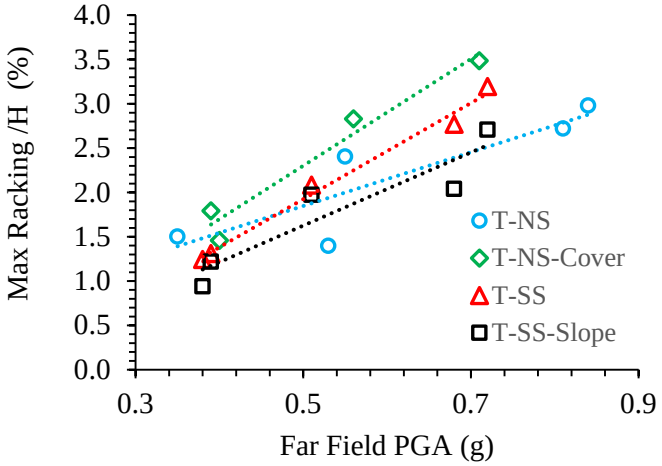

Figure 4-25. Experimental racking vs. far-field PGA.

The use of a compacted silty sand backfill soil in T-SS increased G_m to a value closer to the structure's racking stiffness in this case (e.g., F≈1). Therefore, the structure underwent racking

deformations that were similar to those in the far-field soil (i.e., R≈1). A similar trend was observed previously in the acceleration response of structure and far-field soil in T-SS. The addition of the slope in T-SS-Slope slightly reduced the racking of the structure compared to T-SS. Further, the change in ground motion intensity did not alter R significantly during the tests with site-specific backfill soil, as in all cases the structure was observed to primarily follow the deformation of the backfill soil.

Seismic Lateral Earth Pressures

The dynamic increment of pressure ($\Delta\sigma_E$) was estimated as the difference between total and pre-shake, static lateral earth pressure recordings. To reduce scatter, the data obtained from nine sensels were averaged to represent a larger pressure area after removing the nonworking sensels (Hushmand et al. 2016). Then, the pressure time histories were averaged over the corresponding row of sensels to obtain one time history at a given depth. This method was successful in reducing the scatter in pressure recordings, particularly when in contact with granular materials with local inhomogeneities (Gillis et al. 2015).

The dynamic increment of thrust was estimated by numerically integrating the dynamic pressure profile along the wall at each instance of time, using the trapezoidal rule. The resulting dynamic thrust time histories during the Northridge-L motion are compared among the four tests in Figure 4-26 along with the acceleration time history of the corresponding base motion. The presented thrust time histories were subject to a band-pass, 5^{th} order, a-causal, Butterworth filter with corner frequencies of 0.1 and 15 Hz, to remove low and high frequency noise that was sometimes present in the tactile sensor record and could affect the estimated peak dynamic thrust. As a result of filtering, however, the permanent change in thrust that is typically expected cannot be obtained from this figure, but the transient thrust may be compared among the four tests.

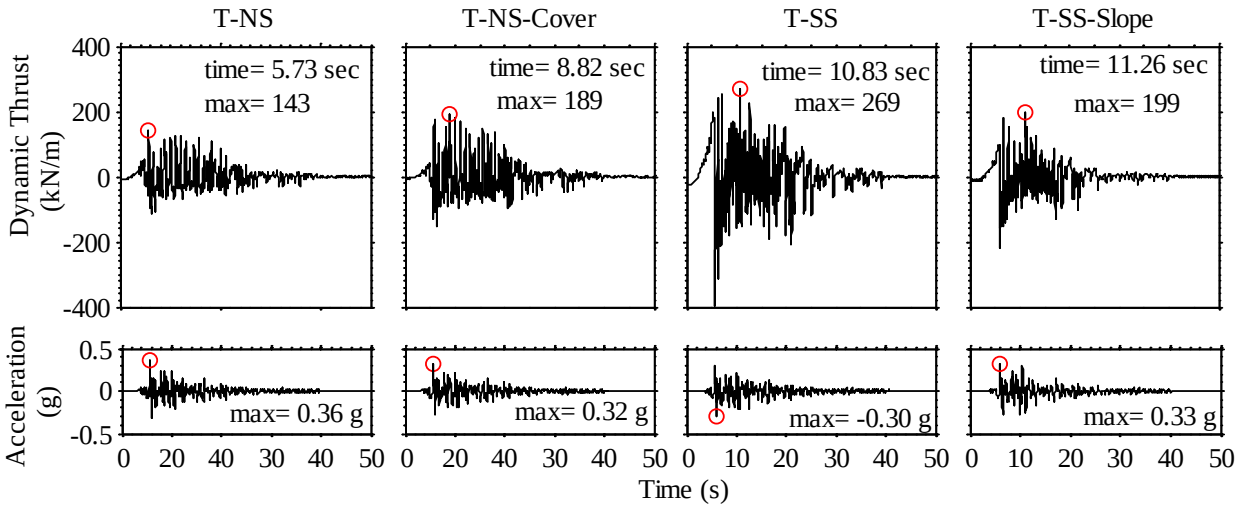

Figure 4-26. Dynamic thrust time histories on the structures in T-NS, T-NS-Cover, T-SS, T-SS-Slope during the Northridge-L motion.

The short-time Fourier transform of accelerations recorded on the container base and structure wall base are compared to those of dynamic thrust during the Northridge-M motion in each of the four tests in Figure 4-27. The energy of the base motion was primarily concentrated near 1 Hz, with some content at 3 Hz. The acceleration energy at 1 Hz was amplified significantly from the container base toward the structure and soil surface in the far-field in all experiments due to site response or resonance. The effective, strain-dependent, fundamental frequency of the site during earthquake motions was estimated from the surface to base acceleration transfer functions to be approximately $f_{so}' \approx 1$ Hz in T-NS, $f_{so}' \approx 1.2$ Hz in T-NS-Cover, and $f_{so}' \approx 1.4$ Hz in T-SS, corresponding to effective average shear wave velocities, $\overline{Vs}' = 4. f_{so}'.H_{site} \approx 75$, 97, and 113 m/s in T-NS, T-NS-Cover, and T-SS, respectively during Northridge-L. Similar to the acceleration at the base of the structure, the frequency content of the thrust was also amplified near 1 Hz. The acceleration and dynamic thrust on the buried structure are both expected to be influenced by site response, structure's fixity, stiffness of the structure relative to soil, height of the structure relative to the propagating wavelength, as well as structural inertia. Therefore, the similarity between their frequency contents was expected. Further, a noticeable content in dynamic thrust was observed

near 2.2 to 2.5 Hz. This content may have been related to kinematic interaction. The wavelength (λ) associated with these frequencies ranged from approximately 32 to 50 m. The corresponding wavelength to structure height ratio ($\lambda / H_{structure}$) ranged from 3 to 8, which was near the peak influence of kinematic interaction on seismic earth thrust, as shown analytically by Brandenberg et al. (2015).

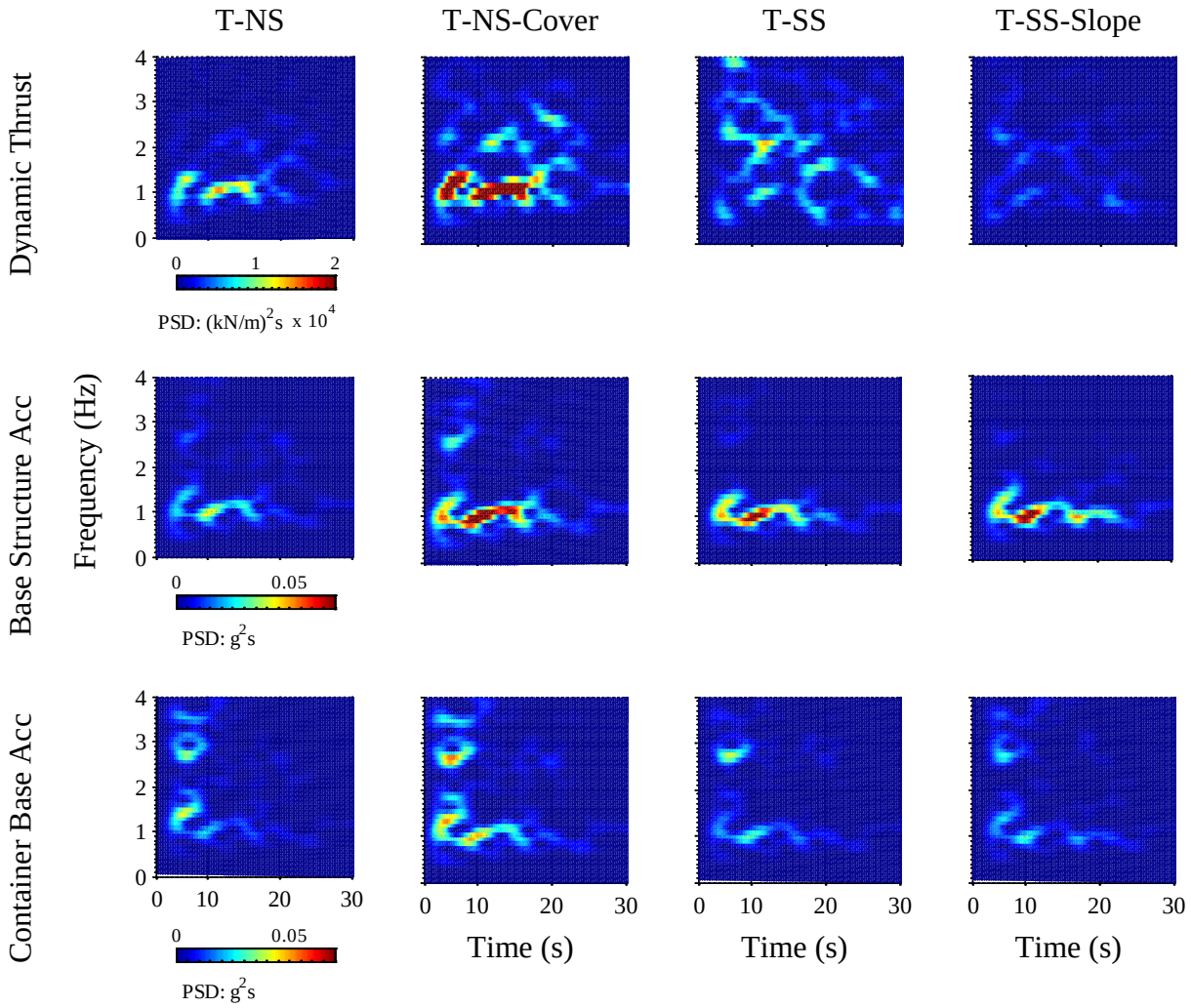

Figure 4-27. Short-time Fourier transform of container base acceleration, base structural wall acceleration, and dynamic thrust recorded on the structure in T-NS, T-NS-Cover, T-SS, and T-SS-Slope during the Northridge-M motion.

The influence of structural inertia on its accelerations or seismic lateral earth pressures was likely minor in these tests, as no significant amplifications were observed near the fundamental frequency of 4 Hz. This was also confirmed in Figure 4-22 when comparing the acceleration of the structure with far-field soil. Nevertheless, the effect of structural inertia may be important for other conditions. Future numerical studies, in which different effects can be properly isolated, can provide valuable insights into the potential influence of structural inertia and conditions at which it may play an important role.

The $\Delta\sigma_E$ profile at the time of maximum thrust is shown in in all four tests during all earthquake motions. A 3rd order polynomial was fit to the $\Delta\sigma_E$ distribution at the time of maximum thrust to estimate the centroid location and to interpret the magnitude and trends despite the scatter present in the recordings. The centroid of $\Delta\sigma_E$ at the time of maximum thrust in all four tests versus the PGA of the far-field surface motion (A4) is shown in Figure 4-29, which was obtained from the polynomial fit. For all the conditions investigated here, the $\Delta\sigma_E$ increased towards the center of the wall and decreased near the top and bottom of the wall. These distributions were more consistent with those predicted analytically, numerically, and experimentally for stiffer structures in different soils (e.g., Veletsos and Younan 1994; Psarropoulos et al. 2005; Richards et al. 1999; Davis 2003; Gazetas et al. 2004; Psarropoulos et al. 2005; Wilson 2009; Taiebat et al. 2011; and Wilson and Elgamal 2015) than those observed experimentally and numerically for more flexible structures (e.g., Mikola 2012; Candia 2013). The differences observed in the distribution of dynamic earth pressures, therefore, are mainly due to the differences in kinematic constrains and flexural rigidity of the wall system employed rather than the stiffness and strength of the backfill soil.

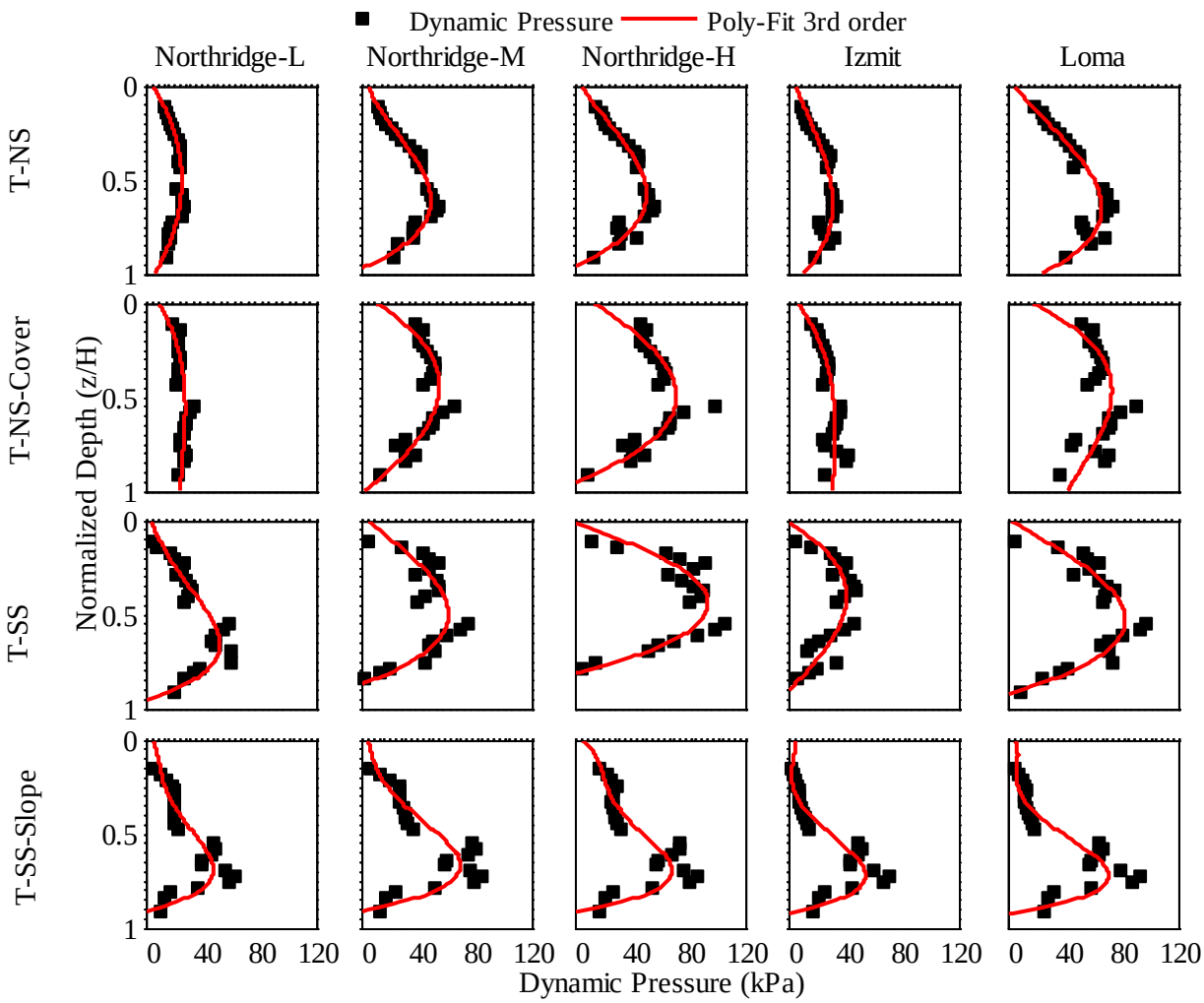

Figure 4-28. Dynamic pressure ($\Delta\sigma_E$) profiles at the time of maximum thrust measured by tactile pressure sensors in T-NS, T-NS-Cover, T-SS, T-SS-Slope during different earthquake motions.

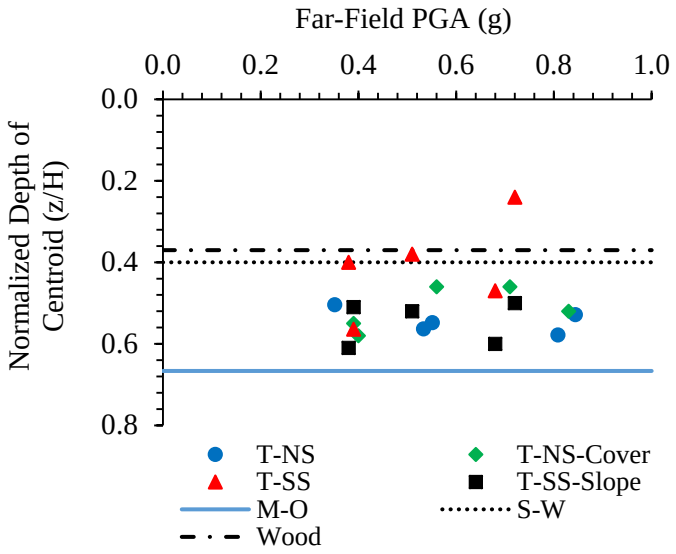

Figure 4-29. Centroid of $\Delta\sigma_E$ at the time of maximum thrust as a function of far-field surface PGA in four centrifuge tests compared with analytical procedures of Mononobe-Okabe, Seed-Whitman, and Wood.

The backfill soil type and geometry also influence the shape and magnitude of $\Delta\sigma_E$ profiles. The addition of a shallow soil cover as well as the increase in backfill soil stiffness during T-NS-Cover slightly increased the dynamic pressures near the top of the wall and shifted the centroid upward when compared to T-NS during stronger motions. The additional apparent cohesion and stiffness of the site-specific, compacted soil in T-SS also slightly altered the distribution of $\Delta\sigma_E$ when compared with T-NS-Cover of the same backfill geometry: $\Delta\sigma_E$ was often observed to increase slightly near the center and decrease near the top and bottom of the wall in T-SS compared to T-NS-Cover. A review of the pressure time histories along the wall shown in Figure 4-30 indicated that $\Delta\sigma_E$ time histories were primarily in phase in T-NS-Cover but not in T-SS. This means that when $\Delta\sigma_E$ peaked near the center, it approached its minimum near the top and bottom of the wall in T-SS during the motions investigated. This observation is consistent with those of Wilson and Elgamal (2015) for a rigid retaining wall with compacted *c*-ϕ backfill soil at lower levels of shaking, when a limit equilibrium failure state is not expected. When comparing the

dynamic thrust, which averages the $\Delta\sigma_E$ distribution along the height of the wall, no significant and consistent difference was observed between T-NS-Cover and T-SS. Therefore, similar to other experimental and numerical observations (e.g., Wilson 2009; Wilson and Elgamal 2015; Candia 2012), cohesion of the backfill soil was observed to have a relatively minor effect on seismic earth thrust regardless of the kinematic constraint or flexural rigidity of the wall employed. The centroid of the $\Delta\sigma_E$ profile, however, appeared to move upward slightly in T-SS compared to T-NS-Cover, particularly during stronger motions. The $\Delta\sigma_E$ values reduced near the top of the wall in T-SS-Slope compared to T-SS, because of the reduction in soil mass and inertia near the surface due to the sloped backfill, as expected.

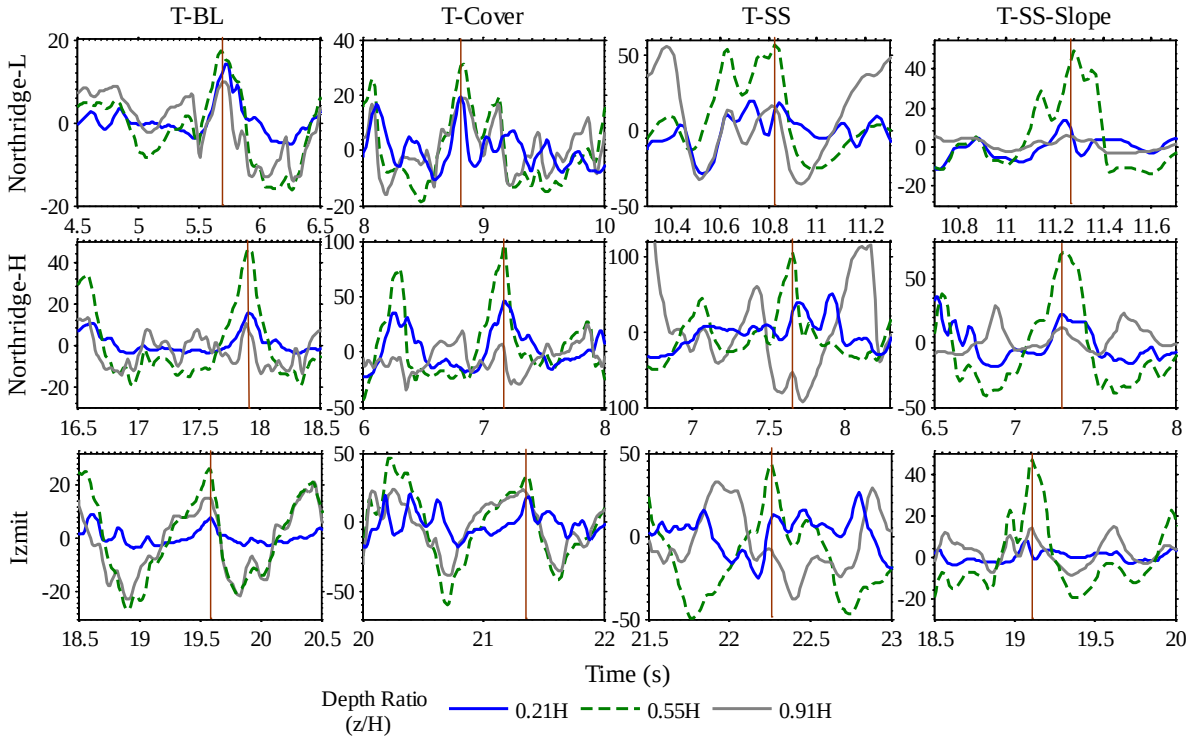

Figure 4-30. Dynamic increment of pressure time histories along top, middle, and bottom of the structure during a few representative (Northridge-L, Northridge-H, Izmit) ground motions. Vertical line identifies the time of maximum dynamic thrust.

The dynamic coefficient of lateral earth pressure (ΔK_E) was calculated for an equivalent triangular dynamic lateral earth pressure profile by dividing the actual dynamic thrust by $\gamma H^2/2$,

where γ is the total unit weight of the corresponding backfill soil and H the wall height. ΔK_E, as originally introduced by Seed and Whitman (1970), was based on a triangular distribution of dynamic lateral earth pressures, while the dynamic lateral earth pressure profiles in these experiments resembled a parabolic shape. The equivalent ΔK_E values calculated based on experimental recordings of pressure were used to compare the magnitude of seismic force among the different experiments, previous centrifuge tests, and the available simplified procedures. The equivalent ΔK_E values obtained experimentally at the time of maximum thrust as a function of the PGA of the far-field surface motion (A4) are shown in Figure 4-31. This figure also includes the results obtained from previous centrifuge experiments performed by Mikola (2012) on a model basement structure retaining a cohesionless soil and Candia (2013) on a basement structure retaining a cohesive soil (both reported at the time of maximum moment), as well as the predictions from the M-O, S-W, Wood, and NCHRP 611 methods for comparison. The NCHRP 611 method is a modified version of M-O that takes into account cohesion and friction parameters of the backfill. The peak and ultimate shear strength parameters obtained from the direct shear tests on the compacted silt sand were used to calculate the ΔK_E values for the NCHRP 611 method.

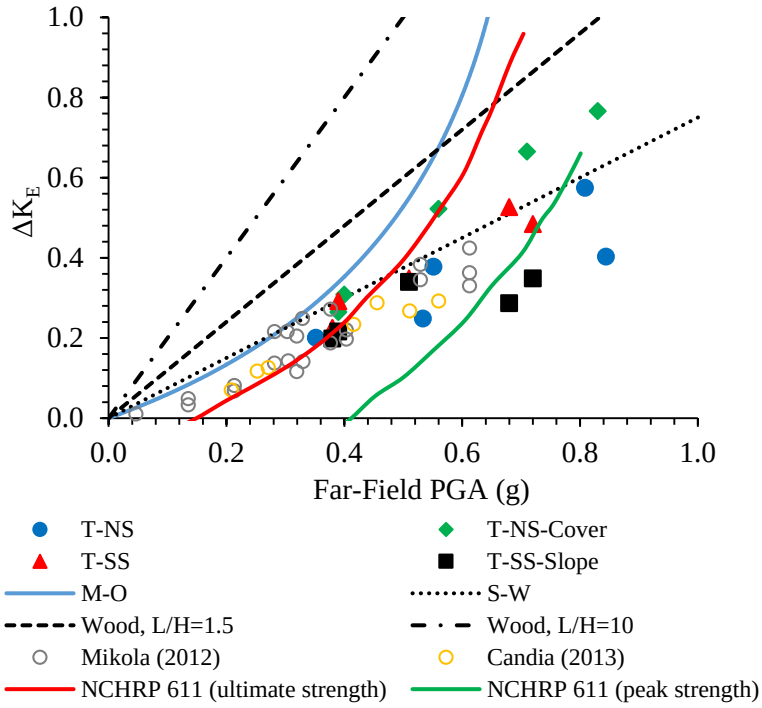

Figure 4-31. Dynamic coefficient of lateral earth pressure (ΔK_E) at the time of maximum thrust as a function of far-field surface PGA in four centrifuge tests compared with analytical procedures of Mononobe-Okabe, Seed-Whitman, Wood, NCHRP 611 and previous centrifuge experiments performed by Mikola (2012) and Candia (2013) on a basement wall.

The ΔK_E values obtained in all experiments generally increased with increasing shaking intensity and were often smaller than those predicted by the S-W procedure. However, the ΔK_E values were larger than S-W during T-NS-Cover, particularly for PGA values greater than about 0.4, possibly due to the added stiffness and pressure from the soil cover. Strong motions with large PGA's are common in the design of buried reservoir structures, since they are considered as a critical component of the lifeline infrastructure. The addition of the soil cover and backfill soil stiffness in T-NS-Cover appeared to have increased the magnitude of dynamic earth pressures compared to T-NS. Even though the magnitude of seismic earth pressures and thrust was not significantly different in T-SS and T-NS-Cover in most cases, ΔK_E was smaller in T-SS due to compaction that increased soil's total unit weight. Neither the ultimate nor the peak ΔK_E based on

the NCHRP 611 method compared well with the experimental data in the range of far-field PGA's tested.

The reliability of pressure sensors, however, is a topic of ongoing research, and therefore it is important to also evaluate bending moments (obtained from strain gauges) in parallel, which are affected by seismic lateral earth pressures and wall inertia simultaneously.

Bending Strains and Moments

Bending strains were measured on both walls during all four tests with strain gauges. Static bending strains increased near the top of the buried structure when soil cover was added in T-NS-Cover compared to T-NS, as shown in Figure 4-32. Tensile surface strain due to bending (i.e., wall curvature outward) is shown as positive in this figure. Strain gauge recordings during earthquake loading did not indicate any permanent change in strains for the type of structures evaluated in this study. The dynamic increment of bending moment (ΔM_E) along the wall was subsequently calculated from the corresponding strain values, as shown in Figure 4-33. The tactile sensors had a separate data acquisition system from other sensors. Therefore, to avoid possible errors associated with time synchronization of responses, dynamic moments (ΔM_E) are reported at the time of maximum moment as opposed to maximum thrust obtained from tactile sensors.

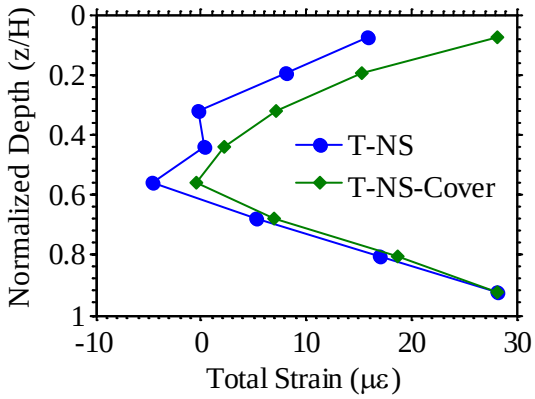

Figure 4-32. Effect of soil cover on static bending strains on the walls of the underground structure comparing T-NS and T-NS-Cover.

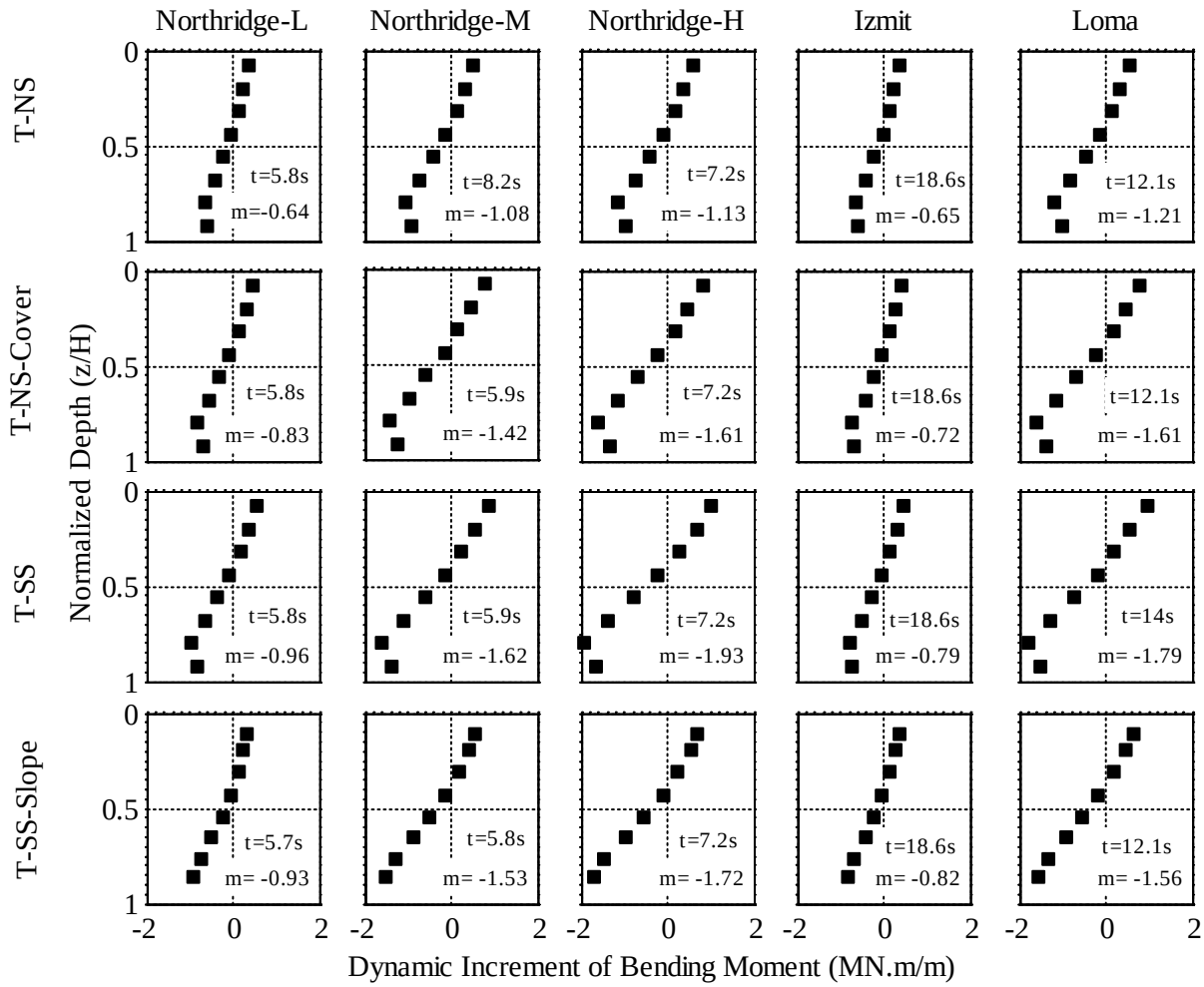

Figure 4-33. Dynamic increment of bending moments (ΔM_E) on the south wall of tests T-NS, T-NS-Cover, T-SS, T-SS-Slope at the time of maximum moment during different motions.

The shape of the ΔM_E profile along the wall was roughly linear in the four tests during all motions, with its peaks near the fixed connections with the roof and base of the reservoir structure. The magnitude of ΔM_E increased slighlty from T-NS to T-NS-Cover, with the added overburden of the soil cover and the increased stiffness of the backfill soil. The change in soil properties did not significantly change ΔM_E in T-SS compared to T-NS-Cover. There was, however, a slight reduction in ΔM_E from T-SS to T-SS-Slope near the top of the wall due to the presence of a sloped backfill, as expected, due to reduce mass near the top. These trends were consistent with those of $\Delta \sigma_E$.

CONCLUSION

Dynamic centrifuge tests were performed on stiff-unyielding, buried reservoir structures to consider the influences of soil cover, backfill soil type, and a sloped backfill on soil-structure interaction, racking deformations, seismic lateral earth pressures, and bending strains and moments in the structure. The primary conclusions of this paper are as follows:

7. In experiments involving dry, medium-dense Nevada sand, accelerations were amplified on the buried structure compared to the far-field soil at shallow depths near the predominant frequency of the base motion. Adding the soil cover and stiffness reduced the independent movement of the structure and hence the amplification of accelerations compared to the far-field soil. The compacted, site-specific, silty sand backfill with a similar cover further limited the independent movement of the buried structure due to soil's greater stiffness, where the structure accelerations primarily followed those of the far-field soil.
8. The increased backfill soil stiffness and flexibility ratio after subsequent shaking together with an added shallow soil cover increased the structure's racking response slightly. Using a compacted, partially saturated backfill increased the soil's stiffness further to a value near the racking stiffness of the structure in this case (i.e., $F \approx 1$). Hence, the structure's racking deformation approached that of the far-field soil (i.e., $R \approx 1$). The addition of a sloped backfill slightly reduced the racking of the structure compared to the case without a slope.
9. The frequency content of dynamic thrust on the walls of the buried structure was often roughly similar to its acceleration, because they were both affected by site response as well as structure's fixity, stiffness relative to soil, and inertia. Both dynamic thrust and acceleration showed a peak near the effective fundamental frequency of the site, pointing to the critical importance of site response on seismic earth pressures. Kinematic interaction

also influenced the observed dynamic thrust where the wavelength to structure height ratio ($\lambda/H_{structure}$) ranged from approximately 3 to 5. The impact of structural inertia alone on its response was likely minor during these experiments.

10. The addition of a shallow soil cover slightly increased seismic earth pressures ($\Delta\sigma_E$) on the structure near its roof. The additional density, stiffness, and apparent cohesion of the site-specific, compacted silty sand slightly increased $\Delta\sigma_E$ near the center and decreased $\Delta\sigma_E$ near the roof and base of the structure. The increased strength of the backfill soil led to a phase difference in $\Delta\sigma_E$ time histories along the height of the wall (i.e., when $\Delta\sigma_E$ peaked near the center, it approached lower values near the top and bottom). But, the additional soil stiffness and apparent cohesion did not have a significant influence on seismic earth thrust, which averages the $\Delta\sigma_E$ distribution along the wall, while it shifted its centroid upward slightly. These results combined with previous studies indicate that soil cohesion has a minor effect on seismic earth thrust, regardless of the kinematic constraints or flexural rigidity of the wall. The sloped backfill caused the dynamic lateral earth pressures to decrease near the top and its centroid to move downward, because of the reduction in soil mass and inertia near the surface.
11. The trends in dynamic bending moments acting on structure walls (ΔM_E) were in line with those of $\Delta\sigma_E$. The addition of a soil cover and backfill soil stiffness increased the magnitude of ΔM_E, particularly near the bottom of the wall. The change in soil properties in the site-specific soil did not significantly affect the magnitude of ΔM_E, but increased it slightly near the bottom of the wall. The sloped backfill, on the other hand, decreased ΔM_E near the top of the wall, because of less confinement.

The methods commonly used to evaluate the response of underground and retaining structures in terms of deformation, magnitude and distribution of seismic earth pressures, and bending moments do not adequately consider the range of backfill soil properties, flexural stiffness, kinematic constraints, and ground motions for which critical underground reservoir facilities must be designed. The experimental results presented in this paper are intended to provide important insights into the influence of backfill soil on the seismic performance of a class of stiff-unyielding buried structures with translational and rotational restraints at the top and bottom. Parallel nonlinear numerical simulations with additional variations are, however, necessary and underway before the results can be used to provide general recommendations for practice.

4.4 Journal Paper 3: Journal of Soil Dynamic and Earthquake Engineering (Status: Under Review)

A Centrifuge Study of the Influence of Site Response, Relative Stiffness, and Kinematic Constraints on the Seismic Performance of Buried Reservoir Structures

A. Hushmand[17], S. Dashti[18], C. Davis[19], J.S. McCartney[20], B. Hushmand[21]

ABSTRACT: The seismic performance of underground reservoir structures depends on the properties of the structure, soil, and ground motion as well as the kinematic constraints imposed on the structure. This paper seeks to understand the influences of site response, structural stiffness, base fixity, and excitation frequency on the performance of buried structures through the evaluation of results from four dynamic centrifuge experiments on relatively stiff and unyielding reservoir structures buried in dry, medium-dense clean sand. The magnitude of seismic thrust increased and the distribution of seismic earth pressures changed from approximately triangular to parabolic with increasing structural stiffness. Heavier and stiffer structures also experienced increased rocking and reduced flexural deflection. Fixing the base of the structure amplified the magnitudes of acceleration, seismic earth pressure, and bending strain compared to tests where the structure was free to translate laterally, settle, or rotate atop a soil layer. The frequency contents of transient tilt, acceleration, dynamic thrust, and bending strain measured on the structure was strongly influenced by the frequency content of the base motion and site response, while it was unaffected by the fundamental frequency of the structure ($f_{structure}$). None of the available simplified procedures could capture the distribution and magnitude of seismic earth pressures experienced by

[17] Graduate Student Researcher, University of Colorado Boulder, Civil, Env. and Arch. Engineering, Boulder, CO.
[18] Assistant Professor, Univ. of Col. Boulder, Civil, Env. and Arch. Eng., Boulder, CO, shideh.dashti@colorado.edu.
[19] Resilience Program Manager, Los Angeles Department of Water and Power, Los Angeles, CA.
[20] Associate Professor, Univ. of California at San Diego, Department of Structural Engineering, San Diego, CA.
[21] President and Principal Engineer, Hushmand Associates, Inc., Irvine, CA.

this class of underground structures. The insight from this experimental study is aimed to help validate analytical and numerical methods used in the seismic design of reservoir structures worldwide.

INTRODUCTION

The seismic response of stiff-unyielding underground structures with minimum to no soil overburden is a fairly new topic at the interface between geotechnical and structural engineering. Buried structures can be classified as stiff-unyielding structures when their deformation or rotation is limited during seismic events unlike cantilever retaining walls due to the kinematic constraints at their roof or base, while they are not completely rigid and deform according to their stiffness. The majority of previous analytical, numerical, and physical model studies on the seismic response of buried structures focused on either yielding or rigid-unyielding underground structures (e.g., Okabe 1926; Mononobe and Matsuo 1929; Seed and Whitman 1970; Wood 1973; Veletsos and Younan 1994; Davis 2003; Ostadan 2005; Stadler 1996; Dewoolkar et al. 2001; Al Atik and Sitar 2010; Mikola 2012). However, a number of important buried structures such as nuclear facilities, bunkers, culverts, and water reservoirs can be categorized as stiff-unyielding. The focus of this paper is on the seismic response of this type of structures, particularly focusing on the buried water reservoirs being built by the Los Angeles Department of Water and Power.

The seismic forces and deformations experienced by stiff-unyielding underground structures are not well understood. Soil-structure interaction near these structures is governed by the dynamic properties of the structure and backfill soil as well as the imposed kinematic constraints on the structure and the intensity, duration, and frequency content of the earthquake motion (Hushmand et al. 2016; Brandenberg et al. 2015). The available simplified procedures for buried structures introduced by Mononobe-Okabe (Okabe 1926; Mononobe and Matsuo 1929), Seed-Whitman

(Seed and Whitman 1970), or Wood (1973) do not consider all of these effects. Although advanced numerical tools can take these effects into account, they may lead to complexities that require validation against the results from field observations or physical model studies.

Several of the previous experimental studies primarily focused on either yielding retaining structures (Stadler 1996; Al Atik 2010; Mikola 2012) or flexible tunnels with large overburden (e.g., Cilinger and Madhabhushi 2011; Tsinidis et al. 2015). However, the seismic response of these structures is different from the stiff-unyielding structures with shallow or no overburden considered in this study. In response to this shortcoming, a series of dynamic centrifuge tests were recently conducted at the University of Colorado Boulder to evaluate the seismic performance of buried reservoirs with varying structural rigidity, soil cover, backfill soil type, backfill geometry, base fixity, and container boundary conditions. Hushmand et al. (2016 and forthcoming) summarized the insight obtained from these experiments regarding the influences of structural stiffness and the type and geometry of the backfill soil during earthquake loading. These experiments showed that stiff-unyielding buried structures could experience notable dynamic earth pressures. However, none of the available simplified procedures for buried structures was able to sufficiently capture the distribution and magnitude of seismic earth pressures or deformations experienced by the class of stiff-unyielding structures under the loading scenarios often used in their design. Further, the critical role of site response was displayed on the forces measured on the buried structures. Yet, the interacting influence of site response, structural stiffness, and base fixity on seismic forces and deformations has not yet been investigated in detail experimentally, as is necessary in the validation of future numerical tools.

The dynamic behavior of underground structures fixed to a stiff rock foundation differs greatly from structures founded on soil, since the lateral base movement is prevented. Past analytical and

numerical studies (e.g., Wood 1973; Li 1999; Richards et al. 1999; Davis 2003; Psarrapolous et al. 2005; Ostadan 2005; Brandenberg et al. 2015) showed that underground structures with a fixed base experience larger dynamic earth pressures compared to structures that can translate laterally. In addition to the magnitude of thrust, the distribution of earth pressures along the wall height can have a great influence on seismic performance. However, there is no consensus among past studies on what shape the pressure profile takes for structures with a fixed base condition, as well as those that can translate laterally. Further, the influence of the frequency content of the base motion on the forces and deformations experienced by stiff-unyielding structures, whether fixed at the base or free to translate, has not been evaluated experimentally.

This paper focuses on the effects of far-field site response, the base fixity and stiffness of the structure, and the frequency content of the base motion in relation to the fundamental frequencies of the structure and backfill soil on the dynamic behavior of stiff-unyielding underground structures. Experimental data was obtained from four dynamic centrifuge tests conducted on small-scale model structures in dry, medium dense Nevada sand with different structure stiffness, structure base fixity, and applied base motions. The model structures represented prototype reinforced concrete reservoirs having 11 to 12 m-high walls that are restrained against rotational movement at their roof and floor levels. A sequence of earthquake and sinusoidal motions with different frequencies was applied to the buried model structures in flight, and the performance of the buried structure was evaluated in terms of accelerations, seismic lateral earth pressures, and bending strains. The application of sinusoidal motions in particular allowed for a comprehensive study of the influence of loading frequency in relation to the fundamental frequency of the site and structure. The insight from these experiments is intended to guide the future modeling and design of an entire class of stiff-unyielding buried reservoir structures to withstand earthquake loading.

EXPERIMENTAL METHOD

Dynamic tests of model reservoir structures were performed at 60g of centrifugal acceleration using the 5.5 m-radius, 400 g-ton geotechnical centrifuge at the University of Colorado Boulder. The model specimens were prepared in a flexible shear beam (FSB) container developed by Ghayoomi et al. (2012; 2013). The four different centrifuge tests considered in this study are referred to as T-Flexible, T-BL (baseline), T-Stiff, and T-Fixed. T-Flexible, T-BL, and T-Stiff had the same test configuration shown in Figure 4-34a, but have different flexural rigidities of the structures, as detailed in Table 4-6. In T-Fixed, the same baseline structure as T-BL was used, which was bolted to the base of the FSB container to emulate a fixed-base condition, as shown in Figure 4-34b.

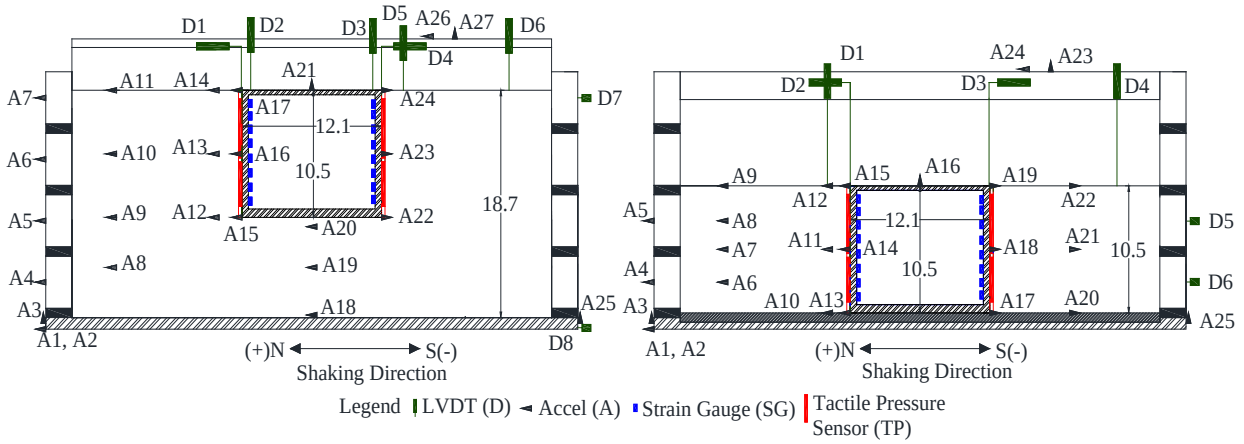

(a) (b)

Figure 4-34. Elevation views of centrifuge models in: (a) T-Flexible, T-BL, T-Stiff; and (b) T-Fixed (dimensions shown in prototype scale meters).

Dry Nevada sand No. 120 (G_s=2.65; e_{min}=0.56; e_{max}=0.84; D_{50}=0.13 mm; C_u=1.67) was placed in the FSB container at a target relative density of D_r=60% (γ_{dry}=15.6 kN/m^3). The soil deposit was pluviated in layers using a hopper at a calibrated height to achieve the target D_r. The experimentally-measured small-strain, fundamental frequency of the far-field soil column (f_{so}) was estimated prior to applying any dynamic motions using the Transfer Function (TF) of accelerations

recorded at the soil surface to those at the container base under centrifuge ambient vibrations (prior to any shaking). The estimated f_{so} corresponding to the peak TF ranged from approximately 2.1 to 2.4 Hz in experiments T-Flexible, T-BL, and T-Stiff, and was approximately 4 Hz in T-Fixed, as shown in Figure 4-35. The corresponding small-strain, average shear wave velocity of soil, $\overline{V_s}$ = 4. $f_{so}.H_{site}$, in the far-field ranged from approximately 157 to 180 m/s in T-Flexible, T-BL, and T-Stiff, and was approximately 166 m/s in T-Fixed.

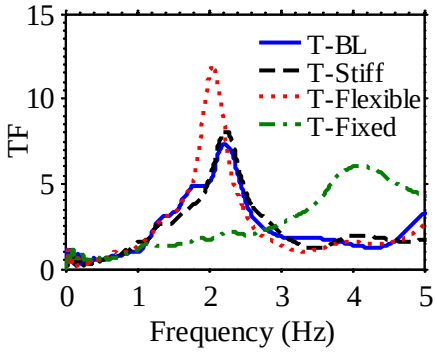

Figure 4-35. Transfer Function (TF) of surface to base accelerations in the far-field under ambient vibrations, to obtain the small-strain fundamental frequency of far-field soil (f_{so}) in four tests (T-BL, T-Stiff, T-Flexible, T-Fixed).

The model structures were designed based on a simplified version of the prototype reservoir structures by maintaining a similar natural frequency and lateral stiffness (detailed by Hushmand et al. 2016). The model structures were constructed of four pieces of welded 1018 Carbon Steel (density = 7870 kg/m^3; Young's modulus = 2×10^8 kPa). The dimensions and natural frequencies of the structures used in different tests are summarized in Table 4-6. Teflon sheets were placed on both ends of the open tubular structure to prevent the backfill sand from entering the structure, and were also placed on the sidewalls of the container to facilitate relative sliding and minimize friction and simulate plane strain conditions.

Table 4-6. Dimensions and properties of model structures used in centrifuge (prototype scale).

Test	Structure	Outer Dimensions (m)	Thickness			Fundamental Frequency (Hz)
			Base (m)	Roof (m)	Walls (m)	
T-BL, T-Fixed	Baseline	H= 10.5 W=12.1	0.69	0.37	0.56	4.0
T-Flexible	Flexible		0.50	0.28	0.28	2.0
T-Stiff	Stiff		1.46	1.12	1.13	9.9

Figure 4-34 shows the large number of sensors, including accelerometers, linearly-variable differential transformers (LVDTs), strain gauges, and tactile pressure transducers that were used to measure the seismic response of the soil-structure system. Miniature piezoelectric accelerometers were used to measure accelerations in the soil, on the structure, and on the FSB container. The settlement of soil and structures and the lateral displacement of the structure, container frames, and container base were measured using LVDTs. Eight strain gauges were mounted along each wall of the structures in a half bridge configuration to measure bending strains. Two tactile pressure sensors were installed along the height of each wall of the structures perpendicular to the direction of shaking to measure static and seismic lateral earth pressures. The tactile sensors were equilibrated, conditioned, and statically and dynamically calibrated prior to use in centrifuge, following the procedure recommended by Dashti et al. (2012), Gillis et al. (2015), and El Ganainy et al. (2014). The acceleration, displacement, and strain data were recorded at a sampling frequency of 3,000 samples per second (sps). The tactile sensors were attached to a different data acquisition system and had a sampling frequency of 4,000 sps per sensel.

The motions were applied to the container base in flight using the servo-controlled, electro-hydraulic shake table (Ketcham et al. 1991). The selected earthquake motions consisted of the following scaled horizontal records: Sylmar Converter Station of the 1994 Northridge Earthquake, the LGPC Station of the 1989 Loma Prieta Earthquake, and the Istanbul Station of the 1999 Izmit Earthquake in Turkey. The achieved base motions are referred to as Northridge-L (low intensity),

Northridge-M (medium intensity), Northridge-H (high intensity), Izmit and Loma. Figure 4-36 presents the acceleration response spectra (5% damped) of the achieved (recorded) base motions in each of the four experiments and Table 4-7 includes a summary of the ground motion properties achieved in each test, in terms of peak ground acceleration (PGA), Arias Intensity (I_a), significant duration ($D_{5\text{-}95}$), and mean frequency (f_m). As expected, the largest difference in the properties of the achieved motions was observed during T-Fixed, in which the total weight of the model specimen was significantly different from the other tests.

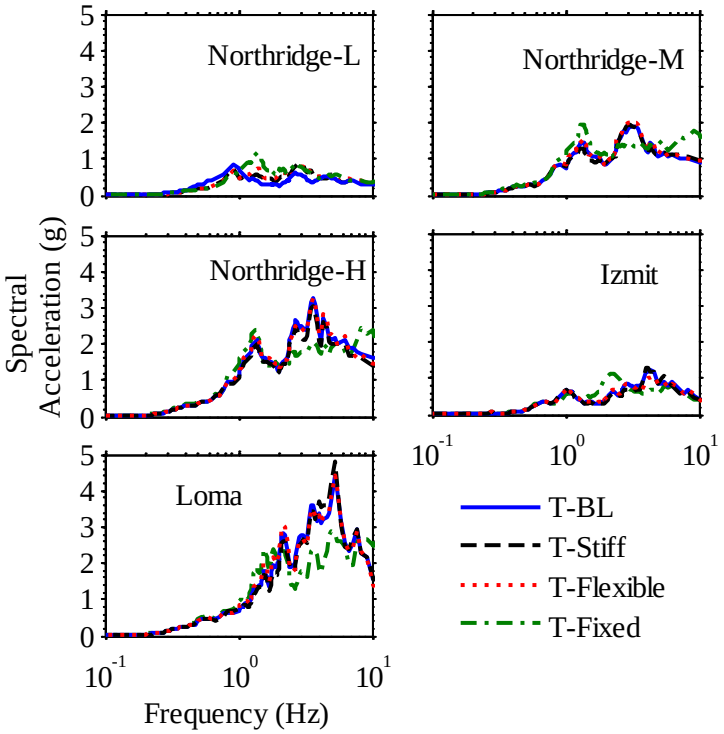

Figure 4-36. Comparison of Northridge-L, Northridge-M, Northridge-H, Izmit, and Loma achieved base motion spectral accelerations (5%-damped) in four tests: T-BL, T-Stiff, T-Flexible, T-Fixed.

Table 4-7. Ground motion properties in T-BL, T-Fixed, T-Stiff, and T-Flexible.

	Input motion parameters			
Shaking Event	PGA (g)	I_a (m/s)	$D_{5\text{-}95}$ (s)	f_m (Hz)
Northridge-L1	0.26	1.3	21.6	0.9
Northridge-M	0.73	5.8	26.7	1.5
Northridge-H	1.26	12.9	26.7	1.7
Izmit-1	0.3	2.6	37.6	1.8
Sine 0.3	0.27	3.7	36.6	0.5
Sine 1	0.31	3.4	12.8	1.2
Sine 2	0.40	3.6	6.2	2.8
Sine 3	0.44	5.2	4.1	3.1
Sine 4	0.41	3.3	3.0	4.0
Sine 5	0.92	17.8	2.4	5.0
Sine 6	0.50	4.4	2.1	5.9
Northridge-L2	0.31	1.8	18.4	1.3
Izmit-2	0.32	2.8	39.1	1.8
Loma	1.05	15.0	12.8	2.3
Sine 6.7	0.50	4.6	15.1	6.9

The earthquake motions in each test were followed by a sequence of eight sinusoidal motions with similar amplitudes (primarily ranging from 0.3 to 0.5g) but different frequencies (0.33 Hz, 1 Hz, 2 Hz, 3 Hz, 4 Hz, 5 Hz, 6 Hz). Each sinusoidal motion had fifteen cycles. These motions enabled a comprehensive evaluation of the impact of the frequency of base motion on the response of the soil-structure system. As shown in Table 4-7, two of earthquake motions were repeated after the sinusoidal motions to evaluate the response of the system after soil densification, followed by one final intense motion (Loma) and the highest frequency sinusoidal motion (6.7 Hz).

EXPERIMENTAL RESULTS

Soil Densification after Subsequent Motions

The application of successive motions changes the soil characteristics through shearing and densification, which consequently affects the accelerations, strains, and earth pressures experienced by the soil-structure system during shaking. Notable cumulative soil and structure settlements were observed after each successive ground motion in the centrifuge. Figure 4-37 shows the cumulative settlement of the structure and soil in the near- and far-field during all the

applied ground motions in one representative test (T-Flexible). The relative density of the far-field soil increased from approximately 60 to 73% during this test. The largest settlement occurred during the first three ground motions when the soil was at its loosest state. During T-Flexible, the lighter structure (as compared to the baseline and stiff structures) settled less than the adjacent soil and far-field. The settlement of the buried structure increased as its weight increased, as expected.

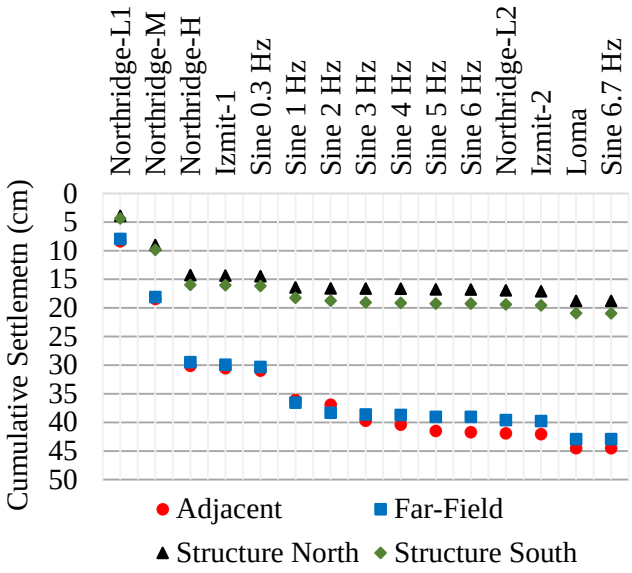

Figure 4-37. Cumulative settlement of far-field soil, adjacent to structure, and structure during T-Flexible subject to different earthquake and sinusoidal motions.

The relative density of the granular backfill soil increased from 72 to 81% and from 60 to 75% in the centrifuge experiments conducted by Al Atik (2010) and Stadler (1996), respectively. However, the influence of soil densification and seismic history could not be evaluated in these experiments because the same motion was not repeated after multiple ground motions. The Northridge-L and Izmit ground motions in the presented experiments were repeated towards the end of the test (Table 4-7), which are referred to as Northridge-L2 and Izmit-2, in order to evaluate

the influence of repetitive soil densification and shearing on the response of the soil-structure system.

The change in relative density (D_r) of the far-field soil was estimated to be ~12% between the Northridge-L1 and Northridge-L2 motions and 3% between the Izmit-1 and Izmit-2 motions. Figure 4-38 compares the transfer function (TF) of accelerations at the surface to base in the far-field soil during Northridge-L1 or Izmit-1 with those during Northridge-L2 or Izmit-2, which were applied after several motions. The effective, strain-dependent, fundamental frequency of the far-field soil (f_{so}') corresponding to the peak TF increased only slightly from Northridge-L1 to Northridge-L2 due to soil settlement and densification. No change was observed in soil fundamental frequency from Izmit-1 to Izmit-2 due to a smaller degree of settlement and densification.

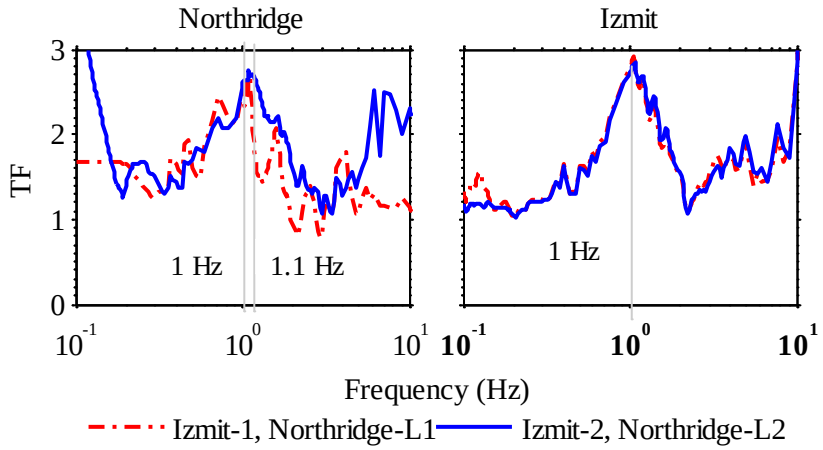

Figure 4-38. Transfer functions of surface to base accelerations in the far-field soil in T-Flexible during the two sets of Izmit and Northridge-L motions.

Figure 4-39 compares the amplification in peak ground accelerations (PGAs) along the far-field soil column from the base during the two sets of Northridge-L and Izmit motions. A de-amplification of PGAs was prominent during the Northridge-L1 motion, with a looser soil column. After soil densification and subsequent shaking, during Northridge-L2, amplification of PGA was

prominent. The change in PGA amplification patterns was minimum from Izmit-1 to Izmit-2 motions, again because of minor soil densifications that occurred in between those two motions.

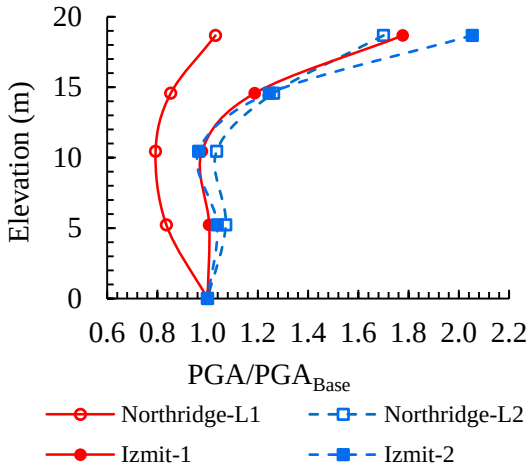

Figure 4-39. PGA ratios versus depth in T-Flexible during the two sets of Izmit and Northridge-L motions.

The dynamic increment of lateral earth pressures recorded on each structure during the two sets of Northridge-L and Izmit motions at the time corresponding to peak dynamic thrust is compared in Figure 4-40. In general, the distribution and magnitude of seismic earth pressures were consistent during the two sets of motions, increasing slightly during the second set primarily due to densification. There was, however, one exception. As will be discussed in more detail in later sections, the distribution of seismic earth pressures was generally observed to change from linearly increasing with depth to a higher order polynomial as the structure's flexural stiffness was increased (Hushmand et al. 2016). However, the flexible structure during T-Flexible, Northridge-L1 did not show the linearly increasing trend that was expected based on trends observed in the other tests and motions. This may be because of looser soil conditions near the wall face in this particular test leading to less contact between the backfill soil and the wall (or sensor) prior to the first motion. However, the distributions of earth pressures immediately following the first motion were more linear during T-Flexible due to the densification effect mentioned earlier. The influence

of soil densification on the dynamic response of underground structures can also be evaluated in terms of dynamic strain profiles at the time of maximum moment (or strain), as shown in Figure 4-41. The dynamic increment of strain was consistently slightly larger during the Northridge-L2 motion compared to L1. The change was negligible during the Izmit motions, as expected, with little soil densification between the two shakes.

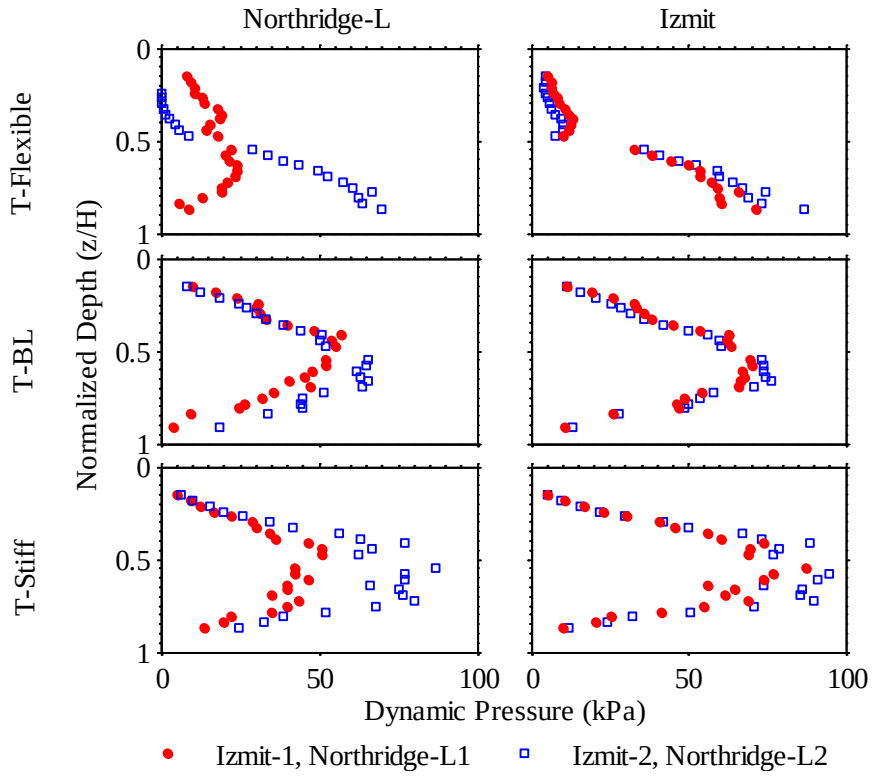

Figure 4-40. Dynamic increment of earth pressures ($\Delta\sigma_E$) at time of maximum thrust during the two sets of Northridge-L and Izmit motions in T-Flexible, T-BL, and T-Stiff.

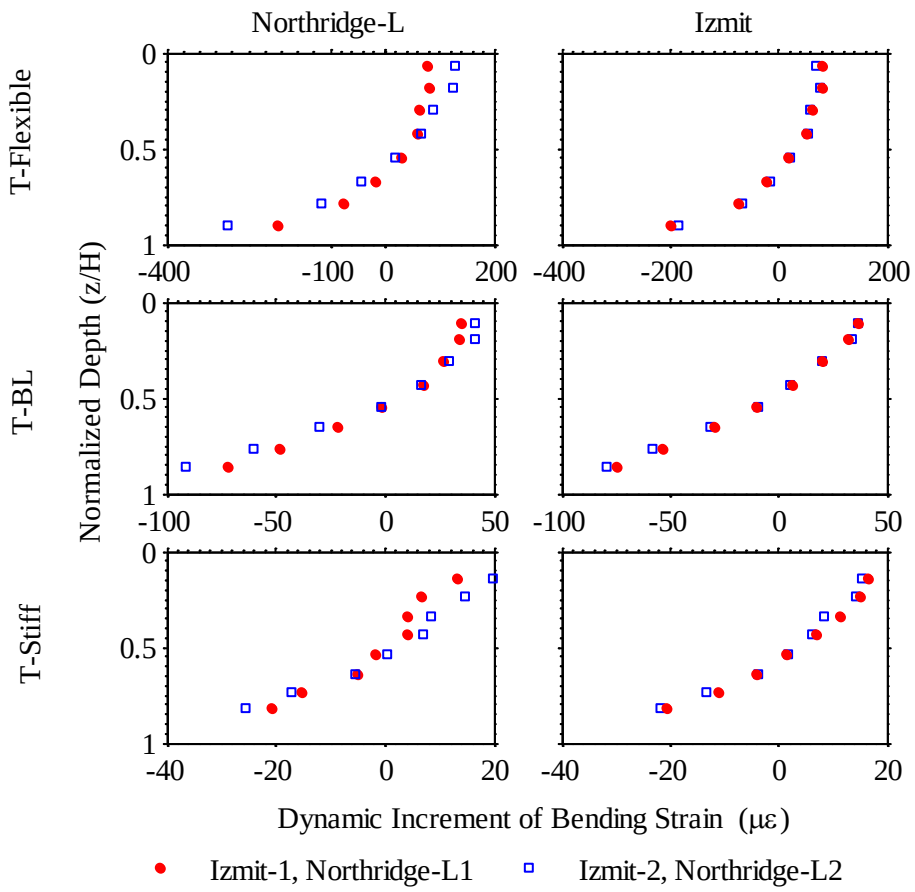

Figure 4-41. The dynamic increment of bending strains ($\Delta\varepsilon_E$) at the time of maximum moment during the two sets of Northridge-L and Izmit motions in T-Flexible, T-BL, and T-Stiff.

Accelerations

The transfer functions of far-field soil surface to container base accelerations as well as structure roof to container base accelerations for the different structures and earthquake motions are shown in Figure 4-42. The highlighted area shows the approximate range of effective, strain-dependent, fundamental frequencies (f_{so}') of the far-field soil and the soil-structure system. The f_{so}' ranged from approximately 0.92 to 1.3 Hz during T-BL, T-Stiff, and T-Flexible for both the far-field soil column and the soil-structure system. The estimated f_{so}' in T-Fixed ranged from approximately 2.2 to 3.5 Hz. The fundamental frequency of the buried structure-soil system was

primarily controlled by the response of the far-field soil rather than the fixed-base fundamental frequency of the isolated structure.

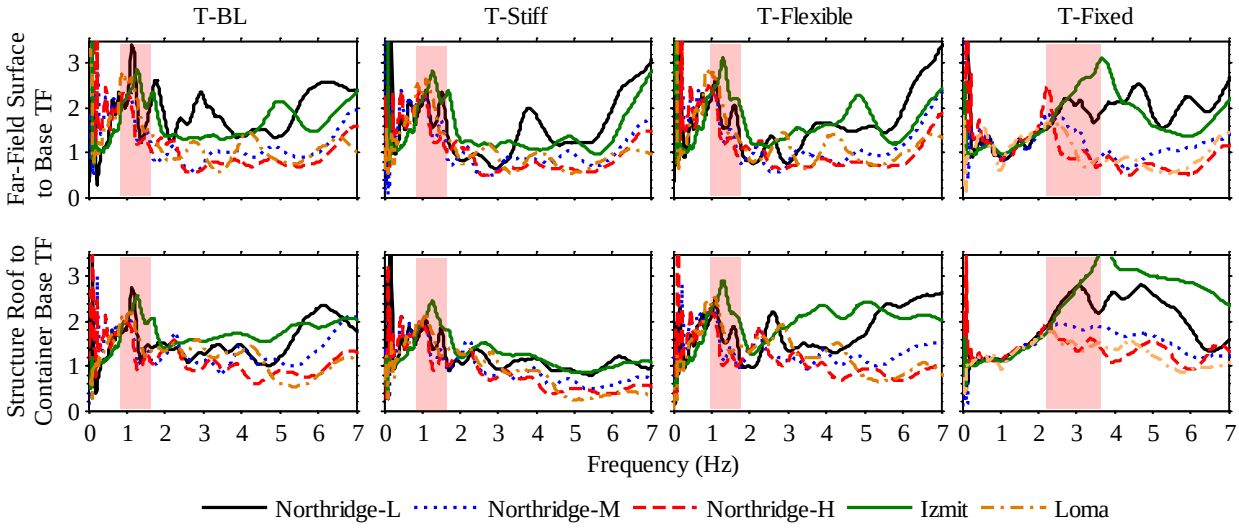

Figure 4-42. Transfer functions of far-field surface to container base as well as structure roof to container base accelerations during different experiments and earthquake motions. The highlighted area marks the range of effective, strain-dependent, fundamental frequencies (f_{so}') near the peak values of TF.

The amplification or de-amplification of peak accelerations from the base of the container to the soil surface in the far-field or to the structure roof in T-BL, T-Flexible, T-Stiff, and T-Fixed during the different earthquake motions are shown in Figure 4-43. The base motion accelerations were amplified at the lower levels of shaking ($PGA_{base} \sim 0.3g$) and started to de-amplify at higher levels of shaking ($PGA_{base} > 0.6g$), as expected, due to additional soil nonlinearity and damping. Larger accelerations were recorded on the structure in T-Fixed compared to the other experiments that allowed transient rocking, settlement, and damping of seismic energy.

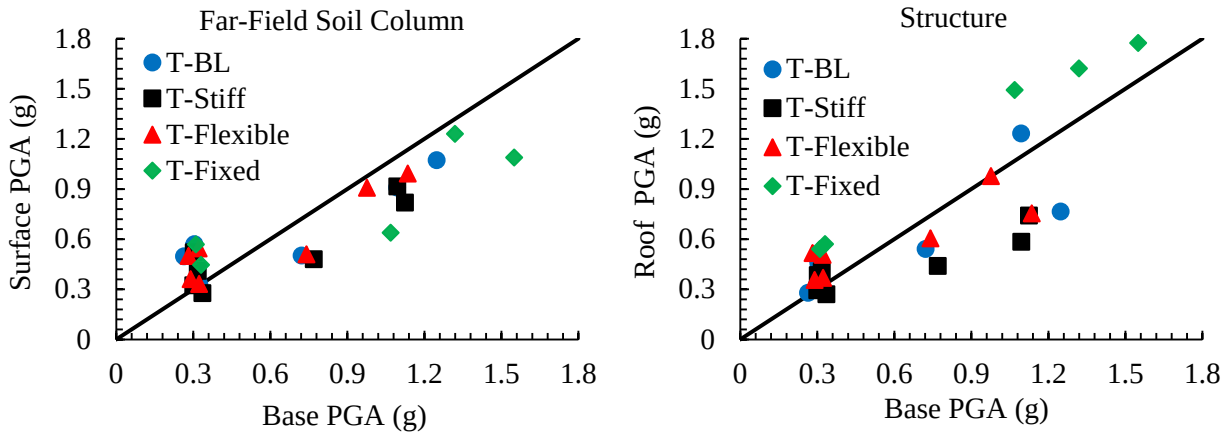

Figure 4-43. Base motion amplification/de-amplification of peak ground acceleration (PGA) in: (a) the far-field soil; and (b) on the four structures (BL, Stiff, Flexible, Fixed) during different earthquake motions.

The spectral ratios of acceleration at the top of the structure to those in the far-field soil in each test during different earthquake motions are compared in Figure 4-44. Overall, the acceleration response of the structure was amplified compared to the far-field in frequencies ranging from about 2 to 5 Hz for all motions and structures. Increasing the flexibility of the structure often slightly increased its acceleration amplification with respect to the far-field due to a greater deflection near the roof. The spectral ratio of the structure in T-Fixed was greater compared to the other three tests, because of the kinematic constraint imposed at the base of the structure, amplifying its acceleration more pronouncedly relative to the far-field soil.

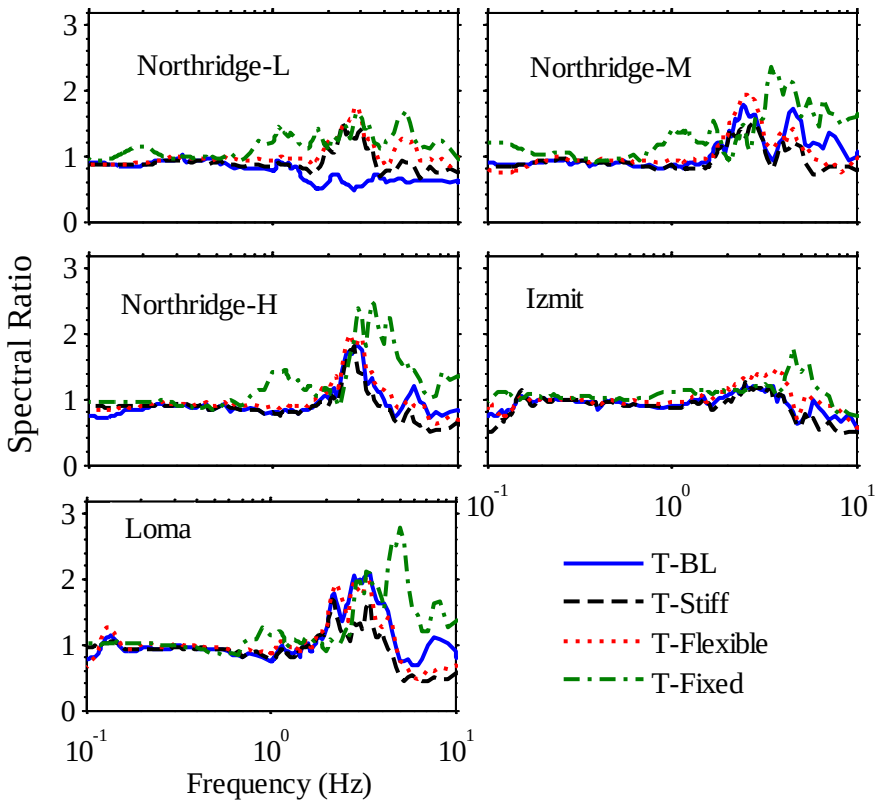

Figure 4-44. Spectral ratio (5% damped) of structure to far-field accelerations at the elevation corresponding to the roof of the structure in four tests (T-BL, Flexible, Stiff, Fixed) during different earthquake motions.

Structural Tilt

The time histories and Fourier Amplitude Spectra of tilt measured on the three structures with a flexible base (i.e., T-Flexible, T-BL, and T-Stiff) during three representative shaking events (Northridge-L, Northridge-M, Northridge-H) are compared in Figure 4-45. The tilt of the structure was obtained by dividing the difference in the recordings of vertical LVDTs on the edges of the structure roof (D2 and D3) by the width of the structure. The degree of structural tilt or rocking was observed to amplify as the shaking intensity increased, as expected. Increasing the structural mass (i.e., from Flexible to BL to Stiff) consistently increased its transient and residual tilt during all shaking events, which was expected due to a greater inertia and seismic moment that would amplify the rocking response of the buried structure. The frequency content of the structural tilt was observed to be similar among the different tests, however. The primary frequency content of

structural tilt was observed at approximately 1 Hz, which was near the mean frequency of the base motion (f_m) as well as the site's effective fundamental frequency (f_{so}') during these experiments and motions, regardless of variations in the fundamental frequency of the isolated structure. The rocking response of the structure was expected to influence the distribution and amplitude of lateral earth pressures, which is discussed in more detail in the following section.

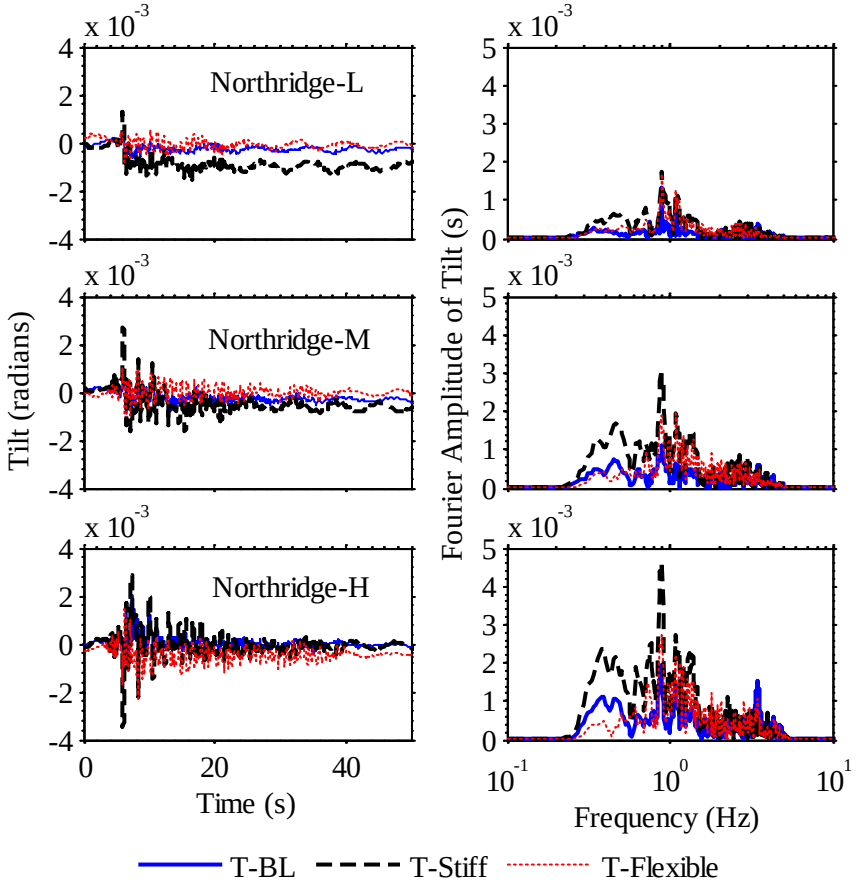

Figure 4-45. Time histories and Fourier Amplitude Spectra of structural tilt in T-Flexible, T-BL, and T-Stiff during the Northridge motions.

Seismic Earth Pressures

The dynamic increment of pressure ($\Delta\sigma_E$) was obtained directly from tactile pressure sensors by subtracting the pre-shake static pressure from the total value at a given depth. Dynamic thrust acting on each structure during a given motion was estimated by numerically integrating the dynamic distribution of earth pressures at each instance of time. The values of $\Delta\sigma_E$ at the time of

maximum dynamic thrust in four tests (T-BL, T-Stiff, T-Flexible, T-Fixed) during different earthquake motions are compared in Figure 4-46. A few of the most common analytical methods used to calculate dynamic earth pressures on retaining structures are also plotted for comparison: Mononobe-Okabe (M-O) and Seed-Whitman (S-W) assuming yielding (or active) conditions, and Wood, assuming rigid-unyielding conditions.

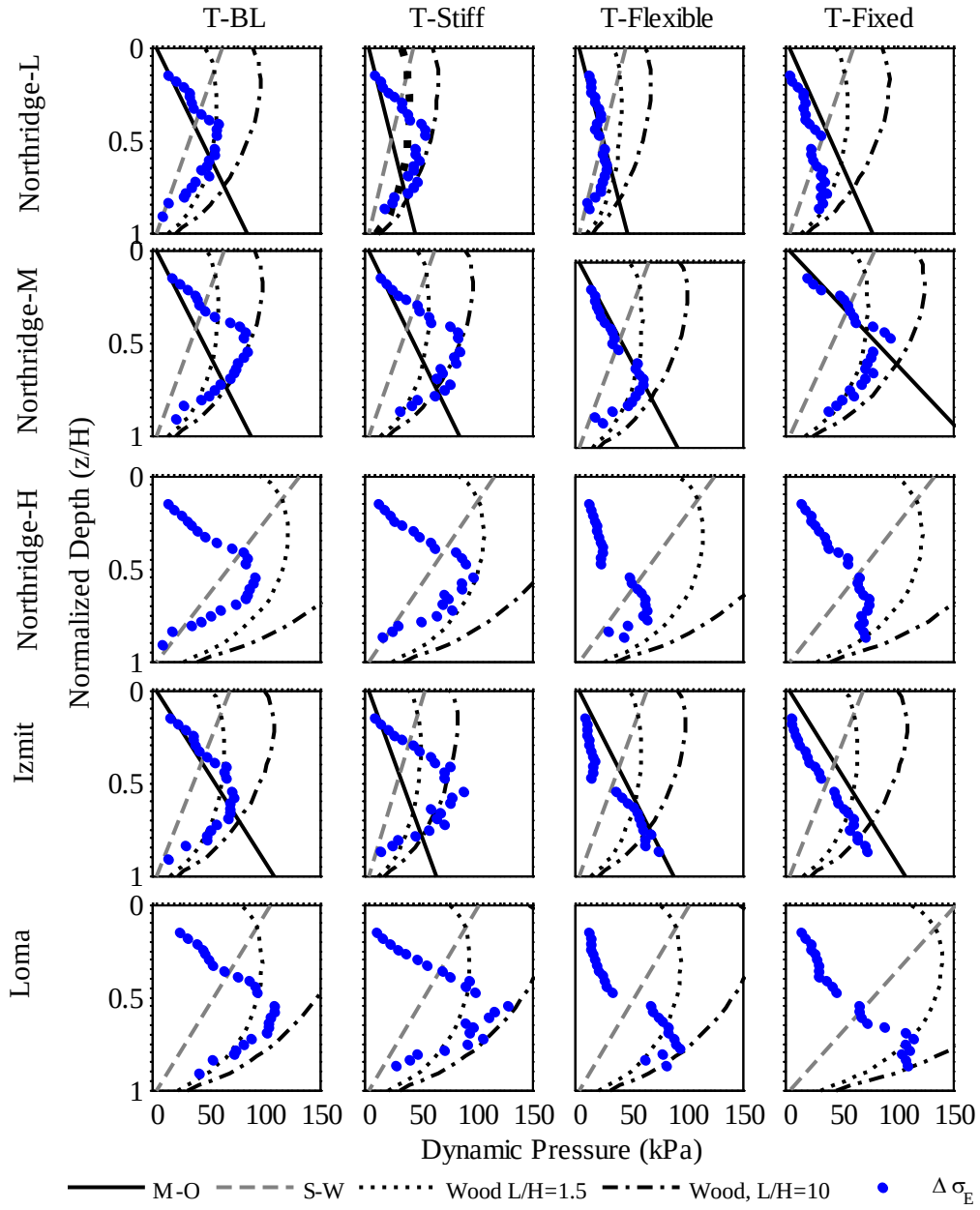

Figure 4-46. Dynamic increment of earth pressure ($\Delta\sigma_E$) at the time of maximum thrust during four experiments (T-BL, T-Stiff, T-Flexible, T-Fixed) compared to the M-O, S-W, and Wood analytical methods.

To obtain analytical solutions of seismic earth pressures during each motion, 100% of the PGA recorded in the far-field soil surface (i.e., using sensor A9 in T-Fixed and A11 in the other tests) was employed. The M-O method provided indeterminate values of earth pressure at PGA values greater than 0.7g for a soil friction angle of 35°. Therefore, the M-O solution is not presented in

Figure 4-46 during the Northridge-H and Loma motions. The S-W procedure uses an inverted triangle dynamic earth pressure profile, as shown in Figure 4-46. Wood's simplified procedure was computed based on an L/H ratio of 1.5 corresponding to the centrifuge tests, but was also computed based on a larger L/H of 10 to provide an upper bound for comparison, where L is the lateral extent of the backfill soil and H the wall height. Wood's procedure does not take into account the increase in soil shear modulus with depth and therefore predicted large $\Delta\sigma_E$ values near the top of the wall compared to those observed.

The distribution of $\Delta\sigma_E$ in experiments T-BL, T-Stiff, and T-Flexible depended greatly on the flexural rigidity of the structure, as also confirmed by other studies (Veletsos and Younan 1997; Gazetas et al. 2004; Psarropoulos et al. 2005; Jung and Bobet 2008). Increasing the flexibility of the structure (e.g., T-Flexible compared to T-BL and T-Stiff) tended in general to change the distribution of $\Delta\sigma_E$ from a parabola to an approximately triangular distribution mainly increasing with depth. The fixed structure in T-fixed experienced higher $\Delta\sigma_E$ values near the base compared to BL structure, because the energy of the shake table was transferred directly to the structure without being damped by lateral or rocking movement of the foundation. This observation is consistent with the numerical results presented by Psaropoullos (2005). Importantly, none of analytical solutions could sufficiently capture the distribution and magnitude of seismic earth pressures experienced on this class of underground structures in a consistent manner.

Time histories of the dynamic increment of lateral earth pressure at the top, middle, and bottom of the structures during four representative earthquake and sinusoidal motions (e.g., Northridge-L, Northridge-H, Sine 1 Hz, Sine 2 Hz) in each test are compared in Figure 4-47, with the time corresponding to maximum thrust marked. In general, the $\Delta\sigma_E$ time histories were observed to be in phase along the height of the wall for the stiffer structures (T-BL, T-Stiff, and T-Fixed). The

more flexible structure in T-Flexible, however, experienced $\Delta\sigma_E$ time histories that were slightly out of phase. The pressures peaked near the bottom before the middle and top. This was due to larger wall deflections increasing from the base to roof of the flexible structure as shown in Figure 4-41, which contributed to the overall reduction of dynamic earth pressures and forces as compared to the other cases.

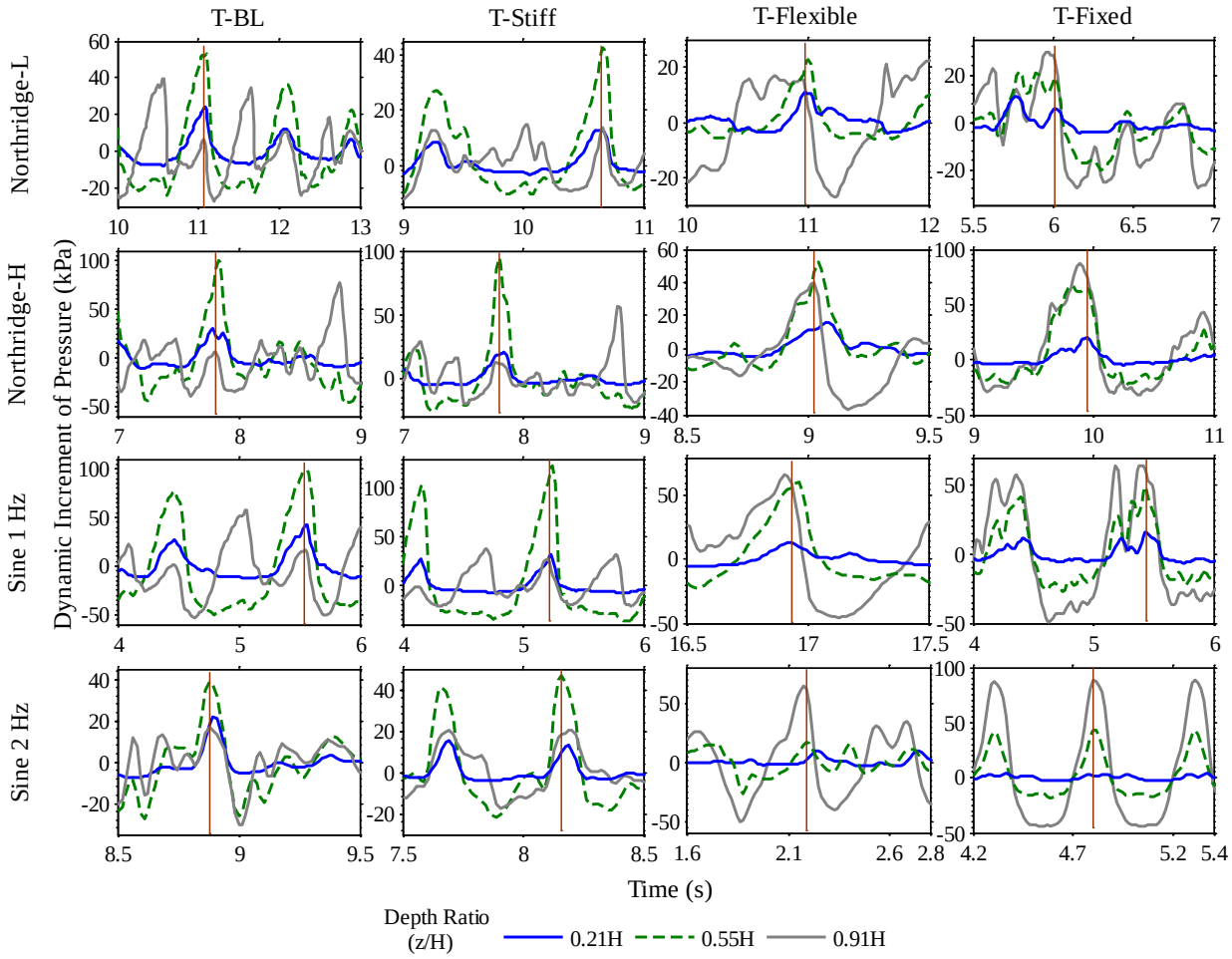

Figure 4-47. Dynamic increment of pressure time histories along top, middle, and bottom of the structure during a few representative (Northridge-L, Northridge-H, Sine 1 Hz, Sine 2 Hz) ground motions. Vertical line identifies the time of maximum dynamic thrust.

The short-time Fourier transform of accelerations recorded on the container base and mid-depth of the structure wall are compared to those of dynamic thrust during the Northridge-L motion in each of the four tests in Figure 4-48. The base acceleration contained a significant content near

1 Hz in all experiments during Northridge-L, particularly in the early part of the record. Similarly, the accelerations recorded at the mid-depth of the structure and the dynamic thrust in T-Flexible, BL, and Stiff showed maximum content near 1 to 1.5 Hz, which coincided with the effective natural frequency of the site (f_{so}') in those tests.

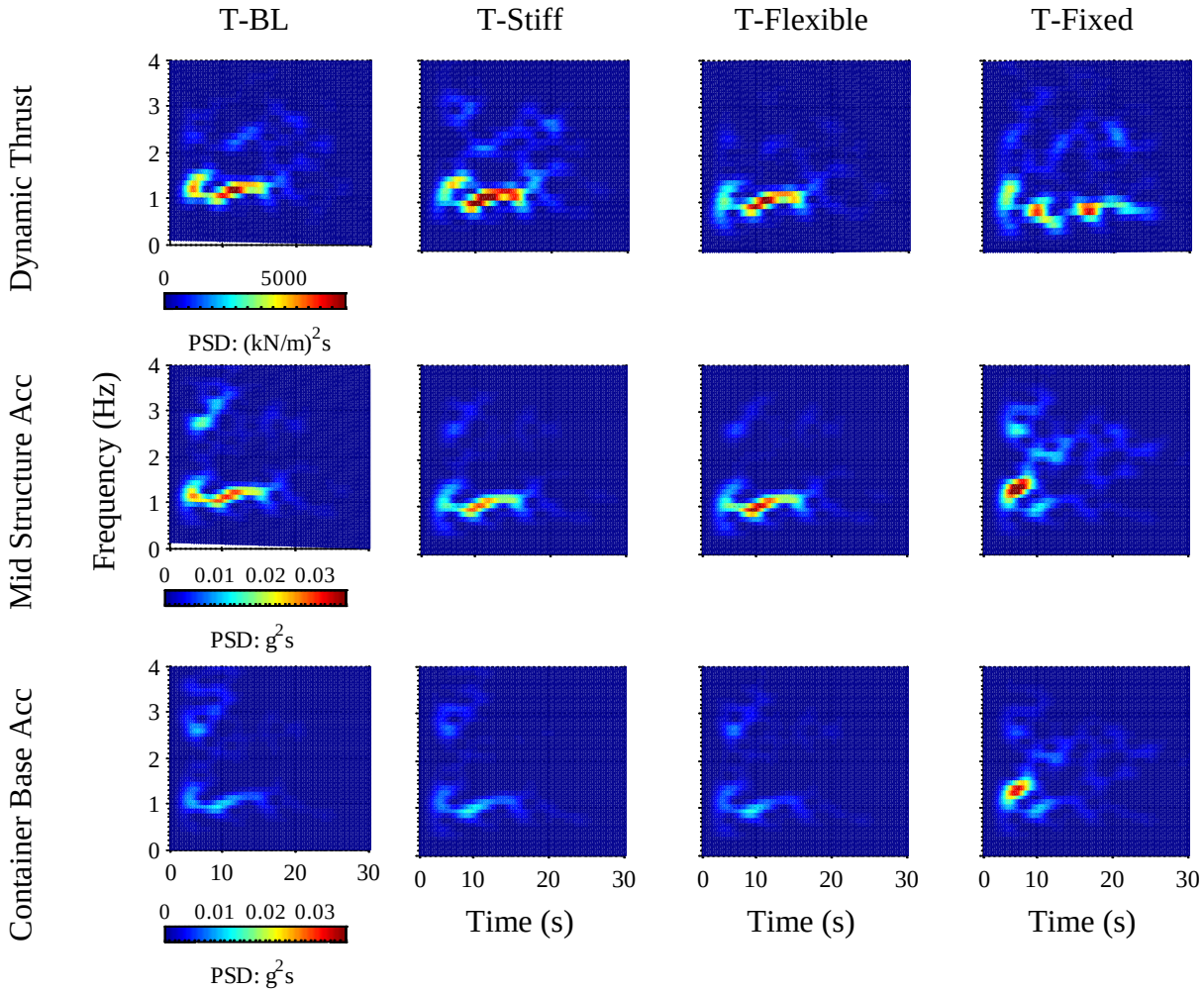

Figure 4-48. Short-time Fourier transform of container base acceleration, mid-depth structural wall acceleration, and dynamic thrust recorded on the structure in T-Flexible, T-BL, T-Stiff, and T-Fixed during the Northridge-L motion.

In T-Fixed, the f_{so}' of the shallower soil deposit ranged from approximately 2.2 to 3.5 Hz during different motions, corresponding to the peak of the surface to base transfer functions in the far-field. An important frequency content was observed in the structure's acceleration and dynamic

thrust near 2 to 3 Hz in this test, but this frequency range was not dominant. The base of the fixed structure experienced the same motion as the base of the container, with no influence from site response. However, along the height of the wall, the structure's acceleration was influenced slightly by site response, as also shown previously in Figure 4-42 and Figure 4-44. Hence, the Fourier amplitude of accelerations at the mid-depth of the wall showed amplification compared to the base near f_{so}' of approximately 2 to 3 Hz in T-Fixed. The dynamic thrust during this test also showed some content near 2 to 3 Hz corresponding to f_{so}', but the primary content was observed near 1 Hz over an extend period of time, corresponding to the mean frequency (f_m) of the base motion. The sinusoidal motions (with a narrow frequency content) allowed an easier evaluation of the impact of f_{so}' alone on the response of the structure.

The profiles of $\Delta\sigma_E$ at the time of maximum thrust are compared in Figure 4-49 for four tests (T-BL, T-Stiff, T-Flexible, T-Fixed) during sinusoidal motions with roughly similar amplitudes (mostly ranging from about 0.3 to 0.5g) but frequencies that varied between 0.33 Hz and 6.7 Hz. The shape of the $\Delta\sigma_E$ profile did not appear to have a significant dependence on the excitation frequency, and was primarily affected by the relative stiffness of the structure and base fixity, as observed previously during broadband earthquake motions. The largest dynamic pressures for all tests occurred when the base excitation frequency of the sinusoidal motion approached the far-field soil f_{so}'. In tests T-BL, T-Stiff, and T-Flexible the largest pressures were recorded at an excitation frequency of 1 Hz, near f_{so}' in those tests. The largest dynamic pressures in T-Fixed were recorded at an excitation frequency near 2 to 3 Hz, which was again near f_{so}' in that test. At higher frequencies, the dynamic increment of pressure reduced greatly compared to the resonance condition.

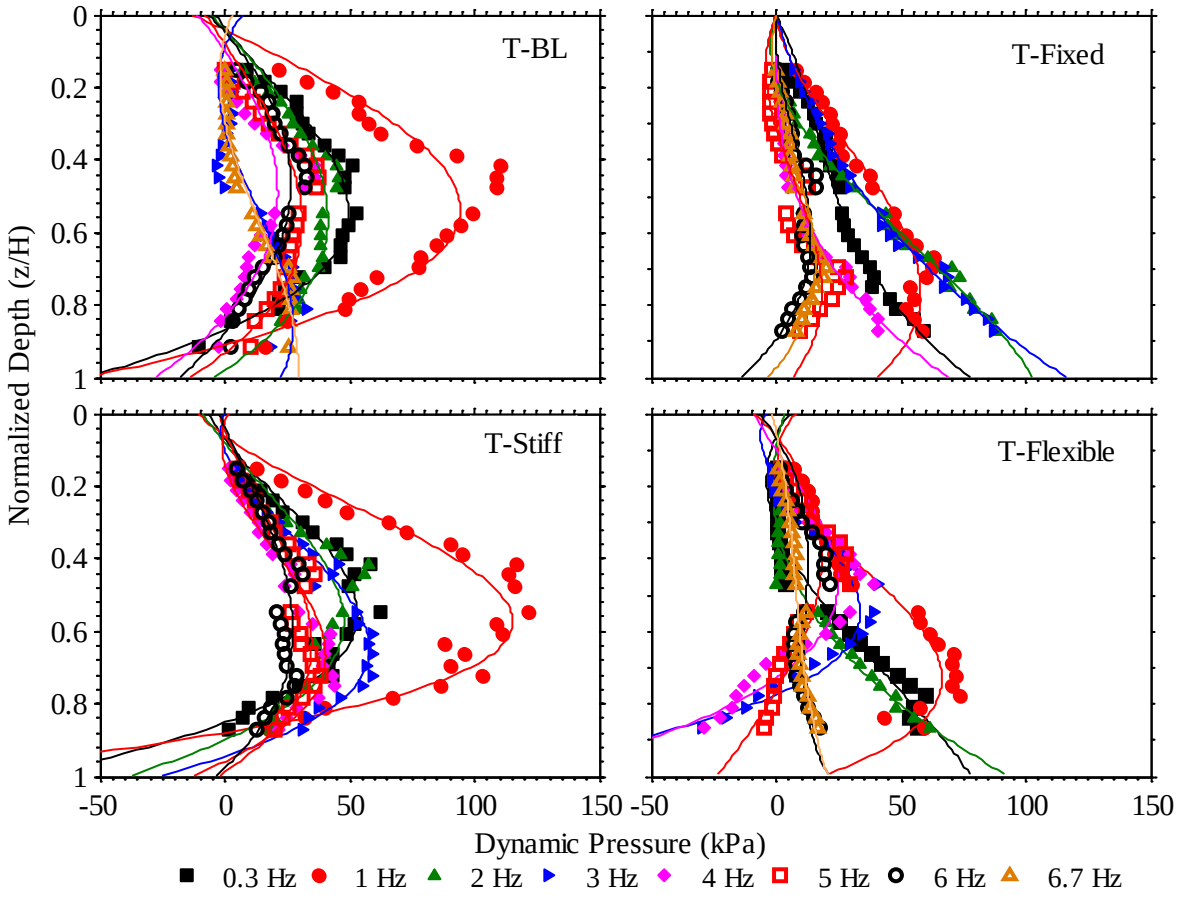

Figure 4-49. Dynamic increment of pressure ($\Delta\sigma_E$) at time of maximum thrust during four tests and eight sinusoidal motions (0.3 Hz, 1 Hz, 2 Hz, 3 Hz, 4 Hz, 5 Hz, 6 Hz, and 6.7 Hz). Note: pressure recordings were not obtained in T-Stiff during Sine-6.7Hz.

The reliability of pressure transducers for geotechnical applications is a concern to many researchers and hence, caution was taken in interpreting the results. Centrifuge tests T-BL, T-Stiff, T-Flexible, and T-Fixed were repeated and dynamic pressure readings were compared to previous results, as shown in Figure 4-50 to assess consistency and reliability of the tactile sensors in measuring dynamic earth pressures in centrifuge. The comparison shows that the pressure distributions of the old and repeat tests were quite similar in terms of magnitude and shape for a range of different ground motions.

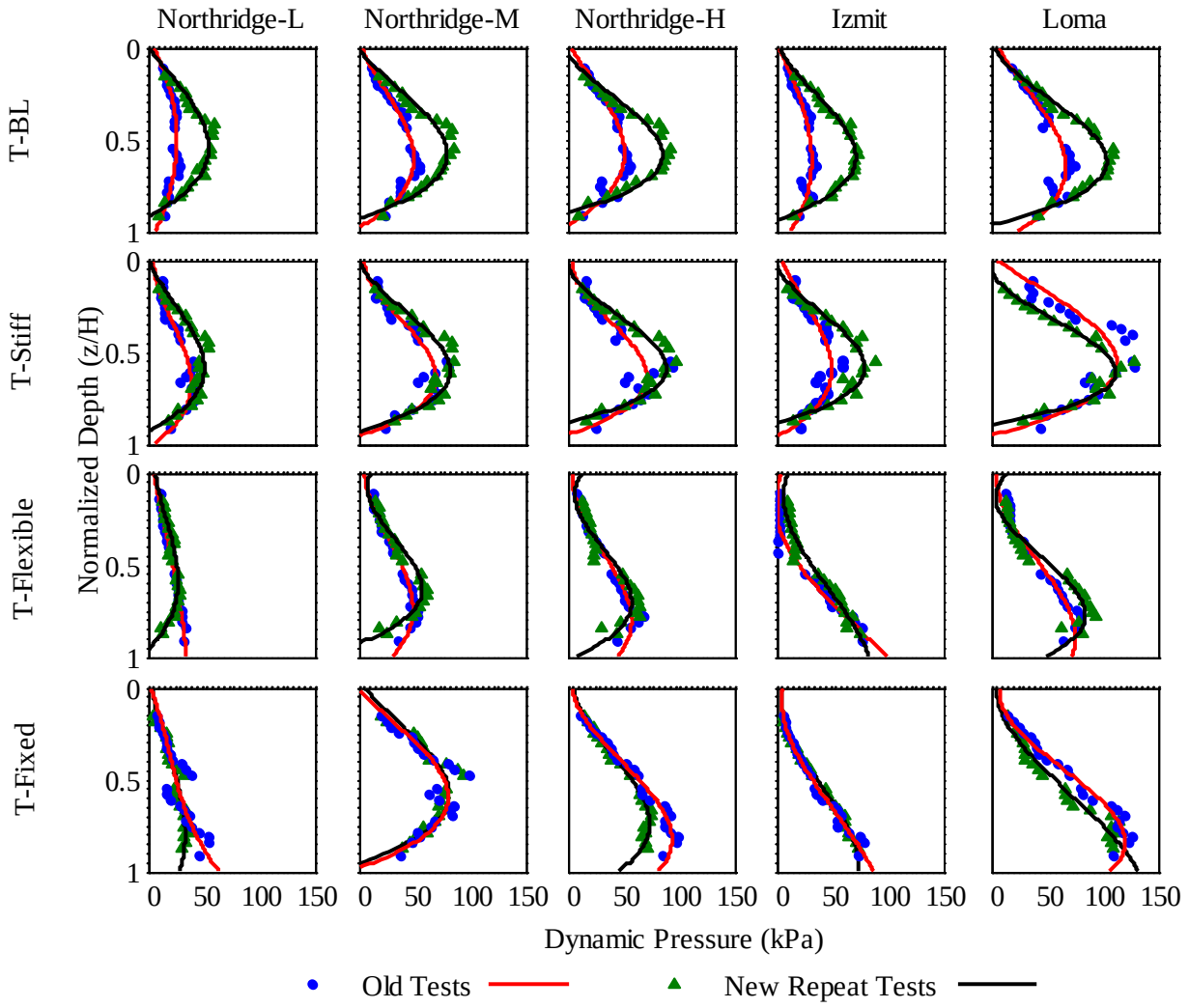

Figure 4-50. Comparison of dynamic earth pressure profiles during the first and repeat set of experiments and different ground motions.

Dynamic Strains and Racking Deformations

Bending strains were measured with strain gagues installed on the inside walls of the structures during and after each ground motion. The largest dynamic bending strains ($\Delta\varepsilon_E$) were often recorded near the base of the structure. The dynamic bending strain ($\Delta\varepsilon_E$) profiles are shown in Figure 4-51 and Figure 4-53 at the times of maximum moment (or maximum strain) during different earthquake and sinusoidal motions, respectively. Tensile surface bending strain (i.e., outward wall curvature) is shown as positive in these figures. As expected, bending strains

decreased when increasing the flexural stiffness of the structure. Additionally, fixing the base of the structure to the container in T-Fixed amplified dynamic strains (particularly at the base) compared to T-BL as shown in Figure 4-52. Similar to dynamic earth pressures in Figure 4-49, dynamic strains in Figure 4-53 were observed to peak when the excitation frequency approached the effective fundamental frequency of the site in the corresponding test (f_{so}' near 1 Hz in T-BL, T-Stiff, T-Flexible; and f_{so}' near 2 to 3 Hz in T-Fixed).

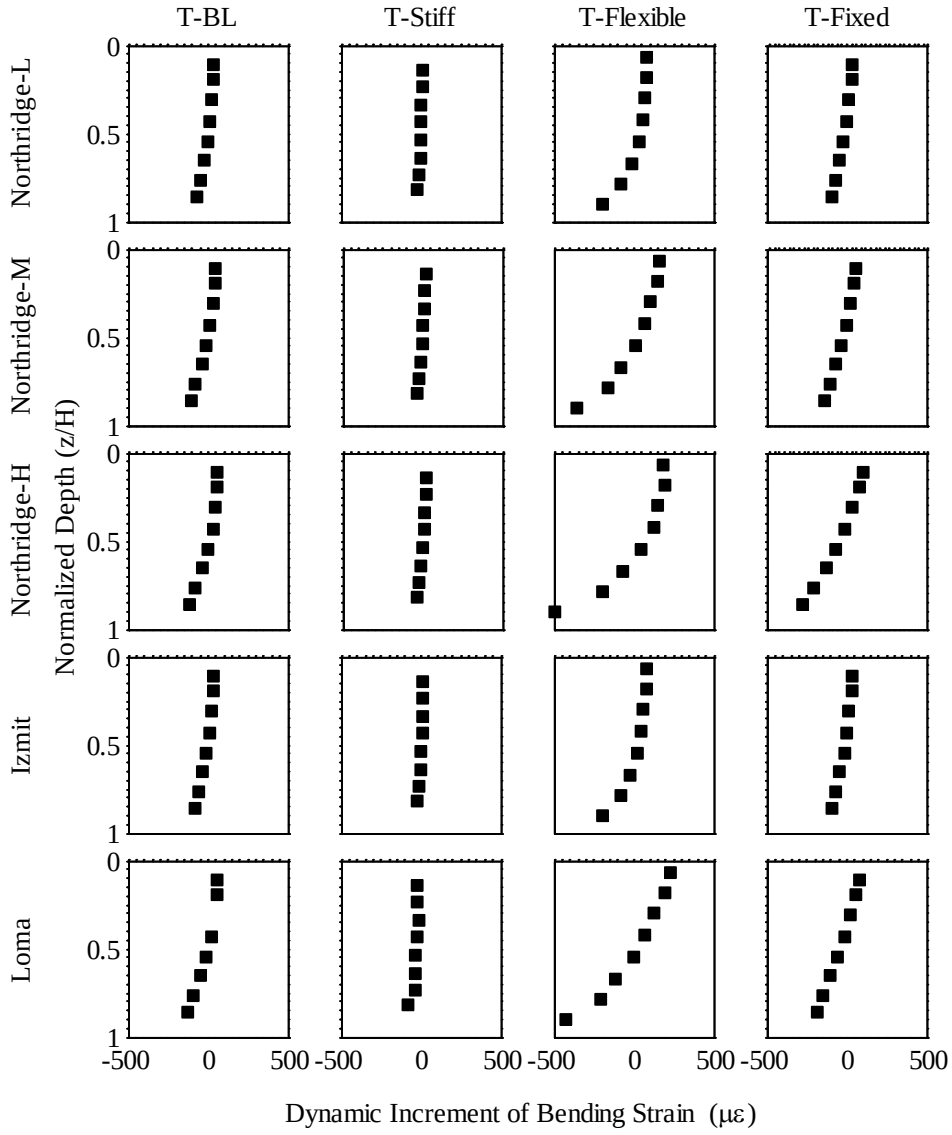

Figure 4-51. Dynamic increment of bending strain ($\Delta\varepsilon_E$) at the time of maximum moment during four experiments (T-BL, T-Stiff, T-Flexible, T-Fixed) and different earthquake motions.

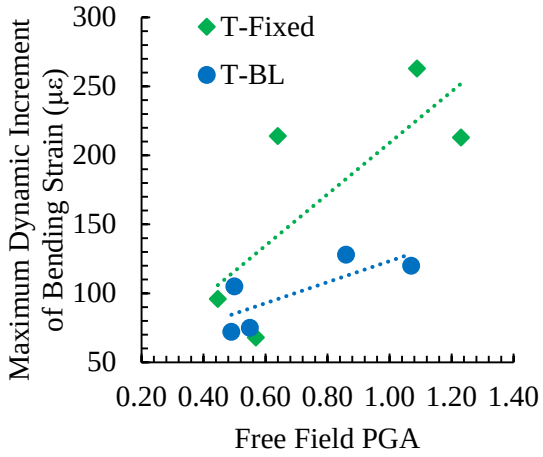

Figure 4-52. Maximum dynamic increment of bending strain at base of structure vs base PGA during T-Fixed and T-BL.

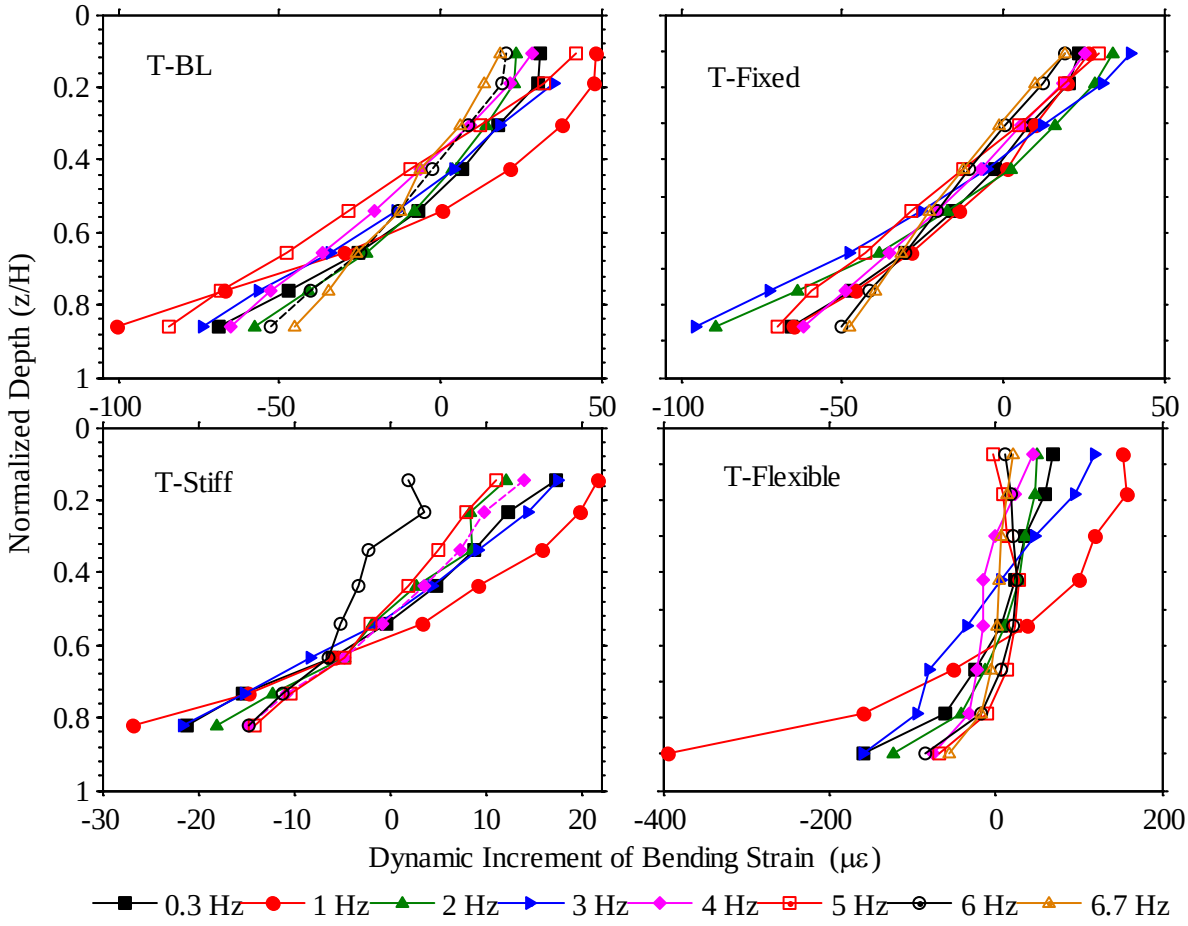

Figure 4-53. The dynamic increment of bending strains ($\Delta\varepsilon_E$) at the time of maximum moment during four tests (T-BL, T-Stiff, T-Flexible, T-Fixed) and eight sinusoidal motions with different frequencies.

The racking deformatoin of the structures was also largest (similar to dynamic strain and pressure) when the excitation frequency (around 1 Hz) was similar to the effective fundamental frequency of the site as shown in Figure 4-54 below.

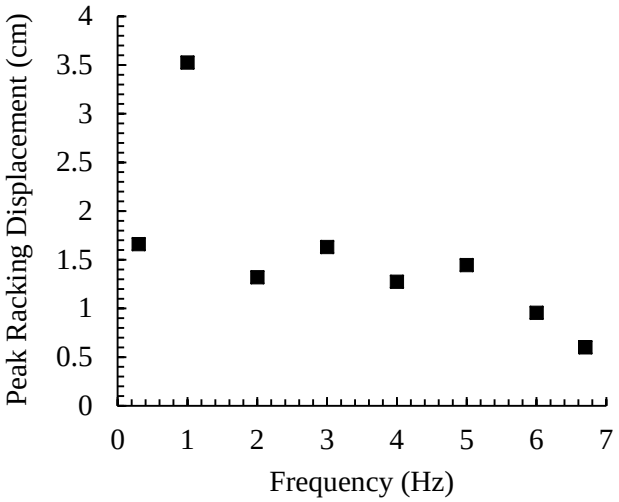

Figure 4-54. Peak structural racking for T-BL during eight sinusoidal motions with varying frequencies

CONCLUDING REMARKS

A series of dynamic centrifuge tests were conducted to study 10.5 m-high box structures with varying flexural rigidities and fixity conditions, buried in medium-dense, dry sand undergoing one-dimensional shaking. All structures had their roofs at the ground surface. The base motions consisted of various earthquake motions with PGAs ranging from 0.26 to 1.39 g and sinusoidal motions with similar amplitudes (mostly ranging from about 0.3 to 0.5g), but frequencies ranging from 0.33 Hz to 6.7 Hz. The results of this experimental study indicate the following trends:

1. Soil densification (D_r increase from approximately 60% to 72%) and shearing after multiple motions resulted in greater PGA amplifications along the far-field soil column, greater static and seismic lateral earth pressures, and slightly greater dynamic bending strains along the height of the wall, but did not noticeably influence the effective fundamental frequency of the site (f_{so}').

2. The seismic response of the buried structure fixed at the base was noticeably different from the structures resting on soil with the ability to settle or rock. The structure to far-field acceleration spectral ratios greater on the fixed structure compared to others. The dynamic strains and dynamic pressures were amplified near the base of the structure.
3. The seismic performance of the buried structure in terms of tilt, acceleration, dynamic thrust, and dynamic bending strains was influenced greatly by the frequency content of the base motion as well as far-field site response. During the sinusoidal motions (with a narrower frequency band compared to earthquake motions), the dynamic earth pressures and bending strains always peaked when the excitation frequency approached f_{so}', regardless of the fundamental frequency of the structure or base fixity. This observation points to the critical importance of site response on the performance of buried reservoir structures.
4. The magnitude of seismic thrust increased and the distribution of seismic earth pressures changed from approximately triangular to parabolic with increasing structural stiffness. The shape or distribution of dynamic earth pressures was shown as relatively independent of the excitation frequency and mainly dependent on the structure's relative stiffness and base fixity.
5. None of the analytical solutions could consistently capture the distribution and magnitude of seismic earth pressures for the range of flexural stiffness, boundary conditions, and ground motion intensities often used in the design of underground reservoir structures.

The analytical procedures commonly employed to evaluate the seismic response of underground structures do not adequately consider the range of soil properties, flexural stiffness, kinematic constrains, and ground motion characteristics for which critical underground reservoir

structures must be designed. Advanced numerical methods may also assume simplistic soil properties, boundary conditions, or seismic loading that may not be applicable to realistic conditions and may at times lead to misleading conclusions. The experimental results presented in this paper are intended to help systematically evaluate the influence of soil densification, flexural stiffness, base fixity, site response, and ground motion characteristics on the seismic performance of stiff-unyielding buried structures. Parallel nonlinear numerical simulations validated using the centrifuge results but considering other variations than those permitted in the experiments are necessary and underway. These simulations are needed before generalized recommendations may be provided.

Chapter 5 SUMMARY AND CONCLUSIONS

The seismic response of stiff-unyielding underground structures with minimum to no soil overburden is a fairly new topic at the interface between geotechnical and structural engineering. There is an increasing need in engineering practice to obtain a better understanding of the seismic performance of these underground structures. This dissertation describes an experimental study of the effects of seismic loading on relatively stiff underground structures. The original idea of this research came from the need at the Los Angeles Department of Water and Power (LADWP) to more rigorously evaluate the seismic behavior of its underground reservoir structures. The main focus of the study was to understand the dynamic increment of lateral earth pressures on these structures, lateral deformations, bending strains/moments and soil-structure-interaction (SSI).

A series of sixteen dynamic centrifuge tests on 10.5 m-high models of underground box structures were conducted using the shake table onboard the 400 g-ton geotechnical centrifuge at the University of Colorado Boulder. The base motions consisted of various earthquake motions and sinusoidal motions with similar amplitudes (mostly ranging from about 0.3 to 0.5g), but frequencies ranging from 0.33 Hz to 6.7 Hz. The structure stiffness, backfill soil type and slope, embedment, container type (rigid versus flexible boundaries), fixity conditions, and ground motion characteristics were varied to evaluate their influence and relative importance on structural performance.

The following issues were addressed with some success related to the experimental study of the seismic response of underground structures and centrifuge modeling in general:

- The experiments were examined in detail to understand the basic behavior of underground box structure-soil systems;

- Repeat tests were performed to improve previous tests, evaluate and compare the response of different pressure transducers, and verify repeatability;
- The existing simplified analytical methods were reviewed and compared with experimental results in terms of box structure racking and seismic earth pressures;
- The variation of earth pressures across the tactile sensors was studied to evaluate the extent of scatter in granular materials and the effects of averaging as shown in Appendix A.

The conclusions made in this dissertation are preliminary and based on centrifuge experiments only. Although insightful in evaluating trends and the underlying mechanisms, experiments alone are affected by instrument uncertainties and limited by the simplified configurations employed. Numerical simulations are needed before providing generalized conclusions and recommendations for practice. The results of this experimental study indicate the following trends:

5.1 Tactile Pressure Sensors

- Tactile sensors need to be carefully de-aired, conditioned, equilibrated, and statically and dynamically calibrated prior to use in dynamic centrifuge modeling.
- Static pressures measured by the tactile sensors showed reasonable trends and compared well with analytically calculated at-rest lateral earth pressures. There was a slight increase in static pressure after each shake due to soil densification.
- The magnitude and distribution of the dynamic increment of earth pressures ($\Delta\sigma_E$) was shown to be fairly repeatable among different tests with similar soil and structural conditions.

5.2 Influence of Structural Flexibility on Performance

- The magnitude of seismic thrust increased and the distribution of seismic earth pressures changed from approximately triangular to parabolic with increasing structural stiffness. The estimated centroid locations on the Flexible structure were close to the M-O predictions, and the centroid locations on the BL and Stiff structures generally fell between those predicted by M-O, S-W, and Wood's methods.
- The ΔK_E values on the more flexible structures (BL and Flexible) were in line with previous experiments conducted on relatively flexible basement walls and were either close to or smaller than those predicted by the S-W method. The ΔK_E values on the Stiff structure, however, often exceeded the predictions of the S-W method and approached those of Wood's.
- Racking displacements increased with the flexibility of the structure. The trends of racking displacements observed on the Baseline and Flexible structures were consistent with the NCHRP 611 guideline analysis methods, but the NCHRP 611 overestimated the racking deformations for the Flexible structure slightly and underestimated deformations for the stiffer structure. Again, it must be emphasized that the measurement of flexural racking is based on total racking obtained from accelerometers, and rocking of the structure was not considered.

5.3 Influence of Backfill Soil Type and Properties on Performance

- Soil densification (D_r increase from approximately 60% to 72%) and shearing after multiple motions resulted in greater PGA amplifications along the far-field soil column, greater static and seismic lateral earth pressures, and slightly greater dynamic

bending strains along the height of the wall, but did not noticeably influence the effective fundamental frequency of the site (f_{so}').

- The greater stiffness of the compacted, silty sand backfill resulted in the structures acceleration response to be very similar to the far-field soil. The increased stiffness of the soil increased the flexibility ratio to around 1 and thus the racking ratio to 1 as well.
- The increased strength of the backfill soil led to a phase difference in $\Delta\sigma_E$ time histories along the height of the wall (i.e., when $\Delta\sigma_E$ peaked near the center, it approached lower values near the top and bottom). But, the additional soil stiffness and apparent cohesion did not have a significant influence on seismic earth thrust, which averages the $\Delta\sigma_E$ distribution along the wall, while it shifted its centroid upward slightly. These results combined with previous studies indicate that soil cohesion has a minor effect on seismic earth thrust, regardless of the kinematic constraints or flexural rigidity of the wall.

5.4 Influence of Backfill Soil Cover and Geometry on Performance

- Adding a shallow soil cover and the resulting slight increase in confinement reduced the acceleration response of the structure with respect to the far-field. The racking distortion was also increased likely because of the added inertia of the soil cover.
- The addition of a shallow soil cover caused the lateral earth pressures ($\Delta\sigma_E$) to increase slightly near the top of the structure and shift the centroid upwards during higher intensity ground motions.
- The addition of a sloped backfill slightly reduced the racking of the structure compared to the case without a slope.

- The sloped backfill caused the dynamic lateral earth pressures to decrease near the top and its centroid to move downward, because of the reduction in soil mass and inertia near the surface.

5.5 Influence of Base Fixity and Site Response

- The dynamic strain and dynamic pressure were amplified near the base of the fixed based structure compared to the structure resting on a layer of soil.
- The response of the structure-soil system was dominated by the surrounding soil regardless of the stiffness of the structure.
- The seismic performance of the buried structure in terms of tilt, acceleration, racking, dynamic thrust, and dynamic bending strains was influenced greatly by the frequency content of the base motion as well as far-field site response. During the sinusoidal motions (with a narrower frequency band compared to earthquake motions), the dynamic earth pressures, structural racking, and bending strains always peaked when the excitation frequency approached f_{so}', regardless of the fundamental frequency of the structure or base fixity.

Chapter 6 LIMITATIONS AND RECOMMENDATIONS FOR FUTURE WORK

Based on the observations and challenges during the presented centrifuge experiments, the following recommendations can be made for future research and improvements needed in physical modeling of buried structures:

1. A brief study comparing the response of earth pressure cells with tactile sensors was attempted in this research as summarized in Appendix B. The results among different sensors were not consistent and conclusive. It is anticipated that traditional strain-based earth pressure cells are not appropriate for this purpose, as they are affected by soil arching effects. However, despite a number of previous studies on the topic, a more detailed and extensive study is needed on different types of pressure sensors for different types of soils, to fully understand their static and dynamic behavior. Once the properties of the sensors and their limitations are well understood under different loading conditions, they can be improved and used more reliably in the testing and monitoring of underground structures.
2. A large amount of high quality data on the static and dynamic behavior of relatively stiff box structures was generated in this research. This data may be used to calibrate and or validate numerical models in future studies. A number of centrifuge tests have been numerically simulated by our research team (e.g., Deng et al. forthcoming) and more are underway. The validated numerical tools can be used to model more complex underground structures and future parametric studies with more variations in the properties of soil, geometry, structure, and ground motions that are not possible experimentally.
3. Future centrifuge studies are recommended to evaluate the response of stiff-unyielding buried structures with different levels of water inside. The impact of sloshing on the overall

performance of the system is currently not well-understood and physical modeling can provide insights on this topic.

4. More extensive documentation of the seismic response of relatively stiff box structures should be taken during actual earthquake events. Instruments such as accelerometers and tactile pressure transducers should be installed on a variety of these critical structures in a systematic manner. The data from instrumented structures can provide us with a better understanding of their response during earthquakes under more realistic conditions that is possible experimentally.

REFERENCES

Al Atik, L. and Sitar, N. (2010), "Seismic Earth Pressures on Cantilever Retaining Structures," *Journal of Geotechnical and Geoenvironmental Engineering*, October, (136) 10, pp. 1324-1333.

Al-Homoud, A.S. and Whitman, R.V. (1999). "Seismic analysis and design of rigid bridge abutments considering rotation and sliding incorporating non-linear soil behavior." *Soil Dynamics and Earthquake Engineering*, 18, 247–277.

Andersen, G.R., Whitman, R.V., and Germaine, J.T. (1991). "Seismic response of rigid tilting walls." *Centrifuge 91*, H.Y. Ko and F.G. McLean, eds., Balkema, Rotterdam, The Netherlands, 417–423.

Anderson, D.G., Martin, G.R., Lam, I.P. and Wang, J.N. (2008). *Seismic Design and Analysis of Retaining Walls, Buried Structures, Slopes and Embankments*. NCHRP Report 611. Transportation Research Board, National Cooperative Highway Research Program, Washington, D.C.

Athanasopoulos-Zekkos, A., Vlachakis, V.S. and Athanasopoulos, G.A. (2013). "Phasing issues in the seismic response of yielding, gravity-type earth retaining walls – Overview and results from a FEM study." *Soil Dynamics and Earthquake Engineering*, 55, 59-70

Bardet, J.P., Huang, Q., and Chi, S.W. (1993). "Numerical prediction for model no. 1." *Proceedings of the International Conference on the Verification of Numerical Procedures for the Analysis of Soil Liquefaction Problems* (Vol. 1, pp. 67-86). Balkema, Netherlands.

Bolton M.D. and Steedman, R.S. (1982). "Centrifugal testing of micro-concrete retaining walls subject to base shaking," *Proceedings of Conference on Soil dynamics and Earthquake Engineering*, Southampton, 311-329, Balkema, Rotterdam.

Brandenberg, S.J., Mylonakis, G. and Stewart, J.P. (2015). “Kinematic framework for evaluating seismic earth pressures on retaining walls.” *Journal of Geotechnical and Geoenvironmental Engineering*. 10.1061/(ASCE)GT.1943-5606.0001312, 04015031.

Candia, G., and Sitar, N. (2013) “Seismic earth pressures on retaining structures in cohesive soils.” Report to the California Department of Transportation under Contract No. 65A0367, University of California Berkeley, Berkeley, CA

Cilingir, U., and Madabhushi, S.P.G. (2011) "A model study on the effects of input motion on the seismic behaviour of tunnels." *Soil Dynamics and Earthquake Engineering* 31.3 452-462.

Darendeli, M. B. (2001). *Development of a new family of normalized modulus reduction and material damping curves*. PhD Dissertation, Univ. of Texas at Austin, Austin, TX.

Dashti, S., Gillis, K., Ghayoomi, M., and Hashash, Y. (2012). “Sensing of lateral seismic earth pressures in geotechnical centrifuge modeling.” *Proceedings of 15th World Conf. on Earthquake Eng*., Lisbon, Portugal.

Davis, C.A. (2003). “Lateral seismic pressures for design of rigid underground lifeline structures.” *Proceedings of the 6th U.S. Conference on Lifeline Earthquake Engineering,* ASCE. 1001-1010.

Deng, Y.H., Dashti, S., Hushmand, A., Davis, C.A., and Hushmand, B. (forthcoming). “Seismic response of underground reservoir structures in sand: evaluation of numerical simulations using centrifuge experiments.” *Soil Dynamics and Earthquake Engineering* (under review).

Derrick, T.R. (2004). “Signal Processing. In: Research Methods for Biomechanics.” Chapter 11, Robertson, D.G.E., Hamill, J. Caldwell, G.E., Kamen, G. (eds). Human Kinetics Publishers, Champaign, IL, pp. 227-238.

Dewoolkar, M.M., Ko, H. and Pak R.Y.S. (2001). “Seismic behavior of cantilever retaining walls with liquefiable backfills.” *Journal of Geotechnical and Geoenvironmental Engineering, ASCE*, (127) 5, 424-435.

Ebeling, M.E. and Morrison, E.M. (1992). *The Seismic Design of Waterfront Retaining Structures.* Technical Report ITL-92-11. U.S. Army Corps of Engineers, Washington, D.C.

Gazetas, G, Psarropoulos, PN, Anastasopoulos, I. and Gerolymos, N. (2004). “Seismic Behaviour of Flexible Retaining Systems Subjected to Short-Duration Moderately Strong Excitation,” *Soil Dynamics and Earthquake Engineering*, (24), 537-550.

Ghayoomi, M., Dashti, S., and McCartney, J.S. (2013). “Performance of a transparent Flexible Shear Beam container for geotechnical centrifuge modeling of dynamic problems”. *Soil Dynamics and Earthquake Engineering, 53,* 230-239

Ghayoomi, M., Dashti, S., and McCartney, J.S. (2012). “Effect of boundary conditions on the performance of a transparent flexible Shear Beam-type container,” *2nd International Conference on Performance.-Based Design Earthquake Geotechnical Engineering.* Taormina, Italy.

Gillis, K., Dashti, S., and Hashash, Y. (2015) “Dynamic Calibration of Tactile Sensors for Measurement of Soil Pressures in Centrifuge,” *ASTM Geotechnical Testing Journal*

Hashash, Y.M.A., Karina, K., Koutsoftas, D., and O'Riordan, N. (2010). "Seismic design considerations for underground box structures." *Earth Retention Conference*. Vol. 3.

Hradilek, P. J. (1972). *Behavior of Underground Box Conduits in the San Earthquake of 9 February 1971.* Report No. TR-E-72-1, U.S. Army Corps of Engineers, Los Angeles

Jaky, J. (1944), “The coefficient of earth pressure at rest.” *Journal for Society of Hungarian Architects and Engineers*, October, pp. 355-358.

Ketcham, S. A., Ko, H. Y., and Sture, S. (1991). ‘‘Performance of an earthquake motion simulator for a small geotechnical centrifuge.’’ *Centrifuge 91*, H. Y. Ko and F. G. McLean, eds., Balkema, Rotterdam, The Netherlands, 361–368.

Ketcham, S.A. (1989). *Development of an earthquake motion simulator for centrifuge testing and the dynamic and the dynamic response of a model sand embankment*. PhD Thesis, University of Colorado, Boulder, CO.

Kloukinas, P., Langoussis, M., and Mylonakis, G. (2012). “Simple wave solution for seismic earth pressures on non-yielding walls.” *J. Geotech. Geoenviron. Eng*., 1514–1519.

Ko, H. Y. (1988). ‘‘The Colorado centrifuge facility.’’ *Centrifuge 88*, J. F. Corte, ed., Balkema, Rotterdam, The Netherlands, 73–75.

Lew, M., Sitar, N., Al Atik, L., Pourzanjani, M. and Hudson, M.B. (2010). “Seismic earth pressures on deep building basements.” *Structural Engineers Association. of California, Proceedings of the Annual Convention, 2010*.

Li, X. (1999). “Dynamic analysis of rigid walls considering flexible foundation.” *J. Geotech. Geoenviron. Eng*. 803–806.

Mason, H.B., Bray, J.D., Kutter, B.L., Wilson, D.W., and Choy, B.Y. (2010). “Earthquake motion selection and calibration for use in a geotechnical centrifuge.” In *Physical Modelling in Geotechnics, Proceedings of the 7th International Conference on Physical Modelling in Geotechnics (ICPMG 2010),* Zurich, Switzerland (Vol. 1, p. 361).

Matsuo, H., and Ohara, S. (1960). “Lateral earthquake pressure and stability of quay walls during earthquakes.” *Proceedings of the 2nd World Conference on Earthquake Engineering*, Tokyo, Japan, Vol. 1, pp. 165-181.

Mononobe, N. and Matsuo M. (1929). “On the determination of earth pressures during earthquakes.” *Proc. World Engineering Congress*, Vol. 9, 179-187.

Nakamura, S. (2006). “Reexamination of Mononobe-Okabe theory of gravity retaining walls using centrifuge model tests.” *Soils and Foundations*, (46) 2, 135-146.

Okabe S. (1926). “General theory of earth pressure.” *Journal of the Japanese Society of Civil Engineers*, Tokyo, Japan, (12)

Ertugrul, O.L. (2014). “Seismic behavior of box-shaped culverts buried in cohesionless soils.” *Pipelines 2014: From Underground to the Forefront of Innovation and Sustainability*. ASCE. 2149-2160.

Olson, S.M., Hashash, Y., Polito, C., Phillips, C., and Muszynski, M. (2011). “Measuring pressures in the geotechnical centrifuge using tactile pressure pads.” *7th Annual NEES Centrifuge Research and Training Workshop Rensselaer Polytechnic Institute*. PowerPoint Presentation.

Ortiz, L.A., Scott, R.F., and Lee, J. (1983). “Dynamic centrifuge testing of a cantilever retaining wall.” *Earthquake Engineering & Structural Dynamics*, 11(2), 251-268.

Ostadan, F. (2005). “Seismic soil pressure for building walls: An updated approach.” *Soil Dynamics and Earthquake Engineering*, *25*(7), 785-793.

Popescu, R., and Prevost, J. H. (1993). “Centrifuge validation of a numerical model for dynamic soil liquefaction.” *Soil Dynamics and Earthquake Engineering*, *12*(2), 73-90.

Provost, D. (2015) *Cyclic Triaxial Testing of Nevada Sand.* MS Thesis, University of Colorado, Boulder, CO.

Psarropoulos, P. N., Klonaris, G., and Gazetas, G. (2005). “Seismic earth pressures on rigid and flexible retaining walls.” *Int. J. Soil Dyn. Earthquake Eng.*, 25, 795–809.

Psarropoulos, P.N., Tsompanakis, Y., and Papazafeiropoulos, G. (2011). “Effects of soil non-linearity on the seismic response of restrained retaining walls.” *Structure and Infrastructure Engineering* 7.12: 931-942.

Richards, R., Huang, C. and Fishman, K.L. (1999). “Seismic earth pressure on retaining structures,” *Journal of Geotechnical and Geoenvironmental Engineering*, ASCE, 125(9): 771–778.

Roth, W.H. and Mehrain, M. (2010). “The meaning of seismic earth pressure.” *Annual SEAOC Convention*

Scott, R.F. (1973). “Earthquake-induced earth pressures on retaining walls,” *Proceedings, Fifth World Conference on Earthquake Engineering*, Vol. 2, Rome, Italy.

Seed, H.B. and Whitman, R.V. (1970). “Design of earth retaining structures for dynamic loads.” *ASCE Specialty Conference, Lateral Stresses in the Ground and Design of Earth Retaining Structures*, Cornell Univ., Ithaca, New York, 103–147.

Sherif, M. A., Ishibashi, I., and Lee, C. D. (1982). ‘‘Earth pressures against rigid retaining walls.’’ *J. Geotech. Engrg. Div.*, ASCE, 108(5), 679–695.

Stadler, A. T. (1996). *Dynamic Centrifuge Testing of Cantilever Retaining Walls*. Ph.D. Thesis. Univ. of Colorado at Boulder, Boulder, Colo.

Steedman, R. S., and Zeng, X. (1991). “Centrifuge modeling of the effects of earthquakes on free cantilever walls”. Centrifuge’91.

Taiebat, M., Ahmadnia, A., Liam Finn, W.D., Ventura, C.E., Naesgaard, E., and Devall, R.H. (2011) "Seismic assessment of basement walls for different design criteria." *Proceedings of the 4th Pan-American and 64th CGS Conference, Toronto, Ont. Paper ID*. Vol. 1069.

Tessari, A., Abdoun, T., Sasanakul, I., and Wroe, E. (2014) “Boundary corrected calibration of tactile pressure sensors.” *ICPMG2014 – Physical Modelling in Geotechnics*., Jan 2014, 331 - 336

Tsinidis, G., Pitilakis, K., Heron, C., and Madabhushi, S.P.G. (2013) “Experimental and numerical investigation of the seismic behavior of rectangular tunnels in soft soils.” *Computational methods in structural dynamics and earthquake engineering conference (COMPDYN 2013), Kos, Greece*. Vol. 11.

Tsinidis, G., Pitilakis, K., Madabhushi, G., and Heron, C. (2015). “Dynamic response of flexible square tunnels: centrifuge testing and validation of existing design methodologies.” *Geo-technique*, 65(5), 401-417

Veletsos, A.S., and Younan, A.H. (1994a). ‘‘Dynamic soil pressures on rigid vertical walls.’’ *Earthquake Engrg. and Struct. Dyn.*, 23(3), 275–301.

Veletsos, A. S., and A. H. Younan (1994b) “Dynamic modeling and response of soil-wall systems,” *Journal of Geotechnical and Geoenvironmental Engineering, ASCE*, Vol. 120, No. 12, pp. 2155-2179.

Veletsos, A.S. and Younan, A.H. (1997). “Dynamic response of cantilever retaining walls.” *Journal of Geotechnical and Geoenvironmental Engineering*, (123) 2: 161-172.

Wang, J.N. (1993) *Seismic Design of Tunnels: A State-of-the-Art Approach*. Monograph 7. New York, NY: Parsons Brinckerhoff Quade & Douglas, Inc.

Wilson, P. (2009). *Large Scale Passive Force-Displacement and Dynamic Earth Pressure Experiments and Simulations*. PhD Thesis, University of California, San Diego, CA.

Wilson, P., and Elgamal, A. (2015). “Shake table lateral earth pressure testing with dense c-ϕ backfill,” *Soil Dynamics and Earthquake Engineering*, 71, 13-26.

Wood, J.H. (1973). *Earthquake Induced Soil Pressures on Structures*. PhD Thesis, California Institute of Technology, Pasadena, CA.

Yang, Z., Elgamal, A., and Parra, E. (2003). "Computational model for cyclic mobility and associated shear deformation." *J. Geotech. Geoenviron. Eng.* , 129 (12), 1119–1127

Zhai, E., Davis, C.A., Yan, L., and Hu, J. (2013). "Numerical simulations of geotechnical centrifuge Modeling of seismic earth pressures on an underground restrained structure." *International Efforts in Lifeline Earthquake Engineering*. ASCE. December 2013, 369-376.

APPENDIX A Pressure Scatter Analysis

One of the advantages of using tactile pressure sensors is they can measure pressure over a large continuous area providing a more complete pressure distribution as opposed to measuring pressure of a small area using pressure cells.. However, because of the large amount of sensels, presenting the static/dynamic pressure profiles with depth can be confusing if all sensels are plotted together. Further, there will be some scatter in the pressure distribution with depth across the sensor because of local inhomogenities of granular material and variability of sensor behavior.

The variability of static pressure across the sensor was studied at all elevations and plotted as shown in Figure A-1 through Figure A-5 below. The study was done for T-BL prior to the Northridge-L, Northridge-M, Northridge-H, Izmit and Loma ground motions. The pressure data obtained by all sensels were first plotted as shown in part 'a' of the figures. The average pressure for each row was also plotted in each figure to compare with the individual pressure sensel readings. The theoretical lateral static pressures were plotted for reference. The variability of the pressure at each elevation was quantified by plotting the standard deviation.

Scatter in pressure data in the lower Tekscan sensor was greater than in the upper Tekscan for all ground motions observed. In an ideal situation the pressure sensels in a certain elevation (row) should have the same or very similar readings. But that is not possible in a granular material, even with an ideal sensor. Normally, the best way to reduce the scatter in a uniform material is by equilibriating the sensels. However, in centrifuge modeling, due to the long time delay between sensor calibration and equilibration and the time of actual testing, equilibration may not be effective. Further, the scatter in pressure at the same depth due to the presence of a granularly material is expected in these experiments and cannot be avoided. Nine cell averaging was performed to provide a better representation of pressure

at a given depth as plotted in part ‘b’ and ‘d’ in the figures below. The variation in pressure at all elevations was reduced greatly after nine cell averaging.

The scatter was also analyzed for the dynamic increment of pressure as shown in Figure A-6 through Figure A-10 for T-BL during the Northridge-L, Northridge-M, Northridge-H, Izmit and Loma motions. The analytical methods of Mononobe-Okabe (M-O), Seed-Whitman (S-W), and Wood, are plotted as comparison. There is a noticeable amount of scatter in the magnitude of dynamic increment of pressure, but the overall shapes and trends are similar across the sensor. Similar to the static condition, nine cell averaging reduced the scatter for dynamic increment of pressure along the height of the structure wall.

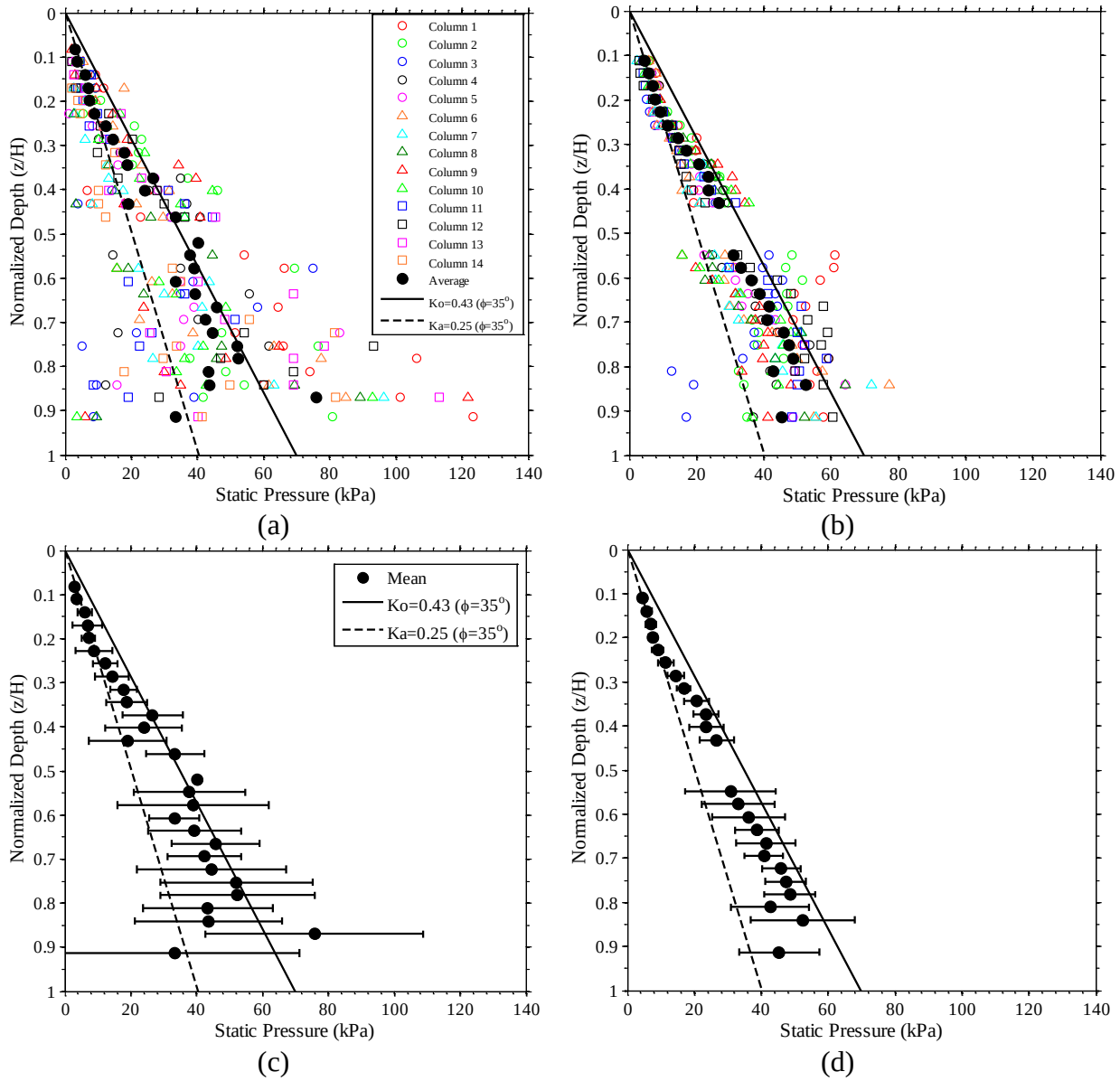

Figure A-1. Distribution of static pressures on the north wall prior to the Northridge-L motion during T-BL: (a) before nine cell averaging; (b) after nine cell averaging; (c) standard deviation and mean before nine cell averaging; and (d) standard deviation and mean after nine-cell averaging

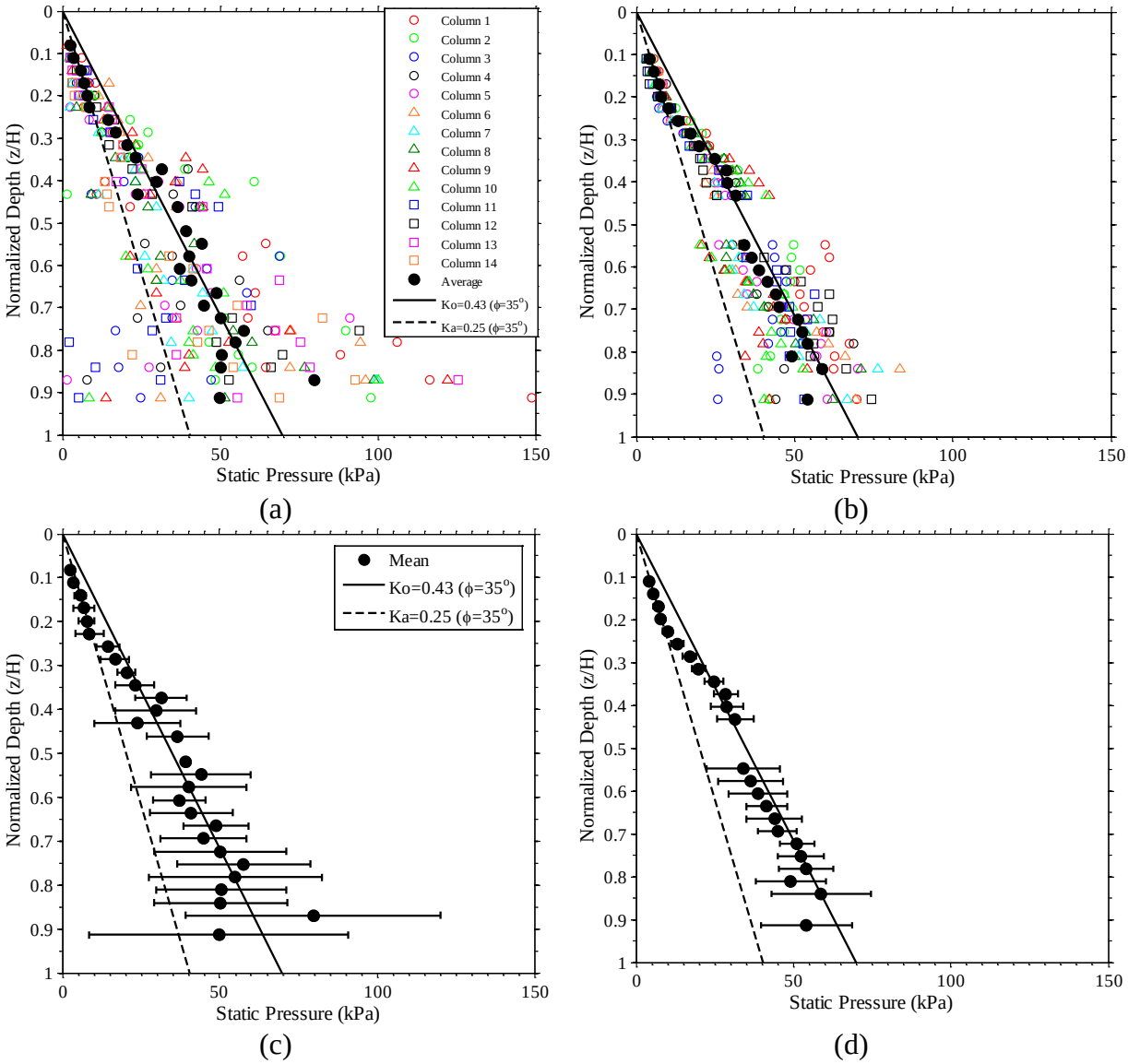

Figure A-2. Distribution of static pressures on the north wall prior to the Northridge-M motion during T-BL: (a) before nine cell averaging; (b) after nine cell averaging; (c) standard deviation and mean before nine cell averaging; and (d) standard deviation and mean after nine-cell averaging

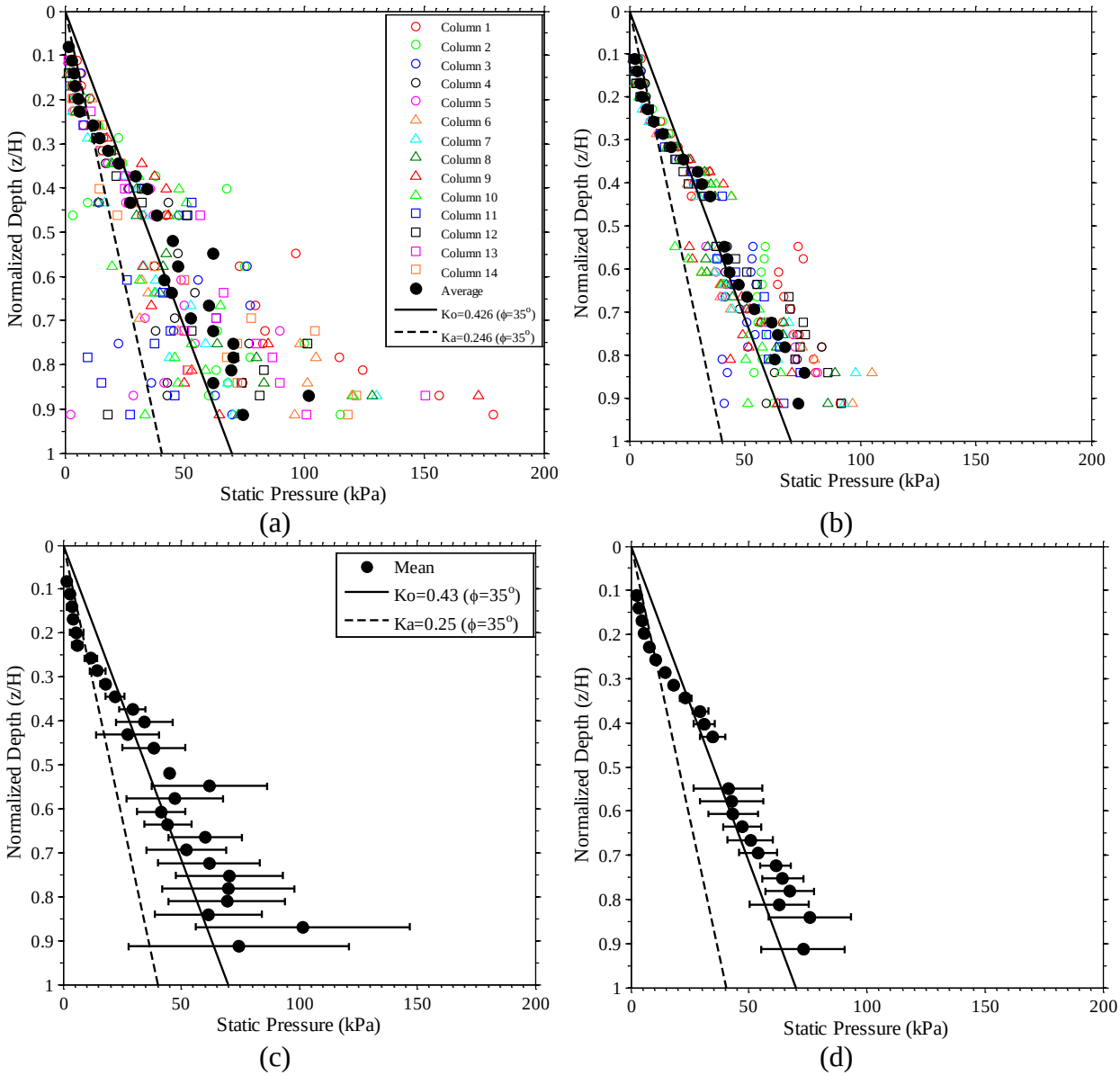

Figure A-3. Distribution of static pressures on the north wall prior to the Northridge-H motion during T-BL: (a) before nine cell averaging; (b) after nine cell averaging; (c) standard deviation and mean before nine cell averaging; and (d) standard deviation and mean after nine-cell averaging

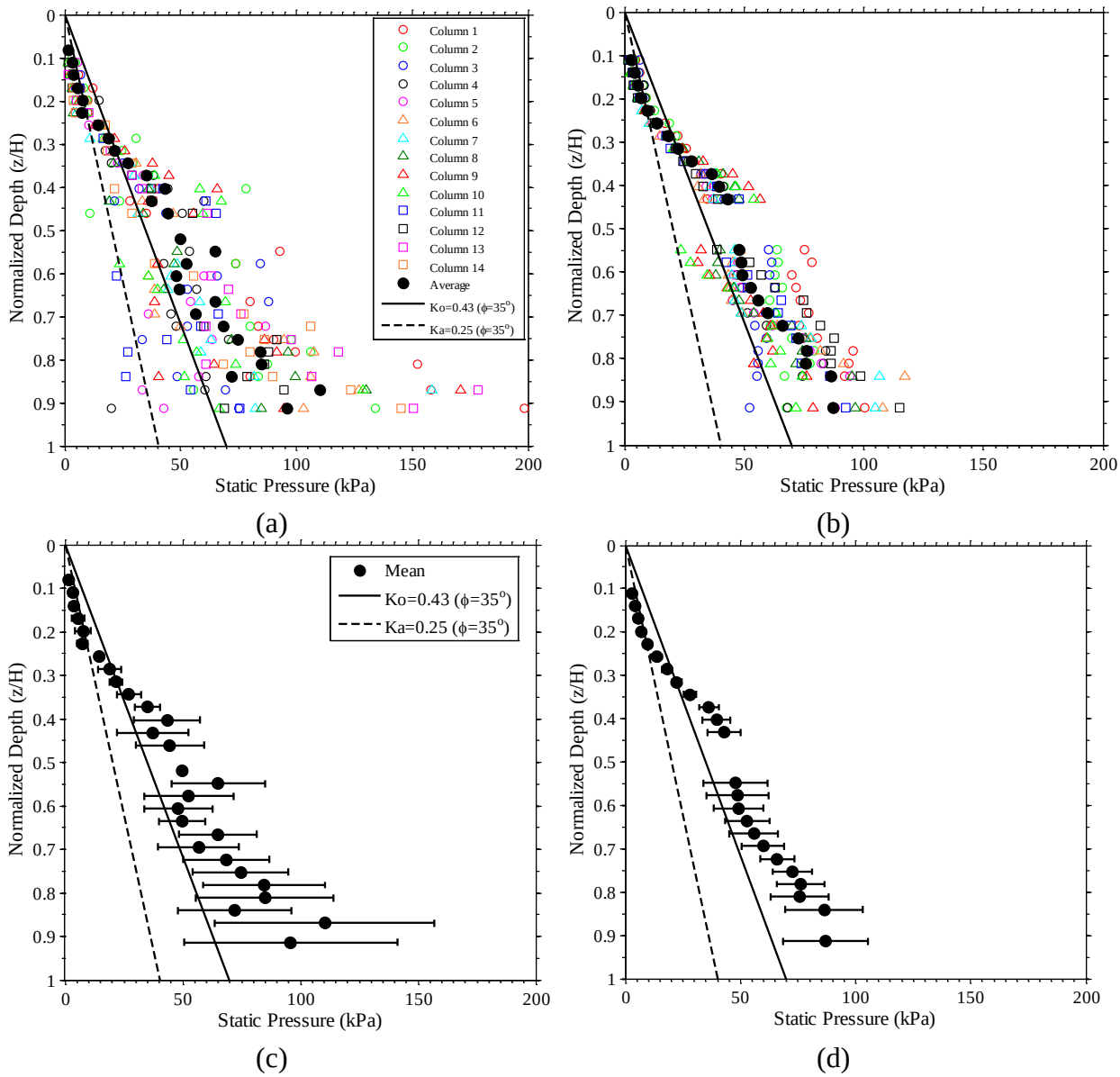

Figure A-4. Distribution of static pressures on the north wall prior to the Izmit motion during T-BL: (a) before nine cell averaging; (b) after nine cell averaging; (c) standard deviation and mean before nine cell averaging; and (d) standard deviation and mean after nine-cell averaging

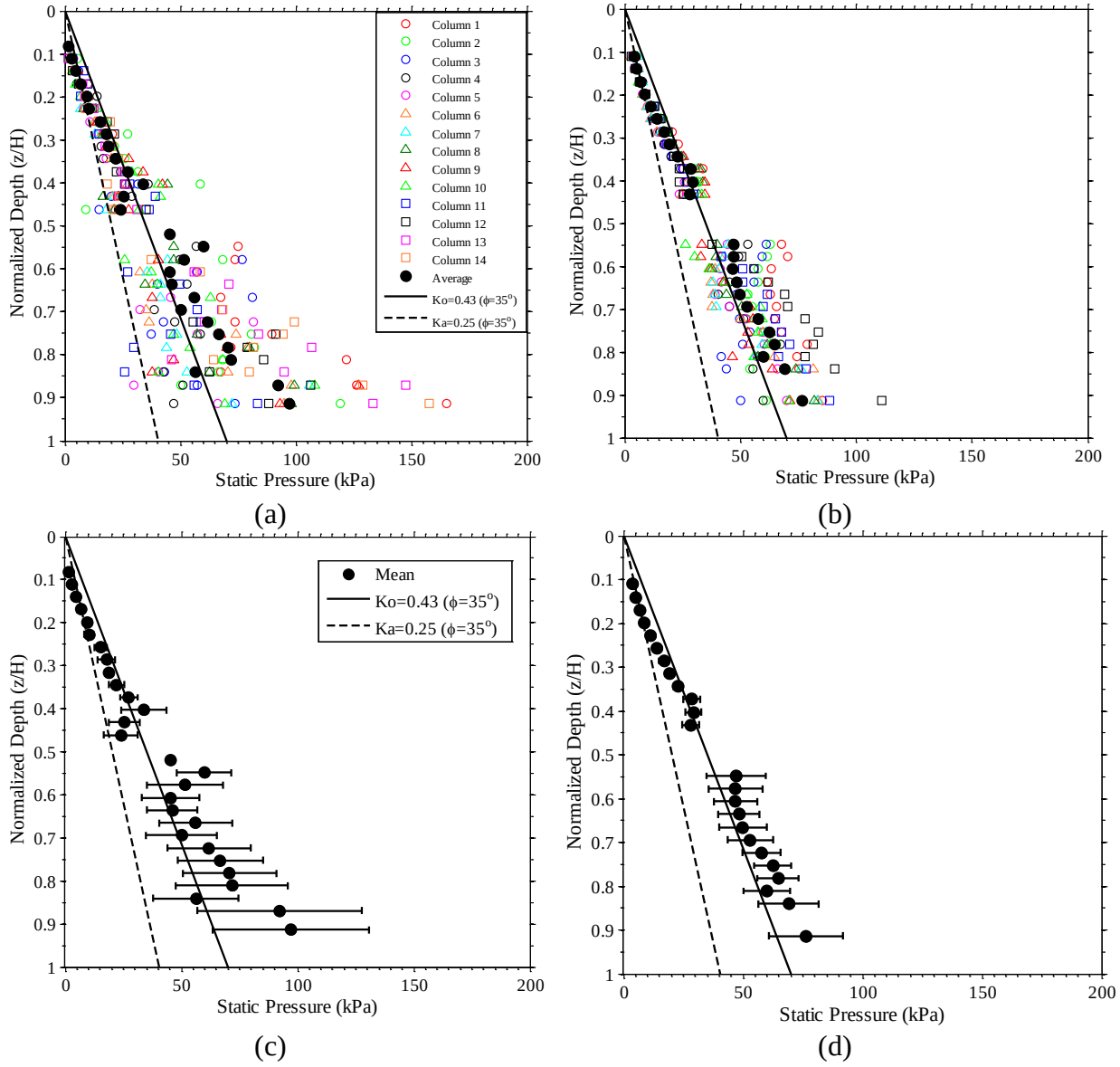

Figure A-5. Distribution of static pressures on the north wall prior to the Loma motion during T-BL: (a) before nine cell averaging; (b) after nine cell averaging; (c) standard deviation and mean before nine cell averaging; and (d) standard deviation and mean after nine-cell averaging

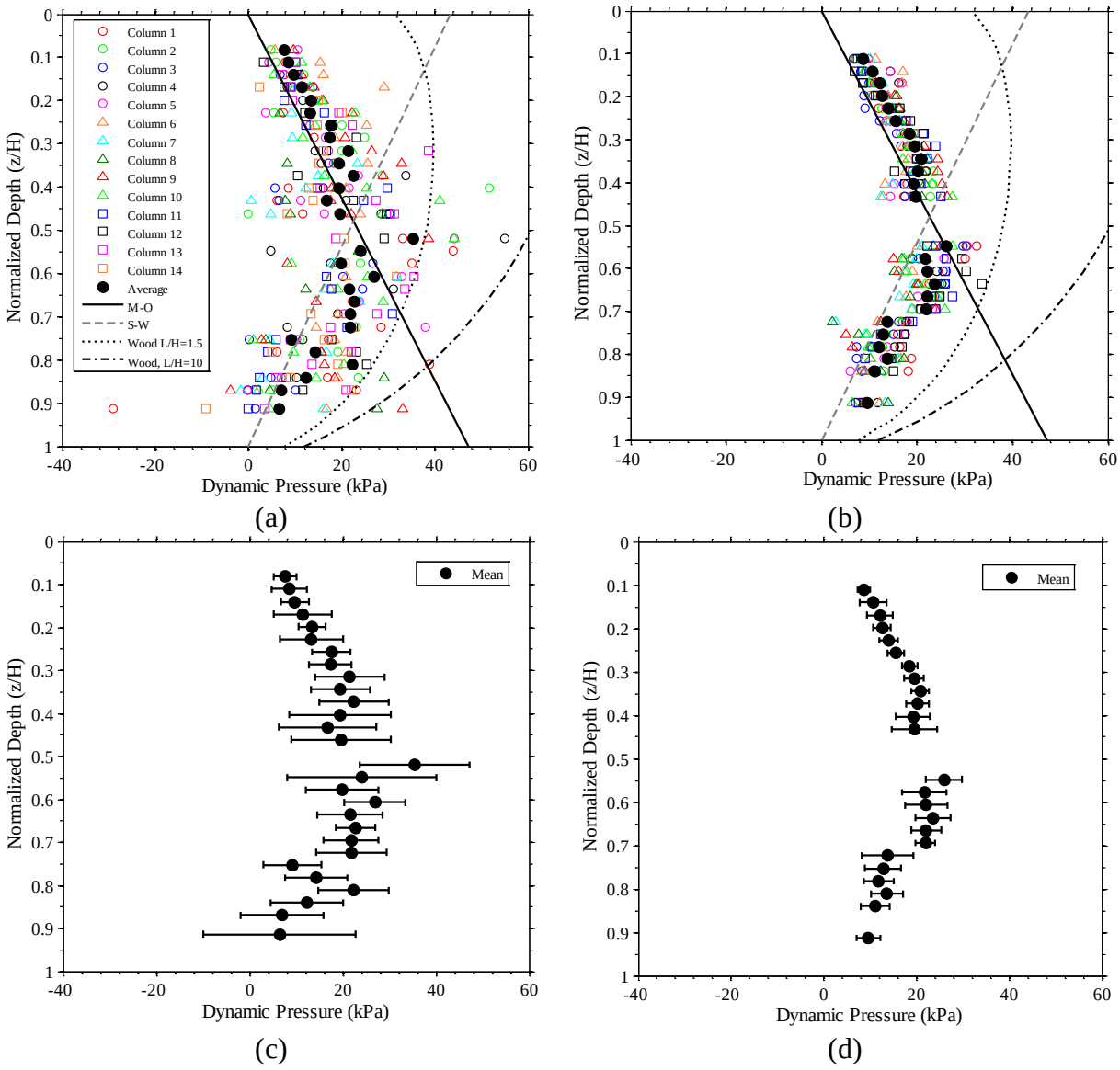

Figure A-6. Distribution of dynamic increment of pressure on the north wall prior to the Northridge-L motion during T-BL: (a) before nine cell averaging; (b) after nine cell averaging; (c) standard deviation and mean before nine cell averaging; and (d) standard deviation and mean after nine-cell averaging

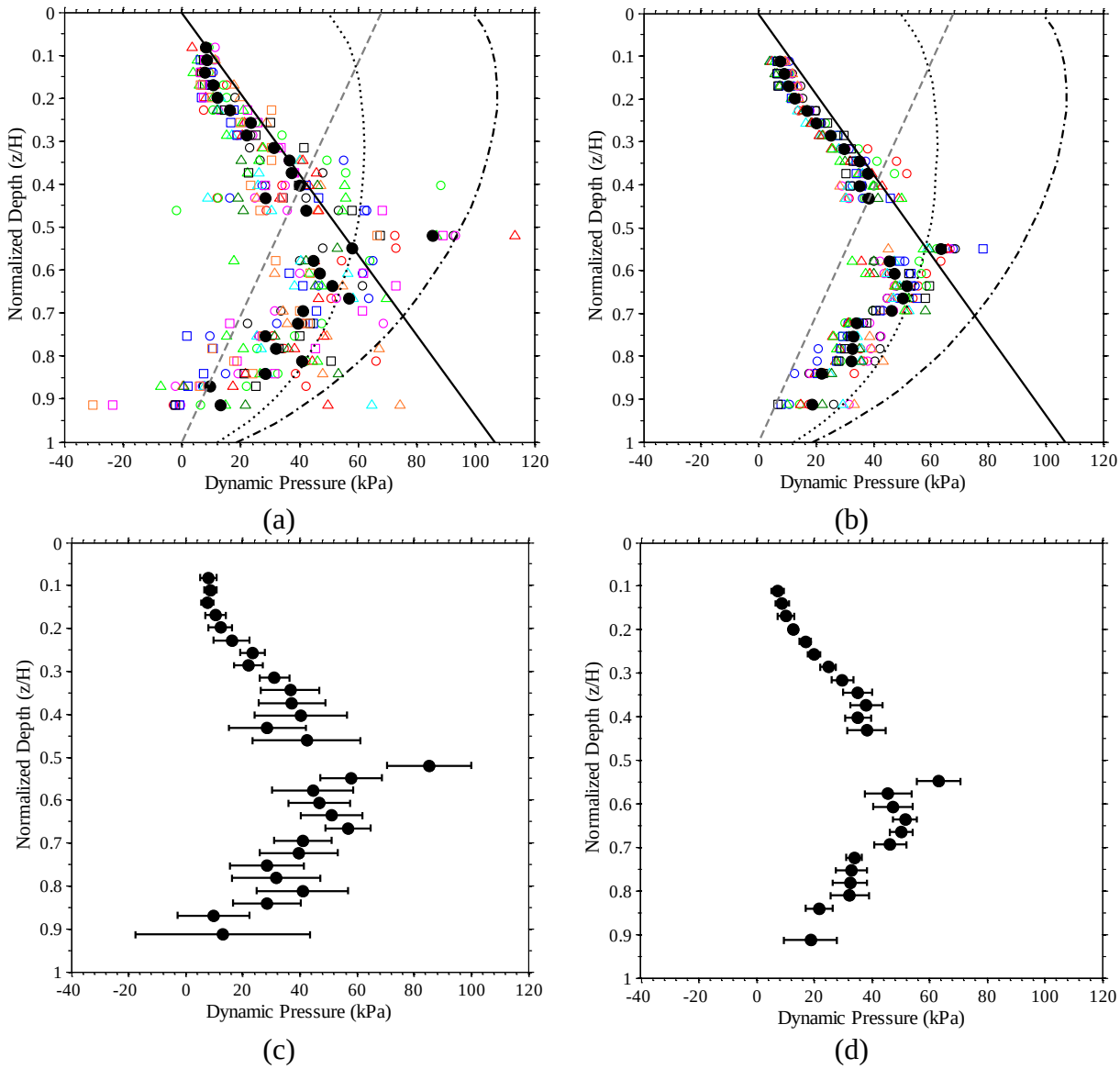

Figure A-7. Distribution of dynamic increment of pressure on the north wall prior to the Northridge-M motion during T-BL: (a) before nine cell averaging; (b) after nine cell averaging; (c) standard deviation and mean before nine cell averaging; and (d) standard deviation and mean after nine-cell averaging

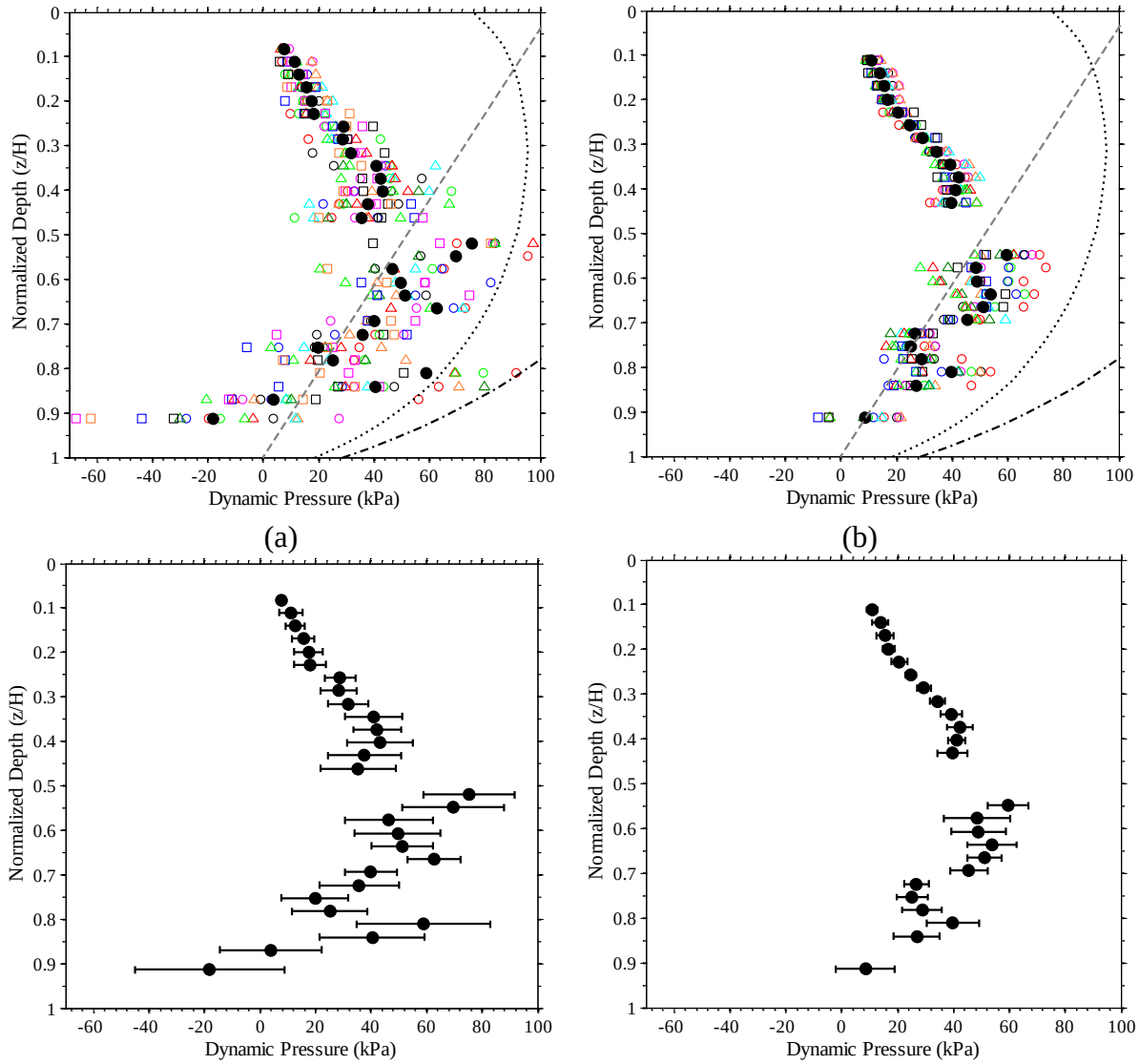

Figure A-8. Distribution of dynamic increment of pressure on the north wall prior to the Northridge-H motion during T-BL: (a) before nine cell averaging; (b) after nine cell averaging; (c) standard deviation and mean before nine cell averaging; and (d) standard deviation and mean after nine-cell averaging

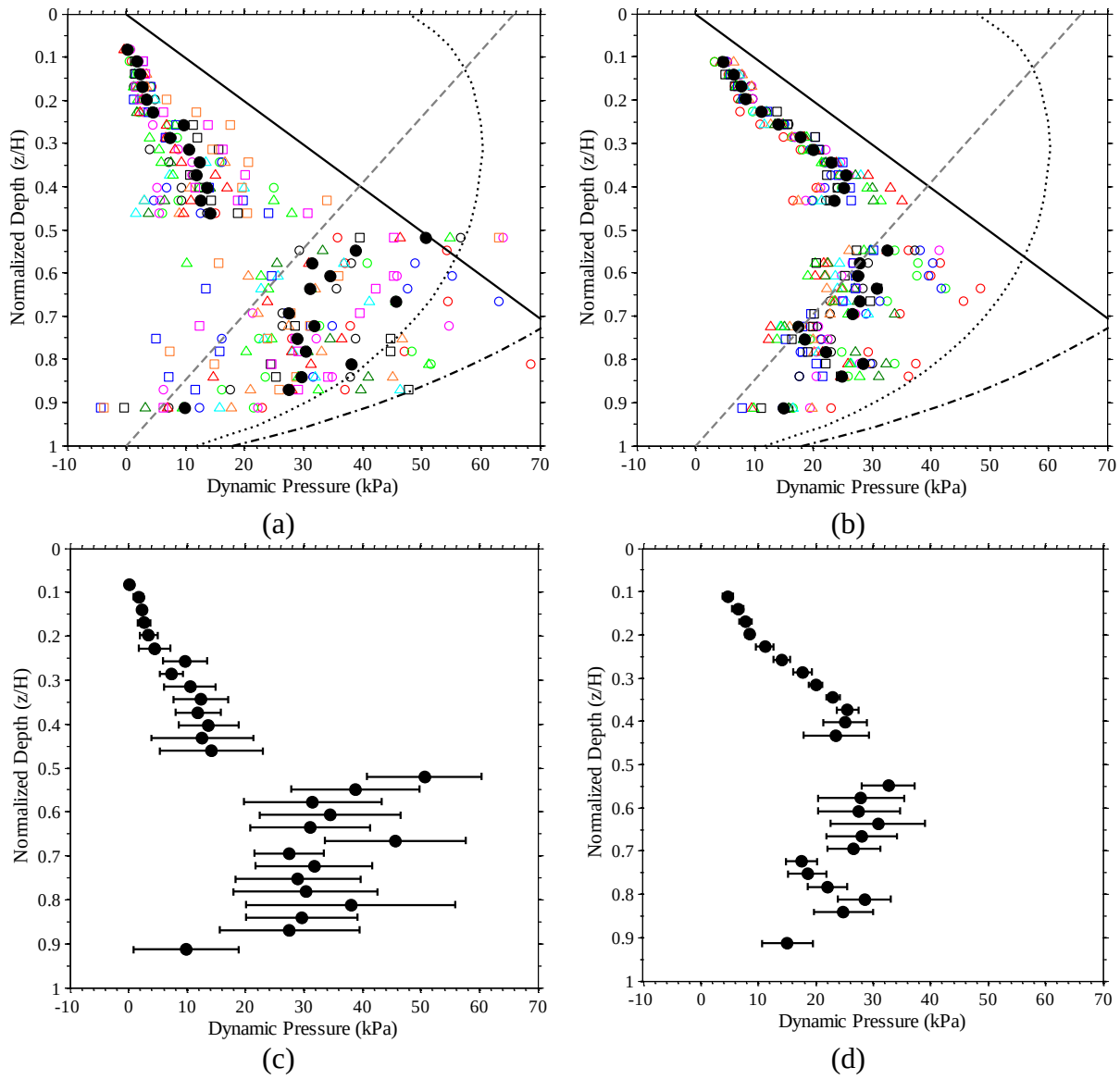

Figure A-9. Distribution of dynamic increment of pressure on the north wall prior to the Izmit motion during T-BL: (a) before nine cell averaging; (b) after nine cell averaging; (c) standard deviation and mean before nine cell averaging; and (d) standard deviation and mean after nine-cell averaging

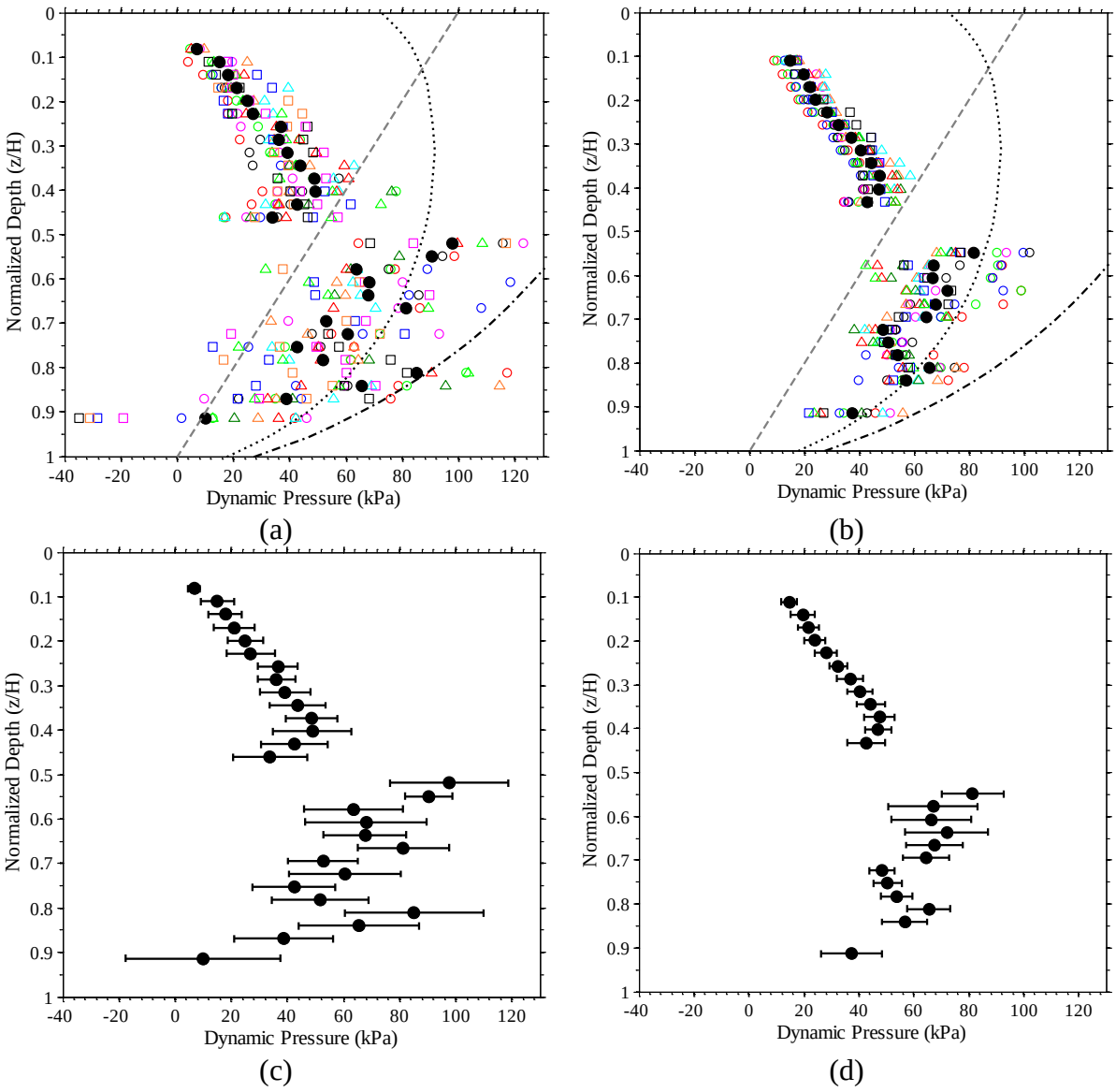

Figure A-10. Distribution of dynamic increment of pressure on the north wall prior to the Loma motion during T-BL: (a) before nine cell averaging; (b) after nine cell averaging; (c) standard deviation and mean before nine cell averaging; and (d) standard deviation and mean after nine-cell averaging

APPENDIX B Comparison of Tactile Sensors and Pressure Cells

Because of the uncertainties in measuring earth pressures it was decided to use pressure cells as an alternative way to measure pressures and to compare with tactile sensors during Test 1A-R2, 3A-R, and 4A-R2 (repeat tests). Pressure cells have been used extensively in previous geotechnical centrifuge research in studying shallow foundation response, retaining walls, and tunnels (e.g., Ortiz and Scott 1983; Hushmand 1983; Stadler 1996; Dewoolkar et al. 2001; Madabhushi and Khokher 2010; Tsinidis et al. 2015) resulting in descent results especially for saturated soils.

Static and dynamic centrifuge tests were performed on cantilever walls retaining dry medium dense Nevada sand by Stadler 1996 and saturated Nevada sand by Dewoolkar et al. 2001 at CU Boulder. The walls were instrumented along their entire height with Entran pressure cells to measure pressures directly. Figure B-1 shows the lateral static earth pressure profile measured by Stadler 1996. There are two plots (a and b) because the author repeated tests to observe repeatability. There is some scatter in the pressure profile but there are no extreme outliers. This scatter could be due to many reasons such as inconsistent relative density, improper machining of pressure cell housing, improper installation of pressure cells, and arching.

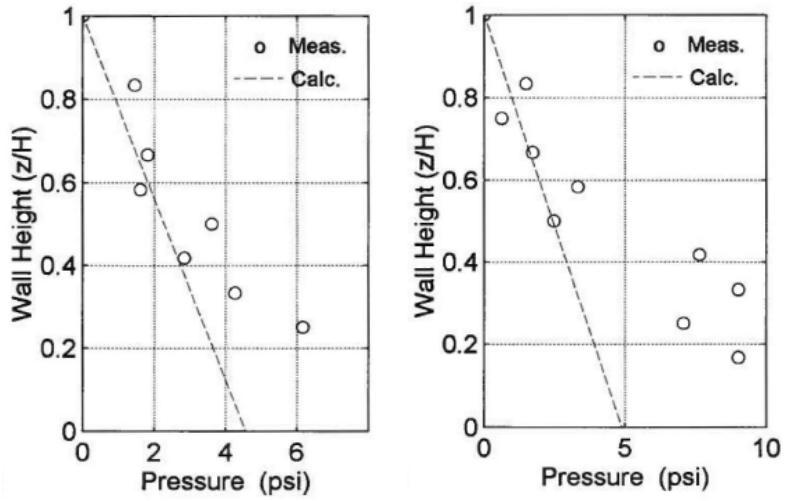

(a) (b)

Figure B-1. Static pressure profiles for a 30 ft retaining wall with 60% Dr Nevada Sand backfill (Stadler, 1996)

Figure B-2 below shows the static and dynamic lateral earth pressure profiles measured on a cantilever wall retaining saturated (a: water and b: metolose) backfill performed by Dewoolkar et al. 2001. The plus sign in the plots represents the static pressure and star signs represent total dynamic and static pressures. The pressure trends in these tests seem to be more reasonable than those conducted using dry cohesionless backfill. Arching effects are pronounced when the sensors are used to measure pressures in dry cohesionless backfill.

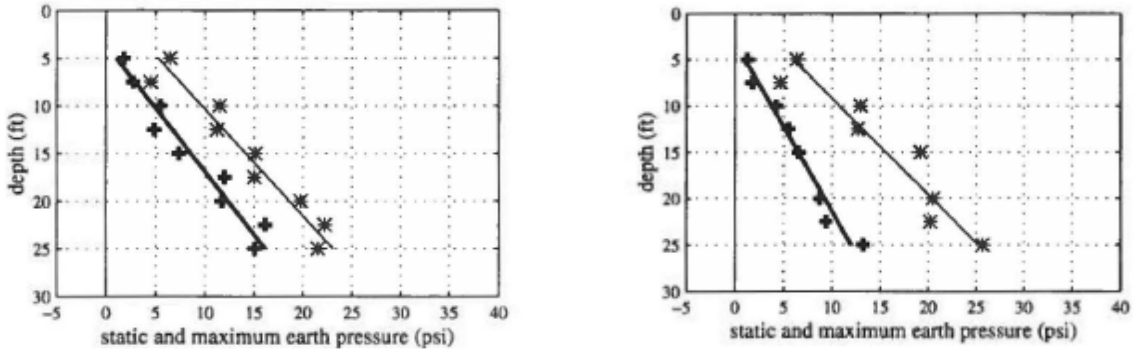

(a) (b)

Figure B-2. Static pressure profiles for a 30 ft retaining wall with 60% Dr saturated with (a) water and (b) metolose (Dewoolkar 1996)

Figure B-3 compares the static lateral earth pressures measured by the tactile sensors and pressure cells in T-BL, T-Stiff, and T-Flexible prior to the Northridge-L, Northridge-M, and Northridge-H motions. The theoretical Ko and Ka pressures are also plotted as reference. The magnitude of the pressure measured by the pressure cells in T-BL were unusually small compared to those measured by the tactile sensors and the theoretical pressures because of a problem with their connection to the centrifuge panel. The pressure cell and tactile pressure results compared reasonably well with each other during T-Stiff and T-Flexible. Figure B-4 compares the dynamic increment of pressure measured by the tactile sensors and pressure cells in T-BL, T-Stiff, and T-Flexible during the Northridge-L, Northridge-M, Northridge-H, Izmit, and Loma ground motions. Overall, the dynamic increment of pressure from the pressure cells did not compare very well with the tactile sensors.

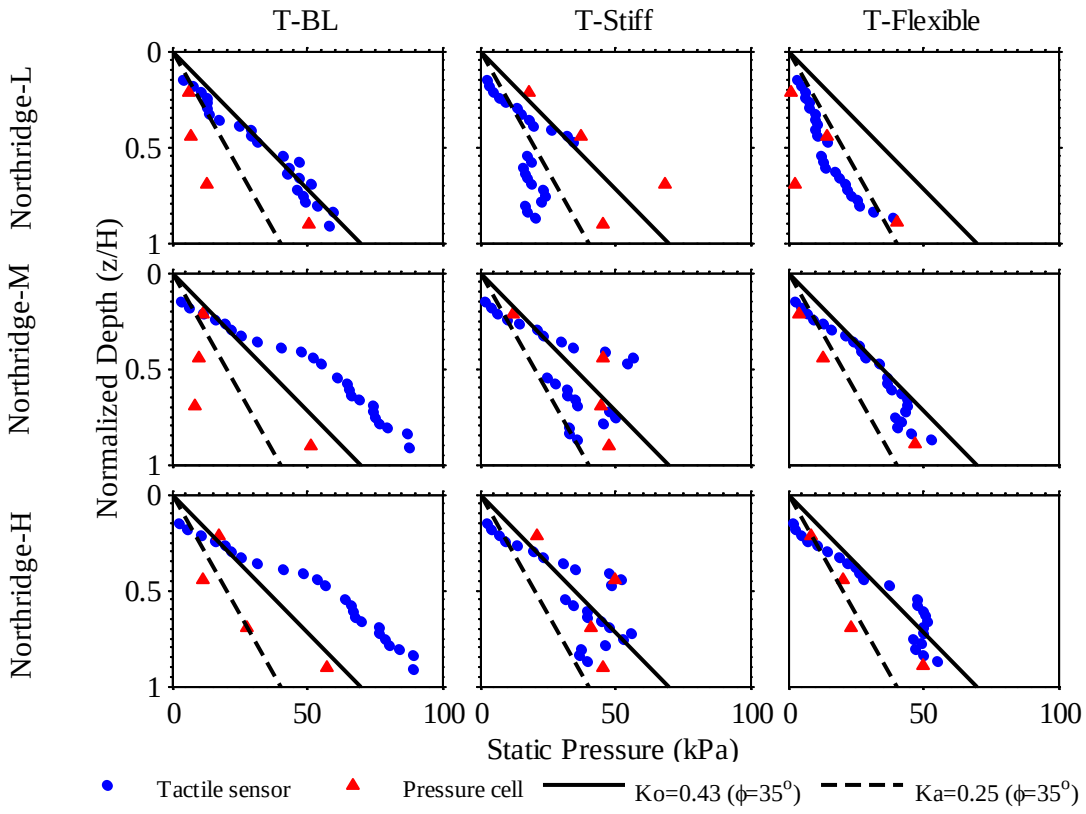

Figure B-3. Static lateral earth pressure measured with tactile sensors and pressure cells in T-BL, T-Stiff, and T-Flexible prior to the Northridge-L, Northridge-M, and Northridge-H motions.

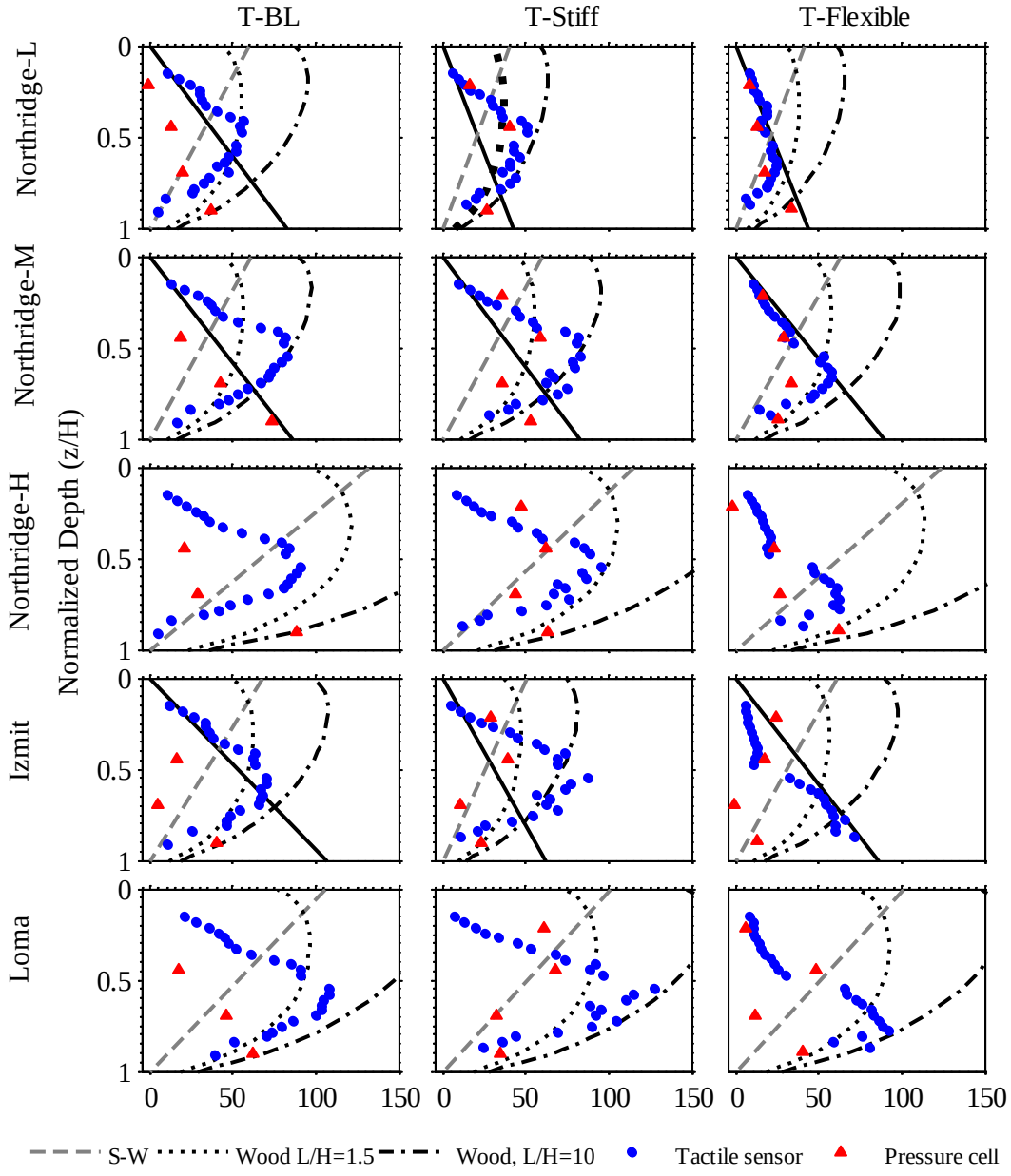

Figure B-4. Dynamic increment of pressure at time of maximum thrust measured by tactile sensors and pressure cells in T-BL, T-Stiff, and T-Flexible during Northridge-L, Northridge-M, Northridge-H, Izmit and Loma ground motions.